A NUMERICAL STUDY OF SHALE GAS FLOW IN TIGHT POROUS MEDIA THROUGH NONLINEAR TRANSPORT MODELS

BY

IFTIKHAR ALI

A Dissertation Presented to the
DEANSHIP OF GRADUATE STUDIES

KING FAHD UNIVERSITY OF PETROLEUM & MINERALS
DHAHRAN, SAUDI ARABIA

In Partial Fulfillment of the
Requirements for the Degree of

DOCTOR OF PHILOSOPHY
In
MATHEMATICS

MARCH 2016

KING FAHD UNIVERSITY OF PETROLEUM & MINERALS
DHAHRAN 31261, SAUDI ARABIA

DEANSHIP OF GRADUATE STUDIES

This thesis, written by **IFTIKHAR ALI** under the direction of his thesis adviser and approved by his thesis committee, has been presented to and accepted by the Dean of Graduate Studies, in partial fulfillment of the requirements for the degree of **DOCTOR OF PHILOSOPHY IN MATHEMATICS**.

Dissertation Committee

N.A.Malik
Dr. Nadeem A. Malik (Adviser)

Prof. Bilal Chanane (Co-adviser)

Zaman
Prof. Fiazud D. Zaman (Member)

Prof. Khaled M. Furati (Member)

K. Sepehrnoori
Prof. Kamy Sepehrnoori (Member)

Dr. Hussain Al Attas
Department Chairman

Prof. Salam A. Zummo
Dean of Graduate Studies

25/5/16
Date

To my family

ACKNOWLEDGMENTS

I am very pleased to pay my deepest gratitude to my supervisor Prof. Nadeem A. Malik for his continuous guidance and support during my PhD studies. I owe my special thanks to him for facilitating me to use freely his computing facilities and also books from his collections.

I would also like to thank Prof. Bilal Chanane, my co-supervisor, whose comments and feedback always helped me to understand the difficult concepts.

I gratefully express my deep gratitude to Dr. Hussain Al-Attass, Chairman of Mathematics Department, for his continuous encouragement. I have learnt a lot through his integrity, lustrous personality, striking ideas and solemnity with my studies during my academic period at KFUPM.

I would like to thank Prof. Kamy Sepehrnoori for providing intellectual assistance and advice. He has also provided useful data that helped me in my dissertation. Also I would like to thank committee members Prof. Khalid Furati and Prof. Faiz ud Din Zaman for their comments and feedback.

I would like to thank Information Technology Center of KFUPM for providing technical support to use latest computing facilities available at KFUPM.

I would like to thank King Fahd University for providing financial support to complete my studies. I also thank to NSTIP (KACST) for providing financial support to complete the research work through project numbers 11-OIL1663-04 and 14-OIL280-04.

Moreover, my sincere and warm thanks to all the faculty members of the Department of Mathematics, especially, Prof. Salim Messoudi, Prof. Abdelkader Boucherif, Prof. Mustapha Kassem, who taught me courses.

I also owe my immense gratitude from the depths of my heart to my parents and my family who provided me a full opportunity to devote myself for PhD studies and whose prayers are the main course of my success. Moreover, I also thanks my friends and colleagues for their cheerful and moral encouragement throughout my work.

Iftikhar Ali
May 13, 2016

TABLE OF CONTENTS

LIST OF TABLES

LIST OF FIGURES

THESIS ABSTRACT

NAME:	IFTIKHAR ALI
TITLE OF STUDY:	A NUMERICAL STUDY OF SHALE GAS FLOW IN TIGHT POROUS MEDIA THROUGH NONLINEAR TRANSPORT MODELS
MAJOR FIELD:	MATHEMATICS
DATE OF DEGREE:	March 2016

Flow through tight porous media, especially shale gas flow, is an important and fast developing discipline. At the current times, little is known about the governing equations that describe these systems. Here, we explore a range of transport equations both conventional and fractional transport equations that describe the transport systems in tight porous media, such as in shale rocks.

First, we report upon the development and application of new conventional transport model for gas flow in tight porous media. The main goal was the construction of a new realistic advection-diffusion transport model with nonlinear advection and diffusion terms, U_a and D_a respectively. $U_a(p, p_x)$ is a function of pressure $p(x,t)$ and the pressure gradient $\partial p/\partial x$, and $D_a(p)$ is a function of the pressure p. This model is based upon mass balance, and momentum balance equations, and consideration of the adsorption of the gas in the tight porous media. The model includes turbulence effects through the inclusion of a Forchchiemer's quadratic term, and it also includes the four flow regimes, that is, slip flow, Knudsen diffusion flow, transition flow, and free continuous flow, through Hagen-Poiseuille-type equation formulated in terms of a local Knudsen number, K_n. The transport equation contains compressibility coefficient, $\zeta(p)$, for each model parameter which are functions of the pressure. Thus the new model is a transient advection-diffusion partial differential equation for the pressure field, $p(x, t)$, with highly nonlinear and pressure dependent coefficients, apparent diffusivity $D_a(p)$, and apparent advection velocity $U_a(p, p_x)$.

These features give the new model a high degree of realism, and it incorporates previous models as limiting cases. The model is first developed for three-dimensional porous media, although in application we solve the simpler 1-dimensional case for which we have also developed an implicit finite volume solver containing a flux limiter for increased stability. The solver is validated by matching the simulation results against previous model results, and also against some exact solutions in limiting cases (such as steady state problems). The effectiveness of the model and solver are demonstrated by applying it to determine rock properties of shale core samples using the available data sets. From sixteen different models that were analyzed, the model in which all the parameters were pressure dependent produces the smallest relative error of the order of $O(10^{-5})$.

Its estimate of rock properties, such as the porosity ϕ and the permeability K, are more realistic than previous models. Sensitivity analysis on the model parameters show that different parameters are critical under different conditions, and that all model parameters should be retained for general applications. The model is moderately sensitive to the turbulence parameters for the cases considered. Including the turbulence term greatly improves the estimates for the shale rock characteristics such as porosity and permeability to within realistic values, indicating the importance of including turbulence effects in such types of transport models. Finally, the ability of new model to simulate pressure distributions, p, over a period of time is demonstrated with application to a shale rock core sample.

In a second part of this study, we explore fractional transport models. Fractional derivatives contain a certain type of memory retention, and are typical of non-Gaussian processes. Several different types of fractional derivatives exist (Caputo, Riemann-Liouville, Hilfer), and from these a large number of possible transport models could be posed. Here, we have considered several cases, the most important of which was the transport model containing the Hilfer derivative of fractional order $0 < \alpha < 1$, and type $0 \leq \beta \leq 1$. The Hilfer fractional derivative is essentially an interpolation between the Caputo derivative, $\beta = 0$, and the R-L derivative, $\beta = 1$. This transport model for the pressure field $p(x,t)$ was solved using the Variation Iteration Method, VIM. A parametric study of the numerical solutions for $p(x,t)$ shows that the solution converges exponentially fast for a wide range of α. Similar types of studies were carried out for other linear and non-linear fractional transport models, such as: with a time-fractional Caputo derivative in a linear model; with a time-fractional Caputo derivative in a non-linear model. These studies lay the foundations for application to fractional shale gas transport models.

LIST OF PUBLICATIONS

Here, we list the publications which are an outcome of this dissertation. Some of the results in this dissertation have appeared in the following publications, one of them is published in an ISI journal, and four of them are published in conference proceedings, and three are in preparation stages.

A: Journal Publications (ISI)

1. Iftikhar Ali and Nadeem A. Malik, "Hilfer fractional advection-diffusion equations with power-law initial condition: a Numerical study using variational iteration method", *Computer & Mathematics with Applications*, 68.10 (2014) 1161 - 1179.

B: Conference Proceedings

2. Iftikhar Ali, Nadeem A. Malik, and Bilal Chanane, "Compressibility Coefficients of Nonlinear Transport Models in Unconventional Gas Reservoirs", in "Mathematical and Computational Approaches in Advancing Modern Science and Engineering", J. Belair et al. (eds.), Springer International Publishing Switzerland 2016. DOI $10.1007/978-3-319-30379-6_1$

3. Iftikhar Ali, Nadeem A. Malik, and Bilal Chanane, "Time-Fractional Nonlinear Gas Transport Equation in Tight Porous Media: An Application in Unconventional Gas Reservoirs" in "7th International Conference on Fractional Differentiation and its Applications", June 25-27,2014, Italy.
   DOI: 10.1109/ICFDA.2014.6967353, Published by IEEE, (2014)
   http://ieeexplore.ieee.org/xpls

4. Iftikhar Ali, Nadeem A. Malik, and Bilal Chanane, "Fractional diffusion model for transport through porous media" in "5th International Conference on Porous Media and Their Applications in Science, Engineering and Industry", June 22-27, 2014, USA.
   http://dc.engconfintl.org/porous_media_V/31

5. Nadeem A. Malik, Iftikhar Ali, and Bilal Chanane, "Numerical solutions of non-linear fractional transport models in unconventional hydrocarbon reservoirs using variational iteration method" in "5th International Conference on Porous Media and Their Applications in Science, Engineering and Industry", June 22-27, 2014, USA.
   http://dc.engconfintl.org/porous_media_V/43

C: Papers in preparation

6. " A New Nonlinear Transport Model for Fluid Flow in Shale Gas Reservoirs", Nadeem A. Malik, Iftikhar Ali. In preparation, 2016.

7. “Numerical Investigation of Nonlinear Transport Models describing Gas Flow through Tight Porous Media”, Nadeem A. Malik, Iftikhar Ali. In preparation, 2016.

8. “Numerical Investigation of Time-Fractional Transport Models describing Gas Flow through Tight Porous Media.”, Nadeem A. Malik, Iftikhar Ali. In preparation, 2016.

D: Conference Abstracts - Accepted

9. “ Time Fractional Transport Model for Flow Through Tight Porous Media”, Nadeem A. Malik, Iftikhar Ali, Bilal Chanane, and Ryad A. Ghanam, 6th International Conference on Porous Media and Their Applications in Science, Engineering and Industry, 3-8 July, Hawaii 2016.

10. “Reservoir simulations of shale gas in tight rocks using a non-Linear transport model with fully pressure dependent model parameters”, Iftikhar Ali, Nadeem A. Malik, 6th International Conference on Porous Media and Their Applications in Science, Engineering and Industry, 3-8 July, Hawaii 2016.

11. “A non - Linear transport model for determining shale rock characteristics”, Iftikhar Ali, Nadeem A. Malik. Geophysical Research Abstracts, Vol. 18, EGU2016-7264, 2016, European Geophysical Union General Assembly, 17-22 April, 2016.

Nomenclature

Symbol	**Description**
D_a	Apparent transport coefficient (or hydraulic diffusivity) (m^2/s)
D_h	diameter of hydraulic tube
D_0	Characteristic transport coefficient (or hydraulic diffusivity) (m^2/s)
E_u	Upstream boundary flux error (Pa.s/m)
E_d	Downstream boundary flux error (Pa.s/m)
E_{uD}	Dimensionless upstream boundary flux error
E_{dD}	Dimensionless downstream boundary flux error
$f(K_n)$	Flow condition function (dimensionless)
$\mathbf{g}$	Gravitational acceleration vector(m^2/s)
h	hydraulic tube
$\mathbf{K}_a$	Apparent permeability tensor of gas (m^2)
L_a	Parameter (m^3 gas/m^3 solid
K_n	Knudsen number (dimensionless)

K	Intrinsic permeability (m^2)
H_a	Hydraulic length scale (m)
L_h	length of mean hydraulic flow tube
L_b	length of porous medium
M_g	Molecular weight of gas (kg/kmol)
$\mathbf{n}$	Unit vector (dimensionless)
n	number of hydraulic tubes
p	Absolute gas pressure (Pa)
p_d	Downstream gas pressure (Pa)
p_D	Dimensionless pressure
p_{dD}	Dimensionless value of the measured values of p_d
P_e	Peclet number (dimensionless)
p_L	Langmuir gas pressure (Pa)
p_u	Upstream gas pressure (Pa)
p_{uD}	Dimensionless value of the measured values of p_u
q	Mass of gas adsorbed per solid volume ($\mathrm{kg/m}^3$)
q_a	Standard volume of gas adsorbed per solid mass (std m^3/kg)
q_L	Langmuir gas volume (std m^3/kg)
R_h	Hydraulic radius of flow tube (m)
R_g	Universal gas constant (8314 J/kmol/K)

std.	Denotes standard conditions (273.15°K and 101 325Pa)
t_D	Dimensionless time
T	Absolute temperature, K
$\mathbf{u}$	Volumetric flux vector (m^3/m^2-s)
U_a	apparent convective flux vector (m/s)
U_o	Characteristic convective flux (m/s)
V_b	Bulk(total) volume of core plug (m^3)
V_d	Downstream reservoir volume (m^3)
V_D	Dimensionless convective flux vector (dimensionless)
V_p	Effective pore volume (m^3)
V_{std}	Molar volume of gas at standard temperature (273.15^{o}K) and pressure (101,325 Pa) (std m^3/kmol)
V_u	Upstream reservoir volume (m^3)
v_h	capillary tube cross-sectional average velocity of flowing gas
x	Cartesian distance in the horizontal flow direction (m)
x_D	Dimensionless distance

z	Cartesian distance in the gravitational acceleration vector direction (m)
Z	Real gas deviation factor (dimensionless)
α	Dimensionless rarefaction coefficient (dimensionless)
α_o	Asymptotic limit value of dimensionless rarefaction coefficient (dimensionless)
ζ_f	Isothermal coefficient of compressibility for the flow condition function (Pa^{-1})
ζ_ρ	Isothermal coefficient of compressibility for fluid density (Pa^{-1})
ζ_μ	Isothermal coefficient of compressibility for fluid viscosity (Pa^{-1})
ζ_ϕ	Isothermal coefficient of compressibility for porosity (Pa^{-1})
ζ_{K_a}	Isothermal coefficient of compressibility for apparent permeability (Pa^{-1})
ζ_K	Isothermal coefficient of compressibility for intrinsic permeability (Pa^{-1})
ζ_{τ_h}	Isothermal coefficient of compressibility for tortuosity (Pa^{-1})
ϕ	Porosity of porous media (fraction)

ϕ_a	Effective porosity of porous media (fraction)
λ	Mean-free-path of molecules (m)
τ_h	Tortuosity of porous media (dimensionless)
ρ	Density (kg/m^3)
ρ_s	Material density of the porous sample (kg/m^3)
μ	Dynamic viscosity of gas (Pa s)

CHAPTER 1

INTRODUCTION

1.1 Global Energy Perspective

At the current time, global energy demand is met by a number of energy resources that includes oil, gas, coal, biomass, nuclear, solar, hydro, wind and other renewable energy sources. Hydrocarbon based fuels meet more than 80% of the world's current energy requirements and the dependence on carbon based fuels still continues to grow, Figure 1.1. Oil is mostly used in the transportation industry, whereas gas and coal are mainly used to generate electricity, Figure 1.2.

World Energy Outlook [2015], a report published by International Energy Agency (IEA), says that nearly 1.3 billion people in the world are living without electricity and approximately 2.7 billion people are still relying on the traditional use of energy resources, such as, biomass or wood, for cooking. Global Energy Perspective [2014], a report published by International Institute for Applied Systems Analysis (IIASA) and the World Energy Council (WEC) says that the world population is expected to double by 2050 and that electricity demand will increase by 1.5 to 3 folds.

The world energy supply will continue to depend heavily on carbon based fuels compared to renewable energy resources (solar, wind, tidal, etc.) because they are abundant and inexpensive. In order to provide an uninterrupted supply of hydrocarbon fuels and to meet the future energy demands, new avenues must be explored, both conventional and unconventional, Islam [91].

During the past two decades, great efforts have been made to maintain a continuous supply of gas, and new gas reserves have been discovered that are different from conventional gas resources. Among them, the discovery of shale gas and tight gas has created a boom in the oil and gas industry. Shale gas is found in rocks with ultra low permeability and tight gas is found in rocks with very low porosity. The rock structure in such reservoirs is very complex and new advanced technologies are required for the extraction of gas at reasonable flow rate.

Shale gas reservoirs are found in many countries, for example, USA, Argentina, Algeria, Canada, Mexico, Australia, Saudi Arabia, see Boyer et al. [25] and KPMG [98]. Technologically recoverable global shale gas reserves are estimated in trillions of cubic feet, see Table 1.1. Advanced technologies needed to extract unconventional resources of gas at a reasonable rate include, hydraulic fracturing, horizontal drilling, accurate estimation of reservoir parameters and rock properties, and developing new transport models for reservoir simulations, Aziz and Settari [14], Peaceman [131], Chen [34], Marcondes and Sepehrnoori [113], Marcondes et al.

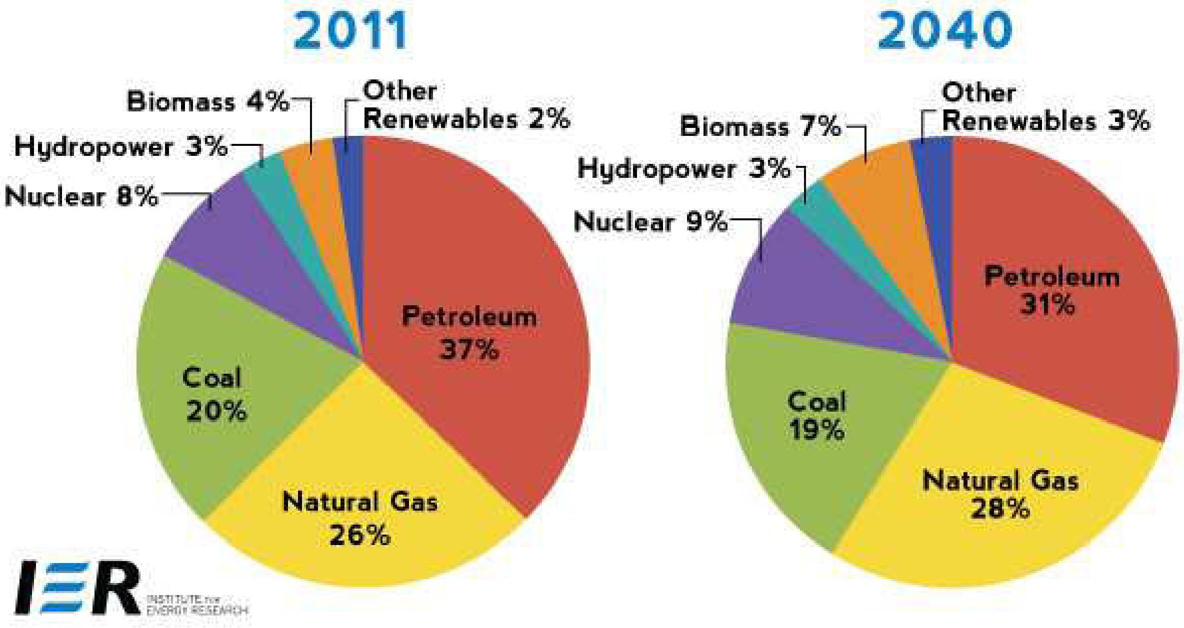

Figure 1.1: Fuel shares in energy consumption, in 2011 and projection in 2040. Source: Institute for Energy Research, IER [90]

[114], Aybar et al. [13], Fernandes et al. [62]. The geological structure of shale and tight gas rock is shown in Figure 1.3.

1.2 Unconventional Energy Resources

Unconventional resources of hydrocarbons include shale gas, tight gas, coalbed methane, deep natural gas, and gas hydrates, among others, Darishchev et al. [47]. A particular focus of attention in recent years has been put in to the extraction of hydrocarbons from unconventional reservoirs, Soeder [151] and Arthur et al. [12]. A brief description of the characteristics of some of the different types of gas reservoirs is given below.

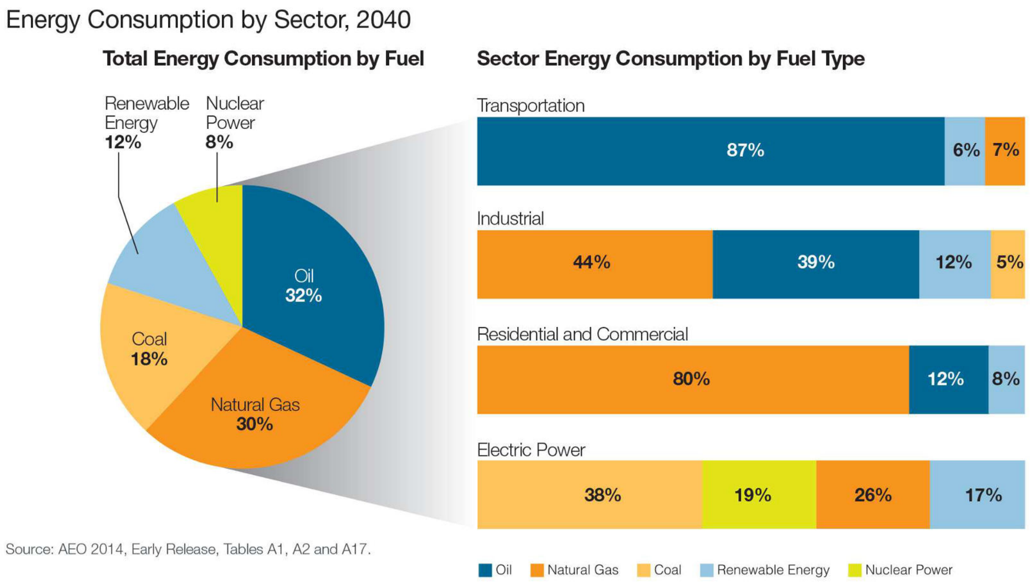

Figure 1.2: Energy consumption by sector. Source: U.S. Energy Information Administration, EIA [53]

Shale Gas

Shale gas is essentially natural gas which is created in shales (fine-grained sedimentary rocks formed by compression of successive layers), and stays within the shales. Shales serve both as the source rock, where gas is created and as the reservoir rock where gas is stored. Shales have very small pore size compared to tight and conventional gas formations. Pore size varies with respect to the location of reservoirs. Different ranges of pore size are reported in the literature, which varies from 50 nm to 200 µm, Wang et al. [166], Nia et al. [126]. Gas is stored in the network of pores and a fraction of the gas is adsorbed into the kerogen material which is the solid organic material, and a fraction of the gas is trapped inside the fractures which are the cracks or faults in the rock formation. Vesters

	Shale Gas Reserves	
Country	Trillion cubic feet [ft^3]	Trillion Cubic Meter [m^3]
France	180	5.097
Poland	187	5.295
Brazil	226	6.399
Algeria	231	6.541
Libya	290	8.211
Canada	388	10.986
Australia	396	11.213
South Africa	485	13.733
Mexico	681	19.283
Argentina	774	21.917
US	862	24.409
China	1,275	36.103
Others	647	18.321

Table 1.1: Technologically recoverable global shale gas reserve estimates, KPMG [98].

et al. [163] reported that the porosity can vary from 9% to 20%, and Darishchev et al. [47] reported that the porosity can vary from 4% to 15%. Gas shales have extremely low permeability which makes the movement of gas molecules very difficult, Aguilera [2, 3]. The permeability of shale rocks can vary from tens of nanoDarcys (nD) to microDarcys (µD), Darishchev et al. [47]. The pressure varies from 27 MPa to 60 MPa; temperature varies from 325 K to 450 K. Shale gas is typically found at depth from 2000 m to 4000 m, Figure 1.3.

Tight Gas

Tight gas is natural gas which is created in a different part of the rock formations, but is then transported into the tight rocks, Spencer [152], Darishchev et al. [47]. It is stored in interstices (the small narrow space between minerals) which may spread over large areas ranging from 20 km to 200 km. There is usually little or no water in such formations, so the gas is formed alone and spreads

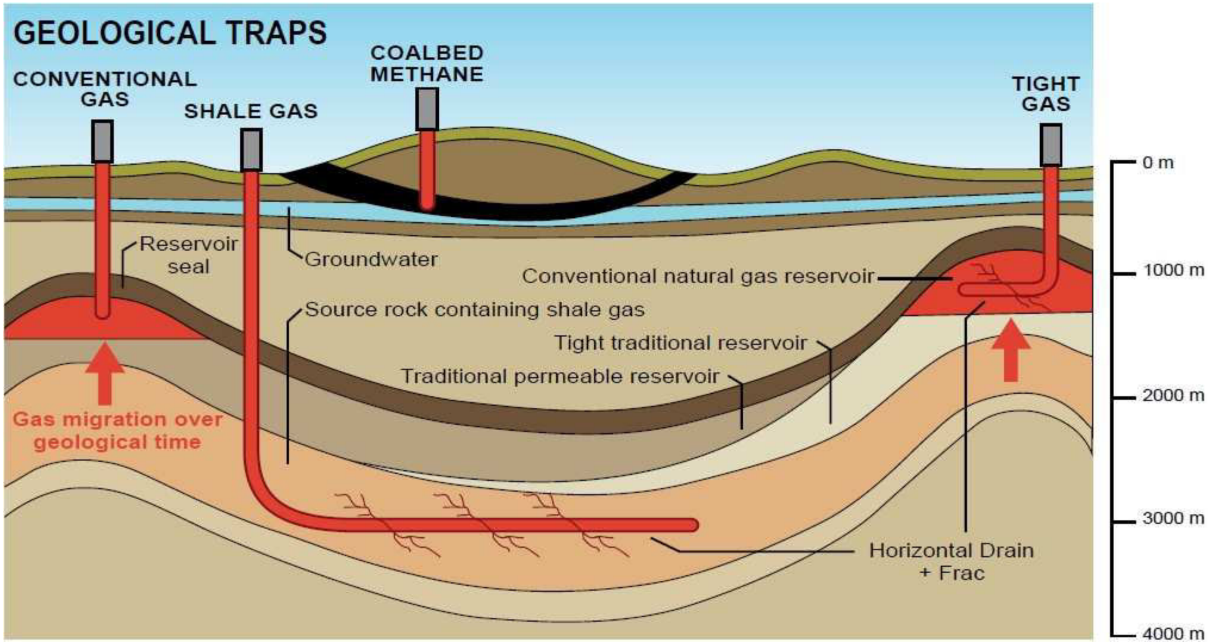

Figure 1.3: Geological structure of the hydrocarbon reservoirs is shown. Shale rocks are found at a depth of 3000 m to 4000 m. Source: U.S. Energy Information Administration, EIA [53]

continuously throughout the formations. Pore size is a little greater than the pore size of shale rocks and porosity ranges from 2% and above. Tight gas reservoirs have permeability values, greater than $1\ \mu D$ and less than $100\ \mu D$, and are found typically at depth of 3000 m to 6000 m. The temperature in such reservoirs is greater than 375 K and the effects of compaction where the rock layers are pressed very closely and hence the void spaces are reduced are significant. Furthermore, abnormally low pressures 20 MPa or high pressures 62 MPa are observed in such tight formations, Aguilera [2, 3].

Coalbed methane

Coalbed methane (CBM) is a form of natural gas extracted from coal beds. Gas is adsorbed into the solid matrix of coal by the process of adsorption, Fedorov and Fedorchenko [61], Li et al. [102]. Porosity ranges from 0.1 % to 10 %. Gas contents vary from 0.0312 m^3/kg to 0.25 m^3/kg. Permeability lies in the range of 0.1 mD to 50 mD. The thickness of coal seams changes from 0.1 m to 0.2 m. The recovery of the gas is done by the process of adsorption-desorption.

1.3 Challenges in the Extraction of Unconventional Gas Reservoirs

Unconventional gas resources, although found in large quantities, generally are difficult to produce at an economical rate. Advanced technologies are therefore needed for the exploration and extraction of unconventional gas. Low permeabilities make it necessary to induce fractures by hydraulic fracturing (fracking), and moreover since the tight gas and the shale gas reservoirs are spread over long distances wells are drilled not only in the vertical direction but also in the horizontal direction. Advances in drilling and extraction technologies makes it possible to extract gas at a much faster rate than before as it is evident from the recent shale gas boom in USA, Figure 1.4 and 1.5.

Hydraulic fracturing was first introduced in the mid-1940's as a stimulation technique to enhance the oil recovery process, and by the beginning of 1950's field experiments were conducted to check the applicability of fracturing techniques, see Economides et al. [52]. The massive use of hydraulic fracturing began in 2003, when oil companies began to explore unconventional gas resources, in particular in the shale formations in USA. Currently, hydraulic fracturing has become an

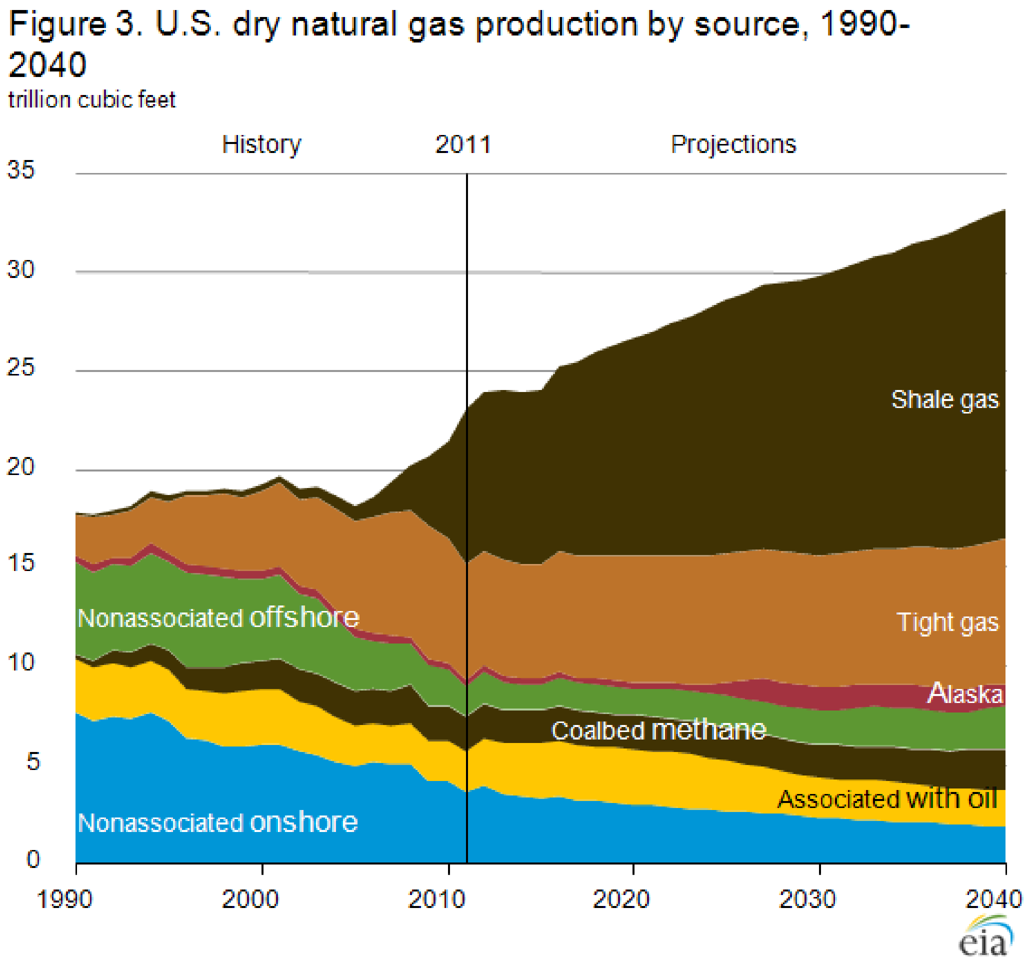

Figure 1.4: Production of dry natural gas in US. Source: U.S. Energy Information Administration, EIA [53]

important tool in the extraction of shale gas recovery.

In hydraulic fracturing, a fluid which is a mixture of water, sand, and some chemicals is injected into the wellbore at very high pressure. When the pressure exceeds the breakdown pressure of the formation, fractures are created in the rocks and the fluid starts flowing into the induced fractures. Hydraulic fracturing is also combined with horizontal drilling in order to cover more area inside the reservoir.

Advanced drilling and extraction techniques, such as hydraulic fracturing and

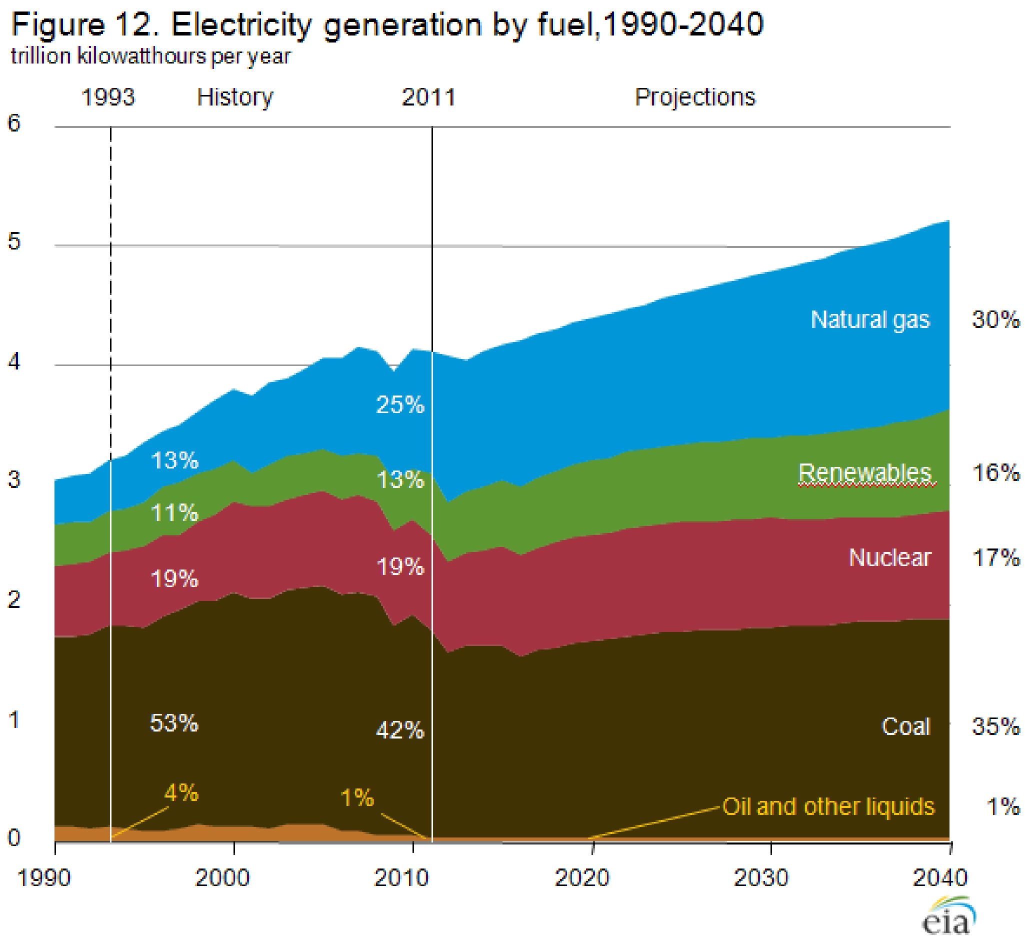

Figure 1.5: Power generation by fuel. Source: U.S. Energy Information Administration, EIA [53]

horizontal drilling, are very expensive and in order to maximize the benefits of such techniques, the drilling and the extraction process is augmented with field experiments and reservoir simulations. Experiments are carried out to determine the rock properties of the shale gas formations. One of the most important property is the rock permeability. Many techniques have been employed to determine this, but the most efficient and reliable technique is the use of transient pressure pulse techniques. In this method, a reservoir sub-surface rock core sample is placed in the core plug whose two ends are connected to two reservoirs, one is called upstream reservoir and the other is called downstream reservoir. Initially, the pressure is at the equilibrium level; and then a sudden pulse is introduced in the upstream reservoir and the pressure is monitored at both the upstream and the downstream reservoirs, Figure 1.6.

A drawback with transient pressure pulse tests is that they are time consuming and have to be repeated several times in order to be certain about the measured properties of rocks.

Pressure pulse tests are therefore, often complimented by mathematical transport models to describe the fluid flow through the tight porous rocks. A realistic transport model is an important tool in the petroleum industry because it allows the transport of gas and future pressure distributions to be estimated to an accuracy which assists in planning drilling strategies, and future recovery levels, and policy, Satter et al. [149], Hanea et al. [77], Møyner et al. [122]. A realistic transport model can save the oil industry some of the huge costs of field experiments and unsuccessful drilling that would otherwise be needed.

Transport models are obtained by considering the continuity equation combined with a momentum equation (e.g., the Darcy-Forchhemier law). The resulting equations are transient advection-diffusion equations together with initial and boundary conditions. The mathematical model is used to simulate the pressure pulse decay test. The simulations are carried out for different parameter values and the results are matched with the experimental data to get a best estimate for the permeability, Civan et al. [41], Cui et al. [44].

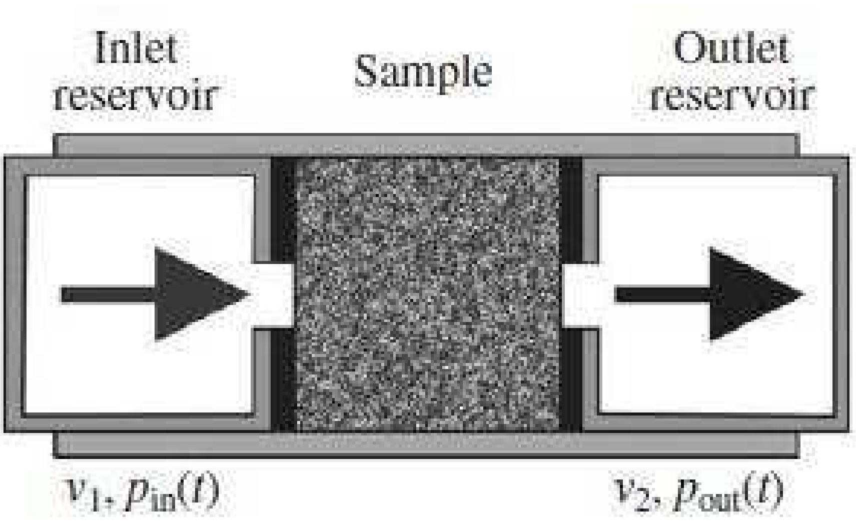

Figure 1.6: Transient pressure pulse test, Malkovsky et al. [112].

Figure 1.6 depicts the transient pressure pulse test process. Various studies have been performed to analyze the pressure pulse tests by using different transport models (as described in the section of transport models survey in Chapter 2). Some researchers have developed nonlinear transport models to investigate the fluid flow in the reservoir and to determine the hydraulic properties of the shale gas reservoirs. However, current shale gas transport models are still at an early stage of development, and there is an urgent need to further develop transport models that incorporate more realism of the gas transport process in the tight porous media.

Transport models arise mathematically as advection-diffusion partial differential equations (PDE's). In conventional fluid mechanics only two parameters govern the transport, namely the fluid viscosity (μ) and the diffusivity (D) both of which are often constants in many applications. In tight gas flow in porous media, many more modeling parameters appear and the transport equation may be highly nonlinear because the apparent velocity U_a and apparent diffusivity D_a are nonlinear functions of the pressure $p(x, t)$, and of the pressure gradient $p_x(x, t)$. The system is complex and much more difficult to solve numerically, and special numerical methods must be developed.

Some progress has been made in developing such nonlinear transport models, notably by Cui et al. [44] and Civan et al. [41], each of which incorporate a certain degree of realism, but still fall short of the level of realism that is needed in current shale gas reservoirs.

Recent interest has grown in fractional transport models in porous media, see Raghavan et al. [139], Raghavan [138], Mohan et al. [120], and Ozcan [130]. As yet little is known about transport in tight porous media, and it is worth exploring non-standard, fractional models, since these models could potentially describe such systems in a better and simpler way.

The main aim here therefore is to explore different types of models for gas flow in tight porous media, both conventional transport models and non-conventional fractional transport models. We develop upon the knowledge gained from previous works and construct a new nonlinear transport model for the flow of gas in tight porous media with a greater degree of realism. A further aim is to demonstrate the ability of the new model in application to two types of problems. First, to estimate rock properties such as the permeability and porosity through fitting the model simulations to the available data - a type of inverse problem. Second, the new transport model will be used as the basis for reservoir simulations to predict future pressure distributions in different reservoirs over a period of time.

A second phase of the work has been carried out to explore an alternative type of transport model for fluid flow, within the framework of newly emerging mathematical methods using fractional calculus. It incorporates a greater degree of "memory effect", and leads to anomalous diffusion regimes. We explore this method with application to fluid transport in porous media.

The outline of the dissertation is as follows.

In Chapter 2 we discuss the geophysical properties of unconventional reservoirs, such as rock types and how the fluids are transported through them. We discuss the various flow regimes that occur in the reservoir and we give the classification of flow regimes based on the Knudsen number. We also detail the process of modeling transport phenomena through porous media. The significance of Darcy's law and the Forchheimer correction is also presented. Moreover, we review some of the transport models that are used to analyzed the pressure distribution in porous materials.

In Chapter 3 we present the derivation of the new nonlinear transport model for fluid flow through the tight porous media, including shale rocks. The model is derived using mass and momentum balance equations in a 3D formulation. The model is cast as a pressure equation and presented in terms of compressibility coefficients ($\zeta_\gamma(p)$) which are associated with each model parameter and are functions of pressure. Moreover, we also give the 1D form of the transport model with appropriate boundary conditions. Steady state and dimensionless versions of the transport model are also given.

In Chapter 4 we explain the various model parameters and their compressibility coefficients that appear in the transport model. We give the definitions of the gas deviation factor, the gas density, the gas viscosity, the porosity, the tortuosity, the turbulence factor, the Knudsen number, the mean free path, the radius, the intrinsic permeability, the apparent permeability, the permeability correction factor, and we also derive expressions for their compressibility coefficients. The inter-dependence of various model parameters and their compressibility coefficients is also discussed. Moreover, we also discuss some of the limiting cases of the new transport model which reduce to the previous transport models.

In Chapter 5 we describe the numerical solver. We have used finite volume method for calculating the approximate solutions of the new transport model. The spatial domain is partitioned into elements of equal volume. Discretization of transient, convection, diffusion, and source terms is explained. For the convection term, we implement an upwind scheme, which is further improved by the use of second order flux limiters. Boundary conditions are discretized by considering ghost cells adjacent to the boundaries. Finally, we give the matrix form of the system of non-linear algebraic equations. We give the numerical algorithms for finding the approximate solutions. The validation of numerical solver is shown by finding the numerical solutions of three partial differential equations, and compared the results with the exact solutions. The order of convergence of the numerical solver is also determined.

In Chapter 6 we present the validation of the steady state transport model with our new approach. We validate the model against experimental data. We consider sixteen cases where we show that the incorporation of the full pressure dependent parameters provides the best match against the data. Furthermore, we analyze the sensitivity of the model to the various model parameters, which helps us to fix some of the parameter values and thus reduce the number of model parameters. The sensitivity analysis is carried out using one-at-a-time (OAT) methodology.

In Chapter 7 we validate the unsteady (transient) new transport model, and model solver, by reproducing the results of previous transport models which are limiting cases of the new transport model. We use the full nonlinear transport model to simulate the results of the pressure pulse decay test. Finally, we demonstrate the full capacity of the new model by applying it as a reservoir simulator for predicting the pressure field $p(x, t)$ in a horizontal shale gas reservoir over a period of two years.

In Chapter 8 we report on the additional work which is based on the method of fractional calculus and is particularly useful for explaining anomalous diffusion observed in many physical contexts.

In Chapter 9 we summarize the conclusions of the current study, and in Chapter 10 we set out the directions for the future work.

CHAPTER 2

FLUID FLOW IN POROUS MEDIA

2.1 Rock Types and Transport Processes

Rocks are naturally formed solid matter which are broadly classified into three main categories, sedimentary, metamorphic, and igneous. Among them sedimentary rocks contain the energy-rich material called kerogen which is composed of carbon compounds. Sedimentary rocks are further classified into shales, sandstones and carbonates, Figure 2.1. Shales are sedimentary rocks and are found abundantly (40%) on earth. These are the source of natural fuels which are produced through extraction process. Sandstones are porous rocks which are formed above shale beds and trap low density carbon compounds. These are created from grains of minerals like quartz bound by other compounds, such as silica. Within sandstone beds, carbon compounds exist in liquid form. Carbonates are found in

Figure 2.1: Different types of rocks. Source: www.Imageck.com

conjunction with shale and are formed usually from the remains of marine life, such as shells, bones combined with other minerals. Since these rocks are full of calcium they are further classified into limestone and dolomites, Raymond [142], Boggs [23].

Extraction is the process of releasing hydrocarbons from rocks. It is a complex process which sometimes involves heating the kerogen within the shale and then producing liquid oil and gas. Oftentimes, hydraulic fracturing is used to enhance the oil and gas recovery process, Hubbert and Willis [88], Middleton et al. [118], Zhang et al. [178], Behnia et al. [17], Xie et al. [171], Huang et al. [87], Yu et al. [175], Aybar et al. [13].

Fluid flow in porous media occurs in interconnected void spaces. The fluid may be of single phase (either liquid or gas), or two phase (both liquid and gas), or even multiphase because solid particles can also be transported within the pores. Furthermore, the fluid may contain several chemical species (sometimes deliberately added, such as, methanol, lead, sulfuric acid, silica, water, and etc). Solvents are used to open up channels/ pore spaces and coagulants to block pores and channels. Fluid flow in porous media is a highly complex phenomenon involving many variables and many sub-processes, Bird [20], Bear [16], Mahdi et al. [109], Zhang et al. [177], Su and Davidson [154], Muljadi et al. [123], Ramakrishnan and Goode [140]. Unlike conventional fluid flow, such as flow through pipes where the exact balance equations (Navier-Stokes) are known and only the properties of the fluid, viscosity and density, and a single parameter, the Reynold's number, describe the system, in porous media the exact balance equations are unknown and the properties of the porous media itself, such as the porosity and the permeability, also play a leading role, Cui et al. [44], Chen et al. [32], Civan [39]. Sometimes, you also have to deal with turbulence and multiphase flow, and there are several flow regimes present, such as surface diffusion and Knudsen diffusion. It is also possible that the rock properties change in response to changes in the pressure and to the prevailing conditions; pore passages may become blocked over time, or same passages may opened up. A general theory for flow in porous media is unknown, so we have to resort to empirical relationships, like Darcy's law, in order to model the system at hand, Vafai [157], Müller-Huber et al. [124], Faybishenko et al. [60], Benzerga [18].

2.2 Modeling Transport in Porous Media

Mathematical models that describe the transport of gas through tight reservoirs are based upon consideration of the amount of gas that is transported through the reservoir and the amount of gas that is retained in it. Such models appear in the form of partial differential equations (PDE's). The principal parameters upon which most models are based are the intrinsic rock permeability (K) and the rock porosity (ϕ). An accurate determination of these properties is therefore an essential prerequisite for describing the transport of fluid through porous media, Freeman et al. [68], Sun et al. [155], Guo et al. [74].

2.2.1 Darcy's Law and Forchheimer's Correction

Darcy [46] proposed an equation for the pressure field in porous media,

$$-\nabla p = \frac{\mu}{\kappa} u \tag{2.2.1}$$

where p, κ, μ, and u denote the pressure, the permeability, the viscosity, and the velocity, respectively. Darcy's law yields good results for laminar flow in high porosity porous media, but in case of high velocity flow rate it does not produce satisfactory results, Prada and Civan [135], Xu et al. [172], Guo et al. [73]. Several studies have shown that the use of the mathematical models based on Darcy's law are inadequate to study transport process through unconventional porous rocks because different non-laminar flow regimes occur in tight porous media other than the continuous (viscous) flow, Thauvin and Mohanty [156], Cui et al. [44], Civan et al. [41], Macini et al. [108]. The results obtained by models based upon the conventional Darcy's law show significant deviations from experimental data. To correct for this, Forchheimer [67] first introduced a quadratic term in the Darcy's law, that is,

$$-\nabla p = \frac{\mu}{\kappa} u + \rho \beta u^2, \tag{2.2.2}$$

to account for high velocity flow rates and also for inertial effects. Here ρ denotes the gas density and β denotes the non-Darcy effects. Many attempts have been made by different researchers, e.g. Li et al. [103], to modify the Darcy's law and to propose generalized models of Forchheimer's equation to explain such deviations. It has been suggested that different approaches, other than Darcy's law, have to be employed in order to describe the gas flow through tight porous media, Huang et al. [86]. Different flow regimes have been observed in the interconnected pores and such flow regimes are caused by different physical effects, such as the prevailing pore structure and inter-connectivity (network) between the pores, the pore size distribution, the flow conditions, and the molecular mean free path.

2.3 Classifications of flow regimes based on Knudsen numbers

Different flow conditions including viscous flow, slip flow, transition flow, and Knudsen flow, occur in conventional rocks, and in tight rock formations, and in shale rock formations. These regimes deviate from the continuous flow, and require a different treatment than Darcy's law. The flow regimes can, however, be classified through the Knudsen number, Ziarani and Aguilera [181], which is defined as the ratio of the molecular mean free path to the radius of the flow

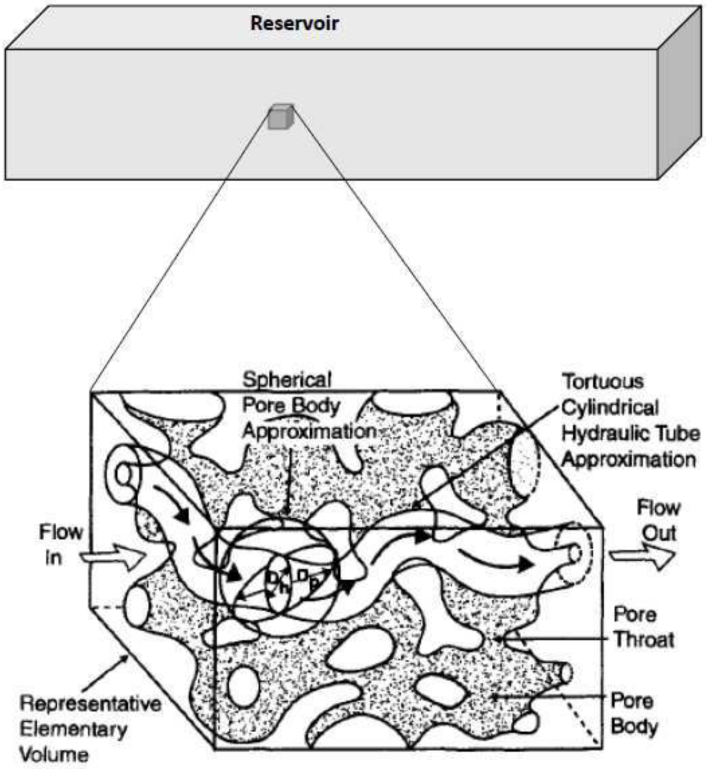

Figure 2.2: Representative elementary volume of a porous media which represents the structure of the solid matrix. Notice that the pores are given spherical geometry and flow channels are represented as cylindrical tubes. Civan [37]

channels,

$$K_n = \frac{\lambda}{R_h} \tag{2.3.1}$$

where R_h denotes the hydraulic radius and λ denotes the mean free path of molecules, given by Loeb [106],

$$\lambda = \frac{\mu}{p}\sqrt{\frac{\pi R_g T}{2M}}, \tag{2.3.2}$$

where p is the absolute gas pressure (Pascal), T is the absolute temperature (Kelvin), M is the molecular mass (kilogram per kilomole), $R_g = 8134 J/kmol/K$ is the universal gas constant, and μ is the viscosity of gas (Pascal-second).

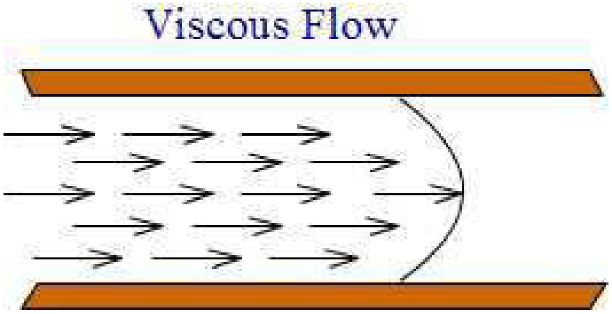

Figure 2.3: Viscous flow occurs when the radius of the flow channels is very large compared to the mean free path of the gas molecules. Darcy's law is used to describe the continuous (laminar) flow.

The hydraulic radius R_h is the mean radius of a system of pores and is given by, Carman and Carman [29] and Civan [38],

$$R_h = 2\sqrt{2\tau_h}\sqrt{\frac{K}{\phi}}, \tag{2.3.3}$$

where τ_h is the tortuosity which is the ratio of apparent length of the effective mean hydraulic tube to the physical length of the bulk porous media, and ϕ is the porosity which is the fraction of volume of void spaces to the bulk volume of the porous media.

Substituting Eqs. (2.3.2) and (2.3.3) into Eq. (2.3.1), yields an expression for the Knudsen number,

$$K_n = \frac{\mu}{4p}\sqrt{\frac{\pi R_g T \phi}{M_g \tau_h K}}. \tag{2.3.4}$$

With this definition of the Knudsen number, K_n, the flow regimes are classified as follows:

- Continuum (Viscous, Cussler [45]) Flow. For $K_n < 0.01$, viscous flow is dominant, and conventional Darcy's law can be used to describe the flow. Darcy's

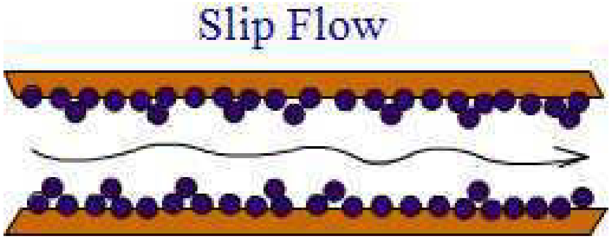

Figure 2.4: Slip flow occurs due to accumulation of gas molecules along pore surface. When more gas molecules collide with the pore surface movement in the gas molecules occur because of hopping. Darcy's law starts to fail in the slip and transition flow regimes.

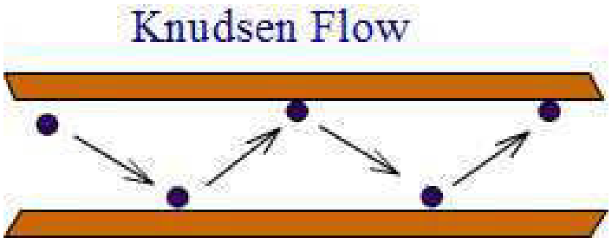

Figure 2.5: Knudsen diffusion or free molecular flow occurs when the radius of the flow channels is very small compared to the mean free path of the gas molecules. Darcy's law completely fails in this regime.

law was derived on the assumption of laminar flow for small Reynolds number $Re \approx O(1)$, Figure 2.3.

- Slip Flow(Cussler [45]). For $0.01 < K_n < 0.1$, gas molecules accumulate along the inside surface of the pore Figure 2.4 and they push gas molecules towards the pore interfaces. Conventional flow equations, Darcy's law, can be employed with some modifications.

- Transition Flow (Ziarani and Aguilera [181]). For $0.1 < K_n < 10$, during the slipping phenomenon, when the gas molecules collide with the gas molecules already stuck to the surface of the porous rocks, they exert some force on the molecules and some of the gas molecules leave the pore surface and become a part of the continuous flow. This is a flow regime in which the conventional fluid dynamics equations fail, and the higher the Knudsen number, the higher the probability of failure. The validity of conventional equations is questionable, and it is safer to use Knudsen diffusion equations especially for flow at higher Knudsen numbers.

- Knudsen (free molecular) Flow (Ziarani and Aguilera [181]). For $K_n > 10$, the mean free path of the gas molecules is much greater than the radius of the flow channels and gas molecules collide more frequently with the pore walls compared to the collision rate between gas molecules. Darcy's law completely breaks down, and alternative equations, such as a diffusion-based formulations, must be used. In this type of flow, gas molecules flow with minimal or no interaction with neighboring molecules. It usually occurs in systems with low pressures or very tight pore throats as in the case of shale gas or coalbed methane formations, Figure 2.5.

The aim here is to derive a transport equation that encompasses all of these regimes in a single universal formulation.

2.4 Intrinsic Permeability and Apparent Permeability

The transport of gas through tight rocks and shale formations include different flow regimes, and is governed by many fluid and rock properties. Gas slippage in a porous medium leads to higher than expected measured gas permeability, the apparent permeability $\mathbf{K}_a$, compared to the liquid permeability also called the intrinsic permeability $\mathbf{K}$, Chen et al. [32]. Many correlations between intrinsic and apparent permeabilities have been proposed in the literature, Klinkenberg et al. [97], Jones et al. [95]. An improved formula, derived from Hagen-Poiseuille-type equation, is given by Beskok and Karniadakis [19] as,

$$K_a = K f(K_n) \tag{2.4.1}$$

where $f(K_n)$ is the flow condition function and is given by

$$f(K_n) = (1 + \alpha K_n)\left(1 + \frac{4K_n}{1 - bK_n}\right), \tag{2.4.2}$$

where α is called the Rarefaction Coefficient Correlation, Civan [38], and it is given by

$$\alpha = \alpha_o\left(\frac{K_n^B}{K_n^B + A}\right), \tag{2.4.3}$$

where A and B are empirical constants and b in Eq. (2.4.2) is called the slip factor.

2.5 Gas Adsorption Isotherm

As the gas is transported through the tight pore network, some of the gas adheres (clings) to pore surfaces due to the diffusion of gas molecules. Cui et al. [44] and Civan et al. [41] developed a formula for estimating the amount of adsorbed gas based on Langmuir isotherms and is given by

$$q = \frac{\rho_s M_g}{V_{std}} q_a = \frac{\rho_s M_g}{V_{std}} \frac{q_L p}{p_L + p}, \tag{2.5.1}$$

where ρ_s (kg/m^3) denotes the material density of the porous sample, q (kg/m^3) is the mass of gas adsorbed per solid volume, q_a (std m^3/kg) is the standard volume of gas adsorbed per solid mass, q_L (std m^3/kg) is the Langmuir gas volume, V_{std} (std m^3/kmol) is the molar volume of gas at standard temperature (273.15K) and pressure (101,325Pa), p (Pa) is the gas pressure, p_L (Pa) is the Langmuir gas pressure, and M_g (kg/kmol) is the molecular weight of gas.

Cui et al. [44] has also defined a non-dimensional parameter L_a (m^3 gas/ m^3 solid) which is given by

$$L_a \equiv \frac{\partial q}{\partial \rho} = \frac{\rho_s M_g}{\rho \zeta_\rho(p) V_{std}} \frac{q_L p_L}{(p_L + p)^2} \tag{2.5.2}$$

where the gas density ρ (kg/m^3) is given by the real-gas equation of state as

$$\rho = \frac{p M_g}{Z R_g T} \tag{2.5.3}$$

where Z (dimensionless) is the real gas deviation factor. Combining equations (2.5.1) and (2.5.3) yields

$$\frac{q}{\rho} = \frac{\rho_s q_L Z R_g T}{V_{std}(p_L + p)}. \tag{2.5.4}$$

2.6 Previous Mathematical Models

Low permeability and low porosity are the main features of unconventional gas reservoirs. A knowledge of the permeability and porosity are essential in the investigation of the shale formations. In reservoir simulations, permeability plays a leading role in the modeling of the gas flow. Both time and money is required in the measurement of permeabilities of tight and shale rock samples and the experiments have to be repeated several times on different rock samples in order to obtain accurate values for the rock permeability and porosity.

Many researchers have used mathematical models to obtain estimates for the permeability under steady state and unsteady flow conditions. Here, we give a brief review of some of the transport models that have been used to estimate rock properties.

Hsieh et al. [84] and Neuzil et al. [125] derived a model to describe fluid flow in a transient pulse test by considering the compressive storage of the rock sample. They measured the hydraulic properties of rock samples with low permeabilities. They also employed transient pulse tests in the laboratory to estimate the sample properties. The transport model is a simple diffusion equation,

$$\frac{\partial^2 h}{\partial x^2} - \frac{S_s}{K}\frac{\partial h}{\partial t} = 0 \qquad \text{for } 0 < x < 1 \text{ and } t > 0, \tag{2.6.1}$$

with the initial and boundary conditions,

$$\begin{aligned} h(x,0) &= 0 && \text{for } 0 < x < 1 \\ h(0,t) &= h_d(t) && \text{for } t \geq 0 \\ h(L,t) &= h_u(t) && \text{for } t \geq 0. \end{aligned}$$

Flux conditions at the left and the right boundaries are,

$$\begin{aligned} \frac{S_d}{KA}\frac{dh_d}{dt} - \left(\frac{\partial h}{\partial x}\right)_{x=0} &= 0 && \text{for } t \geq 0 \\ h_d(0) &= 0 \\ \frac{S_u}{KA}\frac{dh_u}{dt} + \left(\frac{\partial h}{\partial x}\right)_{x=L} &= 0 && \text{for } t \geq 0 \\ h_u(0) &= H, \end{aligned}$$

where, h is the hydraulic head in the sample, h_d is the hydraulic head in the downstream reservoir, h_u is the hydraulic head in the upstream reservoir, x denotes the distance along the sample, $x = 0$ is the down stream face, and $x = L$ is the upstream face of the sample, t is the time from the start of the experiment, H is the instantaneous increase in hydraulic head, A is the cross-sectional area of the sample, L is the length of the sample, S_u is the compressive storage of the upstream reservoir, S_d is the compressive storage of the downstream reservoir, K is the hydraulic conductivity of the sample.

The transport model Eq. (2.6.1) is a nonlinear initial-boundary value problem which was solved analytically under some assumptions, for example, linearization of the model, or assuming that the permeability and specific storage of the test sample to be constants. The analytical solutions were then used to compute the permeability and the specific storage of the test sample, and the simulated pressure was compared with the measured pressure values at the inlet point. They obtained good match with the experimental data and estimated the value of permeability equal to $K = 6.3 \times 10^{-15}$ m^2.

Liang et al. [104] estimated the permeability of tight rocks by using a nonlinear pressure diffusion equations to model the transient pressure pulse decay test. Their model is,

$$\frac{\partial p}{\partial t} = D\frac{\partial^2 p}{\partial x^2} + D\left(\frac{1}{K}\frac{\partial K}{\partial p} + \beta_f\right)\left(\frac{\partial p}{\partial x}\right)^2 \qquad \text{for } 0 < x < L, \quad t > 0. \tag{2.6.2}$$

The flux conditions at the boundaries are given by,

$$\begin{aligned} \frac{dp_1}{\partial dt} &= \frac{DA\phi}{V_1}\left(\frac{\partial p}{\partial x}\right)_{x=0,t>0} \\ \frac{dp_2}{\partial dt} &= -\frac{DA\phi}{V_2}\left(\frac{\partial p}{\partial x}\right)_{x=L,t>0} \end{aligned}$$

The initial condition is given by

$$p(x,0) = p_1(0) \text{ for } 0 < x \leq L,$$

$$p(x,0) = p_2(0) \text{ at } x = 0.$$

and

$$D = \frac{K}{\phi \mu (\beta_f + \beta_v)}$$

where x is the distance along the sample, t is the time from the start of the experiment, A is the cross-sectional area of the sample, L is the length of the sample, ϕ is porosity, p_1 is pressure at upstream reservoir, p_2 is pressure at downstream reservoir, V_1 is volume of upstream reservoir, V_2 is volume of downstream reservoir, μ is viscosity, β_f is isothermal compressibility of fluid, β_v is pore volume compressibility, D is function of pressure and is called the diffusivity coefficient.

Liang's model Eq. (2.6.2) is a nonlinear advection-diffusion equation together with initial condition and flux conditions which are prescribed at the inlet and the outlet boundaries. Liang found the approximate solutions of Eq. (2.6.2) by perturbation methods. He then matched the approximate solutions with the laboratory measured pulse decay data to estimate the permeability of the test sample. They estimated the following value permeability $K = 1.71 \times 10^{-21}$ m^2 where the porosity was $\phi = 0.03$. Liang's calculations are valid when the volume and pressure of the interconnected pore fluid is much smaller than the volume and pressure of the upstream reservoir.

Malkovsky et al. [112] modified the pressure pulse transient method to measure the permeability of rock samples. Their mathematical model for the pressure pulse transient method is,

$$\frac{\mu\phi}{K}\left(\beta_f + \frac{\beta_r}{\phi} - \frac{1+\phi}{\phi}\beta_s\right)\frac{\partial p}{\partial t} = \frac{\partial^2 p}{\partial x^2} \qquad \text{for } 0 < x < L, \quad t > 0, \qquad (2.6.3)$$

with initial condition

$$p(x,0) = \begin{cases} p_0 & \text{for } 0 < x < L \\ p_0 + \Delta p & \text{for } x = 0 \end{cases}$$

and flux conditions

$$\frac{\partial p}{\partial x} = \frac{\mu V_1 \beta_f}{AK}\left(\frac{\partial p}{\partial t}\right)_{x=0,t>0}$$
$$\frac{\partial p}{\partial x} = \frac{\mu V_2 \mu \beta_f}{AK}\left(\frac{\partial p}{\partial t}\right)_{x=L,t>0}$$

where, p is pressure, x is distance from entry end of sample, t is time from the start of the experiment, A is cross-sectional area of the sample, L is the length of the sample, ζ_f is compressibility of fluid, ζ_r is the integral rock compressibility, ζ_s is the compressibility of rock sample, μ is viscosity, V_1 is volume of upstream reservoir, V_2 is volume of downstream reservoir.

Malkovsky's model Eq. (2.6.3) is a nonlinear diffusion equation together with initial condition, and flux conditions which are prescribed at the inlet and the outlet boundaries. The model was derived for a single phase fluid in a porous media under normal conditions and also under high pressure and temperature conditions. Malkovsky used the numerical solutions of the above model to determine the permeability of the layered rock sample to be in the range of 10^{-22} m^2 to 10^{-15} m^2, the porosity was $\phi = 0.13$. They obtained a very good match with the experimental data.

Cui et al. [44] considered the effects of gas adsorption and developed a relation Eq. (2.5.2) to use in the model for calculating the permeability and diffusivity values of tight gas reservoirs. Cui's model is,

$$\begin{aligned} \phi\frac{\partial \rho}{\partial t} + (1-\phi)\frac{\partial q}{\partial t} &= \frac{1}{r^m}\frac{\partial}{\partial r}\left(r^m \frac{\rho K}{\mu}\frac{\partial p}{\partial r}\right) \\ \frac{\partial p}{\partial t} &= \frac{K}{r^m}\frac{\partial}{\partial r}\left(r^m \frac{\partial p}{\partial r}\right) \\ K &= \frac{k}{\mu c_g[\phi + (1-\phi)K_a]} \end{aligned} \tag{2.6.4}$$

where t is time, ρ is gas density, q is adsorbate density, ϕ is porosity, p is pressure, k is permeability, μ is gas viscosity, r is displacement, and r is distance when $m = 0$, r is radius in axis-symmetric cylindrical coordinates system when $m = 1$, and r is radius in spherical coordinates system when $m = 2$.

Cui's model Eq. (2.6.4) incorporates the effects of gas adsorption in the tight porous rock, it describes the gas transport in the regions where the Darcy's law prevails. Cui used the late time experimental data for the measurement of rock properties of tight rocks instead of early time experimental data. Cui also mentioned in his work that the permeability determined from small sample size may not represent the true permeability of the entire rock matrix in fractured reservoir, and hence the permeability values need to be scaled as required. Moreover, he suggested that the experimental data and the numerical results for the estimation of the permeability and the diffusivity must be combined with field tests for a complete description of the reservoir. Cui estimated the value of permeability equal to $K = 5 \times 10^{-18}$ m^2, where the porosity was $\phi = 0.05$.

Civan et al. [41] produced an improved model for the determination of shale gas permeability and diffusivity. His transport model was based on the idea of relevant gas retention (amount of gas adsorbed in the porous material) and the amount of gas present in the void spaces. Civan's model is

$$\frac{\partial p}{\partial t} + U_a(p, p_x)\frac{\partial p}{\partial x} = D_a(p)\frac{\partial^2 p}{\partial x^2} \qquad \text{for } 0 \le x \le L, t > 0 \tag{2.6.5}$$

where x, t, and p denote distance, time and pressure, respectively. The apparent velocity, denoted by $U_a = U_a(p, p_x)$, is given by,

$$U_a(p, p_x) = -[\zeta_\rho(p) + \zeta_K(p) + \zeta_f(p) - \zeta_\mu(p)] D_a \frac{\partial p}{\partial x},$$

and the diffusivity coefficient $D_a = D_a(p)$ is given by,

$$D_a(p) = \frac{K}{\mu\left[\phi(\zeta_\rho(p) + \zeta_\phi(p)) + (1-\phi)\left(K_a\zeta_\rho - \left(\frac{\phi}{1-\phi}\frac{q}{\rho}\zeta_\phi(p)\right)\right)\right]}.$$

Note that the ζs represent compressibility coefficients of various parameters.

Initial and boundary conditions are given by,

$$\begin{aligned} p(x,0) &= p_0 && \text{for } 0 \leq x \leq 1 \\ p(0,t) &= p_u(t) && \text{for } t \geq 0 \\ p(L,t) &= p_d(t) && \text{for } t \geq 0 \end{aligned}$$

Flux conditions at the left and the right boundaries are given by,

$$\begin{aligned} \frac{V_u \mu \phi L}{V_p K} \zeta_\rho(p) \left(\frac{\partial p}{\partial t} \right) &= \frac{\partial p}{\partial x} && \text{for } p = p_u, x = 0, t > 0 \\ -\frac{V_d \mu \phi L}{V_p K} \zeta_\rho(p) \left(\frac{\partial p}{\partial t} \right) &= \frac{\partial p}{\partial x} && \text{for } p = p_d, x = L, t > 0 \end{aligned}$$

Civan's model Eq. (2.6.5) encompasses all the flow regimes by the use of Knudsen number and thus presents a universal treatment of gas transport process in tight porous media. Civan obtained the numerical solutions of the model and matched the results with the experimental data to obtain estimates for the permeability $K = 1.97 \times 10^{-19}$ m^2, where the value of porosity was $\phi = 0.05$. In Civan's model, various gas and reservoir properties are taken as pressure dependent, but in actual calculations he took them to be constant for many of these parameters.

CHAPTER 3

A NEW NONLINEAR TRANSPORT MODEL FOR GAS FLOW IN TIGHT POROUS MEDIA

3.1 Introduction

The exploitation of shale gas reservoirs needs new technologies and new models to describe the gas flow and recovery process from extremely low permeability gas reservoirs. The conventional methods fail to explain gas flow through such tight formations and recent attention has been focused on new methods and new transport models to investigate fluid flow through shale gas reservoirs. In such reservoirs, different flow conditions occur which initiate the transport of gas, Roy et al. [144], Javadpour et al. [94], Civan et al. [43]. The results obtained from conventional Darcy's law show deviation from experimental data, one such example is that the permeability values determined from Darcy's equation are significantly different from the experimentally determined permeability values. Many researchers have proposed new transport models based on modified Darcy's law for accurate determination of various reservoir properties, but each has its own limit of applicability as described in Chapter-2.

In this Chapter, the aim is to construct a new transport model which develops upon the previous models by including more realism into the model. We will give a rigorous derivation of the model. An advantage of the new transport model is that reservoir properties, for example the porosity, the permeability, and the tortuosity, etc., can be estimated by matching numerical results with the experimental data obtained from pressure-pulse decay test. Furthermore, the model developed here incorporates previous models as limiting cases and as such is more universal in its range of applicability.

The estimation of the permeability of shale rocks can be accomplished through many techniques, but the most commonly used method is the application of pressure-pulse decay tests. Many researchers have employed transient pressure pulse test combined with transport models for determination of permeability of samples obtained from shale reservoirs. The idea is to place the rock sample in a core plug and a pressure pulse is suddenly applied at the upstream reservoirs, and then the pressure is measured at different times, see Brace et al. [26], Hsieh et al. [84], Neuzil et al. [125], Liang et al. [104], Malkovsky et al. [112], Cui et al. [44], Civan et al. [41]. However, in each of the above mentioned models they have restrictive applicability. For example, Hsieh et al. [84] used linearization assumption for finding the solution and also assumed that the permeability is constant. Liang et al. [104]'s model is useful only when the pressure in pores is very small. Malkovsky et al. [112] and Cui et al. [44] neglected the advection terms. Moreover, all of these models are based on a single flow regime assumption, see Chapter-2. Civan et al. [41] incorporated the term for gas adsorption and advection term, and he assumed that the reservoir parameters change with the change in pressure; but in actual numerical simulations, Civan simplified the model to constant values for reservoir parameters.

In this work, the aim is to include as much physics as possible, and to let the model parameters and compressibility coefficients to be genuine functions of pressure in theory as well as in simulations. This enhances the realism in the model. That is, instead of estimating the values of model parameters at average pressure, we estimate the values of model parameters at the pressure values, $p(x, t)$, across the entire reservoir and at all times. Moreover, we use the empirical relations for the various model parameters and find their compressibility coefficients from those relations. Furthermore, we also include the Forchheimer's correction term in the new transport model which is essential in the gas reservoirs because gas flows at very high speed as compared to liquids.

Our approach is first to develop a general model which possesses the properties of the previous models and is rigorous in construction. The new model encompasses all the different flow regimes through the Knudsen number. The turbulent effects are included in the model by Forchheimer's correction formula. A complete derivation of various compressibility coefficients is given in three-dimensional flow. Our approach uses various up-to-date empirical correlations for various parameters.

In this chapter, after constructing the new transport model along the lines described above, the model solver is developed (Chapter 5) and in the first place used to obtain estimates of rock core samples through a type of inverse problem, the model simulations are best fitted to available data by adjusting the model parameters. Secondly, in Chapter 6, a sensitivity analysis of all model parameters is carried out in order to determine the most important model parameters.

3.2 Conservation of Mass and Momentum

Mass conservation of gas transport through the tight porous media is described by including the loss of mass of gas by adsorption per unit bulk volume of porous media and per unit time (the term on the right below) and is given by,

$$\frac{\partial(\rho\phi)}{\partial t} + \frac{\partial[(1-\phi)q]}{\partial t} = -\nabla \cdot (\rho\mathbf{u}) + Q \tag{3.2.1}$$

Momentum conservation of gas flowing through porous media is described by modified Darcy's law and is given by Evans and Civan [56]

$$\begin{aligned} -(\nabla p - \rho g \nabla D) &= \mu \mathbf{K}_a^{-1} \cdot \mathbf{u} + \rho \beta |\mathbf{u}| \cdot \mathbf{u} \\ &= \mu \mathbf{K}_a^{-1} \left(\mathbf{I} + \frac{\rho}{\mu} \beta \mathbf{K}_a |\mathbf{u}| \right) \cdot \mathbf{u} \end{aligned} \tag{3.2.2}$$

where ρ (kg/m^3) is the density, $\mathbf{u}$ (m^3/s/m^2) is the volumetric flux, μ (Pa s) is the dynamic viscosity of the flowing gas, g (m^2/s) is the gravitational acceleration vector, D (m) is the depth function, $\mathbf{K}_a$ (m^2) denotes the apparent permeability tensor of the gas, p is the pressure, and β represents the inertial effects, or turbulent effects near the well bore or in the fractures where the velocity is very high.

Setting

$$\mathbf{F}^{-1} = \left(\mathbf{I} + \frac{\rho}{\mu} \mathbf{K}_a \beta |\mathbf{u}| \right) \tag{3.2.3}$$

$$\Rightarrow \mathbf{F} = \left(\mathbf{I} + \frac{\rho}{\mu} \mathbf{K}_a \beta |\mathbf{u}| \right)^{-1}, \tag{3.2.4}$$

then Eq. (3.2.2) can be written as

$$-(\nabla p - \rho g \nabla D) = \mu (\mathbf{F} \mathbf{K}_a)^{-1} \cdot \mathbf{u} \tag{3.2.5}$$

from which it follows that,

$$\mathbf{u} = -\frac{1}{\mu}\left(\mathbf{F}\mathbf{K}_a\right) \cdot (\nabla p - \rho g \nabla D). \tag{3.2.6}$$

Combining Eq. (3.2.1) and Eq. (3.2.6), and after rearranging, we obtain

$$\begin{aligned}
\frac{\partial(\rho\phi)}{\partial t} + \frac{\partial[(1-\phi)q]}{\partial t} &= \nabla \cdot \left(\frac{\rho}{\mu}\left(\mathbf{F}\mathbf{K}_a\right) \cdot (\nabla p - \rho g \nabla D)\right) + Q \\
&= \nabla \cdot \left(\frac{\rho}{\mu}\left(\mathbf{F}\mathbf{K}_a\right) \cdot \nabla p\right) - \nabla \cdot \left(\frac{\rho^2 g}{\mu}\left(\mathbf{F}\mathbf{K}_a\right) \cdot \nabla D\right)\right) + Q \\
&= \frac{\rho}{\mu}\left(\mathbf{F}\mathbf{K}_a\right) : \nabla\nabla p + \nabla \cdot \left(\frac{\rho}{\mu}\left(\mathbf{F}\mathbf{K}_a\right)\right) \cdot \nabla p \\
&- \quad \frac{\rho^2 g}{\mu}\left(\mathbf{F}\mathbf{K}_a\right) : \nabla\nabla D - \nabla \cdot \left(\frac{\rho^2 g}{\mu}\left(\mathbf{F}\mathbf{K}_a\right)\right) \cdot \nabla D + Q
\end{aligned} \tag{3.2.7}$$

Tensor Notation Bird [20] has given the definition of tensor in the following way. Let $\mathbf{e}_1$, $\mathbf{e}_2$, and $\mathbf{e}_3$ be the unit vectors in the x, y, and z directions respectively. Then a vector $\mathbf{v}$ can be written as $\mathbf{v} = \sum_{i=1}^{3} \mathbf{e}_i v_i$, and a matrix (tensor of rank two) can be written as $\mathbf{A} = \sum_{i=1}^{3}\sum_{j=1}^{3} \mathbf{e}_i\mathbf{e}_j a_{ij}$. Let $\mathbf{u}$ be another vector $\mathbf{u} = \sum_{j=1}^{3} \mathbf{e}_j u_j$, then $(\mathbf{A} : \mathbf{u}\mathbf{v})$ is defined as $(\mathbf{A} : \mathbf{u}\mathbf{v}) = \sum_{i=1}^{3}\sum_{j=1}^{3} a_{ij} u_j v_i$.

3.3 The Pressure Equation

When pressure is applied, it changes the physical properties of the system, such as, gas density and viscosity, porosity and permeability of the porous medium. The changes in the physical quantities is measured in terms of *compressibility* *coefficients.* The compressibility with respect to a parameter, $\gamma(p)$, is the relative change in $\gamma(p)$ in response to the pressure change. The *isothermal coefficient of compressibility*, $\zeta_\gamma(p)$, of γ is defined as,

$$\zeta_\gamma(p) = \gamma^{-1}\frac{\partial}{\partial p}\gamma = \frac{\partial}{\partial p}(\ln \gamma). \tag{3.3.1}$$

Thus the isothermal coefficients of compressibility for fluid density is,

$$\zeta_\rho(p) = \frac{1}{\rho}\frac{\partial \rho}{\partial p} = \frac{1}{p} - \frac{1}{Z}\frac{\partial Z}{\partial p} = \frac{1}{p} - \zeta_Z(p); \quad \rho = \frac{pM_g}{ZR_gT}. \tag{3.3.2}$$

For quantities, such as the fluid viscosity (μ), rock porosity (ϕ), we assume an exponential integral relation, (more details are given in Chapter 4). Thus

$$\zeta_\mu(p) = \frac{1}{\mu}\frac{\partial \mu}{\partial p}; \qquad \text{where } \ \mu = \mu_0 \exp\left(\int_{p_0}^{p} \zeta_\mu(p)dp\right) \tag{3.3.3}$$

and,

$$\zeta_\phi(p) = \frac{1}{\phi}\frac{\partial \phi}{\partial p}; \qquad \text{where } \ \phi = \phi_0 \exp\left(\int_{p_0}^{p} \zeta_\phi(p)dp\right) \tag{3.3.4}$$

For a matrix (tensor) quantity like the rock permeability, $\mathbf{K}_a$, we define $\zeta_{\mathbf{K}_a}$ as follows,

$$\zeta_{\mathbf{K}_a}(p)\mathbf{I} = \mathbf{K}_a^{-1}\frac{\partial}{\partial p}\left(\mathbf{K}_a\right); \qquad \text{where } \ \mathbf{K}_a = (\mathbf{K}_a)_0 \exp\left(\int_{p_0}^{p} \zeta_{\mathbf{K}_a}(p)dp\right) \tag{3.3.5}$$

Notice that the integral of a matrix is the matrix of integrals. With this assumption, various other coefficients of compressibility can be derived as follows,

$$\zeta_1(p) = \frac{1}{\rho\phi}\frac{\partial(\rho\phi)}{\partial p} = \frac{1}{\rho}\frac{\partial\rho}{\partial p} + \frac{1}{\phi}\frac{\partial\phi}{\partial p} = \zeta_\rho(p) + \zeta_\phi(p) \tag{3.3.6}$$

$$\zeta_2(p) = \frac{1}{(1-\phi)q}\frac{\partial[(1-\phi)q}{\partial p} = \zeta_q(p) - \left(\frac{\phi}{1-\phi}\right)\zeta_\phi(p) \tag{3.3.7}$$

$$\begin{aligned}
\zeta_3(p)\mathbf{I} &= \left(\frac{\rho}{\mu}\left(\mathbf{F}\mathbf{K}_a\right)\right)^{-1}\frac{\partial}{\partial p}\left(\frac{\rho}{\mu}\left(\mathbf{F}\mathbf{K}_a\right)\right)\\
&= \left(\frac{\rho}{\mu}\right)^{-1}\left(\mathbf{F}\mathbf{K}_a\right)^{-1}\left[\frac{\partial}{\partial p}\left(\frac{\rho}{\mu}\right)\left(\mathbf{F}\mathbf{K}_a\right) + \frac{\rho}{\mu}\frac{\partial}{\partial p}\left(\mathbf{F}\mathbf{K}_a\right)\right]\\
&= \left(\frac{\rho}{\mu}\right)^{-1}\frac{\partial}{\partial p}\left(\frac{\rho}{\mu}\right) + \left(\mathbf{F}\mathbf{K}_a\right)^{-1}\frac{\partial}{\partial p}\left(\mathbf{F}\mathbf{K}_a\right)\\
&= [\zeta_\rho(p) - \zeta_\mu(p) + \zeta_{(\mathbf{F}\mathbf{K}_a)}(p)]\mathbf{I}\\
\Rightarrow \zeta_3(p) &= \zeta_\rho(p) - \zeta_\mu(p) + \zeta_{(\mathbf{F}\mathbf{K}_a)}(p),
\end{aligned} \tag{3.3.8}$$

where,

$$\begin{aligned}
\zeta_{(\mathbf{F}\mathbf{K}_a)}(p)\mathbf{I} &= \left(\mathbf{F}\mathbf{K}_a\right)^{-1}\frac{\partial}{\partial p}\left(\mathbf{F}\mathbf{K}_a\right)\\
&= \mathbf{K}_a^{-1}\mathbf{F}^{-1}\left[\left(\frac{\partial}{\partial p}\mathbf{F}\right)\mathbf{K}_a + \mathbf{F}\left(\frac{\partial}{\partial p}\mathbf{K}_a\right)\right]\\
&= \mathbf{K}_a^{-1}\left(\mathbf{F}^{-1}\frac{\partial}{\partial p}\mathbf{F}\right)\mathbf{K}_a + \mathbf{K}_a^{-1}\mathbf{F}^{-1}\mathbf{F}\left(\frac{\partial}{\partial p}\mathbf{K}_a\right)\\
&= [\mathbf{K}_a^{-1}\zeta_{\mathbf{F}}(p)\mathbf{K}_a + \zeta_{\mathbf{K}_a}(p)]\mathbf{I}\\
\Rightarrow \zeta_{(\mathbf{F}\mathbf{K}_a)}(p) &= \zeta_{\mathbf{F}}(p) + \zeta_{\mathbf{K}_a}(p).
\end{aligned} \tag{3.3.9}$$

Equation (3.3.8) then becomes

$$\zeta_3(p) = \zeta_\rho(p) - \zeta_\mu(p) + \zeta_{\mathbf{F}}(p) + \zeta_{\mathbf{K}_a}(p). \tag{3.3.10}$$

From Eq. (3.2.3), we have

$$\mathbf{F}^{-1} - \mathbf{I} \quad = \quad \frac{\rho}{\mu}\mathbf{K}_a\beta|\mathbf{u}| \tag{3.3.11}$$

$$\zeta_{\mathbf{F}}(p)\mathbf{I} = \mathbf{F}^{-1}\frac{\partial}{\partial p}\mathbf{F} \tag{3.3.12}$$

Using the relation,

$$\text{using } \frac{\partial}{\partial p}\mathbf{A}^{-1} = -\mathbf{A}^{-1}\frac{\partial \mathbf{A}}{\partial p}\mathbf{A}^{-1},$$

leads to,

$$\begin{aligned}
\zeta_{\mathbf{F}}(p)\mathbf{I} &= -\mathbf{F}^{-1}\mathbf{F}\left(\frac{\partial}{\partial p}\mathbf{F}^{-1}\right)\mathbf{F} \\
&= -\mathbf{I}\frac{\partial}{\partial p}\left[\mathbf{I} + \frac{\rho}{\mu}\mathbf{K}_a\beta|\mathbf{u}|\right]\mathbf{F} \\
&= -\frac{\partial}{\partial p}\left[\frac{\rho}{\mu}\mathbf{K}_a\beta|\mathbf{u}|\right]\mathbf{F} \\
&= -\left[\frac{\partial}{\partial p}\left(\frac{\rho}{\mu}\right)(\mathbf{K}_a\beta)\,|\mathbf{u}| + \frac{\rho}{\mu}\frac{\partial}{\partial p}(\mathbf{K}_a\beta)\,|\mathbf{u}| + \frac{\rho}{\mu}(\mathbf{K}_a\beta)\,\frac{\partial}{\partial p}|\mathbf{u}|\right]\mathbf{F} \\
&= -\frac{\rho}{\mu}(\mathbf{K}_a\beta)\,|\mathbf{u}|\left[\left(\frac{\rho}{\mu}\right)^{-1}\frac{\partial}{\partial p}\left(\frac{\rho}{\mu}\right)\mathbf{I} + (\mathbf{K}_a\beta)^{-1}\frac{\partial}{\partial p}(\mathbf{K}_a\beta) + |\mathbf{u}|^{-1}\frac{\partial}{\partial p}|\mathbf{u}|\right]\mathbf{F}
\end{aligned} \tag{3.3.13}$$

Again, from Eq. (3.2.3) , we have

$$\mathbf{F}^{-1} - \mathbf{I} = \frac{\rho}{\mu}\mathbf{K}_a\beta|\mathbf{u}|, \tag{3.3.14}$$

and substituting this into Eq. (3.3.12) , we obtain

$$\zeta_{\mathbf{F}}(p)\mathbf{I} = -(\mathbf{F}^{-1} - \mathbf{I})\left[\zeta_\rho(p) - \zeta_\mu(p) + \zeta_{(\mathbf{K}_a\beta)}(p) + \zeta_{|\mathbf{u}|}(p)\right]\mathbf{F}. \tag{3.3.15}$$

The compressibility coefficient $\zeta_{(\mathbf{K}_a\beta)}(p)$ can be expressed as the sum of $\zeta_{\mathbf{K}_a}$ and

ζ_β as follows,

$$\begin{aligned}
\zeta_{(\mathbf{K}_a\beta)}(p)\mathbf{I} &= (\mathbf{K}_a\beta)^{-1}\frac{\partial}{\partial p}(\mathbf{K}_a\beta) \\
&= \beta^{-1}\mathbf{K}_a^{-1}\left[\left(\frac{\partial}{\partial p}\mathbf{K}_a\right)\beta + \mathbf{K}_a\left(\frac{\partial}{\partial p}\beta\right)\right] \\
&= \beta^{-1}\mathbf{K}_a^{-1}\left(\frac{\partial}{\partial p}\mathbf{K}_a\right)\beta + \beta^{-1}\mathbf{K}_a^{-1}\mathbf{K}_a\left(\frac{\partial}{\partial p}\beta\right) \\
&= [\beta^{-1}\zeta_{\mathbf{K}_a}(p)\beta + \zeta_\beta(p)]\mathbf{I} \\
\Rightarrow \zeta_{(\mathbf{K}_a\beta)}(p) &= \zeta_{\mathbf{K}_a}(p) + \zeta_\beta(p) \qquad (3.3.16)
\end{aligned}$$

where,

$$\zeta_\beta(p)\mathbf{I} = \beta^{-1}\frac{\partial\beta}{\partial p} \qquad (3.3.17)$$

Substituting Eq. (3.3.16) into Eq. (3.3.15), we obtain

$$\zeta_{\mathbf{F}}(p)\mathbf{I} = (\mathbf{F}-\mathbf{I})\left[\zeta_\rho(p) - \zeta_\mu(p) + \zeta_{\mathbf{K}_a}(p) + \zeta_\beta(p) + \zeta_{|\mathbf{u}|}(p)\right] \qquad (3.3.18)$$

Substituting Eq. (3.3.18) into Eq. (3.3.9) and then into Eq. (3.3.8), we obtain

$$\begin{aligned}
\zeta_3(p) &= (\zeta_\rho(p) + \zeta_{\mathbf{K}_a}(p) - \zeta_\mu(p))\mathbf{I} + \zeta_{\mathbf{F}}(p) \\
&= (\zeta_\rho(p) + \zeta_{\mathbf{K}_a}(p) - \zeta_\mu(p))\mathbf{I} + \\
&\quad (\mathbf{F}-\mathbf{I})\left[\zeta_\rho(p) + \zeta_{\mathbf{K}_a}(p) - \zeta_\mu(p) + \zeta_\beta(p) + \zeta_{|\mathbf{u}|}(p)\right] \\
&= \mathbf{F}[\zeta_\rho(p) + \zeta_{\mathbf{K}_a}(p) - \zeta_\mu(p)] + (\mathbf{F}-\mathbf{I})(\zeta_\beta(p) + \zeta_{|\mathbf{u}|}(p)) \qquad (3.3.19)
\end{aligned}$$

Using Eq. (2.4.1), we have,

$$\begin{aligned}
\zeta_{\mathbf{K}_a}(p)\mathbf{I} &= \mathbf{K}_a^{-1}\frac{\partial}{\partial p}\mathbf{K}_a \\
&= (f\mathbf{K})^{-1}\frac{\partial}{\partial p}f\mathbf{K} \\
&= \mathbf{K}^{-1}f^{-1}\left(\frac{\partial f}{\partial p}\mathbf{K} + f\frac{\partial}{\partial p}\mathbf{K}\right) \\
&= \mathbf{K}^{-1}f^{-1}\frac{\partial f}{\partial p}\mathbf{K} + \mathbf{K}^{-1}f^{-1}f\frac{\partial}{\partial p}\mathbf{K} \\
&= \mathbf{K}^{-1}\zeta_f(p)\mathbf{K} + \zeta_{\mathbf{K}}(p) \\
&= [\zeta_f(p) + \zeta_{\mathbf{K}}(p)]\mathbf{I} \\
\Rightarrow \zeta_{\mathbf{K}_a}(p) &= \zeta_f(p) + \zeta_{\mathbf{K}}(p) \qquad (3.3.20)
\end{aligned}$$

where,

$$\zeta_{\mathbf{K}}(p) = \mathbf{K}^{-1}\frac{\partial}{\partial p}\mathbf{K}; \qquad \text{and} \quad \mathbf{K} = (\mathbf{K})_0 \exp\left(\int_{p_0}^{p}\zeta_{\mathbf{K}}(p)dp\right), \qquad (3.3.21)$$

and,

$$\zeta_f(p)\mathbf{I} = (f(\mathbf{K}_n))^{-1}\frac{\partial}{\partial p}f(\mathbf{K}_n), \qquad (3.3.22)$$

and,

$$\begin{aligned}
\zeta_{|\mathbf{u}|}(p) &= |\mathbf{u}|^{-1}\frac{\partial}{\partial p}|\mathbf{u}| \\
&= |\mathbf{u}|^{-1}\frac{\partial}{\partial p}(\mathbf{u}\cdot\mathbf{u})^{1/2} \\
&= \frac{1}{2}|\mathbf{u}|^{-1}(\mathbf{u}\cdot\mathbf{u})^{-1/2}\frac{\partial}{\partial p}(\mathbf{u}\cdot\mathbf{u}) \\
&= \frac{1}{2|\mathbf{u}|(\mathbf{u}\cdot\mathbf{u})^{1/2}}\left(\frac{\partial\mathbf{u}}{\partial p}\cdot\mathbf{u}+\mathbf{u}\cdot\frac{\partial\mathbf{u}}{\partial p}\right) \\
&= \frac{1}{\mathbf{u}\cdot\mathbf{u}}\left(\mathbf{u}\cdot\frac{\partial\mathbf{u}}{\partial p}\right). \qquad (3.3.23)
\end{aligned}$$

A detailed discussion of compressibility coefficients is given in Chapter 4.

From equations (3.3.6) and (3.3.7), we derive the following expressions:

$$\frac{\partial(\rho\phi)}{\partial t} = \frac{\partial(\rho\phi)}{\partial p}\frac{\partial p}{\partial t} = \rho\phi\zeta_1(p)\frac{\partial p}{\partial t}, \qquad (3.3.24)$$

and

$$\frac{\partial(1-\phi)q}{\partial t} = \frac{\partial(1-\phi)q}{\partial p}\frac{\partial t}{\partial t} = (1-\phi)q\zeta_2(p)\frac{\partial p}{\partial t}. \qquad (3.3.25)$$

Furthermore, equation (3.3.8) can be written as follows,

$$\begin{aligned}
\nabla\cdot\left(\frac{\rho}{\mu}(\mathbf{F}\mathbf{K}_a)\right) &\equiv \left(\nabla p\frac{d}{dp}\right)\cdot\left(\frac{\rho}{\mu}(\mathbf{F}\mathbf{K}_a)\right) \\
&= \nabla p\cdot\left(\frac{d}{dp}\left(\frac{\rho}{\mu}\mathbf{F}\mathbf{K}_a\right)\right) \\
&= \nabla p\cdot\left(\frac{\rho}{\mu}(\mathbf{F}\mathbf{K}_a)\right)\cdot\zeta_3(p) \qquad (3.3.26)
\end{aligned}$$

Substituting equations. (3.3.24), (3.3.25) and (3.3.26) into (3.2.7), we obtain

$$\rho\phi\zeta_1(p)\frac{\partial p}{\partial t} + (1-\phi)q\zeta_2(p)\frac{\partial p}{\partial t} = \frac{\rho}{\mu}(\mathbf{FK}_a) : \nabla\nabla p + \nabla p \cdot \left(\frac{\rho}{\mu}(\mathbf{FK}_a)\right) \cdot \zeta_3(p) \cdot \nabla p$$
$$- \frac{\rho^2 g}{\mu}(\mathbf{FK}_a) : \nabla\nabla D - \nabla \cdot \left(\frac{\rho^2 g}{\mu}(\mathbf{FK}_a)\right) \cdot \nabla D + Q \tag{3.3.27}$$

Introducing the apparent diffusivity coefficient (or apparent transport coefficient) D_a (m^2/s) as follows,

$$D_a(p) = \frac{\mathbf{FK}_a}{\mu\zeta_t}, \tag{3.3.28}$$

where

$$\zeta_t = \left[\phi\zeta_1(p) + (1-\phi)\frac{q}{\rho}\zeta_2(p)\right]. \tag{3.3.29}$$

Equation (3.3.27) becomes

$$\frac{\partial p}{\partial t} = \mathbf{D}_a(p) : \nabla\nabla p + \nabla p \cdot \mathbf{D}_a(p)\zeta_3(p) \cdot \nabla p$$
$$- \;\; \rho g\mathbf{D}_a : \nabla\nabla D - \rho g\nabla \cdot (\mathbf{D}_a) \cdot \nabla D + \zeta_t Q \tag{3.3.30}$$

3.4 Simplified Models

Various simplified models can be obtained under different further assumptions, as elucidated below.

No Gravitational Effects

Under the assumption of no gravitational effect ($g = 0$), equation (3.3.30) becomes

$$\frac{\partial p}{\partial t} = \mathbf{D}_a(p) : \nabla\nabla p + \nabla p \cdot \mathbf{D}_a(p)\zeta_3(p) \cdot \nabla p + \psi^{-1}Q. \tag{3.4.1}$$

No Source Term

Under the further assumption of no source/sink term ($Q = 0$), equation (3.4.1) becomes

$$\frac{\partial p}{\partial t} = \mathbf{D}_a(p) : \nabla\nabla p + \nabla p \cdot \mathbf{D}_a(p)\zeta_3(p) \cdot \nabla p. \tag{3.4.2}$$

One Dimensional Case

Under the further assumption of one-dimensional flow, equation (3.4.2) becomes

$$\frac{\partial p}{\partial t} + U_a(p, p_x)\frac{\partial p}{\partial x} = D_a(p)\frac{\partial^2 p}{\partial x^2} \tag{3.4.3}$$

where, U_a (m/s) is called the apparent convective flux and is defined by,

$$U_a = -\zeta_3(p)D_a(p)\frac{\partial p}{\partial x} \tag{3.4.4}$$

and

$$D_a(p) = \frac{\rho}{\mu}\frac{FK_a}{(\rho\phi\zeta_1(p) + (1-\phi)q\zeta_2(p))}, \tag{3.4.5}$$

where F and K_a are scalar functions.

Remark

The new transport model (3.3.30) has a number of important features. It incorporates the various flow regimes that occur in porous media, into the model and also the turbulence effects are included through the Forchheimer's correction. The turbulence factor β is considered as a function of $\mathbf{K}_a$, ϕ, and τ. Moreover, the parameters ϕ, μ, ρ are functions of pressure p. Hence the model (3.3.30) has nonlinear coefficients D_a and U_a, that is, neglecting the turbulent effects, it reduces to the Civan's model (2011). Further more, it reduces to the model of Cui's (2009) by neglecting the advection term, (see Civan et al. [41]). Also note that similar models are also considered by Malkovsky et al. [112] and Liang et al. [104] but their models do not include the turbulence effects.

3.5 Non-dimensional Steady State Pressure Equation

A steady state model can be obtained by substituting $\frac{\partial p}{\partial t} = 0$ in equation (3.4.3) to yield

$$U_a(p, p_x)\frac{\partial p}{\partial x} = D_a(p)\frac{\partial^2 p}{\partial x^2}, \tag{3.5.1}$$

which can be rearranged as follows,

$$L_a(p, p_x)\frac{\partial p}{\partial x} = \frac{\partial^2 p}{\partial x^2}, \tag{3.5.2}$$

where L_a is called apparent convective flux and is defined by

$$L_a = -\zeta_3(p)\frac{\partial p}{\partial x}, \tag{3.5.3}$$

where $\zeta_3(p)$ is given by equation (3.3.10).

A dimensionless form of steady state equation can be obtained by considering the following dimensionless variables,

$$x_D = \frac{x}{L} \qquad \text{and} \qquad p_D(x_D) = \frac{p(x) - p_d}{p_u - p_d},$$

which yields,

$$L_a(p_D, (p_D)_x)\frac{\partial p_D}{\partial x_D} = \frac{\partial^2 p_D}{\partial x_D^2}, \qquad 0 \leq x_D \leq 1. \tag{3.5.4}$$

A non-dimensional transient pressure equation can be obtained by introducing the dimensionless variables

$$x_D = \frac{x}{L}, \quad t_D = \frac{t}{t_0}, \quad p_D(x_D, t_D) = \frac{p(x,t) - p_d(t)}{p_u(0) - p_d(0)}. \tag{3.5.5}$$

$$t_0 = \frac{L^2}{D_0}, \quad U_D = \frac{U_a}{U_0}, \quad D_D = \frac{D_a}{D_0}, \quad Pe = \frac{LU_0}{D_0}. \tag{3.5.6}$$

The transient equation (3.4.3) then reduces to the following dimensionless form,

$$\frac{\partial p_D}{\partial t_D} + PeU_D\frac{\partial p_D}{\partial x_D} = D_D\frac{\partial^2 p_D}{\partial x_D^2}, \qquad 0 \leq x_D \leq 1, \qquad t_D > 0 \tag{3.5.7}$$

where Pe is the Peclet number, D_o and U_o are values of the diffusivity coefficient

D_a and the convective flux U_a at some specific pressure, and $p_u(t)$ and $p_d(t)$ are pressures in the upstream and the downstream reservoirs.

3.6 Pressure Pulse-Decay Tests: Laboratory conditions

Civan et al. [41] described pressure pulse-decay test with the following initial and Dirichlet boundary conditions:

Initial Condition

$$p = p_o, \qquad 0 \leq x \leq L, \quad t = 0. \tag{3.6.1}$$

Dirichlet Boundary Conditions:

$$p = p_u(t), \qquad x = 0, \quad t > 0. \tag{3.6.2}$$

$$p = p_d(t), \qquad x = L, \quad t > 0. \tag{3.6.3}$$

Flux Conditions at the Inlet Boundary

Civan describes the flux of gas flow across the upstream boundary face by the mass-balance equation,

$$\frac{d(\rho V_u)}{dt} = -\rho \mathbf{u} \cdot \mathbf{n} A, \tag{3.6.4}$$

where $\mathbf{n}$ denotes the unit vector normal to the open core flow surface, V_u is the volume of upstream reservoir, and A is the cross-sectional area. Rearranging equation (3.6.4) and considering V_u to be constant, we obtain:

$$V_u \frac{dp}{dt}\frac{d\rho}{dp} = V_u \frac{dp}{dt}\rho\zeta_\rho(p) = -\rho\left(-\frac{1}{\mu}\left(\mathbf{FK}_a\right).\nabla p\right).n\frac{V_p}{\phi L} \tag{3.6.5}$$

In one dimension, equation (3.6.5) becomes

$$\frac{\partial p}{\partial x} = \left[\frac{V_u \mu\phi L}{V_p}\frac{\zeta_\rho(p)}{FK_a}\right]\frac{\partial p}{\partial t}, \qquad p = p_u; \quad x = 0, \quad t > 0. \tag{3.6.6}$$

Flux Conditions at the Outlet Boundary:

Civan describes the flux of gas flow across the upstream boundary face by the mass-balance equation,

$$\frac{d(\rho V_d)}{dt} = +\rho\mathbf{u}\cdot\mathbf{n}A. \tag{3.6.7}$$

In one dimension, equation (3.6.7) becomes

$$\frac{\partial p}{\partial x} = -\left[\frac{V_d \mu\phi L}{V_p}\frac{\zeta_\rho(p)}{FK_a}\right]\frac{\partial p}{\partial t}, \qquad p = p_d; \quad x = L, \quad t > 0. \tag{3.6.8}$$

The dimensionless initial condition is given as:

$$p_D(x_D, 0) = \frac{p_u(0) - p_0}{p_u(0) - p_d(0)}. \tag{3.6.9}$$

If $p_0 = p_d(0)$ then $p_D = 1$, $0 \leq x_D \leq 1$, $t_D = 0$.

The dimensionless Dirichlet boundary conditions are given as:

$$p_D = 0, \quad x_D = 0, \quad t_D > 0 \tag{3.6.10}$$

$$p_D = \frac{p_u(t) - p_d(t)}{p_u(0) - p_d(0)}, \quad x_D = 1, \quad t_D > 0 \tag{3.6.11}$$

The dimensionless flux conditions at the inlet and outlet boundary conditions are given as:

$$\frac{\partial p_D}{\partial x_D} = \left[\frac{V_u \mu \phi L U_a}{V_p} \left(\mathbf{F}\mathbf{K}_a\right)^{-1} \zeta_\rho(p_D)\right] \frac{\partial p_D}{\partial t_D}, \qquad p_D = p_{uD}, \quad x_D = 0, \quad t_D > 0. \tag{3.6.12}$$

$$\frac{\partial p_D}{\partial x_D} = -\left[\frac{V_d \mu \phi L U_a}{V_p} \left(\mathbf{F}\mathbf{K}_a\right)^{-1} \zeta_\rho(p_D)\right] \frac{\partial p_D}{\partial t_D}, \qquad p_D = p_{dD}, \quad x_D = 1, \quad t_D > 0. \tag{3.6.13}$$

3.7 Summary

In this chapter, we have derived a nonlinear transport model for fluid flow through tight porous media, with an aim to apply it to study gas transport in shale rocks. The model is cast as a nonlinear advection-diffusion PDE for the pressure field, and a full treatment of compressibility coefficients is given. Moreover, we have also given the 1D form, and pressure-dependent steady-state form of the transport model which will be used in subsequent chapters for analyzing the experimental data obtained from the pressure pulse decay tests.

CHAPTER 4

COMPRESSIBILITY COEFFICIENTS AND REGULARITY OF SOLUTIONS

4.1 The New Transport Model

The expressions for the apparent diffusivity D_a and the apparent convective flux U_a in the new transport model, equations (3.4.4) and (3.4.5), are highly non-linear and complicated in form. They depend upon many parameters, such as, the porosity, the permeability, the viscosity, the tortuosity, and the associated compressibility coefficients. Note that these parameters and their compressibility coefficients appear in the model because of the assumption that the reservoir properties change with the pressure - they are functions of pressure.

Our aim, in this chapter, is to carry out a sensitivity analysis of the new transport model with respect to changes in the compressibility coefficients brought in response to changes in the pressure. In order to do this, we first find the relationships for the compressibility coefficients based on the empirical expressions. We develop Matlab codes for computing compressibility coefficients. We then analyze the effects of pressure on the physical parameters and their compressibility coefficients, see Ali et al. [10].

The new transport model, (Chapter 3), equation (3.4.3) under the assumption of 1D flow, zero gravity, and no external source, is

$$\frac{\partial p}{\partial t} + U_a(p, p_x)\frac{\partial p}{\partial x} = D_a(p)\frac{\partial^2 p}{\partial x^2} \tag{4.1.1}$$

where D_a, U_a, ψ, F, $\zeta_1(p)$, $\zeta_2(p)$, and ζ_3 are defined in equations (3.4.4), (3.4.5), (3.3.29), (3.2.3), (3.3.6), (3.3.7), and (3.3.19), respectively. In application, equation (4.1.1) is solved with given boundary and initial conditions, to yield the pressure distribution $p(x, t)$ in a reservoir or rock sample.

4.2 Correlations for Model Parameters

The Gas Deviation Factor (Z) is the ratio of the molar volume of a gas to the molar volume of an ideal gas at the same temperature and pressure, Kumar [99]. Mahmoud [110] have obtained a correlation for the gas deviation factor Z in terms of the reduced pressure p_r and the reduced temperature t_r, where pressure p and temperature t are normalized by critical pressure p_c and critical temperature

t_c, respectively, that is, $p_r = p/p_c$ and $t_r = t/t_c$. The critical temperature t_c is the temperature above which vapour cannot be made to liquify, and the critical pressure p_c is the pressure required to liquify vapour at the critical temperature. Mahmood's relationship for the gas deviation factor are given by,

$$Z = a_Z p_r^2 + b_Z p_r + c_Z \tag{4.2.1}$$

$$a_Z = 0.702 \exp(-2.5 t_r) \tag{4.2.2}$$

$$b_Z = -5.524 \exp(-2.5 t_r) \tag{4.2.3}$$

$$c_Z = 0.044 t_r^2 - 0.164 t_r + 1.15. \tag{4.2.4}$$

Note that Z is a function of both p_r and t_r, that is, $Z = Z(p_r, t_r)$. The behavior of Z is described as follows: first note that a_Z and c_Z are positive and b_Z is negative for all $t_r > 0$. As $t_r \to \infty$, both a_Z and b_Z tend to zero and c_Z tends to ∞. Hence, for a fixed value of p_r, Z increases with increase in temperature t_r, on the other hand, for a fixed value of t_r, Z behaves like a quadratic function in p_r. For fixed t_r, $Z(p_r)$ decreases in the interval $(0, -b_z/2a_z)$ and increases in the interval $(-b_Z/2a_Z, \infty)$ as p_r increases, where $-b_Z/2a_Z = 3.9344$ from equation (4.2.1). It implies that $Z \to \infty$ as $p_r \to \infty$, whereas, $Z \to c_Z$ as $p_r \to 0$. Moreover, at higher (but fixed) values of t_r, a_Z and b_Z are approximately zero, and hence Z remains constant at the level of $c_Z(t_r)$.

These features are illustrated in Figure 4.1 which shows the plots of gas deviation factor Z against reduced pressure p_r at different values of reduced temperature t_r. The minimum gas deviation factor Z occurs at $p_r = -b_Z/2a_Z$. Furthermore,

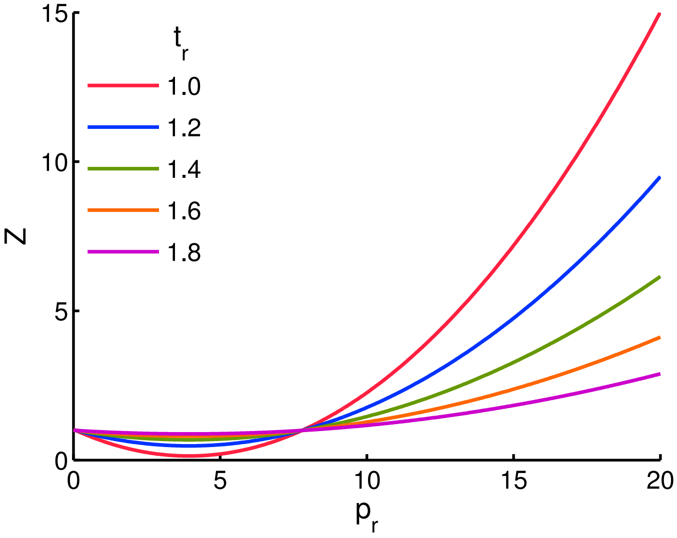

Figure 4.1: Plots of the gas deviation factor Z against the reduced pressure p_r at selected values of the reduced temperature t_r are obtained by the Eq. (4.2.1).

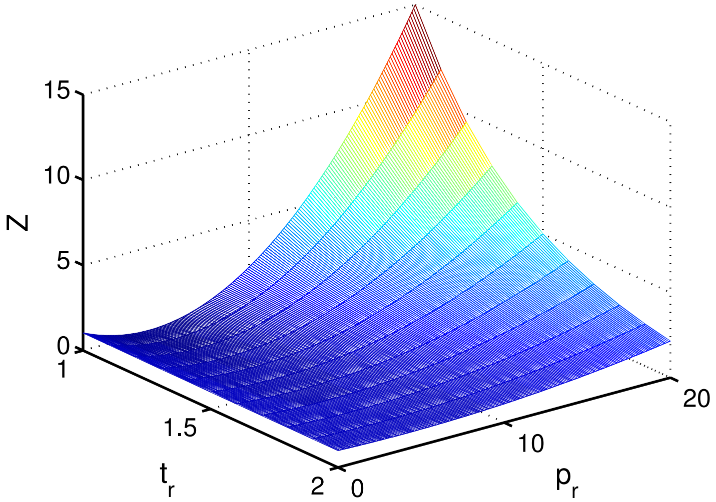

Figure 4.2: 3D graph of gas deviation factor Z plotted against the reduced pressure p_r and the reduced temperature t_r by using Eq. (4.2.1).

with an increase in the values of reduced temperature t_r, Z does not show much deviation from the ideal gas behavior, especially, for the values of t_r near 2. There are two values of reduced pressure p_r which gives $Z = 1$ and those values of p_r are obtained by solving the equation $a_Z p_r^2 + b_Z p_r + c_Z - 1 = 0$. It gives

$$p_r = -\frac{b_Z}{2a_Z} \pm \frac{\sqrt{b_Z^2 - 4a_Z(c_Z - 1)}}{2a_Z}, \tag{4.2.5}$$

which are roughly 0 and 8. Figure 4.2 shows 3D plot of the gas deviation factor Z against p_r and t_r.

The Density (ρ) of real gases is defined by the relationship, $\rho = \frac{pM_g}{ZR_g t}$, where M_g is the molecular mass of the gas, R_g is the universal gas constant, Z is the gas deviation factor, p and t represent pressure and temperature, respectively. Since the gas deviation factor is given as a function of reduced pressure and temperature, therefore, we express the equation of real gas density as a function of reduced temperature and pressure as follows,

$$\rho = \frac{p_r M_g}{t_r R_g Z(p_r)}. \tag{4.2.6}$$

Note that ρ is a function of both p_r and t_r, that is, $\rho = \rho(p_r, t_r)$. Since the gas deviation factor Z is positive and $Z \approx O(p_r^2)$ as $p_r \to \infty$, as discussed above, the gas density ρ is zero when p_r is zero and it means that $\rho \to 0$ as $p_r \to \infty$. It has an asymptotic behavior equivalent to $1/p_r$ for large values of p_r. Moreover, equating to zero the partial derivative of gas density ρ with respect to the reduced pressure

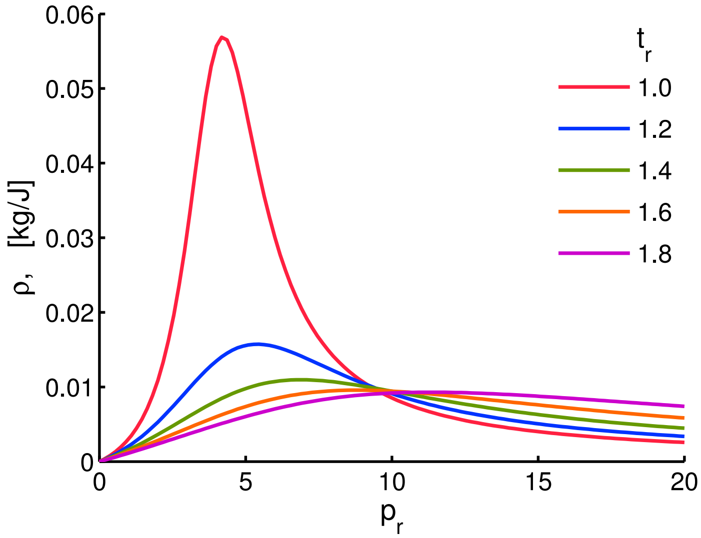

Figure 4.3: Plots of the gas density ρ against the reduced pressure p_r at various values of the reduced temperature t_r are obtained by using Eq. (4.2.6). Graphs show that gas density first increases but then it starts decreasing with the increase in pressure.

p_r gives $p_r = \sqrt{c_Z/a_Z}$. Hence, for a fixed value of t_r, ρ increases in the interval $(0, \sqrt{c_Z/a_Z})$ and decreases on the interval $(\sqrt{c_Z/a_Z}, \infty)$, and ρ has a maximum at $p_r = \sqrt{c_Z/a_Z}$.

Figure 4.3 shows the variation in gas density against the reduced pressure p_r for different values of the reduced temperature t_r.

The Compressibility Coefficient of Gas Density (ζ_ρ) is given by

$$\begin{aligned}\zeta_\rho(p) &= \frac{d}{dp}\ln\rho = \frac{1}{p} - \frac{1}{Z}\frac{dZ}{dp} \\ &= \frac{1}{p} - \frac{1}{p_c Z}\left(\frac{2a_Z p}{p_c} + b_Z\right). \end{aligned} \tag{4.2.7}$$

Figure 4.4 shows plots of ζ_ρ against p for different fixed values of the temperature t_r. For values of the reduced temperature t_r, the compressibility coefficient ζ_ρ is decreasing and positive on the interval $(0, \sqrt{c_Z/a_z})$, zero at $p_r = \sqrt{c_Z/a_z}$,

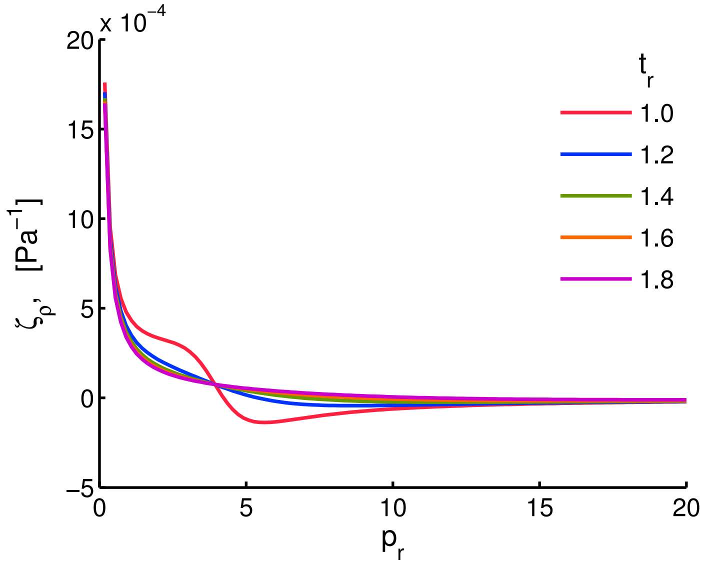

Figure 4.4: Compressibility coefficient of gas density ζ_ρ is plotted against reduced pressure p_r by using Eq. (4.2.7), where the value of critical pressure is $p_c = 3384$ kPa. It is observed that the values of ζ_ρ is positive for $p_r < 5$ and negative for $p_r > 5$.

and negative on the interval $(\sqrt{c_Z/a_z}, \infty)$. The relative change in the gas density with respect to the change in the pressure is very small for large values of pressure. Moreover, at higher values of temperature, the compressibility coefficient ζ_ρ remains positive at larger values of pressure. As noted earlier, $\sqrt{(\frac{c_Z}{a_Z})} \to \infty$ as $t_r \to \infty$, so in this limit ζ_ρ is decreasing but positive in $(0, \infty)$, and in fact $\zeta_\rho \to 0$ as $p_r \to \infty$ and $t_r \to \infty$.

Setting

$$\zeta_Z(p) = \frac{1}{Z}\frac{\partial Z}{\partial p}, \tag{4.2.8}$$

then equation (4.2.7) can be written as

$$\zeta_{gas}(p) = \zeta_\rho(p) + \zeta_z(p) = \frac{1}{p}. \tag{4.2.9}$$

The Gas Viscosity (μ) is a measure of the gas resistance to the flow. Com-

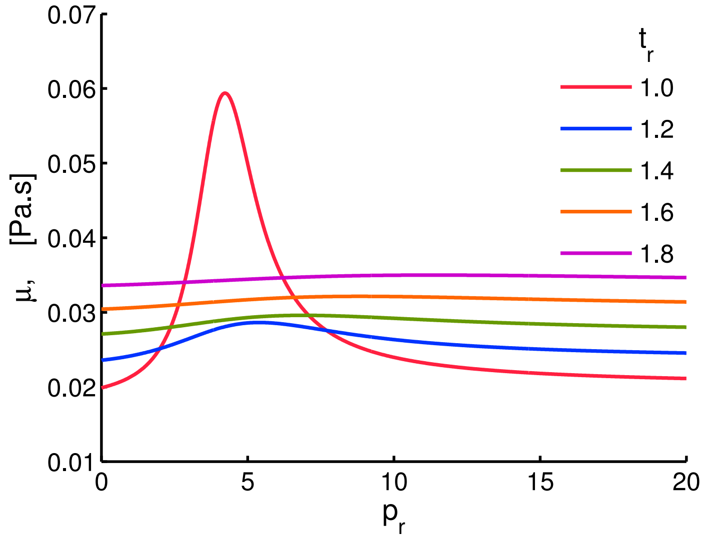

Figure 4.5: Gas viscosity is plotted against reduced pressure p_r by using Eq. (4.2.10) and at $p_c = 3384$ kPa, and $t_c = 130$ K. The viscosity almost remains at a constant level for $t_r > 1.4$, but for $t_r < 1.4$, there is large variation for $p_r < 10$.

monly used unit for viscosity is centipoise (cp) and S.I. unit of viscosity is Pa-s (= kg/s.m). Mahmoud [110] has given a correlation for determining the gas viscosity,

$$\mu = \mu_{S_c} \exp(A_\mu \rho^{B_\mu}) \tag{4.2.10}$$

$$A_\mu = 3.47 + 1588t^{-1} + 0.0009M_g$$

$$B_\mu = 1.66378 - 0.04679A_\mu$$

$$\mu_{S_c} = \frac{1}{(10.5)^4}\left[\frac{M_g^3 p_c^4}{t_c}\right]^{1/6} \times$$

$$\left[0.807t_r^{0.618} - 0.357\exp(0.449t_r) + 0.34\exp(-4.058t_r) + 0.018\right]$$

It is observed from Figure 4.5 that the gas viscosity is generally higher at higher temperatures, but it's behavior is more complex with respect to pressure. The gas viscosity increases with increasing pressure, peaking at around $p_r = 5-10$

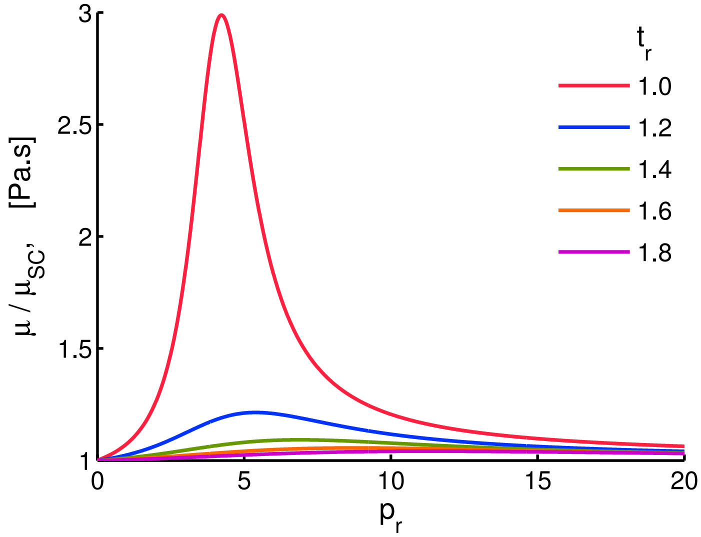

Figure 4.6: Ratio of gas viscosity μ/μ_{SC} is plotted against reduced pressure p_r by using Eq. (4.2.10) and at $p_c = 3384$ kPa, and $t_c = 130$ K. The viscosity almost remains at a constant level of 1 for $p_r > 20$, but for $p_r < 15$, there is large variation in the viscosity ratios.

in the range of p_r considered. Then μ decreases with the further increase in the pressure. Furthermore, at elevated temperatures, gas viscosity is nearly constant at all values of pressures considered. It is observed when the reservoir temperature is equal to the critical temperature the gas viscosity peaks sharply at $p_r \approx 5$, but returns to the general trend and decreases slowly with further increase in the pressure. The gas shows maximum resistance to it's flow when $\partial\mu/\partial p_r = 0$, which means that the gas viscosity is at a maximum when $p_r = \sqrt{c_Z/a_Z}$, which is the same point as where the gas density has a maximum, see Figure 4.3. But the gas viscosity is much smaller compared to oil or water viscosities, which implies that gas moves very quickly inside the reservoir. Also, note that when $p_r \to 0$ and also when $p_r \to \infty$, then $\rho \to 0$, which implies that $\mu \to \mu_{SC}$ in these limits.

From equation (4.2.10) the ratio of viscosity to standard condition viscosity

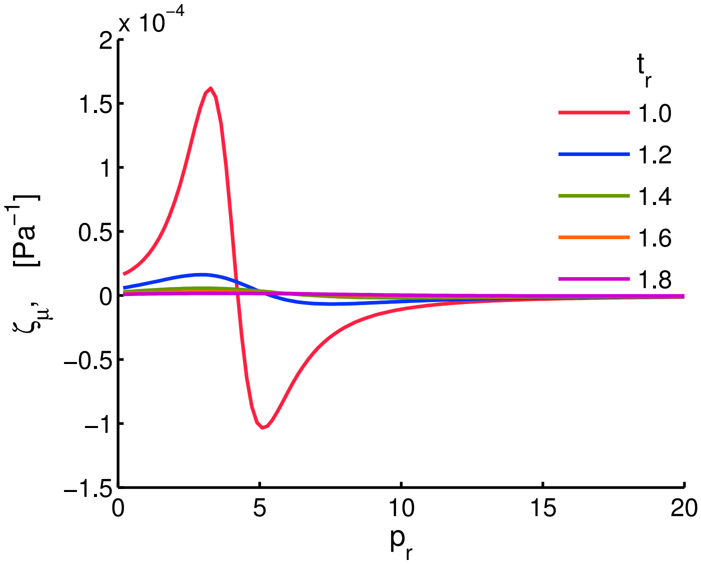

Figure 4.7: Compressibility coefficient of gas viscosity (ζ_μ) plotted against the reduced pressure p_r are obtained by using Eq. (4.2.11). For $t_r \geq 1.4$, there is no significant changes in ζ_μ, but for $t_r < 1.4$, there are large variations in the values of ζ_μ for $p_r < 15$.

can be written as $\mu/\mu_{S_c} = \exp(A_\mu \rho^{B_\mu})$, which is plotted in Figure 4.6. The trends displayed in the Figure 4.6 are similar to the graphs of density shown in the Figure 4.3 because the viscosity ratio μ/μ_{S_c} is just the exponential of the gas density raised to some power.

The Compressibility Coefficient of Gas Viscosity (ζ_μ) is given by

$$\zeta_\mu(p) = \frac{d}{dp} \ln \mu = A_\mu B_\mu \rho^{B_\mu} \zeta_\rho(p) \tag{4.2.11}$$

Figure 4.7 shows that the compressibility coefficient of gas viscosity against the pressure at different values of temperature. We observe that it varies greatly for small values of temperature $t_r < 1.4$ but then it asymptotes to zero for $t_r \geq 1.4$. The magnitude of the compressibility coefficient of viscosity is less than 10^{-4} for the range of temperatures and pressures considered in Fig. 4.7.

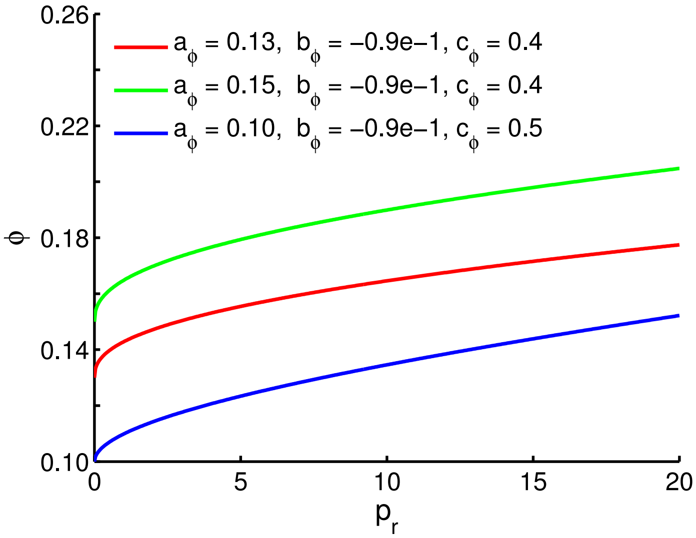

Figure 4.8: Correlation of porosity and pressure, from equation (4.2.12).

4.2.1 Kozeny-Carman Equation

Porosity, ϕ, and permeability, K, are the two most important reservoir properties in simulation models. ϕ and K depend on many variables and they must be modeled as an input to any transport model. Experimental measurement of these quantities is time consuming and expensive, so, scientists and engineers have proposed many empirical relations for the estimation of these properties. Some correlations are reviewed below.

Porosity, ϕ is the measure of pore (void) spaces in a porous media and it is defined as the ratio of the pore volume to the bulk volume of the reservoir rock. The gas is stored in the empty spaces of the reservoir rock and it flows through the interconnected network of pores. The size of the pores vary a great deal and the ensemble of pores is often modeled by a pore size distribution function. The porosity in shale rocks is very low compared to sandstones, typically in the range

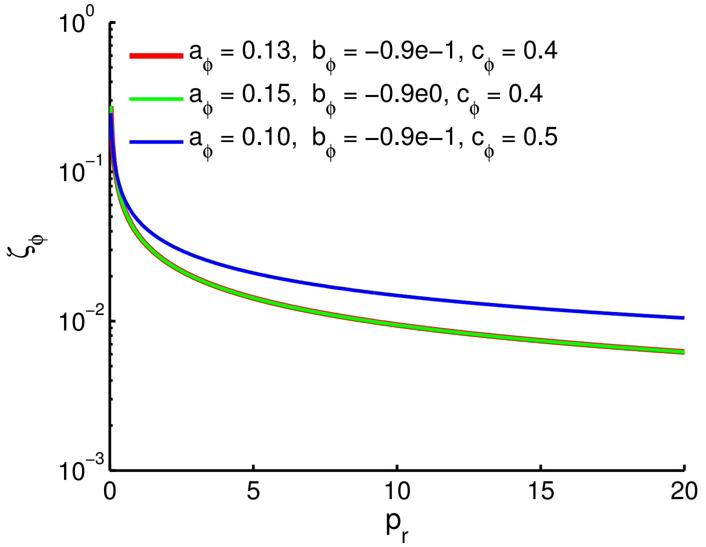

Figure 4.9: Compressibility coefficient of porosity

of 4% to 15%. We use the following correlation between the porosity and pressure for the investigation purposes, Bockstiegel [22], Walsh and Brace [164], Regnet et al. [143], Zheng et al. [179],

$$\phi = a_\phi \exp(-b_\phi p^{c_\phi}), \tag{4.2.12}$$

where a_ϕ, b_ϕ, and c_ϕ are empirical constants.

Figure 4.8 shows the plots of the porosity against the pressure for different cases of a_ϕ, b_ϕ and c_ϕ. Porosity, in general, increases with the increase in pressure. Knowledge of the rock porosity can be used to estimate the volume and the mass of the gas present in the reservoir rocks.

The Compressibility coefficient of the porosity ζ_ϕ is given by the fol-

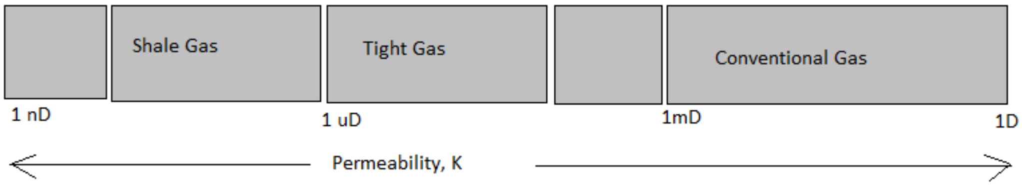

Figure 4.10: Permeability in different rock types.

lowing expression

$$\zeta_\phi(p) = \frac{d}{dp} \ln \phi = -b_\phi c_\phi p^{c_\phi - 1} \tag{4.2.13}$$

Figure 4.9 shows the behavior of ζ_ϕ against pressure for different choices of a_ϕ, b_ϕ, and c_ϕ. We observe that $\zeta_\phi(p)$ decreases with the increase in pressure because $c_\phi - 1 < 0$ for our choice of c_ϕ. With these choices of parameters, ζ_ϕ has magnitude of the order of $O(10^{-2})$ at higher pressures, that is, the relative rate of change in porosity is very small as per unit change in pressure, in the ranges of p_r considered.

The Intrinsic Permeability, K, is another fundamental property of the reservoir rocks. It is the measure of the ability of the reservoir rock to allow fluids to flow through it. The higher the permeability, the higher the flow rate is. Figure 4.10 shows the permeability ranges for different types of rocks.

Different models and empirical relations have been proposed to estimate the permeability of reservoir rocks. One of the most commonly used relation is the Kozeny-Carman equation which is derived on the assumption of continuous flow of fluid through a bundle of parallel tubes of constant diameter, see Xu and Yu [173]. This equation gives good results for the homogeneous porous media with the laminar flow, but it fails to accurately predict the permeability values of the

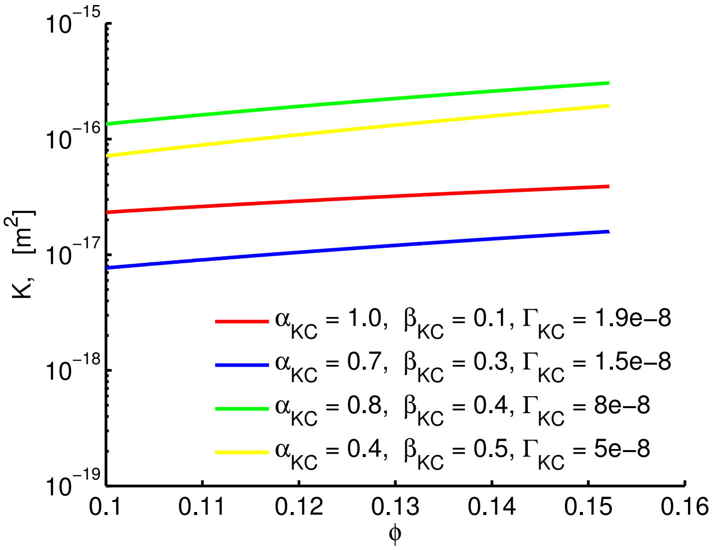

Figure 4.11: Power law form of Kozeny Caraman equation (4.2.14). Intrinsic permeability is plotted against porosity for different cases of α_{KC}, β_{KC}, and Γ_{KC}.

heterogeneous reservoirs with a complex network of pores. It also fails for the reservoirs with very low porosity and low permeability values. Civan [40] has proposed a modified Power-Law form of the Kozeny-Carman equation,

$$\sqrt{\frac{K}{\phi}} = \Gamma_{KC} \left(\frac{\phi}{\alpha_{KC} - \phi} \right)^{\beta_{KC}}, \tag{4.2.14}$$

where α_{KC}, β_{KC}, and Γ_{KC} are empirically determined constants, and $\phi < \alpha_{KC} \leq 1$, $0 \leq \beta_{KC} < \infty$ and $\Gamma_{KC} \geq 0$.

Figure 4.11 shows the plots of the permeability K against the porosity ϕ for different sets of α_{KC}, β_{KC} and Γ_{KC}. Equation (4.2.14) can be rearranged to yield,

$$K = \Gamma_{KC}^2 \frac{\phi^{2\beta_{KC}+1}}{(\alpha_{KC} - \phi)^{2\beta_{KC}}}, \tag{4.2.15}$$

which upon taking derivative with respect to ϕ gives,

$$\frac{dK}{d\phi} = \Gamma_{KC}^2 \frac{\phi^{2\beta_{KC}}}{(\alpha_{KC} - \phi)^{2\beta_{KC}+1}} [2\beta_{KC}\alpha_{KC} + (\alpha_{KC} - \phi)] > 0, \tag{4.2.16}$$

which implies that permeability is an increasing function of porosity.

The Compressibility coefficient of the intrinsic permeability, ζ_K, is given by,

$$\begin{aligned} \zeta_K(p) &= \frac{d}{dp} \ln K \\ &= \left(1 + \frac{2\alpha_{KC}\beta_{KC}}{\alpha_{KC} - \phi}\right) \zeta_\phi(p) \\ &= -b_\phi c_\phi p^{c_\phi - 1} \left(1 + \frac{2\alpha_{KC}\beta_{KC}}{\alpha_{KC} - \phi}\right). \end{aligned} \tag{4.2.17}$$

Since the quantity in the brackets of equation (4.2.17)is positive by equation (4.2.16), therefore the sign of ζ_K depends on the sign of ζ_ϕ; if ζ_ϕ is positive than ζ_K is positive and vice versa. We observe that ζ_K decreases with increasing pressure, Figure 4.12. Moreover, $\zeta_K \to 0$ as $p_r \to +\infty$. Since the intrinsic permeability depends on the porosity through equation (4.2.12), then ζ_K depends ζ_ϕ through equation (4.2.17).

The Tortuosity, τ, is a measure of the geometric complexity of the pore network and inter-connectivity, and it is defined as the ratio of the length of a typical streamline, or path, between two boundaries, to the the bulk length of the reservoir rock. The gas molecules travel through the flow channels of the reservoir rock which are an interconnected network of pores. The smaller values of porosity

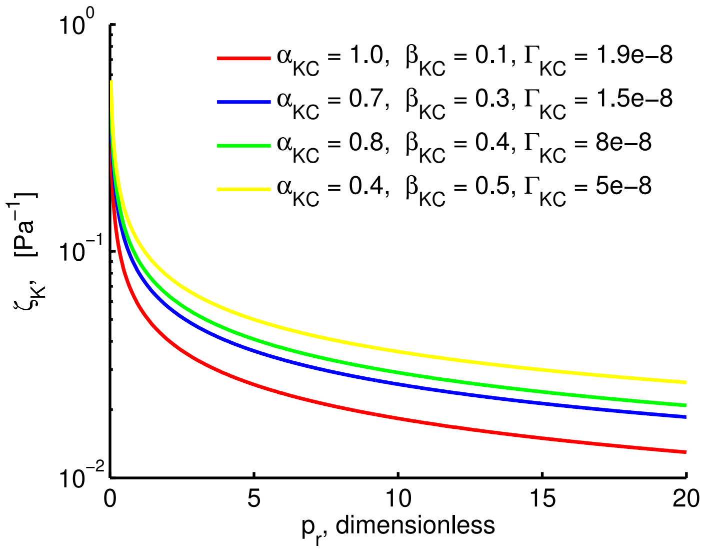

Figure 4.12: Compressibility coefficient of intrinsic permeability K, equation 4.2.17, against pressure.

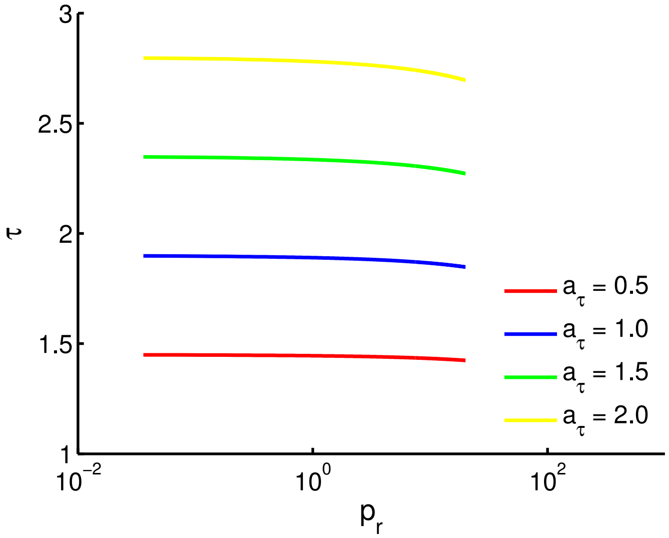

Figure 4.13: Plots of tortuosity against pressure, from equation (4.2.18).

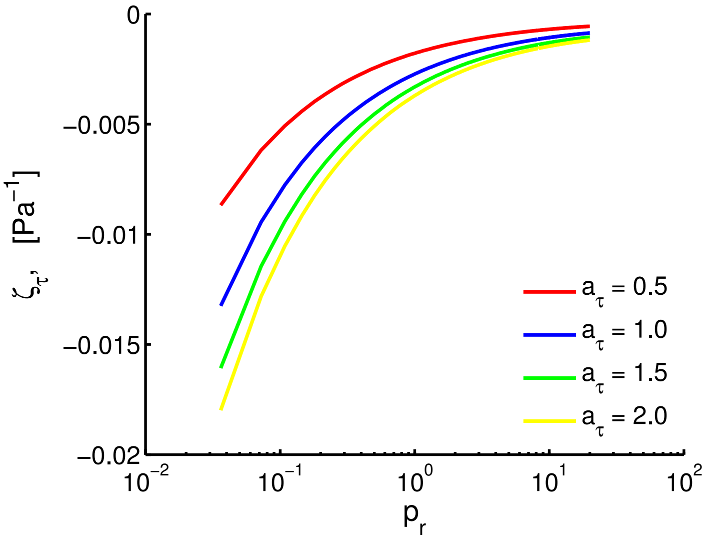

Figure 4.14: Compressibility coefficient of tortuosity from equation (4.2.19), plotted against pressure.

corresponds to larger values of tortuosity and vice versa. The tortuosity of the shale rocks is large compared to the tortuosity of sandstones (for some value of porosity ϕ). There exists several relations between tortuosity and porosity but none of them works for all situations, see Matyka et al. [116]. We use the following correlation between the porosity and pressure for the investigation purposes,

$$\tau = 1 + a_\tau(1 - \phi), \tag{4.2.18}$$

where a_τ is a fitting constant. Tortuosity τ is a decreasing function of ϕ because $d\tau/d\phi = -a_\tau < 0$. Note that as $p \to 0$ then $\phi \to a_\phi$, and, therefore $\tau \to 1 + a_\tau(1 - a_\phi)$.

The information about the tortuosity can be used to describe the well-bore trajectories or it can also be used to describe the pore systems in the rocks.

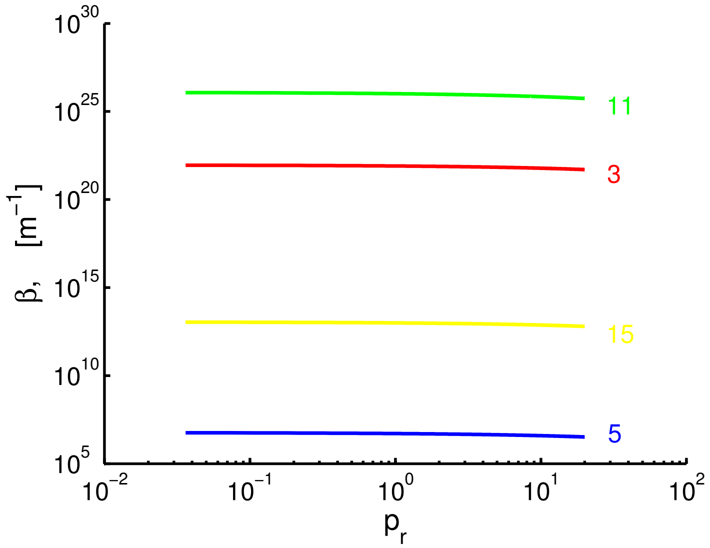

Figure 4.15: Turbulence Factor is plotted against pressure p, from equation (4.2.20).

Figure 4.13 shows the plots of tortuosity τ against pressure for different values of a_τ.

The Compressibility coefficient of tortuosity ζ_τ is given by the expression,

$$\zeta_\tau(p) = \frac{d}{dp}\ln\tau = -a_\tau\frac{\phi}{\tau}\zeta_\phi(p). \tag{4.2.19}$$

Figure 4.14 shows the behavior of ζ_τ against pressure. We observe that ζ_τ increases with increasing pressure and it's value is negative for the range of pressure considered. As $p_r \to \infty$, then $\zeta_\tau \to 0$.

The Turbulence Factor, β, is a measure of the departure of the flow from Darcy's law due to increasing turbulence. The non-Darcy flow is observed in the gas wells when the fluid reaching the well bore velocities high enough for the onset of turbulence. The pressure drop cannot be measured by Darcy's equation.

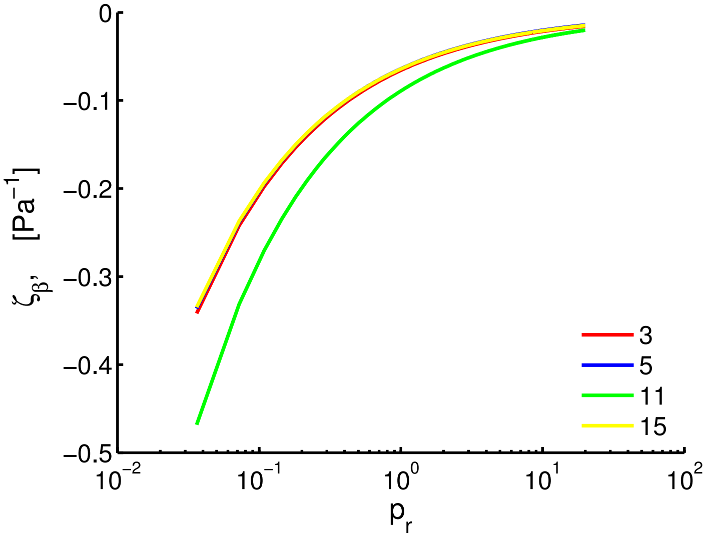

Figure 4.16: Compressibility coefficient of turbulence factor is plotted against pressure p, from (4.2.21).

Forchheimer [67] introduced a quadratic term to account for the turbulence effects equation (3.2.2), in which β is called turbulence factor (it is also referred as non-Darcy coefficient, or inertial coefficient) and we use the following general formula for investigation purposes, Zhang [176],

$$\beta(\phi, K_a, \tau) = \frac{a_\beta \tau^{b_\beta}}{K_a^{c_\beta} \phi^{d_\beta}} \tag{4.2.20}$$

where, a_β, b_β, c_β and d_β are empirical constants. (Note that in a fully 3D setup, β is a tensor.) Figure 4.15 shows plots of turbulence factor β against p_r for the case numbers 3, 5, 11 and 15 from the Table 4.1, collected from Thauvin and Mohanty [156] and Macini et al. [108]. The general trend is that the turbulence factor β remains constant for the range of pressure considered. All other cases listed in Table 4.1 show similar trends.

	a_β	b_β	c_β	d_β
1	1.55e4	3.35	0.98	0.29
2	2.5e5	0.0	1.0	0.0
3	3.1e4	3.0	1.0	0.0
4	2.98e-1	0.0	0.5	5.5
5	0.005	0.0	0.5	0.75
6	1.82e8	0.0	1.25	0.75
7	2.94e7	1.0	1.0	1.0
8	1.0	0.0	0.5	1.5
9	1.0	1.0	1.0	1.0
10	4.8e10	0.0	1.176	0.0
11	2.018	0.0	1.55	0.0
12	1.15e7	0.0	1.0	1.0
13	5.5e9	0.0	1.25	0.75
14	3.5e10	0.0	1.82	-0.449
15	3.1e-5	1.943	1.023	0.0

Table 4.1: Data for Simulating Turbulence Factor β.

The Compressibility coefficient of turbulence factor ζ_β is given by,

$$\zeta_\beta(p) = \frac{d}{dp}\ln\beta = b_\beta\zeta_\tau(p) - c_\beta\zeta_{K_a}(p) - d_\beta\zeta_\phi(p). \tag{4.2.21}$$

Figure 4.16 shows the behavior of ζ_β against p_r. It is observed that ζ_β is negative and approaches 0 as p_r increases.

The Control Factor, F, introduced in Chap. 3 is given by

$$F = \left[1 + \frac{\beta\rho}{\mu}K_a|u|\right]^{-1} \tag{4.2.22}$$

Figure 4.17 shows the plots of the control factor F against p_r for different values of the velocity u. It is noted that F remains constant for the range of pressure considered and for a particular value of velocity u.

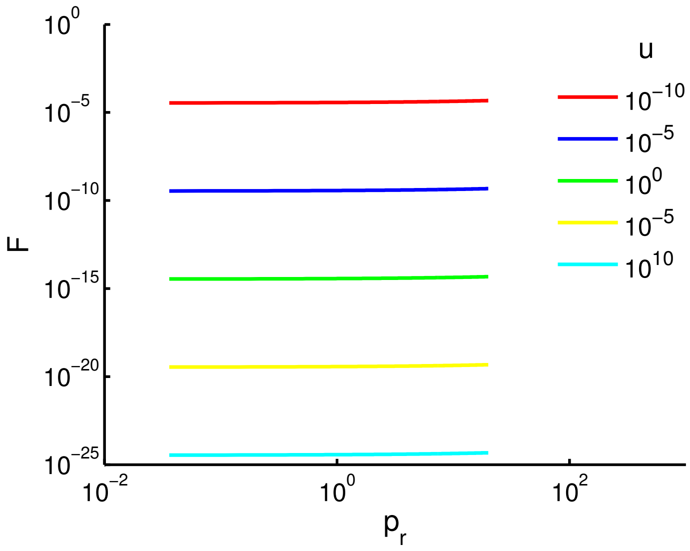

Figure 4.17: Plots of Control Factor F against p_r, for various velocities $\mathbf{u}$.

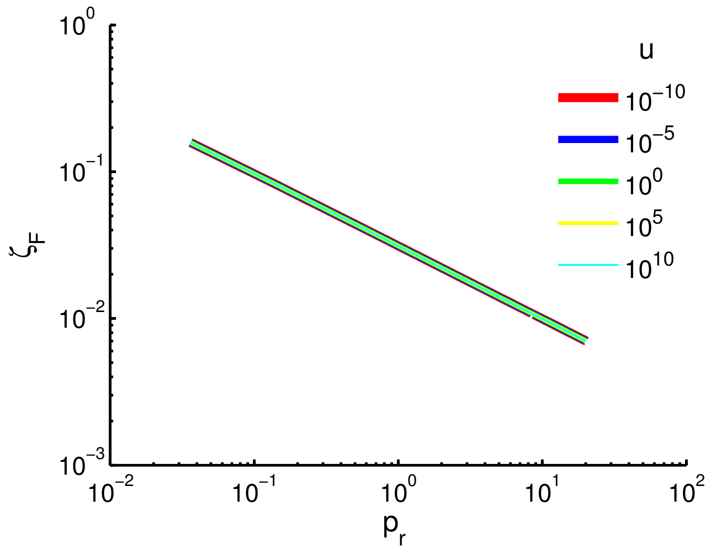

Figure 4.18: Compressibility Coefficient of Control Factor F is plotted against p_r for various velocities $\mathbf{u}$.

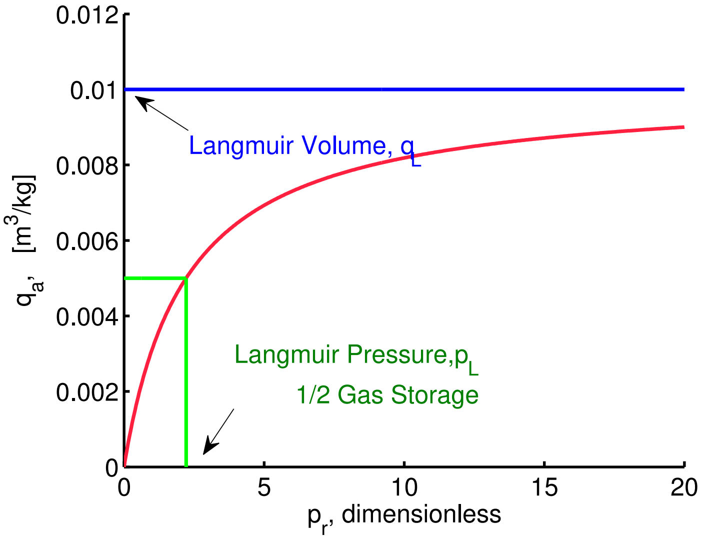

Figure 4.19: Langmuir gas isotherm against p_r.

The Compressibility coefficient of Control Factor ζ_F is given by,

$$\begin{aligned}\zeta_F(p) &= \frac{d}{dp}\ln F \\ &= (F-1)\left[\zeta_\rho(p) - \zeta_\mu(p) + \zeta_{K_a}(p) + \zeta_\beta(p) + \zeta_{|u|}(p)\right], \qquad (4.2.23)\end{aligned}$$

where $\zeta_{K_a}(p) = \zeta_K(p) + \zeta_f(p)$, $\zeta_K(p)$ is given by equation (4.2.17) and $\zeta_f(p)$ is defined below in equation (3.3.22). Figure 4.18 shows plots of ζ_F against p_r for different values of velocity u. We observe a remarkable insensitivity of ζ_F to u - all the plots collapse onto nearly the same plot.

4.2.2 Gas Adsorption Isotherm

Shale gas reservoirs are found in the form of geological layers which are spread over the wide areas ranging from 100 km to 300 km. Since the porosity of the shale rocks is very small and also due to the compact nature of the rock formations, the gas molecules are trapped there for very long periods of times. This process creates a layer of gas along the surface of the pores (molecules of gas are attached to the organic matter) and hence the shale rocks serves as a place for gas storage. This phenomenon is called *adsorption* which is a reversible process, that is, the gas can be released through the process of *desorption*. The amount of gas present in the shale gas rocks due to adsorption is much higher than the free gas present in pores of the shale rocks because of the very low porosity. The relationship between pressure and the volume of adsorbed gas is described by the desorption isotherm. The most commonly used relation to estimate the amount of gas released is the Langmuir Isotherm Formula. A detailed review of adsorption isotherms is given by Foo and Hameed [66]. Cui et al. [44], and Civan et al. [41] used the following formula for estimating the amount of adsorbed gas, which is based on Langmuir adsorption isotherm,

$$q_a = \frac{q_L p}{p_L + p}, \tag{4.2.24}$$

$$q = \frac{\rho_s M_g}{V_{std}} q_a \tag{4.2.25}$$

where ρ_s (kg/m^3) denotes the material density of the porous sample, q (kg/m^3) is the mass of gas adsorbed per solid volume, q_a (std m^3/kg) is the standard volume of gas adsorbed per solid mass, q_L (std m^3/kg) is the Langmuir gas volume, V_{std} (std m^3/kmol) is the molar volume of gas at standard temperature (273.15K) and pressure (101,325Pa), p (Pa) is the gas pressure, p_L (Pa) is the Langmuir gas pressure, and M_g (kg/kmol) is the molecular weight of gas.

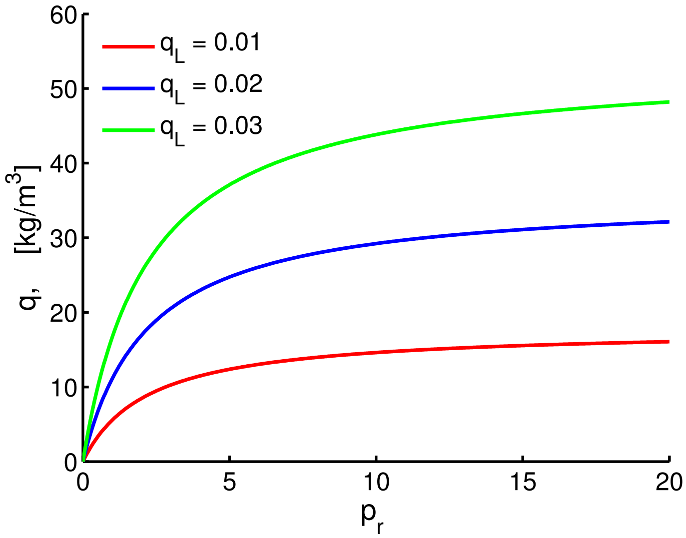

Figure 4.20: The amount of gas adsorbed in the reservoir rocks depends on the density of the solid rock, molecular mass of gas and volume of gas at the standard pressure and temperature.

Note that as $p \to \infty$, then $q_a \to q_L$ and $q \to \rho_s M_g q_L / V_{std}$. Moreover, when $p = p_L$, $q_a = q_L/2$ and $q = \rho_s M_g q_L / 2V_{std}$. Figure 4.19 shows the plot of the Langmuir Adsorption Isotherm q_a defined in equation (4.2.24). It has the property that as the pressure goes to infinity then the amount of gas adsorbed at the surface of the pore approaches the Langmuir volume q_L. Another important property of the Langmuir isotherm is that half of the gas molecules occupies the empty spaces along the surface of the pores at the Langmuir pressure p_L. Figure 4.20 shows the plot of the amount of the adsorbed gas in the reservoir against pressure p_r for different values of Langmuir volume q_L. The amount of adsorbed gas is higher for larger values of q_L.

The Ratio of adsorbed gas density to free gas density can be obtained

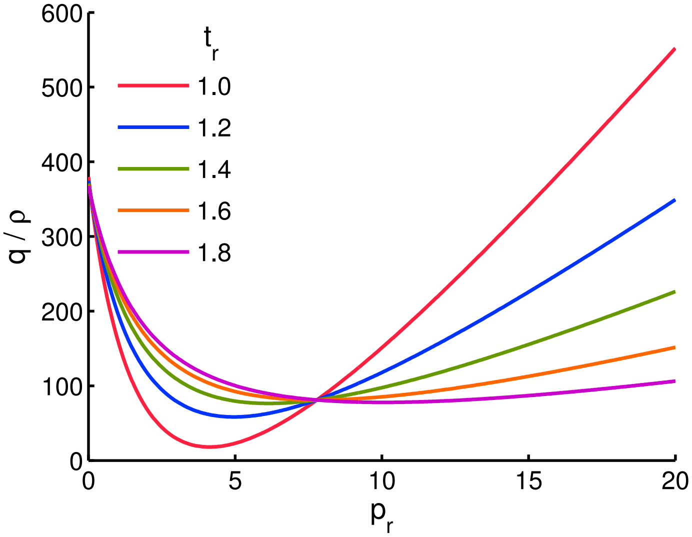

Figure 4.21: Ratio of the adsorbed gas density to the free gas density, against pressure, equation (4.2.26) at different temperatures.

by combining equations (4.2.24) and (4.2.6), that is,

$$\frac{q}{\rho} = \frac{\rho_s q_L R_g T}{V_{std}}.\frac{Z}{p_L + p} \tag{4.2.26}$$

The ratio q/ρ decreases in the interval $(0, \sqrt{c_Z/a_Z})$ and increases in the interval $(\sqrt{c_Z/a_Z}, \infty)$. It is also noted that for large values of pressure $p_r >> \sqrt{c_Z/a_Z}$, $Z \rightarrow p_r^2$, and then the ratio q/ρ asymptotes to a linear relationship with pressure, p_r, and therefore, $q/\rho \rightarrow \infty$ as $p_r \rightarrow \infty$. For small values of pressure ($p_r << \sqrt{c_Z/a_Z}$), we have $q/\rho \approx c_Z/p_L$ which is approximately constant at constant temperature. The behavior of the ratio q/ρ is shown in Figure 4.21 for different temperatures t_r.

The Rate of change of adsorbed gas density with respect to free gas density. Cui et al. [44] defines a parameter L_a (m^3 gas/ m^3 solid) which is the rate of change of adsorbed gas density with respect to free gas density and is defined by

$$L_a \equiv \frac{\partial q}{\partial \rho} = \frac{\rho_s M_g}{\rho \zeta_\rho(p) V_{std}} \frac{q_L p_L}{(p_L + p)^2}. \tag{4.2.27}$$

Using equations (4.2.1), (4.2.6) and (4.2.7), equation (4.2.27) becomes

$$L_a \equiv \frac{\partial q}{\partial \rho} = \frac{\rho_s q_L p_L t_r R_g p_c}{V_{std}} \cdot \frac{1}{(p_L + p)^2} \cdot \frac{Z^2}{(-a_Z p_r^2 + c_Z)} \tag{4.2.28}$$

Equation (4.2.28) is a product of three terms, the first term is a positive constant, the second term is positive and a decreasing function of pressure, and the third term is a ratio of two functions; the function in the numerator is Z^2 which is a positive function of pressure, and the function in the denominator is positive in the interval $(0, \sqrt{c_Z/a_Z})$ and negative in the interval $(\sqrt{c_Z/a_Z}, \infty)$, and is zero at $p_r = \sqrt{c_Z/a_Z}$, where $L_a \to \infty$.

The Relative Rate of Change of Adsorbed Gas Density with respect to Free Gas Density is given by,

$$\frac{L_a}{q} = \frac{1}{q}\frac{\partial q}{\partial \rho} = \frac{p_L t_r R_g p_c}{M_g} \cdot \frac{1}{p(p_L + p)} \cdot \frac{Z^2}{(-a_Z p_r^2 + c_Z)}. \tag{4.2.29}$$

Elasticity of adsorbed gas density with respect to free gas density is given by,

$$\frac{\rho}{q}\frac{\partial q}{\partial \rho} = \frac{p_L p_c}{p_L + p} \cdot \frac{Z}{(-a_Z p_r^2 + c_Z)}. \tag{4.2.30}$$

Figure 4.22 shows this quantity plotted (inversely) against p_r.

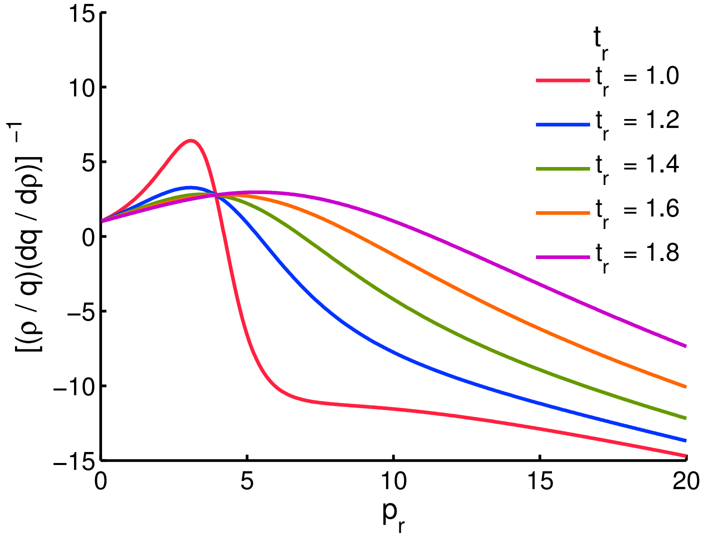

Figure 4.22: Inverse of the elasticity of adsorbed gas density with respect to free gas density is plotted against p_r at different temperatures t_r.

The Compressibility coefficient of the adsorbed gas ζ_q is given by,

$$\zeta_q(p) = \frac{d}{dp} \ln q = \frac{p_L}{p(p_L + p)}. \tag{4.2.31}$$

$\zeta_q(p)$ decreases with increasing pressure. It implies that $\zeta_q(p)$ is limited by the number of empty spaces available at the pore surface. When the pressure is increased the gas molecules occupy the empty spaces along the surface of the pores and once all the spaces are filled with the gas molecules, further increase in the pressure does not change the amount of gas adsorbed into the pore surface. Similarly, when the pressure is decreased, space in the pores become available for the movement of the gas particles and the gas starts desorbing from the pore surface into the pores. It means that a large amount of gas can be recovered by an initial decrease in pressure. Figure 4.23 shows the behavior of the compressibility

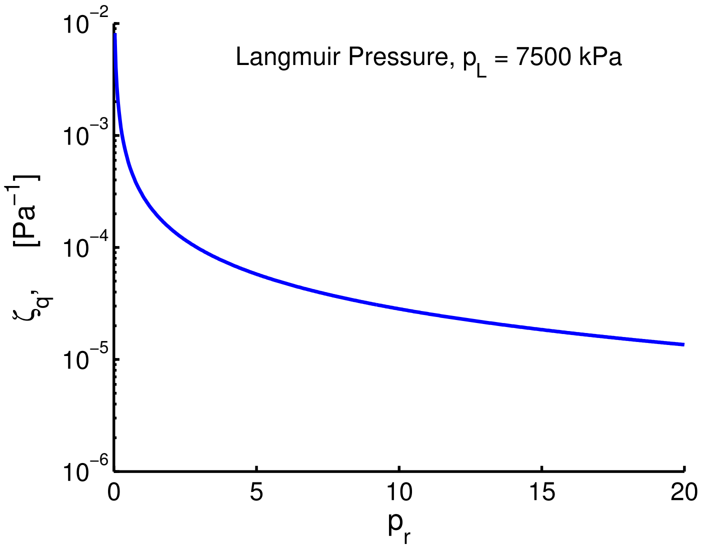

Figure 4.23: Compressibility coefficient of adsorbed gas against p_r.

coefficient $\zeta_q(p)$ against p_r. Note that $\zeta_q(P)$ has single curve because it does not depend on temperature.

Figures 4.24 and 4.25 show the plots of ζ_1 and ζ_2, from equations (3.3.6) and (3.3.7), respectively.

4.2.3 Knudsen Number and Classification of flow regimes

Different flow conditions occur in the small pores of the porous media, some deviating from the continuous flow. There are four important classes of flow regimes, see Cussler [45], and Table 4.2.

1. **Knudsen Diffusion or Free Molecular Flow**, $K_n > 10$, occurs at places where the pore diameter is very small such that the collision between the gas particles and pore walls is dominant over the collision between the gas particles. The mean free path (λ) is less than the mean pore radius, see Fig.

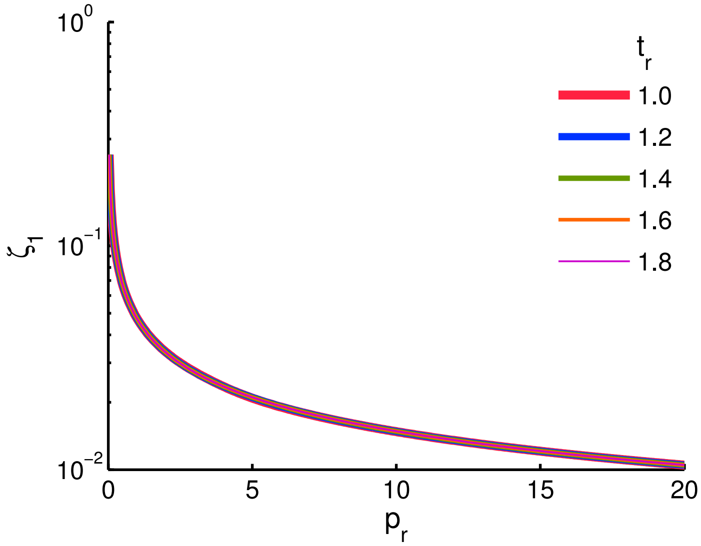

Figure 4.24: Plots of ζ_1 against pressure p, show that the effect of compressibility coefficient of gas density prevails compared to the effect of compressibility coefficient of porosity.

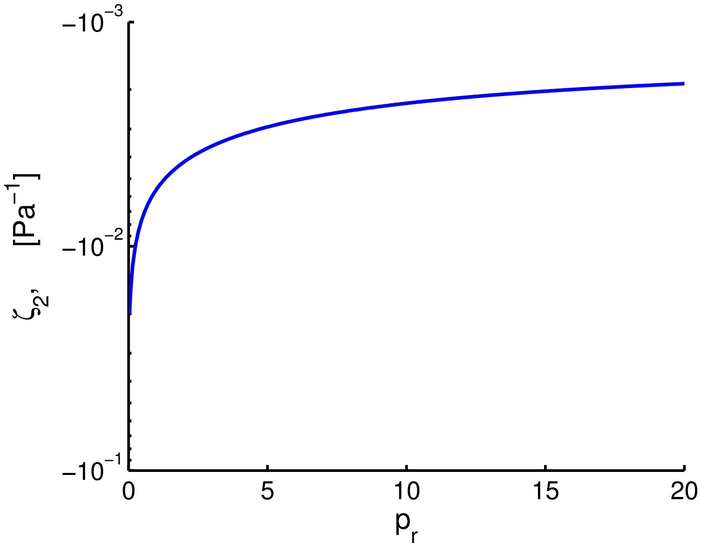

Figure 4.25: Plots of ζ_2 against pressure p, show that the effect of compressibility coefficient of adsorbed gas prevails as compared to the effect of compressibility coefficient of porosity.

2.5 in Chap. 2.

2. **Surface Diffusion or Slip Flow** is another important phenomena that is observed in the flow of gases through the solid rock matrix. A part of the gas is adsorbed on to the walls of the pores. This creates a layer of gas particles on the surface and the gas particles strictly adhere to their position and then the movement occurs by “hopping”, see Fig. 2.4 in Chap. 2. The range of Knudsen number for the slip flow is $0.01 < K_n < 0.1$

3. **Transition Flow** occurs when all the pore walls are covered by gas molecules and no more surface diffusion can occur. Hence, few gas particles leave the surface of the pore walls and start flowing with the other gas particles. The range of Knudsen number for the transition flow is $0.1 < K_n < 10$

4. **Viscous or Continuous Flow** occurs at places where the pore diameter is much greater than the mean free path so that the collisions with the walls is not important, see Fig. 2.3 in Chap. 2. The range of Knudsen number for the viscous flow is $K_n < 0.01$.

The various flow regimes are conveniently parameterized by the Knudsen Number. It is the ratio of mean free path λ to the hydraulic radius R_h, that is,

$$K_n = \frac{\lambda}{R_h}. \tag{4.2.32}$$

Ziarani and Aguilera [181], Rathakrishnan [141] and many other researchers have followed the classification of four flow regimes based on Knudsen numbers, see

Knudsen Number	Flow Regimes
$K_n < 0.01$	Continuous Flow
$0.01 < K_n < 0.1$	Surface Diffusion or Slip Flow
$0.1 < K_n < 10$	Transition Flow
$K_n > 10$	Knudsen Diffusion or Free Molecular Flow

Table 4.2: Classification of Flow Regimes based on Knudsen Number

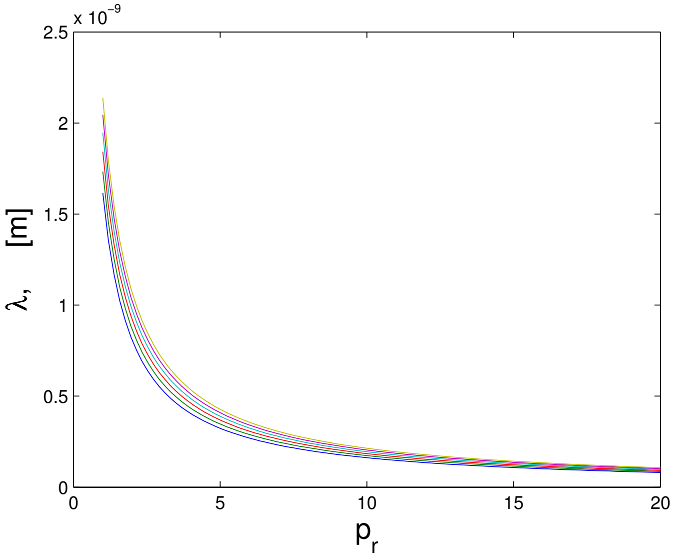

Figure 4.26: Mean free path is plotted against p_r at different temperatures t_r.

Table 4.2.

The Mean Free Path (λ) is the average distance traveled by a gas molecule or other particle between the collisions with another particles. There exists several models for the mean free path, such as given by Loeb [106]. Bird [20] derived a model, equation (4.2.33), which is based on VHS model and showed that it has certain advantages over the previously derived studies. Christou and Kokou Dadzie [36] have recently used this model in their study of direct simulation Monte Carlo methods in porous media with varying Knudsen number. The equation for the

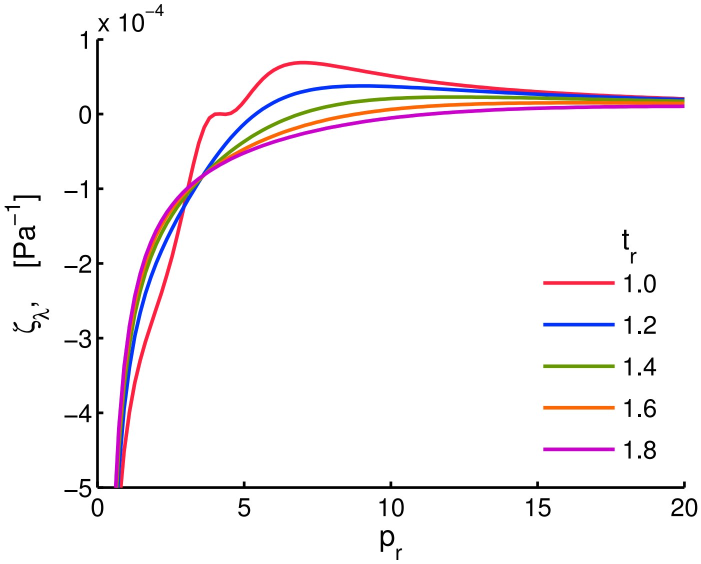

Figure 4.27: Compressibility coefficient of mean free path against p_r, for different temperature t_r.

mean free path is given by,

$$\lambda = \frac{\mu}{p}\sqrt{\frac{\pi R_g T}{2M_g}}, \tag{4.2.33}$$

where ρ is gas density kg/m^3, μ is gas viscosity, T is the absolute temperature in Kelvin, $R_g = 8134 J/kmol/K$ is the universal gas constant.

The Compressibility coefficient of Mean Free Path ζ_λ is given by

$$\zeta_\lambda(p) = \zeta_\mu(p) - \zeta_\rho(p). \tag{4.2.34}$$

Figure 4.27 shows the plots of the compressibility coefficient of mean free path ζ_λ against pressure p. $\zeta_\lambda(p)$ is negative in the interval $(0, \sqrt{c_Z/a_Z})$ and positive in the interval $(\sqrt{c_Z/a_Z}, \infty)$, and is zero at $p_r = \sqrt{c_Z/a_Z}$.

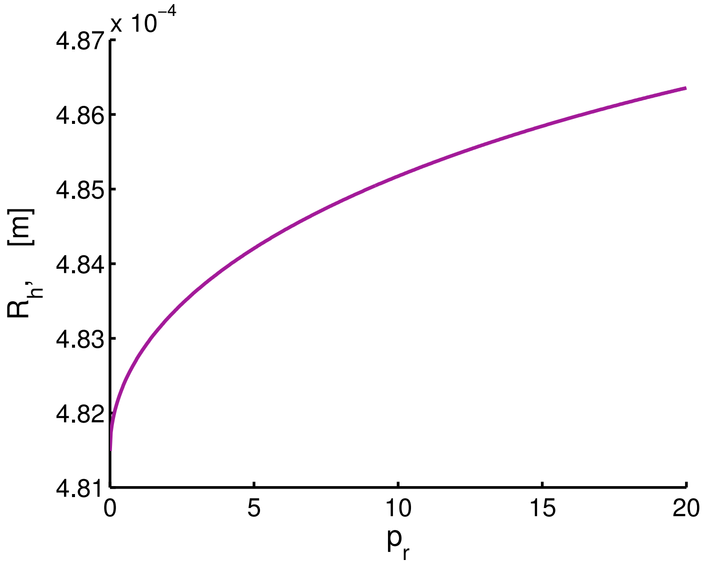

Figure 4.28: Hydraulic Radius of flow channels is plotted against p_r, where the data is, $a_\phi = 0.1$, $b_\phi = 0.0939$, $c_\phi = 0.5$, $\alpha_{KC} = 1.0$, $\beta_{KC} = 0.1$, $\Gamma_{KC} = 1.9e - 8$, $a_\tau = 1.0$.

The Hydraulic Radius, R_h, of the pore network is given by, Carman and Carman [29] and Civan [38],

$$R_h = 2\sqrt{2\tau}\sqrt{\frac{K}{\phi}}, \tag{4.2.35}$$

where τ is the tortuosity and ϕ is the porosity of the porous media.

Figure 4.28 shows the plot of hydraulic radius against pressure p_r. The R_h is computed by using equation (4.2.35) and with $a_\phi = 0.1$, $b_\phi = 0.0939$, $c_\phi = 0.5$, $\alpha_{KC} = 1.0$, $\beta_{KC} = 0.1$, $\Gamma_{KC} = 1.9e - 8$, $a_\tau = 1.0$, see Ali et al. [10]. R_h increases with increase in pressure.

Substituting equations (4.2.14) and (4.2.18) in equation (4.2.35), we obtain

$$R_h = 2\Gamma_{KC}\sqrt{2 + 2a_\tau(1-\phi)}\left(\frac{\phi}{\alpha_{KC} - \phi}\right)^{\beta_{KC}} \tag{4.2.36}$$

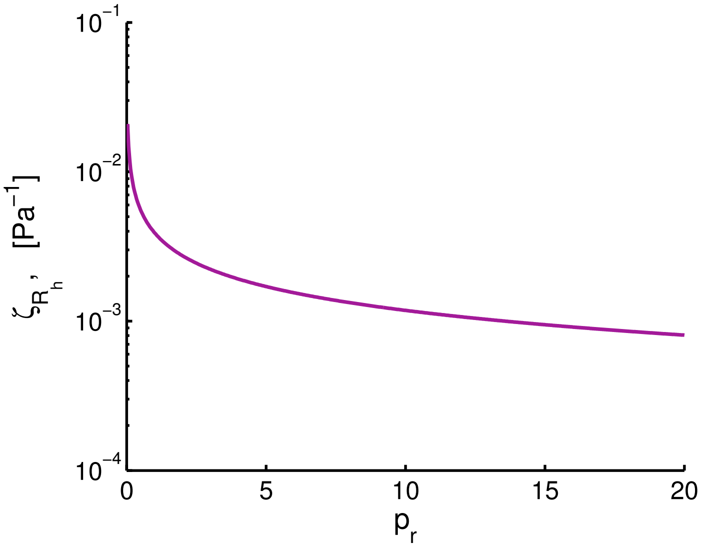

Figure 4.29: Compressibility coefficient of hydraulic radius against p_r, for $a_\phi = 0.1$, $b_\phi = 0.0939$, $c_\phi = 0.5$, $\alpha_{KC} = 1.0$, $\beta_{KC} = 0.1$, $\Gamma_{KC} = 1.9e-8$, $a_\tau = 1.0$, from equation (4.2.38).

As $p \to 0$, then $\phi \to a_\phi$ and hence R_h asymptotes to,

$$R_h = 2\Gamma_{KC}\sqrt{2 + 2a_\tau(1 - a_\phi)}\left(\frac{\phi}{\alpha_{KC} - a_\phi}\right)^{\beta_{KC}}. \qquad (4.2.37)$$

On the other hand, as $p \to \infty$, then $\phi \to 0$ and hence $R_h \to 0$, in this limit.

The Compressibility coefficient of the Hydraulic Radius ζ_R is given by,

$$\zeta_R(p) = \frac{1}{2}\left[\zeta_\tau(p) + \zeta_K - \zeta_\phi(p)\right]. \qquad (4.2.38)$$

Figure 4.29 shows the plot of the compressibility coefficient of the hydraulic radius against p_r for the following choice of model parameters, $a_\phi = 0.1$, $b_\phi = 0.0939$, $c_\phi = 0.5$, $\alpha_{KC} = 1.0$, $\beta_{KC} = 0.1$, $\Gamma_{KC} = 1.9e-8$, $a_\tau = 1.0$, see Ali et al. [10]. In general, ζ_R decreases with the increase in pressure.

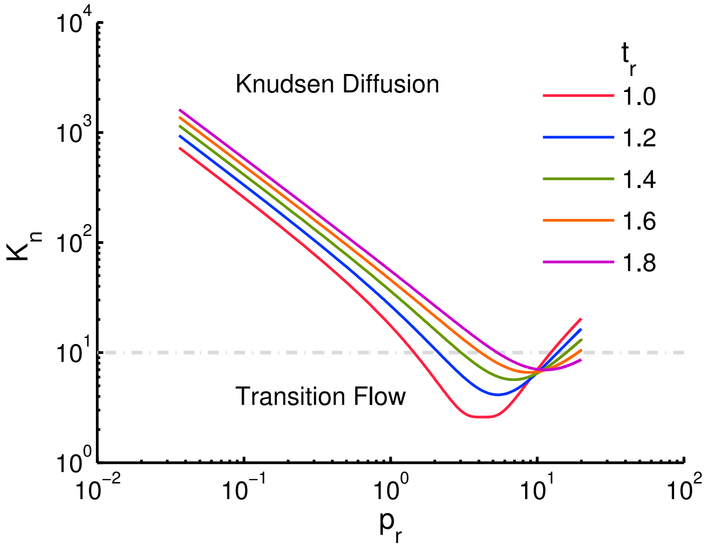

Figure 4.30: Plots of Knudsen number against p_r at different temperatures.

Knudsen Number: A formula for Knudsen number is obtained by substituting equations (4.2.33) and (4.2.36) into equation (4.2.32),

$$K_n = \frac{1}{2\Gamma_{KC}}\sqrt{\frac{\pi}{2R_gT}}\frac{\mu}{\rho\sqrt{2+2a_\tau(1-\phi)}}\left(\frac{\alpha_{KC}-\phi}{\phi}\right)^{\beta_{KC}} \tag{4.2.39}$$

Figure 4.30 shows the plots of Knudsen number against p_r at different temperatures. It is observed that K_n has the same trend as the mean free path. It's intervals of decrease and increase are the same as of λ over the range of pressure considered.

The Compressibility coefficient of Knudsen Number ζ_{K_n} is given by

$$\begin{aligned}\zeta_{K_n}(p) &= \zeta_\lambda(p) - \zeta_R(p)\\ &= \zeta_\mu(p) - \zeta_\rho(p) + \frac{1}{2}\left[\zeta_\phi(p) - \zeta_\tau(p) - \zeta_K(p)\right].\end{aligned} \tag{4.2.40}$$

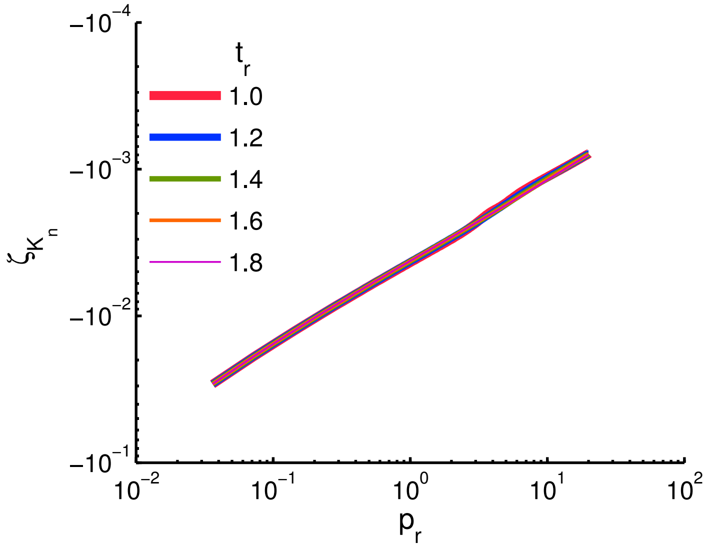

Figure 4.31: Compressibility Coefficient of Knudsen Number, ζ_{K_n}, against p_r at different temperatures.

Figure 4.31 shows the plots of ζ_{K_n} against p_r at different temperatures. It is noted that ζ_{K_n} has negative values and they are identical for different temperatures.

4.2.4 Intrinsic Permeability and Apparent Permeability

The transport of gas through the tight shale rocks is governed by many factors, such as different flow regimes, as described above in Section 4.2.3. There are two different permeabilities associated with the shale gas reservoirs, one is the intrinsic permeability K and the other is the apparent permeability K_a. Intrinsic permeability does not depend on the type of fluid or the flow conditions, whereas the permeability used in the transport equations for the flow of the fluid is the apparent gas permeability. Therefore an improved formula, derived from Hagen-

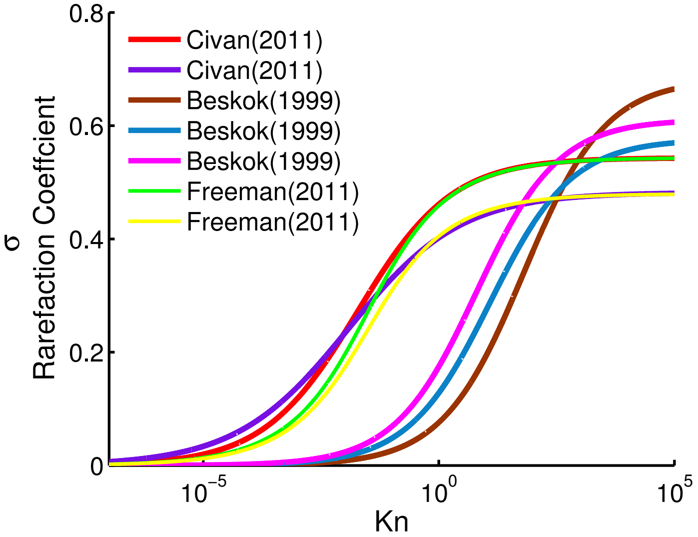

Figure 4.32: Rarefaction correction factor σ against Knudsen number K_n for different correlations, see Beskok and Karniadakis [19], Civan et al. [41], Freeman et al. [68].

Poiseuille-type equation, is given by Beskok and Karniadakis [19] and Civan [38]

$$K_a = K f(K_n) \tag{4.2.41}$$

where $f(K_n)$ is the flow condition function and is given by

$$f(K_n) = (1 + \sigma K_n)\left(1 + \frac{4K_n}{1 - b_{SF}K_n}\right), \tag{4.2.42}$$

where b_{SF} is slip factor and σ is called the Rarefaction Coefficient Correlation. Different correlations for σ are proposed by Beskok and Karniadakis [19], Civan et al. [41], Freeman et al. [68]. In this work, we use the correlation for σ proposed by Civan [38], and it is given by,

$$\sigma = \sigma_0 \left(\frac{K_n^{b_\sigma}}{a_\sigma + K_n^{b_\sigma}}\right) = \sigma_0 \left(1 + \frac{a_\sigma}{K_n^{b_\sigma}}\right)^{-1} \tag{4.2.43}$$

σ_0	a_σ	b_σ
1.38	0.178	0.438
1.205	0.199	0.365
1.7042	8.0	0.5
1.44	3.5	0.5
1.5272	2.5	0.5

Table 4.3: Data for simulating rarefaction coefficient σ, see Beskok and Karniadakis [19], Civan et al. [41], Freeman et al. [68].

where a_σ and b_σ are empirical constants. Variations in σ with respect to Knudsen number K_n are given as follows:

$$\begin{aligned}
\frac{\sigma}{K_n} &= \frac{\sigma_0}{K_n^{1-b_\sigma}(a_\sigma + K_n^{b_\sigma})} \\
\Rightarrow \frac{d\sigma}{dK_n} &= \frac{a_\sigma b_\sigma \sigma_0}{K_n^{1-b_\sigma}(a_\sigma + K_n^{b_\sigma})^2} \\
\Rightarrow \frac{1}{\sigma}\frac{d\sigma}{dK_n} &= \frac{a_\sigma b_\sigma}{K_n(a_\sigma + K_n^{b_\sigma})} \\
\Rightarrow \frac{K_n}{\sigma}\frac{d\sigma}{dK_n} &= \frac{a_\sigma b_\sigma}{a_\sigma + K_n^{b_\sigma}} \qquad (4.2.44)
\end{aligned}$$

Note that as $K_n \to 0$, then $\sigma \to 0$; and as $K_n \to \infty$, then $\sigma \to \sigma_0$. Moreover, the derivative of σ with respect to K_n is $d\sigma/dK_n = \sigma_0/K_n^{1-b_\sigma}(a_\sigma + K_n^{b_\sigma})^2$ which is positive for all values of K_n. Hence, the rarefaction coefficient σ is an increasing function of K_n. Figure 4.32 shows the plots of the rarefaction coefficient σ for different empirical models used in the literature, see Table 4.3.

Variations in the permeability correction factor f with respect to Knudsen number K_n are given as follows:

$$
\begin{aligned}
\frac{f(K_n)}{K_n} &= \left(\frac{1+\sigma K_n}{K_n}\right)\left(1+\frac{4K_n}{1-b_{SF}K_n}\right) \\
\Rightarrow \frac{df}{dK_n} &= \sigma\left(\frac{1+(4-b_{SF})K_n}{1-b_{SF}K_n}\right)\left(1+\frac{K_n}{\sigma}\frac{d\sigma}{dK_n}\right) \\
&\quad + \frac{(4-b_{SF})(1+\sigma K_n)}{(1-b_{SF}K_n)} + \frac{b_{SF}f}{1-b_{SF}K_n} \\
\Rightarrow \frac{1}{f}\frac{df}{dK_n} &= \left(\frac{\sigma}{1+\sigma K_n}\right)\left(1+\frac{K_n}{\sigma}\frac{d\sigma}{dK_n}\right) \\
&\quad + \frac{(4-b_{SF})}{(1+(4-b_{SF})K_n)} + \frac{b_{SF}}{1-b_{SF}K_n} \\
\Rightarrow \frac{K_n}{f}\frac{df}{dK_n} &= \left(\frac{\sigma K_n}{1+\sigma K_n}\right)\left(1+\frac{K_n}{\sigma}\frac{d\sigma}{dK_n}\right) \\
&\quad + \frac{(4-b_{SF})K_n}{(1+(4-b_{SF})K_n)} + \frac{b_{SF}K_n}{1-b_{SF}K_n}
\end{aligned}
$$

In Figure 4.33, we have plotted the permeability correction factor f against Knudsen number K_n by using different definitions of rarefaction correction coefficient σ. The different plots coincide with each other when K_n in the Darcy's regime limit, but there are variations in the plots of f in other flow regimes, especially in transition and Knudsen flow regimes. Moreover, note that in the limit of continuous (Darcy) flow, $K_n \to 0$, then $f \to 1$ and $K_a \to K$. On the other hand, in the limit of Knudsen diffusion, $K_n \to \infty$, then $\sigma \to \sigma_0$, $f \to \infty$ and hence $K_a \to K$. Thus in the two extreme limits we have $K_a \to K$.

Figure 4.34 shows the plot of permeability correction factor f against intrinsic permeability K. It is observed that large values of f are required for extremely small values of K. For instance, at $K = 10^{-20}$ m^2, f varies from 10^3 to 10^5 at

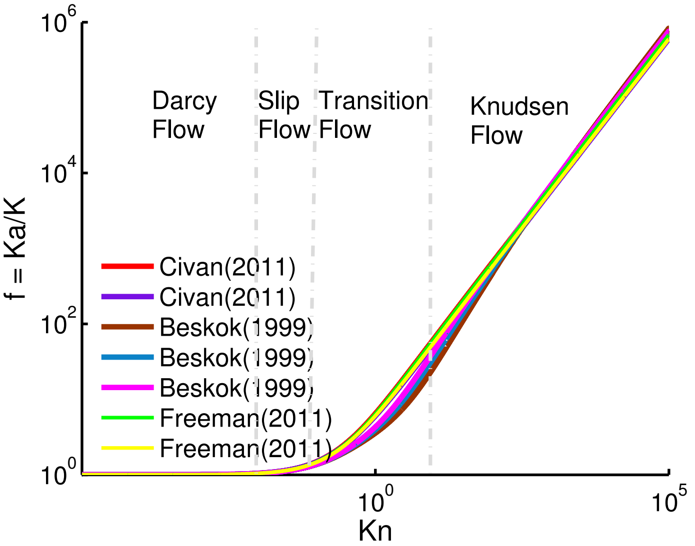

Figure 4.33: Permeability correction factor, f, against Knudsen number K_n.

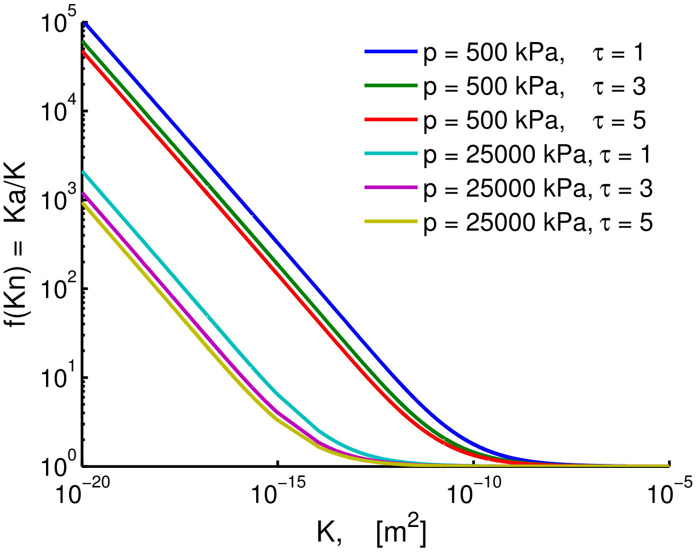

Figure 4.34: Permeability correction factor, f, against intrinsic permeability, K.

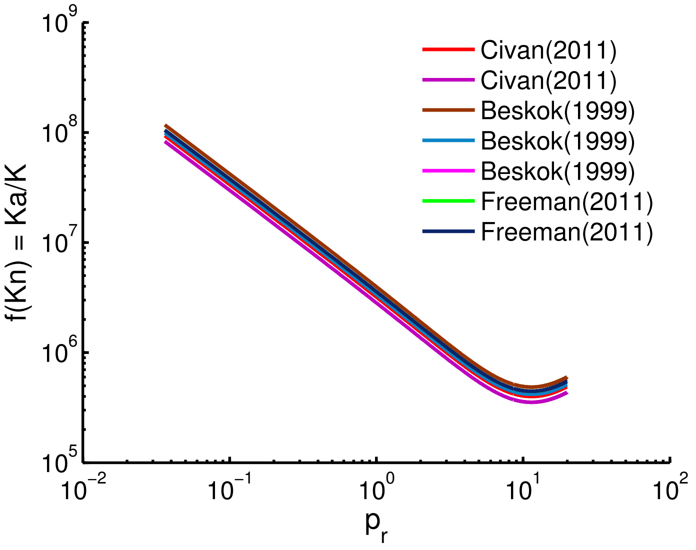

Figure 4.35: Permeability correction factor f against pressure p.

different pressure, and tortuosities. Similarly, f is approximately equals 1 for all $K > 10^{-10}$ m^2, irrespective of the values of pressure and tortuosity.

Figure 4.35 shows the plots of permeability correction factor f against p_r. It is noted that the general behavior of f is very similar for different models of σ. For $p_r < 10^1$, f decreases with increase in pressure, and for $p_r > 10^1$, f increases with increase in pressure. This indicates that apparent permeability has to be adjusted with changes in pressure.

Figure 4.37 shows the plots of apparent permeability K_a against p_r. K_a has similar trend as f. For $p_r < 10^1$, K_a decreases with increase in pressure, and for $p_r > 10^1$, K_a increases with increase in pressure. K_a has magnitude of order 10^{-11} to 10^{-8} for the range of pressure considered.

Figure 4.36 shows the plot of ζ_f against pressure.

Figure 4.38 shows the interconnection between various reservoir parameters and their compressibility coefficients.

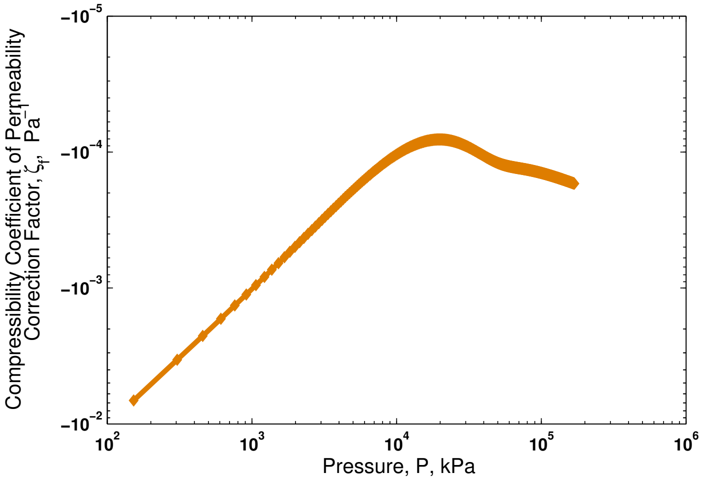

Figure 4.36: Compressibility coefficient of permeability correction factor, ζ_f, against pressure p.

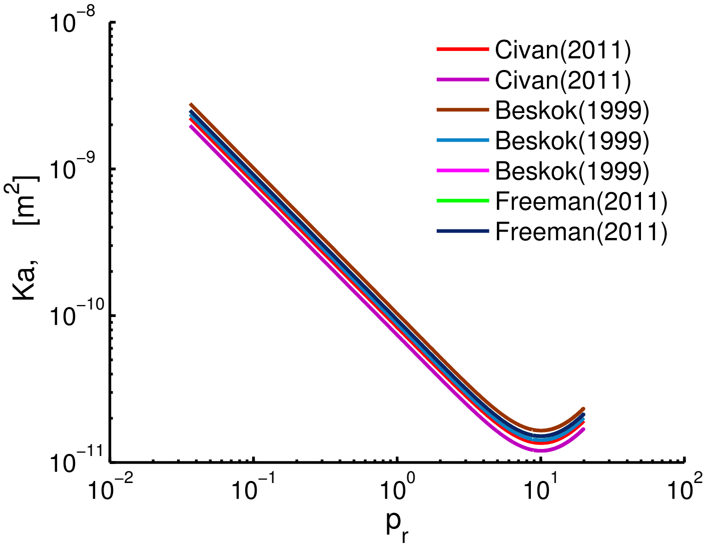

Figure 4.37: Apparent Permeability K_a against p_r for different models.

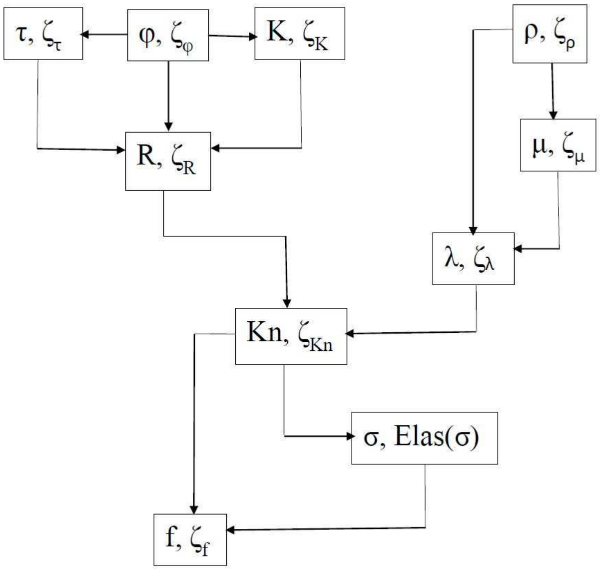

Figure 4.38: Compressibility Flow Chart.

4.3 Regularity of Solutions

The new non-linear transport model is

$$\frac{\partial p}{\partial t} + U_a(p, p_x)\frac{\partial p}{\partial x} = D_a(p)\frac{\partial^2 p}{\partial x^2}. \tag{4.3.1}$$

This solutions of the equation 4.3.1 are regular in the $p-p_x$ domain, where $u_a(p, p_x)$ and $D_a(p)$ are continuous and non-singular.

It is not possible to give a detailed analysis of all existence, uniqueness, and regularity of the solutions of this highly non-linear equation. But we can provide an indication by plotting U_a against $p - p_x$, and D_a against p, for a one particular choice of model parameters. D_a and U_a are smooth for the range of p and p_x, which covers the range in this work. This is shown in Figures 4.39 and 4.40 for model parameters taken in Table 6.1.

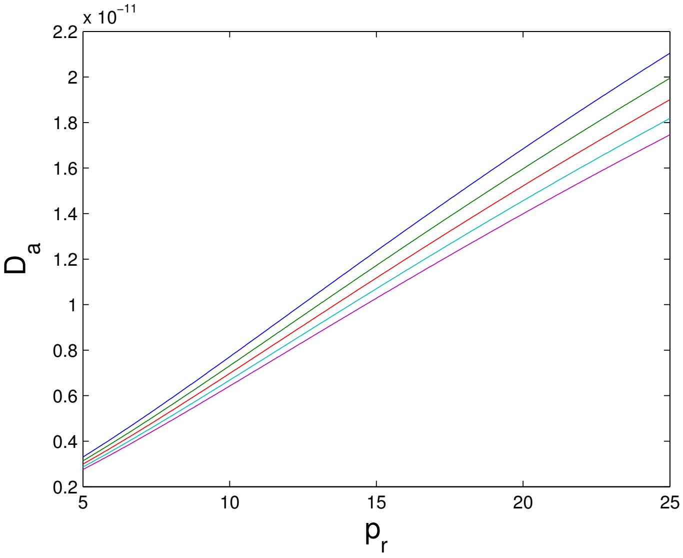

Figure 4.39: Plot of D_a against pressure p, for different temperatures t_r. It shows a smooth curve in the range of pressure considered.

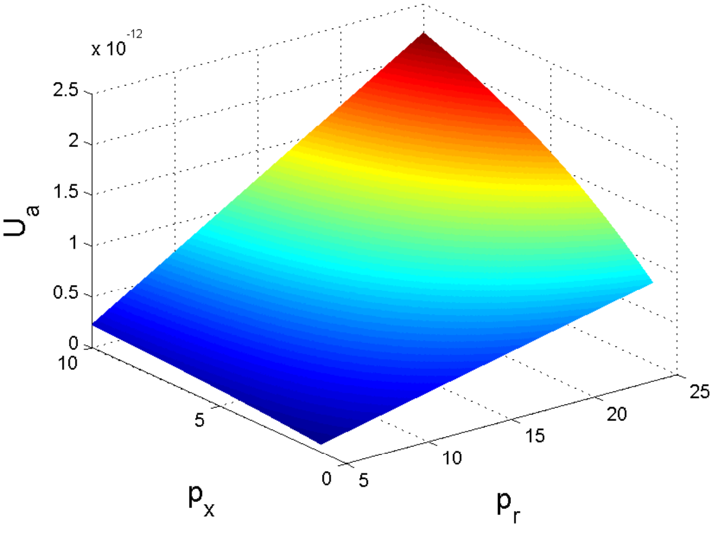

Figure 4.40: Plot of U_a against pressure p and p_x. It shows a smooth surface for the range of pressures considered.

4.4 Some Limiting Cases

In this section, we will discuss some limiting cases of the new transport model (3.4.3). We show that the new transport model reduces to other transport models in these limiting cases.

Case 1: $\phi \to 1$

This represents the case when the porosity is very large, that is, $\phi \to 1$. Under this assumption, D_a (3.4.5) becomes

$$D_a(p) = \frac{FK_a}{\mu \zeta_\rho}. \tag{4.4.1}$$

Since large porosity means that there is a continuous flow of the fluids, therefore, Knudsen number is very small, that is, $K_n \to 0$. This implies that $f \to 1$, and hence $K_a \to K$, that is, apparent permeability becomes equal to intrinsic permeability. Thus equation (4.4.1) becomes

$$D_a(p) = \frac{FK}{\mu \zeta_\rho}. \tag{4.4.2}$$

Case 2: $\beta \to 0$

This represents the scenario that there are no turbulence effects. Hence $F \to 1$, so equation (4.4.2) becomes

$$D_a(p) = \frac{K}{\mu \zeta_\rho}. \tag{4.4.3}$$

Under the assumption that the intrinsic permeability, gas density, and gas viscosity are constants, D_a becomes

$$D_a(p) = \frac{K}{\mu}. \tag{4.4.4}$$

On the other hand, U_a becomes zero because this advection term appears by the assumption of pressure dependent parameters, that is, in case, if model parameters K and μ, are assumed constants, the advection term will not appear in the model. Hence the new transport model reduces to standard Darcy diffusion equation,

$$\frac{\partial p}{\partial t} = \frac{K}{\mu} \frac{\partial^2 p}{\partial x^2}. \tag{4.4.5}$$

4.5 Summary

In this chapter, we have given the definitions of the gas deviation factor, the gas density, the gas viscosity, the porosity, the tortuosity, the turbulence factor, the Knudsen number, the mean free path, the radius, the intrinsic permeability, the apparent permeability, and the permeability correction factor, and we have also derived expressions for their compressibility coefficients. The inter-dependence of various model parameters and their compressibility coefficients is also discussed.

Based upon these definitions, we have shown that the nonlinear diffusivity coefficient D_a and advection coefficient U_a are smooth in the range of pressures considered. Moreover, we have also discussed some of the limiting cases of the new transport model which reduce to the previous transport models.

CHAPTER 5

NUMERICAL METHODS

5.1 Finite Volume Method

The Finite Volume Method (FVM) is a numerical method for finding the approximate solutions of a single or a system of partial differential equations (PDEs). Partial differential equations (PDEs) are classified into three major categories, namely elliptic, parabolic and hyperbolic, and they are used in all branches of science and engineering, such as, biophysics, chemical reaction flows, image processing, finance, and many others. They describe the relations between partial derivatives of unknown scalar or vector fields such as temperature, concentration, pressure, velocity field, density of electrons or probability density function, with respect to independent variables within a domain, usually defined by space, and time, under consideration.

In the finite volume method, the spatial domain is partitioned into small control volumes and the process is called mesh generation. The given PDE is then integrated over each representative control volume. Each integral is treated as a discrete approximation. Fluxes at the boundaries of each control volume are discretized in a way such that the resulting scheme conserves fluxes, and also satisfies the fundamental balance equations upon which the PDE's are based.

The FVM yields a set of algebraic equations in unknowns which may be either linear or non linear depending on the original PDE. Linear systems can be readily made to be fully implicit, but non-linear systems can never be fully implicit and are usually linearized to some approximation and then solved iteratively to convergence. For more details on the finite volume methods, see Hundsdorfer and Verwer [89], Kurganov and Tadmor [100], LeVeque [101], Bressan et al. [27], Versteeg and Malalasekera [162], Fletcher [65, 64], Wendt [169], Bouchut [24], Moukalled et al. [121], Barth and Ohlberger [15], Cheng et al. [35], Hajibeygi and Jenny [76], Dumbser and Casulli [51], Radu et al. [137], Eymard et al. [58], Alcrudo and Garcia-Navarro [5], Marcondes et al. [114], dos Santos et al. [50], Marcondes and Sepehrnoori [113].

The new transport model is of the following form

$$\frac{\partial p}{\partial t} + U_a(p, p_x)\frac{\partial p}{\partial x} = D_a(p)\frac{\partial^2 p}{\partial x^2}, \tag{5.1.1}$$

which can be rearranged into a conservative form,

$$\frac{\partial p}{\partial t} + \frac{\partial}{\partial x}\left(U_a(p, p_x)p\right) = \frac{\partial}{\partial x}\left(D_a(p)\frac{\partial p}{\partial x}\right) + Q(x, t, p, p_x), \tag{5.1.2}$$

where $Q = p\left(\frac{\partial U_a}{\partial x}\right) - \left(\frac{\partial D_a}{\partial x}\right)\left(\frac{\partial p}{\partial x}\right)$.

In this chapter, we describe the numerical method used for solving the nonlinear transient advection-diffusion equation of the type,

$$\underbrace{\frac{\partial p}{\partial t}}_{\text{Transient term}} + \underbrace{\frac{\partial}{\partial x}(up)}_{\text{Convection term}} = \underbrace{\frac{\partial}{\partial x}\left(D\frac{\partial p}{\partial x}\right)}_{\text{Diffusion term}} + \underbrace{Q}_{\text{Source/Sink Term}} \tag{5.1.3}$$

where p represents a 1-dimensional scalar quantity, for example, temperature, pressure, concentration. $D(p)$ is the diffusivity, and $u(x;p)$ is the convective velocity, x and t are the independent spatial and the temporal variables. We assume a 1-dimensional domain , $[0, L]$. We discretize the domain into N control volumes of uniform size $\Delta x = L/N$, as shown in Figure 5.1 - with centers x_i, $i = 1, 2, \cdots, N$, and boundaries at $x_{i-1/2}$, $i = 1, 2, \cdots, N+1$. The time step Δt is chosen in such a way so that it satisfies Courant-Friedrichs-Lewy (CFL) stability condition. For one-dimensional case, the CFL has the following form,

$$C = \frac{U\Delta t}{\Delta x} << C_{\max}, \tag{5.1.4}$$

where the dimensionless number C is called the Courant number, U is the magnitude of the velocity. For explicit numerical scheme, $C_{\max} = 1$, and for implicit numerical schemes we also usually have $C_{\max} = 1$, but larger values of $C_{\max}$ may sometimes be tolerated.

We use the finite volume method to find the numerical solution of equation (5.1.3). Integrating equation (5.1.3) over the control volume V_j: $x_{j-1/2} \leq x \leq$

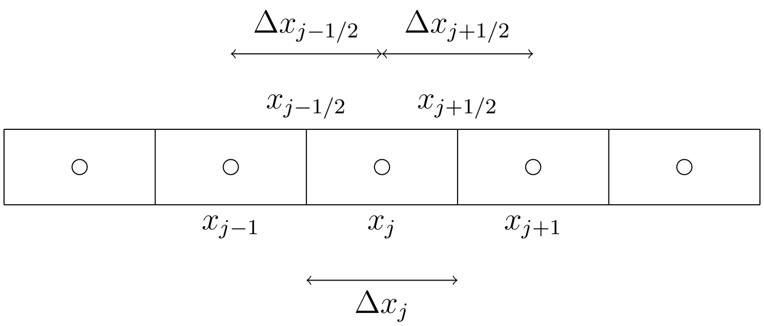

Figure 5.1: Control volume discretization of the 1-dimensional domain where the points x_i are chosen at the center of the block and the boundaries are located at the points $x_{i\pm 1/2}$.

$x_{j+1/2}$, see Figure 5.1, we obtain

$$\int_{x_{j-1/2}}^{x_{j+1/2}} \frac{\partial p}{\partial t} dV + \int_{x_{j-1/2}}^{x_{j+1/2}} \frac{\partial}{\partial x}(up) dV = \int_{x_{j-1/2}}^{x_{j+1/2}} \frac{\partial}{\partial x}\left(D\frac{\partial p}{\partial x}\right) dV + \int_{x_{j-1/2}}^{x_{j+1/2}} Q dV. \tag{5.1.5}$$

In the 1-dimensional case, $dV_j = dx_j$.

5.1.1 Discretization of the Diffusion Term

The diffusion term, the first term in the right hand side of equation (5.1.5), is discretized in the following way,

$$\begin{aligned}
&\int_{x_{j-1/2}}^{x_{j+1/2}} \frac{\partial}{\partial x}\left(D\frac{\partial p}{\partial x}\right) dV \\
=&\left[D\frac{\partial p}{\partial x}\right]_{x_{j+1/2}} - \left[D\frac{\partial p}{\partial x}\right]_{x_{j-1/2}} \\
=&D_{j+1/2}\frac{(p_{j+1}-p_j)}{\Delta x_j^+} - D_{j-1/2}\frac{(p_j - p_{j-1})}{\Delta x_j^-} \\
=&\left[\frac{D_{j-1/2}}{\Delta x_j^-}\right] p_{j-1} - \left[\frac{D_{j-1/2}}{\Delta x_j^-} + \frac{D_{j+1/2}}{\Delta x_j^+}\right] p_j + \left[\frac{D_{j+1/2}}{\Delta x_j^+}\right] p_{j+1},
\end{aligned} \tag{5.1.6}$$

where $\Delta x_j^+ = |x_{j+1} - x_j|$, and $\Delta x_j^- = |x_j - x_{j-1}|$, $p_j = p(x_j)$, $D_j = D(p_j)$.

5.1.2 Discretization of the Convection Term

The convection term, the second term on the left hand side of equation (5.1.5), can be discretized in three different ways, using central, upwind and total variation diminishing (TVD) schemes. We describe each of them below.

Central Scheme

In the central, fluxes at the boundaries, $x_{j\pm1/2}$ are approximated by taking averages of fluxes at the adjacent grid points. This method produces the following scheme,

$$\begin{aligned}\int_{x_{j-1/2}}^{x_{j+1/2}} \frac{\partial}{\partial x}(up)\, dV &= [up]_{x_{j+1/2}} - [up]_{x_{j-1/2}} \\ &= u_{j+1/2}p_{j+1/2} - u_{j-1/2}p_{j-1/2} \\ &= -\frac{u_{j-1/2}}{2}p_{j-1} - \left(\frac{u_{j-1/2}}{2} - \frac{u_{j+1/2}}{2}\right)p_j + \frac{u_{j+1/2}}{2}p_{j+1}. \quad (5.1.7)\end{aligned}$$

where $u_j = u(x_j)$.

Central schemes yield good solutions for smooth solutions but they produce oscillations when there are steep gradients or sharp turns in the solutions.

Upwind Scheme

Equation (5.1.7) can be further rearranged by using upwind scheme which is based on the idea of using the information from the direction of propagation, that is, if the velocity is positive (flow is from left to right) then $p_{j+1/2}$ is approximated as p_j and $p_{j-1/2}$ is approximated as p_{j-1} and if the velocity is negative (flow is from right to left) then $p_{j+1/2}$ is approximated as p_{j+1} and $p_{j-1/2}$ is approximated as p_j. Introducing the notations, $u^+ = \max\{u, 0\}$ and $u^- = \min\{u, 0\}$, equation (5.1.7) is expressed as follows,

$$\int_{x_{j-1/2}}^{x_{j+1/2}} \frac{\partial}{\partial x}(up)\, dV = -u^+_{j-1/2}p_{j-1} - \left(u^-_{j-1/2} - u^+_{j+1/2}\right) p_j + u^-_{j+1/2}p_{j+1}. \quad (5.1.8)$$

Upwind schemes are low precision but high resolution flux preserving schemes. They also have the TVD (total variation diminishing) property.

Total Variation Diminishing (TVD) Schemes

A numerical scheme is TVD if

$$\sum_j |p^{n+1}_{j+1} - p^{n+1}_j| \leq \sum_j |p^n_{j+1} - p^n_j|. \quad (5.1.9)$$

The convection term can be discretized in many different ways, as we have explained above. The upwind differencing scheme in which we approximate the unknown p in such a way that is to utilize the information coming from the direction of velocity. Upwind scheme provides good results at short times, but at long times it loses it's precision. On the other hand, the higher order schemes, such as Lax-Wendroof or Beam-Warming, produces oscillations where there is a steep gradient in the solutions. This problem is tackled by the use of flux (slope) limiters. The idea is to use higher order schemes for the part of the solutions that are smooth as much as possible, but switch back to lower order scheme where there are discontinuities in the solution.

Flux limiters are used to stabilize the numerical codes caused by steep gradients in the variable p, which could lead to excessive flux of p in/out to the control volume, and to instabilities. Flux limiters reduce the gradients thus limiting the flux and so stabilizing the solution. A variety of flux limiters are available in the literature, which preserve the order of the numerical scheme. One of the most widely used flux limiter is the van Leer flux limiter which is nonlinear and second order. For more details, see for example, Van Leer [161, 160, 159, 158], Jasak [93], Moukalled et al. [121]. Many higher order numerical schemes for reservoir simulations has been developed using the notions of flux limiters, see for example, Saad et al. [145], Chang et al. [30], Gupta et al. [75], Liu et al. [105].

Discretization of convection term by upwind scheme can be further improved by the incorporation of flux limiters. The form of the discretized convection term remains the same as Eq. (5.1.8) but an extra term is introduced that appear because of the flux limiters. We write the expression here,

$$\begin{aligned}\int_{x_{j-1/2}}^{x_{j+1/2}} \frac{\partial}{\partial x}(up)\,dV = -u^{+}_{j-1/2}p_{j-1} - \left(u^{-}_{j-1/2} - u^{+}_{j+1/2}\right)p_j + u^{-}_{j+1/2}p_{j+1} \\ + \mathrm{FL}_{j+1/2} - \mathrm{FL}_{j-1/2}. \qquad (5.1.10)\end{aligned}$$

The expression for $\mathrm{FL}_{j+1/2}$ using the second order van Leer flux limiter is,

$$\mathrm{FL}_{j+1/2} = 0.5u^{+}_{j+1/2}\psi^{+}_{j+1/2}\left(1 - u^{+}_{j+1/2}\frac{\Delta t}{\Delta x}\right) - 0.5u^{-}_{j+1/2}\psi^{-}_{j+1/2}\left(1 + u^{-}_{j+1/2}\frac{\Delta t}{\Delta x}\right) \tag{5.1.11}$$

where $\psi^{+}_{j+1/2}$ and $\psi^{-}_{j+1/2}$ are defined by

$$\psi^{+}_{j+1/2} = \theta(w^{+}_{j+1/2})(p_{j+1} - p_j), \qquad w^{+}_{j+1/2} = \frac{p_j - p_{j-1}}{p_{j+1} - p_j}. \tag{5.1.12}$$

and

$$\psi^{-}_{j+1/2} = \theta(w^{-}_{j+1/2})(p_{j+1} - p_j), \qquad w^{-}_{j+1/2} = \frac{p_{j+2} - p_{j+1}}{p_{j+1} - p_j}. \tag{5.1.13}$$

Similarly, the expression for $\mathrm{FL}_{j-1/2}$ using the second order van Leer flux limiter is,

$$\mathrm{FL}_{j-1/2} = 0.5u^{+}_{j-1/2}\psi^{+}_{j-1/2}\left(1 - u^{+}_{j-1/2}\frac{\Delta t}{\Delta x}\right) - 0.5u^{-}_{j-1/2}\psi^{-}_{j-1/2}\left(1 + u^{-}_{j-1/2}\frac{\Delta t}{\Delta x}\right) \tag{5.1.14}$$

where $\psi^{+}_{j-1/2}$ and $\psi^{-}_{j-1/2}$ are defined by

$$\psi^{+}_{j-1/2} = \theta(w^{+}_{j-1/2})(p_j - p_{j-1}), \qquad w^{+}_{j-1/2} = \frac{p_{j-1} - p_{j-2}}{p_j - p_{j-1}}. \tag{5.1.15}$$

and

$$\psi^{-}_{j-1/2} = \theta(w^{-}_{j-1/2})(p_j - p_{j-1}), \qquad w^{-}_{j-1/2} = \frac{p_{j+1} - p_j}{p_j - p_{j-1}}. \tag{5.1.16}$$

where θ is the Van Leer flux limiter function which is defined by,

$$\theta(w) = \frac{w + |w|}{1 + |w|}. \tag{5.1.17}$$

Several other flux limiters exist and are used in second order TVD schems. Some of them are given below.

MUSCL

$$\theta(w) = \max[0, \min(2r, 0.5(1 + r), 2)]. \tag{5.1.18}$$

SuperBee

$$\theta(w) = \max[0, \min(2r, 1), \min(r, 2)]. \tag{5.1.19}$$

Sweby

$$\theta(w) = \max[0, \min(ar, 1), \min(r, a)], \qquad (1 \leq a \leq 2). \tag{5.1.20}$$

Minmod

$$\theta(w) = \max[0, \min(r, 1)]. \tag{5.1.21}$$

Remark

Note that the equation (5.1.10) can be looked at as a sum of two terms, first is the same as the upwind term and the second is the term that arises from flux considerations. we implement the upwind term in implicit way in the numerical code, where the flux correction term is implemented in explicit way in the numerical code.

For more details, see Hundsdorfer and Verwer [89], Kurganov and Tadmor [100], LeVeque [101], Versteeg and Malalasekera [162].

5.1.3 Discretization of the Source/Sink Term

The source/sink term is discretized by approximating the value of Q in the interval $[x_{i-1/2}, x_{i+1/2}]$ by its central value at x_j, $Q(x_j, t) = Q_j(t)$,

$$\begin{aligned} \int_{x_{j-1/2}}^{x_{j+1/2}} Q(x,t)dV &= \int_{x_{j-1/2}}^{x_{j+1/2}} Q(x,t)dx \\ &= Q(x_j,t) \int_{x_{j-1/2}}^{x_{j+1/2}} dx \\ &= Q(x_j,t)\Delta x_j = Q_j(t)\Delta x_j, \end{aligned} \tag{5.1.22}$$

where $\Delta x_j = |x_{j+1/2} - x_{j-1/2}|$, and $Q_j(t) = Q(x_j, t)$ is the value of $Q(x,t)$ at the center of the control volume at time t.

5.1.4 Discretization of the Transient Term

The transient term, the first term on the left hand side of equation (5.1.5) is discretized as follow,

$$\begin{aligned}\int_{x_{j-1/2}}^{x_{j+1/2}} \frac{\partial p}{\partial t} dx &= \frac{\partial}{\partial t} p(x_j, t)\Delta x_j \\ &= \frac{p_j - p_j^o}{\Delta t}\Delta x_j \\ &= \frac{1}{\Delta t} p_j \Delta x_j - \frac{1}{\Delta t} p_j^o \Delta x_j, \end{aligned} \tag{5.1.23}$$

where $\Delta x = |x_{j+1/2} - x_{j-1/2}|$, p_j^o denotes the value of p at the previous time step, and p_j denotes the value of p at the next time step.

5.1.5 Conjunction of Diffusion, Convection, Source and Transient Terms

The four terms (5.1.6), (5.1.10), (5.1.22) and (5.1.23) are combined as follows,

$$\begin{aligned}&\frac{1}{\Delta t} p_j \Delta x - \frac{1}{\Delta t} p_j^o \Delta x - u_{j-1/2}^{+} p_{j-1} - [u_{j-1/2}^{-} - u_{j+1/2}^{+}] p_j + u_{j+1/2}^{-} p_{j+1/2} + \mathrm{FL}_{j+1/2} - \mathrm{FL}_{j-1/2} \\ &= \left[\frac{D_{j-1/2}}{\Delta x_j^{-}}\right] p_{j-1} - \left[\frac{D_{j-1/2}}{\Delta x_j^{-}} + \frac{D_{j+1/2}}{\Delta x_j^{+}}\right] p_j + \left[\frac{D_{j+1/2}}{\Delta x_j^{+}}\right] p_{j+1} + \Delta x_j Q_j(t).\end{aligned} \tag{5.1.24}$$

Assuming uniform partitioning, $\Delta x_j^{-} = \Delta x_j^{+} = \Delta x_j = \Delta x$, the above equation

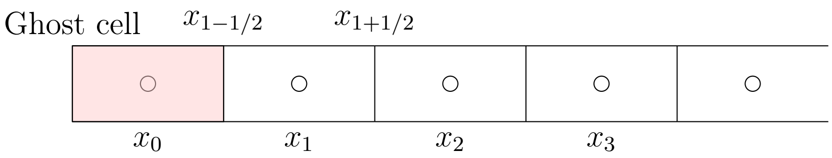

Figure 5.2: The left boundary condition is discretized by taking a ghost cell adjacent to the cell containing the point x_1.

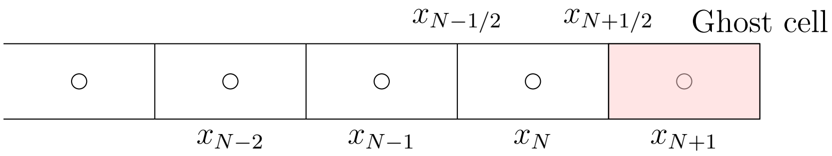

Figure 5.3: The right boundary condition is discretized by taking a ghost cell adjacent to the cell containing the point x_N.

can be rearranged as follows,

$$\begin{aligned}
&\frac{1}{\Delta t}p_j - \frac{u^+_{j-1/2}}{\Delta x}p_{j-1} - \left[\frac{u^-_{j-1/2}}{\Delta x} - \frac{u^+_{j+1/2}}{\Delta x}\right]p_j + \frac{u^-_{j+1/2}}{\Delta x}p_{j+1} \\
&= \left[\frac{D_{j-1/2}}{(\Delta x)^2}\right]p_{j-1} - \left[\frac{D_{j-1/2}}{(\Delta x)^2} + \frac{D_{j+1/2}}{(\Delta x)^2}\right]p_j + \left[\frac{D_{j+1/2}}{(\Delta x)^2}\right]p_{j+1} \\
&\quad + \frac{1}{\Delta t}p^o_j + Q_j + \mathrm{FL}_{j-1/2} - \mathrm{FL}_{j+1/2} \qquad (5.1.25)
\end{aligned}$$

5.2 Treatment of Boundary Conditions

The spatial domain is $0 \le x \le L$, and the mixed boundary conditions at the end points are given by,

$$a_L\frac{\partial p}{\partial x} + b_L p = c_L, \qquad \text{at } x = 0 \qquad (5.2.1)$$

and

$$a_R\frac{\partial p}{\partial x} + b_R p = c_R, \qquad \text{at } x = L, \qquad (5.2.2)$$

where a_L, b_L, a_R, b_R, are constants (assumed known), and c_L and c_R, are some functions of t.

In order to discretize the boundary condition, ghost cells are created to facilitate the discretization process, see figure 5.2. First, for the left boundary at $x_{1/2} = 0$, this yields,

$$\begin{aligned} a_L \frac{p_1 - p_0}{\Delta x} + b_L p_L &= c_L \\ a_L \frac{p_1 - p_0}{\Delta x} + b_L \frac{p_1 + p_0}{2} &= c_L \\ \left(\frac{b_L}{2} - \frac{a_L}{\Delta x} \right) p_0 + \left(\frac{b_L}{2} + \frac{a_L}{\Delta x} \right) p_1 &= c_L. \end{aligned} \tag{5.2.3}$$

Thus given p_0, p_1 can be determined.

Next, we discretize the boundary condition at the right boundary $x_{N+1/2} = L$. This yields,

$$\begin{aligned} a_R \frac{p_{N+1} - p_N}{\Delta x} + b_R p_R &= c_R \\ a_R \frac{p_{N+1} - p_N}{\Delta x} + b_R \frac{p_{N+1} + p_N}{2} &= c_R \\ \left(\frac{b_R}{2} - \frac{a_R}{\Delta x} \right) p_N + \left(\frac{b_R}{2} + \frac{a_R}{\Delta x} \right) p_{N+1} &= c_R. \end{aligned} \tag{5.2.4}$$

Thus, given p_{N+1}, p_N can be determined.

5.3 Matrix Form

The numerical scheme can be written in matrix formulation. We denote the matrix of coefficients arising from the diffusion term by DM which is a tridiagonal matrix

$$DM(p) = \begin{pmatrix} DP_1 & DR_1 & 0 & \cdots & \cdots & \cdots & 0 \\ DL_2 & DP_2 & DR_2 & \cdots & \cdots & \cdots & 0 \\ 0 & DL_3 & DP_3 & \ddots & \cdots & \cdots & 0 \\ \vdots & \vdots & \ddots & \ddots & \ddots & \cdots & \vdots \\ 0 & 0 & \cdots & \ddots & DP_{J-2} & DR_{J-2} & 0 \\ 0 & 0 & \cdots & \cdots & DL_{J-1} & DP_{J-1} & DR_{J-1} \\ 0 & 0 & \cdots & \cdots & 0 & DL_J & DP_J \end{pmatrix}$$

Entries on the main, super and sub diagonals, are obtained by the following expressions $DP_j = -\left[\frac{D_{j-1/2}}{(\Delta x)^2} + \frac{D_{j+1/2}}{(\Delta x)^2}\right]$, $DR_j = \left[\frac{D_{j+1/2}}{(\Delta x)^2}\right]$, and $DL_j = \left[\frac{D_{j-1/2}}{(\Delta x)^2}\right]$ respectively.

We denote the matrix arising from the convection term by CM which is also a tridiagonal matrix

$$CM(p) = \begin{pmatrix} CP_1 & CR_1 & 0 & \cdots & \cdots & \cdots & 0 \\ CL_2 & CP_2 & CR_2 & \cdots & \cdots & \cdots & 0 \\ 0 & CL_3 & CP_3 & \ddots & \cdots & \cdots & 0 \\ \vdots & \vdots & \ddots & \ddots & \ddots & \cdots & \vdots \\ 0 & 0 & \cdots & \ddots & CP_{J-2} & CR_{J-2} & 0 \\ 0 & 0 & \cdots & \cdots & CL_{J-1} & CP_{J-1} & CR_{J-1} \\ 0 & 0 & \cdots & \cdots & 0 & CL_J & CP_J \end{pmatrix}.$$

Entries, on the main, super and sub diagonals, are obtained by the following expressions $CP_j = -\left[\frac{U^+_{j-1/2}}{\Delta x} - \frac{U^-_{j+1/2}}{\Delta x}\right]$, $CR_j = \left[\frac{U^-_{j+1/2}}{\Delta x}\right]$ and $CL_j = -\left[\frac{U^+_{j-1/2}}{\Delta x}\right]$ respectively.

The matrix corresponding to the transient term is denoted by TM and it is given by

$$TM(p) = \begin{pmatrix} TP_1 & 0 & 0 & \cdots & 0 \\ 0 & \ddots & 0 & \cdots & \cdots \\ 0 & 0 & TP_j & \ddots & \cdots \\ \vdots & \vdots & \ddots & \ddots & 0 \\ 0 & 0 & \cdots & 0 & TP_J \end{pmatrix}$$

TM is a diagonal matrix whose entries on the diagonal are $\frac{1}{\Delta t}$.

We denote the vector of unknowns by p and its entries are written as

$$p = \begin{pmatrix} p_1 \\ \vdots \\ p_{j-1} \\ p_j \\ p_{j+1} \\ \vdots \\ p_J \end{pmatrix},$$

and right hand side vector is written as

$$s = \begin{pmatrix} s_1 \\ \vdots \\ s_{j-1} \\ s_j \\ s_{j+1} \\ \vdots \\ s_J \end{pmatrix}.$$

Hence, the numerical scheme can be written compactly as,

$$A(p)p = s(p), \tag{5.3.1}$$

where $A(p) = TM(p) + CM(p) - DM(p)$ is the matrix of coefficients and $s_j(p) = TM_j^0(p) + Q_j(p) + \mathrm{FL}_{j-1/2} - \mathrm{FL}_{j+1/2}$. is equal to right hand side. TM^0 and Q are column vectors given by,

$$TM^0 = \frac{1}{\Delta t}\begin{pmatrix} T_1^0 \vdots \\ T_{j-1}^0 \\ T_j^0 \\ T_{j+1}^0 \\ \vdots \\ T_J^0 \end{pmatrix}$$

and

$$Q = \begin{pmatrix} Q_1 \\ \vdots \\ Q_{j-1} \\ Q_j \\ Q_{j+1} \\ \vdots \\ Q_J \end{pmatrix}$$

and $A(p)$ is the matrix given by,

$$A(p) = \begin{pmatrix} AP_1 & AR_1 & 0 & \cdots & \cdots & \cdots & 0 \\ AL_2 & AP_2 & AR_2 & \cdots & \cdots & \cdots & 0 \\ 0 & AL_3 & AP_3 & \ddots & \cdots & \cdots & 0 \\ \vdots & \vdots & \ddots & \ddots & \ddots & \cdots & \vdots \\ 0 & 0 & \cdots & \ddots & AP_{J-2} & AR_{J-2} & 0 \\ 0 & 0 & \cdots & \cdots & AL_{J-1} & AP_{J-1} & AR_{J-1} \\ 0 & 0 & \cdots & \cdots & 0 & AL_J & AP_J \end{pmatrix},$$

where $AL_j = TL_j + CL_j - DL_j$, $AP_j = TP_j + CP_j - DP_j$, and $AR_j = TR_j + CR_j - DR_j$.

The term $\mathrm{FL}_{j-1/2} - \mathrm{FL}_{j+1/2}$ is calculated in the following manner, $\mathrm{FL}_{j-1/2} - \mathrm{FL}_{j+1/2} = FM.p^o$, where FM is the matrix given by

$$FM(p) = \begin{pmatrix} FP_1 & FR_1 & 0 & \cdots & \cdots & \cdots & 0 \\ FL_2 & FP_2 & FR_2 & \cdots & \cdots & \cdots & 0 \\ 0 & FL_3 & FP_3 & \ddots & \cdots & \cdots & 0 \\ \vdots & \vdots & \ddots & \ddots & \ddots & \cdots & \vdots \\ 0 & 0 & \cdots & \ddots & FP_{J-2} & FR_{J-2} & 0 \\ 0 & 0 & \cdots & \cdots & FL_{J-1} & FP_{J-1} & FR_{J-1} \\ 0 & 0 & \cdots & \cdots & 0 & FL_J & FP_J \end{pmatrix}$$

Entries on the main, super and sub diagonals, are obtained by the following expressions $FP_j = \left[\frac{F_{j-1/2}}{(\Delta x)^2} + \frac{F_{j+1/2}}{(\Delta x)^2}\right]$, $FR_j = -\left[\frac{F_{j+1/2}}{(\Delta x)^2}\right]$, and $FL_j = -\left[\frac{F_{j-1/2}}{(\Delta x)^2}\right]$ respectively, and p^0 is a vector of known values of pressure $p(x,t)$.

In equation (5.3.1), all quantities should be calculated in principle at the next time step, $t + \Delta t$. However, the coefficients in the matrix $A(p)$ and the vector $s(p)$ are non-linear and depend implicitly upon $p(t + \Delta t) = p^{n+1}$, so the system in equation (5.3.1) must be linearized by approximating A and s at the previous iteration. If p^ν is the pressure vector at the current iteration, ν, assumed known, then

$$A \approx A^\nu = A(p^\nu), \tag{5.3.2}$$

$$\text{and} \quad s \approx s^\nu = s(p^\nu), \tag{5.3.3}$$

where, A^ν and s^ν are also assumed known.

Hence, equation (5.3.1) becomes,

$$A^\nu p^{\nu+1} = s^\nu, \tag{5.3.4}$$

and we solve for $p^{\nu+1}$, and then it iterate $\nu \to \nu + 1$, until p^ν converges to, $p^\nu \to p^{n+1} = p(t + \Delta t)$. For more details, see Aziz and Settari [14].

5.3.1 The Numerical Algorithm

We follow the procedure as follows.

1. Given the solution, p^n, at some time step n, that is, at $t = t^n = n\Delta t$, we

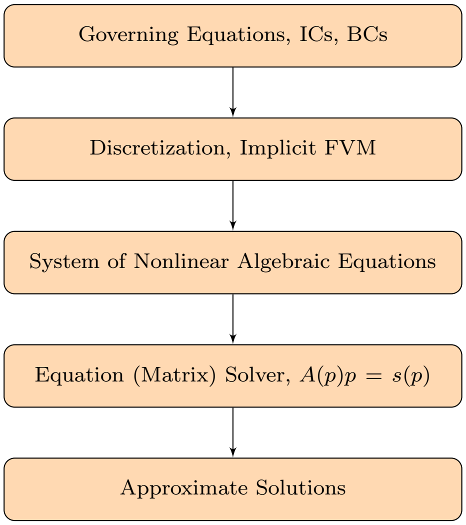

Figure 5.4: Schematic of the model solver.

want to advance the solution to the next time step $(n+1)$ at $t^{n+1} = (n+1)\Delta t$ that is, solve for p^{n+1}. We set a counter ν on the nonlinear system and write

$$A^{\nu} p^{\nu+1} = s^{\nu}, \tag{5.3.5}$$

where A^{ν} and s^{ν} are calculated at previous iteration step, that is, $A^{\nu} = A(p^{\nu})$ and $s^{\nu} = s(p^{\nu})$; p^{ν} is assumed known, and so A^{ν} and s^{ν} can be calculated.

2. Solve the system, $A^{\nu} p^{\nu+1} = s^{\nu}$, for $p^{\nu+1}$. Define the error in $p^{\nu+1}$, U_a, and D_a to be,

$$\epsilon_p^{\nu+1} = \max_j \left\{ \frac{|p_j^{\nu+1} - p_j^{\nu}|}{|p_j^{\nu+1}|} \right\}, \tag{5.3.6}$$

$$\epsilon_{U_a} = \max_j \left\{ \frac{u_j^{\nu+1} - u_j^{\nu}}{u_j^{\nu}} \right\}, \tag{5.3.7}$$

$$\epsilon_{D_a} = \max_j \left\{ \frac{d_j^{\nu+1} - d_j^{\nu}}{d_j^{\nu}} \right\}, \tag{5.3.8}$$

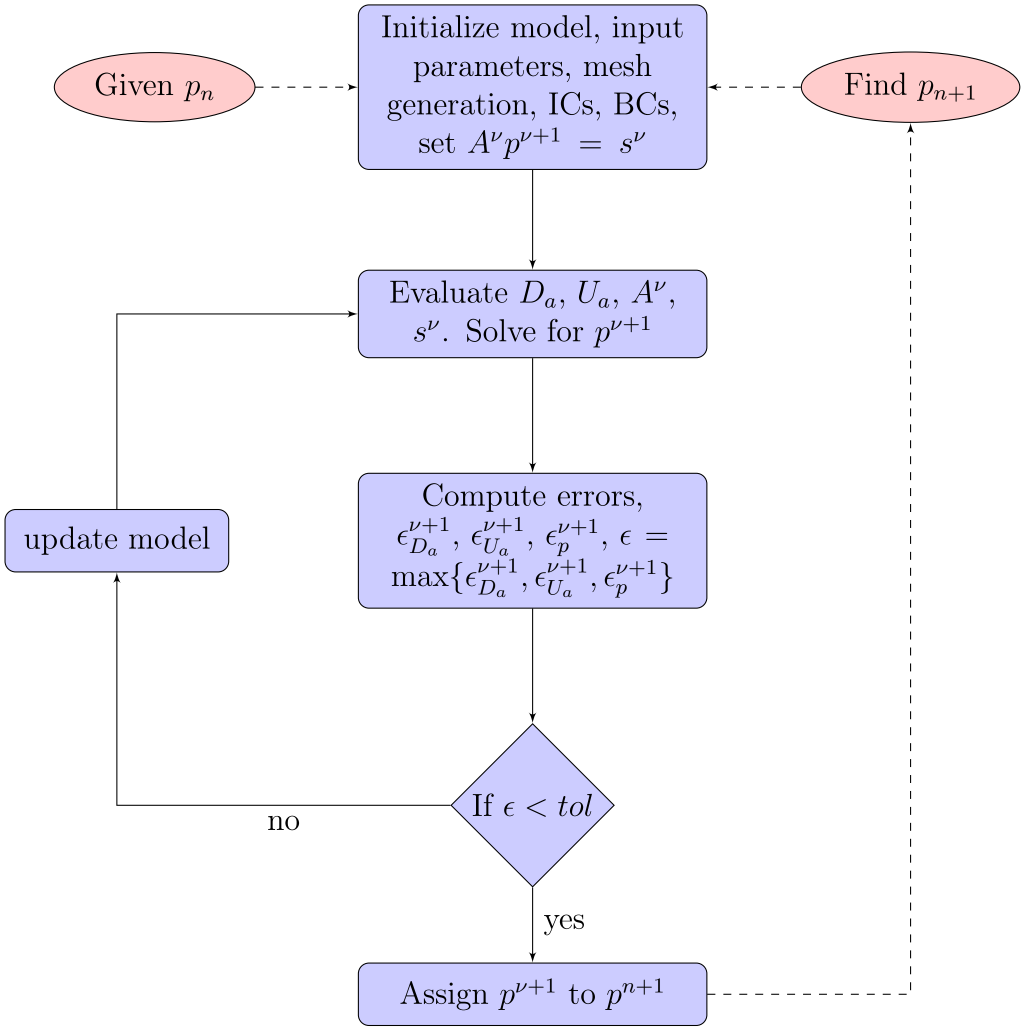

Figure 5.5: Flow chart of the numerical algorithm.

respectively. The tolerance tol is set to some fixed number.

Convergence Criteria. Compute ϵ_p, ϵ_{U_a}, and ϵ_{D_a}. If $\max\{\epsilon_p, \epsilon_{U_a}, \epsilon_{D_a}\} < tol$, then exit the iteration step, and go to step 1 for the next time step. Put $n \to n+1$. Typically, $tol = 10^{-6}$.

3. If $\epsilon_p^{\nu+1} > tol$, then update all parameter coefficients, A and s at the new $p^{\nu+1}$.

4. Iterate $\nu \to \nu + 1$; back to step 1.

5.3.2 Newton's Method

Newton's method (or Newton-Raphson method) is a powerful iteration method for solving nonlinear problems. The system of nonlinear equations given by equation (5.3.1) can be written as

$$f(p) = A(p)p - s(p) = 0. \tag{5.3.9}$$

A system of nonlinear equations of the form given above may be solved by Newton's method as defined below:

$$p^{(\nu)} - p^{(\nu-1)} = -[F^{(\nu-1)}]^{-1} f^{(\nu-1)}, \qquad \nu = 1, 2, \cdots \tag{5.3.10}$$

where F is the Jacobian matrix of the vector function f:

$$F^{(\nu)} = \left(\frac{\partial f_i}{\partial u_i} \right)^{(\nu)} \tag{5.3.11}$$

For computational purposes, equation (5.3.10) is written in the following form,

$$F^{(\nu-1)} \delta^{(\nu)} = -f^{(\nu-1)} \tag{5.3.12}$$

where

$$\delta^{(\nu)} = p^{(\nu)} - p^{(\nu-1)}, \qquad \nu = 1, 2, 3, \cdots \tag{5.3.13}$$

with

$$p^{(0)} = p^n. \tag{5.3.14}$$

Both the δ and f approach 0, as the iteration process continues, provided the method converges. For more details about Newton's iteration method, see Ortega and Rheinboldt [129].

5.4 Validation of Numerical Solver

We present numerical solutions of the time-dependent partial differential equations. The first is a diffusion equation on a finite domain, and the second is a transport equation in an infinite domain. Both of these problems have analytical solutions against which we can compare the numerical solutions. Finally, we have also solved a steady-state advection-diffusion equation and we compare the numerical solutions with the exact solutions.

5.4.1 Diffusion Equation in a Finite Domain

We consider the following flow equation, which is taken from Samardzioska and Popov [147],

$$\frac{\partial h}{\partial t} = K\frac{\partial^2 h}{\partial x^2}, \qquad 0 < x < L, \qquad t > 0. \tag{5.4.1}$$

Initial and boundary conditions are prescribed by $h_3 = h(x, 0) = 1.0$, $h_1 = h(0, t) = 1.05$, and $h_2 = h(L, t) = 1.0$, where $L = 1$, $K = 1$.

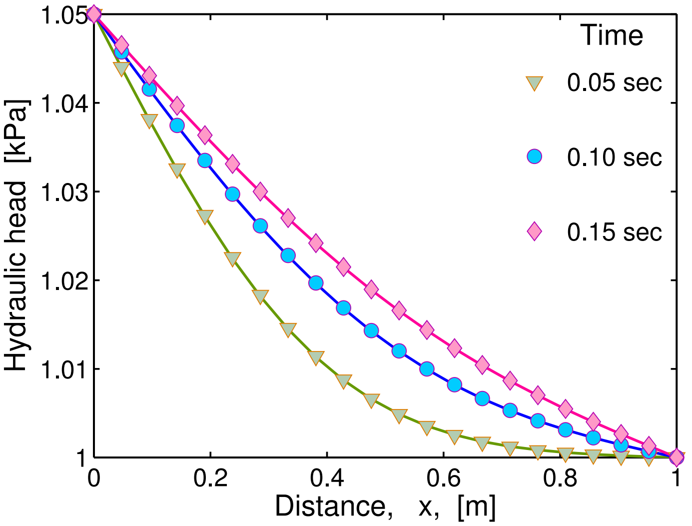

Figure 5.6: The hydraulic head h is plotted against the distance x at time $t = 0.05, 0.01$ and 0.15, for $K = 1$ m/day. Solid line represents the analytical solution, symbols represent the numerical solutions, see Samardzioska and Popov [147].

The analytical solution of the equation (5.4.1) is given by

$$h(x,t) = \frac{h_1 - h_2}{L}x + h_1 + \sum_{n=0}^{\infty} c_n . \sin\left(\frac{n\pi x}{L}\right) \exp\left(-n^2\pi^2 \frac{K}{L^2}t\right), \tag{5.4.2}$$

where

$$c_n = \frac{-2}{n\pi}\left[(h_2 - h_3)(-1)^n + h_3 - h_1\right]. \tag{5.4.3}$$

Numerical solutions of equation (5.4.1) are obtained using the model solver and are compared with the analytical solutions in Figures 5.6 and 5.7. Excellent matches between the analytical and numerical solutions is obtained.

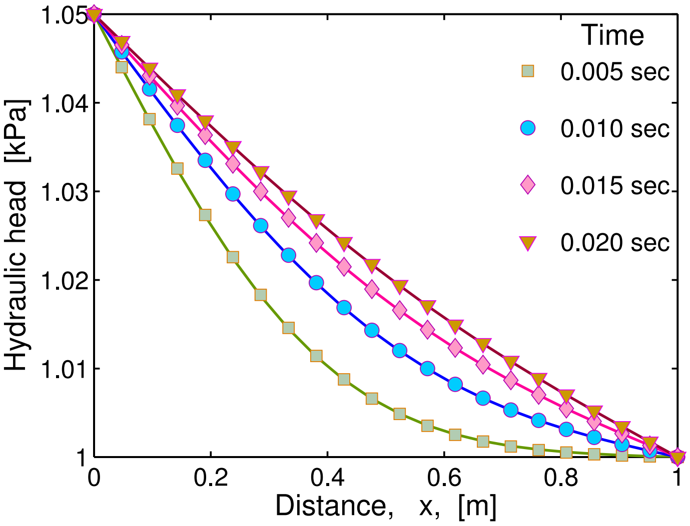

Figure 5.7: The hydraulic head h is plotted against the distance x at time $t = 0.005, 0.01, 0.015$ and 0.02, for $K = 10$ m/day. Solid line represents the analytical solution, symbols represent the numerical solutions, see Samardzioska and Popov [147].

5.4.2 Advection-Diffusion Equation in Semi-infinite Domain

We consider the following transport equation, which is taken from Samardzioska and Popov [147],

$$\frac{\partial c}{\partial t} + u\frac{\partial c}{\partial x} = D\frac{\partial^2 c}{\partial x^2}, \qquad x > 0, \qquad t > 0. \tag{5.4.4}$$

Initial and boundary conditions are prescribed by $c(x,0) = 0$, $c(0,t) = c_0$, and $c(\infty,t) = 0$.

The analytical solution of the equation (5.4.4) is given by

$$\frac{c}{c_0} = \frac{1}{2}\left[\operatorname{erfc}\left(\frac{x - ut}{2\sqrt{DT}}\right) + \exp\left(\frac{ux}{D}\right)\operatorname{erfc}\left(\frac{x + ut}{2\sqrt{DT}}\right)\right]. \tag{5.4.5}$$

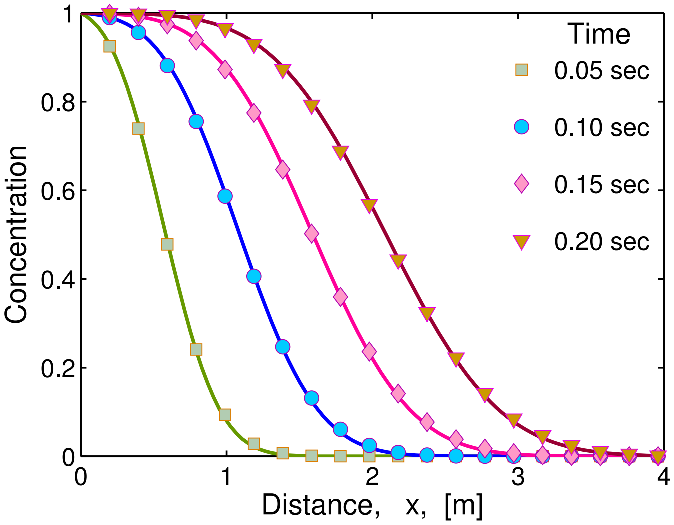

Figure 5.8: Concentration c is plotted against the distance x at time $t = 0.05, 0.01$, 0.15 and 0.2, for $u = 10$, $D = 1$ and $c_0 = 1$. Solid line represents the analytical solution, symbols represent the numerical solutions, see Samardzioska and Popov [147].

Numerical solutions of equation (5.4.4) are obtained using the model solver and are compared with the analytical solutions in Figures 5.8, 5.9 and **??**. An excellent match between the analytical and numerical solutions is obtained.

Figure 5.9

5.4.3 Steady-State Convection-Diffusion Equation

We consider the following steady-state convection-diffusion equation, which is taken from Versteeg and Malalasekera [162],

$$U\frac{\partial p}{\partial x} = D\frac{\partial^2 p}{\partial x^2}, \qquad 0 < x < 1, \tag{5.4.6}$$

Boundary conditions are prescribed by $p(0) = 0$, and $p(1) = 1$.

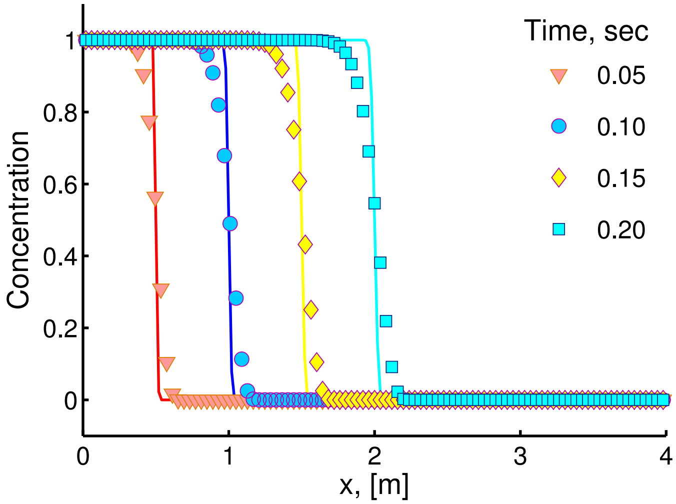

Figure 5.9: Concentration c is plotted against the distance x at time $t = 0.05, 0.01, 0.15$ and 0.2, for $u = 10$, $D = 10^{-3}$ and $c_0 = 1$. Solid line represents the analytical solution, symbols represent the numerical solutions. This also demonstrates the effectiveness of TVD scheme with Van leer flux limiter.

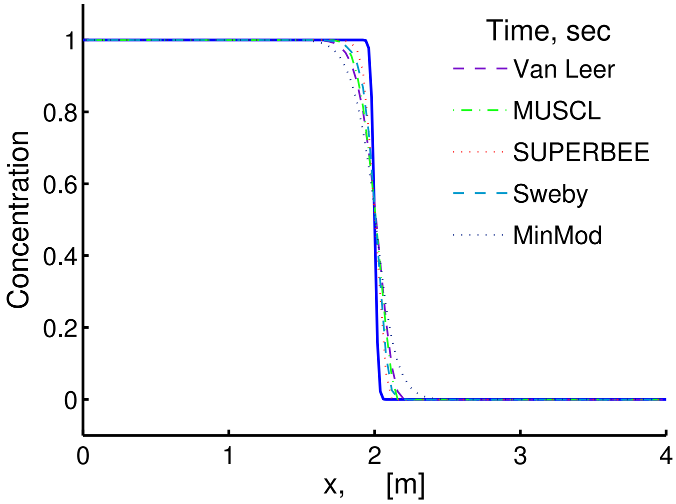

Figure 5.10: Concentration c is plotted against the distance x at time $t = 0.2$, for $u = 10$, $D = 10^{-3}$ and $c_0 = 1$. Solid line represents the analytical solution, and the other lines represent numerical solution obtained from TVD scheme where different flux limiters are used.

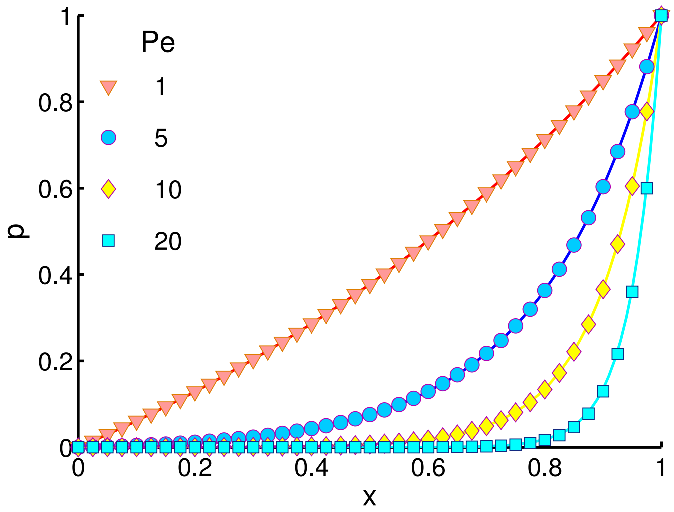

Figure 5.11: Pressure p is plotted against the distance x, for different Peclet numbers Pe $= 1, 5, 10,$ and 20. Solid lines represent the exact solutions, symbols represent the numerical solutions, see Versteeg and Malalasekera [162].

The analytical solution of equation (5.4.6) is given by

$$p(x) = \frac{\exp(\mathrm{Pe}\ x) - 1}{\exp(\mathrm{Pe}\ ) - 1}, \tag{5.4.7}$$

where Pe is Peclet number and is defined by Pe$= \frac{UL}{D}$, where L is length of the domain.

Numerical solutions of equation (5.4.6) are obtained using the model solver and are compared with the analytical solutions in Figure 5.11. An excellent match between the analytical and numerical solutions is obtained.

5.4.4 Inviscid Burger Equation

We consider the inviscid Burger equation,

$$\frac{\partial p}{\partial t} + p\frac{\partial p}{\partial x} = 0. \tag{5.4.8}$$

The initial condition is given by

$$p(x,0) = \begin{cases} 1 & \text{for } x \leq 0 \\ 1 - x & \text{for } 0 < x < 1 \\ 0 & \text{for } x \geq 1 \end{cases}$$

and boundary conditions are prescribed by $p(x,t) = 1$ when $x \to -\infty$, and $p(x,t) = 0$ when $x \to \infty$.

The solution of equation (5.4.8) develops singularity when $t = 1$, hence the analytical solution of equation (5.4.8) is defined for two different ranges when t is less than 1 and when t is greater than 1, see Pinchover and Rubinstein [132]. For $t < 1$, the solution is given by

$$p(x,t) = \begin{cases} 1 & \text{for } x \leq t \\ \frac{x-1}{t-1} & \text{for } t < x < 1 \\ 0 & \text{for } x \geq 1 \end{cases} \tag{5.4.9}$$

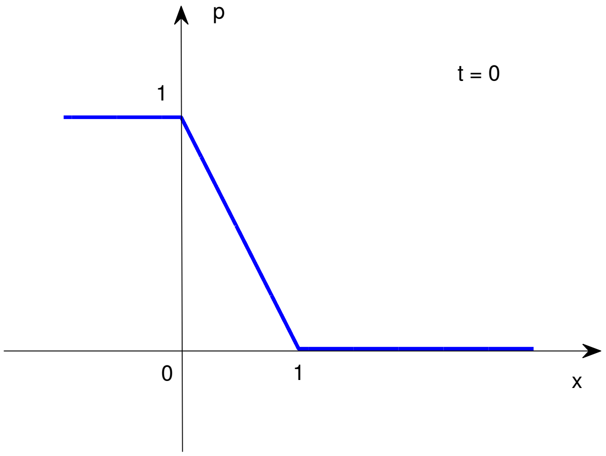

Figure 5.12: Initial condition used for 5.4.8, see Pinchover and Rubinstein [132].

For $t > 1$, the solution is given by

$$p(x,t) = \begin{cases} 1 & \text{for } x < \frac{1}{2}(t+1) \\ 0 & \text{for } x > \frac{1}{2}(t+1) \end{cases} \tag{5.4.10}$$

Numerical solutions of equation (5.4.8) are obtained using the model solver and are compared with the analytical solutions in Figure 5.11. An excellent match between the analytical and numerical solutions is obtained. In Figures 5.14 and 5.15 we see a slight smoothing of the discontinuities for $x \geq \frac{1}{2}(t+1)$, less in the TVD scheme than the upwind scheme, as expected. These results demonstrate that the flux limiter implemented here is satisfactory even close to the limit $Pe \to \infty$.

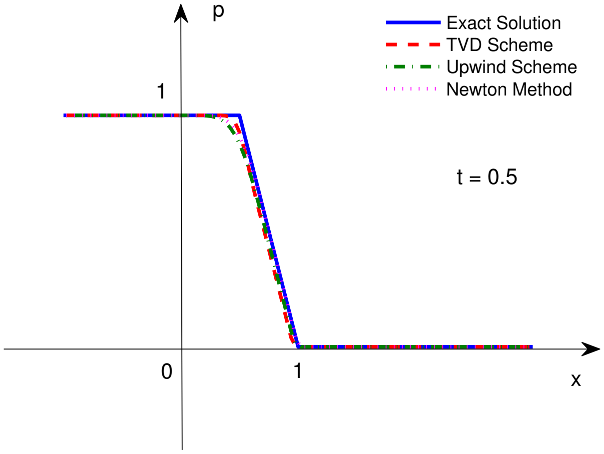

Figure 5.13: Numerical solutions, obtained from upwind scheme and TVD scheme of equation 5.4.8, are plotted against x at time $t = 0.5$. The exact solution (solid line) is also shown for comparison, see Pinchover and Rubinstein [132].

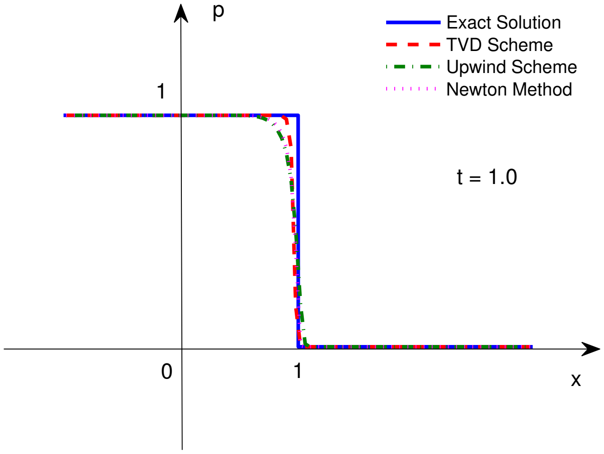

Figure 5.14: Numerical solutions, obtained from upwind scheme and TVD scheme of equation 5.4.8, are plotted against x at time $t = 1.0$. The exact solution (solid line) is also shown for comparison, see Pinchover and Rubinstein [132].

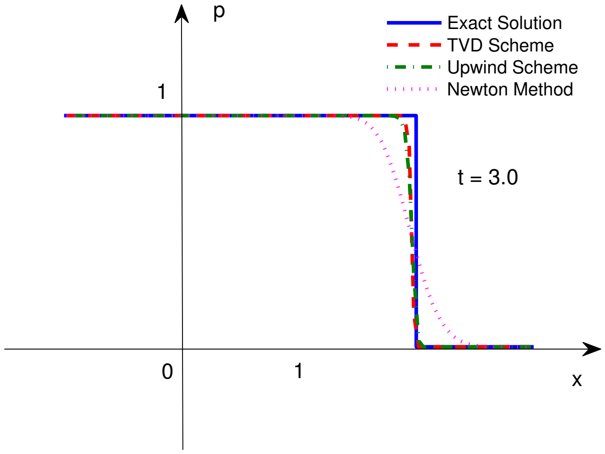

Figure 5.15: Numerical solutions, obtained from upwind scheme and TVD scheme of equation 5.4.8, are plotted against x at time $t = 3.0$. The exact solution (solid line) is also shown for comparison, see Pinchover and Rubinstein [132].

5.4.5 Order of Convergence

Here, we present error analysis of the finite volume scheme discussed in Section 5.1. We find the order of the numerical scheme by applying it to the second example above. We choose different interval sizes in the spatial domain, and then in the time domain, and then compute the error between the exact solution and the numerical solution. Figures 5.16 and 5.17 show the error plots.

The errors are computed by the following formula,

$$\text{Error} = \left| \frac{p_{num} - p_{exact}}{p_{exact}} \right|. \tag{5.4.11}$$

From the Figures 5.16 and 5.17, it is concluded that $\epsilon_{\Delta x} \approx O(\Delta x^{1.6})$ and $\epsilon_{\Delta t} \approx O(\Delta t)$.

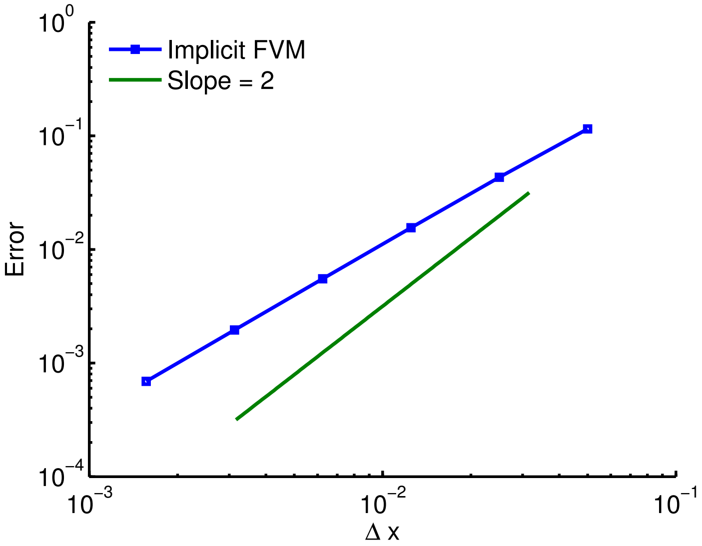

Figure 5.16: Order of the finite volume scheme with respect to spatial variable is found by taking different values of Δx while Δt is taken as a fixed number. Error decreases linearly with respect to Δx on a $\log - \log$ plot and the slope of error line lies between 1 and 2.

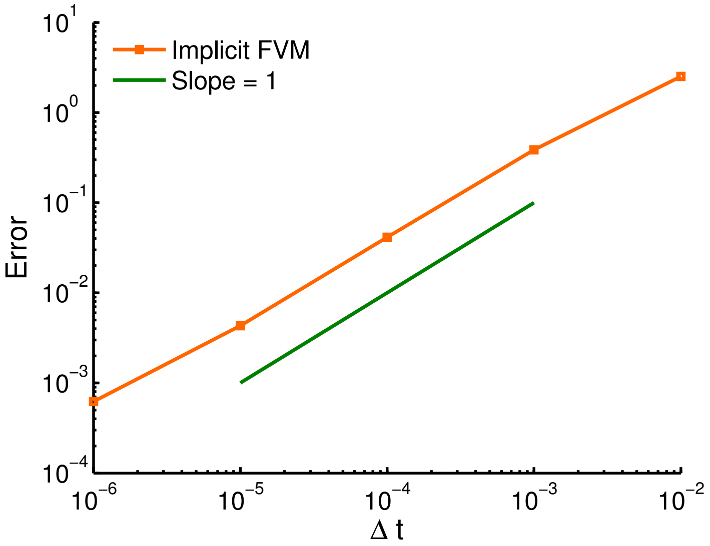

Figure 5.17: Order of the finite volume scheme with respect to temporal variable is found by taking different values of Δt while Δx is taken as a fixed number. Error decreases linearly with respect to Δt on a $\log - \log$ plot and the slope of error line is 1.

5.5 Summary

In this chapter, we have described the finite volume method used to numerically solve the new transport model for pressure field $p(x,t)$. We have validated our scheme against known exact solutions. The FVM combined with the Van Leer flux limiter is the most convenient method for the obtaining the stabilized solutions. It solves the non-linear system in a stable manner, at a reasonable order of convergence. The current numerical scheme can be used to solve a range of linear and non-linear partial differential equations with different initial and boundary conditions. Three examples are given in which we have presented the solutions of time-dependent diffusion equation, time-dependent advection-diffusion equation, and steady-state advection-diffusion equations whose exact solutions are known. We have compared the numerical solutions with the exact solutions, and it has been found that the numerical scheme is of order $O(\Delta t)$ with respect to time variable, and is of order $O(\Delta x^{1.6})$ with respect to space variable. These results validate the numerical solver that we have developed. We will use this FVM scheme in the Chaps.6 and 7.

CHAPTER 6

ROCK PROPERTIES AND SENSITIVITY ANALYSIS FOR STEADY-STATE PROBLEMS

6.1 Introduction

In this chapter and the next, we apply the new nonlinear transport model developed in Chapters 3-5, to solve some important problems in the petroleum industry. The transport model can be used for solving either inverse problems for parameter estimation, and also for predicting future pressure field. We first use the new model for parameter estimation. This is achieved by computing the pressure distributions in a rock core sample and then matching the best fit result to the experimental data. In Chapter 7, we apply the new model for simulating pressure fields over a period of time.

A second part of this study is to carry out a sensitivity analysis of all model parameters in order to see which parameters are the most critical one and which, if any, are not so important with of a view of simplifying the model if possible.

Intrinsic permeability is a rock property. It is a property of the rock structure and the pore network, and it is independent of the gas type and of the experimental conditions, Civan et al. [42]. The pressure pulse decay tests are used to obtain data from different rock samples under different test conditions. These experimental data sets are then analyzed by various theoretically derived models in order to determine the values of rock properties, such as, permeability and porosity. Our approach is to employ the new transport model discussed in Chapter 4 to estimate the rock properties, such as, permeability, porosity, and tortuosity.

The new model incorporates different flow regimes through the unified Hagen-Poiseuille-type equation which is based upon the Knudsen number and upon the rarefaction coefficient. The model also includes inertial effects through the turbulence correction term which we consider to be a function of porosity, tortuosity, and apparent permeability. Furthermore, although our application here is to shale gas reservoirs, it is important to remark that it can also be used for conventional gas reservoirs because in the limit of $K_n \to 0$ and large porosity and high permeability, the model asymptotes to conventional models (Darcy's law, Forchheimer's correction), the details are given in the Section 4.3 of Chapter 4.

As such our model incorporates a high level of realism. Thus, in our simulations we will, in the first instance, take all the correlations to be fully pressure dependent. An advantage of this approach is that all the correlations are related back to more basic formulae and these can be easily adjusted if needed. The adjustments for different cases and for different contexts can be made in the numerical scheme by changing input parameter values, see Ali et al. [10].

Many studies have been conducted to determine the permeability of shale rocks, but in most of the studies either reservoir parameters were assumed to be pressure independent or assumed to be constant in actual application. Such is the case in the works of, Brace et al. [26], Hsieh et al. [84], Neuzil et al. [125], Liang et al. [104], Malkovsky et al. [112], Cui et al. [44], and Civan et al. [41].

However, it is more realistic to consider all model parameters as being pressure dependent because the pressure is different at different locations therefore the reservoir properties change with changes in pressure, see Pong et al. [134], Beskok and Karniadakis [19], Roy et al. [144], Javadpour et al. [94], Civan et al. [43], Ali et al. [10], Roy et al. [144].

6.2 Estimates of Rock Properties

First, we use the transport model equation (3.4.3)

$$L_a(p, p_x)\frac{\partial p}{\partial x} = D_a(p)\frac{\partial^2 p}{\partial x^2}, \tag{6.2.1}$$

in order to estimate rock properties of rock samples for which we have experimental data from pressure-pulse tests.

We have available two data-sets from Pong et al. [134], who carried out pressure-pulse tests under steady state conditions, using Nitrogen and then Helium as the working gases, under different inlet pressure conditions, p_{in}. These data-sets have also been used by Civan et al. [41], Lorinczi et al. [107], Wang et al. [165], Huang et al. [85], and Ali et al. [10].

Pong's data-sets consist of measurements of pressure, p, against the distance from the inlet, x [µm], for different inlet pressures, p_{in}. Our task is to solve the transport equation (6.2.1) for different model parameter cases and determine the model that best fits the data, that is, which minimizes the mean square error, ϵ^2, between model and experimental data.

6.2.1 Pong's Experiment with Nitrogen

We will consider sixteen different transport model cases, labeled $n = 1, 2, \cdots, 16$. We start with case $n = 1$, where all the parameters are pressure independent, and all compressibility coefficients are zero, $\zeta_\gamma = 0$, where γ denotes a reservoir parameter. This collapses to the Darcy law. Cases 2 to 15 have different combinations of pressure-dependent and pressure-independent parameters. Case 16 is the fully pressure dependent and non-zero ζ_γ's case. All sixteen cases are listed in Table 6.4.

For each of the sixteen cases which readily obtained from limiting cases of equation (6.2.1), we solve the system using our finite volume implicit solver described in Chapter 5, with the same configuration and boundary conditions as in

Civan (2011)	
Reservoir Parameters	Values
L (m)	0.003
N_x	100
R_g ($\mathrm{J\,kmol^{-1}\,K^{-1}}$)	8314.4
M_g ($\mathrm{kg\,kmol^{-1}\,K^{-1}}$)	28.013
T (K)	314
p_c (kPa)	3396
t_c (K)	126.19
b_{SF}	-1
σ_0	1.3580
A_σ	0.1780
B_σ	0.4348
τ	1
ζ_τ ($\mathrm{Pa^{-1}}$)	0
ϕ	0.2
ζ_ϕ ($\mathrm{Pa^{-1}}$)	5×10^{-6}
μ (Pa s)	1.85×10^{-5}
ζ_μ ($\mathrm{Pa^{-1}}$)	3×10^{-11}
K	1×10^{-15}
ζ_K ($\mathrm{Pa^{-1}}$)	1×10^{-6}

Table 6.1: Reservoir parameters used in Civan's Model (2011).

the experimental design of Pong et al. [134].

The model parameters are initially chosen from physical considerations, which is given by Civan et al. [42, 41]. But this initial choice of model parameters and cases should only be viewed as an approximation. The task is to refine the model by adjusting the model parameters and then running a new simulations. This eventually yields the best-fit choice of model parameters values in each of the 16 cases. The rock properties K, ϕ, and τ are determined by this method.

New Model	
Reservoir Parameters	Values
L (m)	0.003
N_x	100
R_g ($\mathrm{J\,kmol^{-1}\,K^{-1}}$)	8314.4
M_g ($\mathrm{kg\,kmol^{-1}\,K^{-1}}$)	28.013
T (K)	314
p_c (kPa)	3396
t_c (K)	126.19
b_{SF}	-1
σ_0	1.3580
A_σ	0.1780
B_σ	0.4348
a_τ	1×10^{-6}
a_ϕ	0.15
b_ϕ	-0.939×10^{-6}
c_ϕ	2.2
α_{KC}	1
β_{KC}	0.9
Γ_{KC}	1.9×10^{-9}
tol	1×10^{-6}

Table 6.2: Reservoir parameters used in new transport model (6.3.1). A data set of base values is obtained which will be used for further data analysis and parameter estimation.

6.3 Model Validation Under Steady-State Condition

We consider the steady state transport model (6.3.1) and find its numerical solutions and compare the results to the first set of the experimental data of Pong et al. [134].

The ***Steady State Model*** is given by

$$L_a\left(p, p_x\right) \frac{\partial p}{\partial x} = \frac{\partial^2 p}{\partial x^2}, \qquad 0 \le x \le L, \tag{6.3.1}$$

Civan's Inflow Conditions	
#	p_{inlet}
1	135 kPA
2	170 kPa
3	205 kPa
4	240 kPa
5	275 kPa

Table 6.3: Inflow conditions for Civan's steady state case.

where

$$L_a(p, p_x) = -\zeta_3(p)\frac{\partial p}{\partial x}, \tag{6.3.2}$$

and the most general form for ζ_3 is,

$$\zeta_3(p) = F\left[\zeta_\rho(p) + \zeta_K(p) + \zeta_f(p) - \zeta_\mu(p)\right] + (F-1)\left[\zeta_\beta(p) + \zeta_{|u|}(p)\right] \tag{6.3.3}$$

The Dirichlet boundary conditions are $p(0) = p_L$ and $p(L) = p_R$.

Note that this model was obtained by combining the modified Forchheimer's equation $u = -\frac{1}{\mu}FK_a\frac{\partial p}{\partial x}$ with the continuity equation $-\frac{\partial}{\partial x}(\rho u) = 0$, see Chapter 3. We remark that Civan's model is obtained by taking $F = 1$ in Eq. (6.3.3),

$$\zeta_3(p) = \left[\zeta_\rho(p) + \zeta_K(p) + \zeta_f(p) - \zeta_\mu(p)\right]. \tag{6.3.4}$$

6.3.1 Input Parameters

In a pressure-pulse decay test, a reservoir rock sample is placed in a core plug of length L and cross-sectional area A. The left end of the core plug is attached to an upstream reservoir of volume V_u and the right end is attached to a downstream reservoir of volume V_d, the temperature in the core plug is denoted by T. The experiment is started by injecting a pressure-pulse in the upstream reservoir and then the change in pressure in the upstream and downstream reservoir is noted at different times. The pressure inside the sample is noted at different locations. The data is collected and then the different properties of the reservoir are determined by using different techniques. This is usually repeated several times and then averaged.

One way of analyzing the experimental data is to use transport models that are derived with an aim to describe gas transport in porous media. The new transport model (3.4.3) involves many reservoir parameters, see Table 6.2, whose values must be known before numerically solving the transport model. The values of the input parameters, such as, length (L), temperature (T), type of gas, molecular weight (M_g), universal gas constant (R_g), critical pressure (p_c), critical temperature (t_c), volume of upstream reservoir (V_u), volume of downstream reservoir (V_d), cross-sectional area of core plug (A), are known by the experimental set-up.

The parameters related to gas, such as, gas deviation factor (Z), gas density (ρ), gas viscosity (μ) along with their compressibility coefficients ζ_Z, ζ_ρ, and ζ_μ are determined by the correlations (4.2.1), (4.2.6), (4.2.10), (4.2.8), (4.2.7) (4.2.11), given in Chapter 4. After determining Z, ρ, and μ, we can find the mean free path (λ) of the gas molecules and its compressibility coefficient ζ_λ by the relations (4.2.33) and (4.2.34).

The porosity ϕ and tortuosity τ, and their respective compressibility coefficients are determined by the equations (4.2.12), (4.2.13), (4.2.18), and (4.2.19), and by specifying the values of the parameters a_ϕ, b_ϕ, c_ϕ and a_τ.

The values of intrinsic permeability (K) and it's compressibility coefficients (ζ_K), are estimated by power law form of Kozeny Carman equation (4.2.14) and (4.2.15), and by utilizing the values of porosity (determined in the previous step) and by specifying α_{KC}, β_{KC}, and Γ_{KC}. After determining intrinsic permeability, porosity and tortuosity, we can determine the value of the radius (R) of the flow channels and it's compressibility coefficient, ζ_R, by the relations (4.2.35) and (4.2.38).

In the next step, we determine the Knudsen number (K_n) by substituting the values of mean free path (λ) and radius (R) in equation (4.2.32). The compressibility coefficient of Knudsen number (ζ_{K_n}) is calculated by the equation (4.2.40). After this, we determine the value of rarefaction coefficient (σ) by using equation (4.2.43) and σ_0, A_σ and B_σ from Table 4.3, which are assumed given.

Next, we determine the values of permeability correction factor f and its compressibility coefficient, ζ_f, by substituting the values of Knudsen number K_n and rarefaction coefficient σ in the equation (4.2.42). Thus, the values of apparent permeability (K_a) are found by taking the product of the values of intrinsic permeability (K) and the values of permeability correction factor (f).

The value of the turbulence factor (β) and it's compressibility coefficient (ζ_β) are determined by the equations (4.2.20) and (4.2.21), and by specifying the values of the parameters a_β, b_β, c_β and d_β.

6.3.2 Error Analysis

We consider sixteen different cases, and for each case we determine the relative error between the simulated values and the experimental values of Pong et al. [134], from the relation,

$$\epsilon^2 = \text{Error} = \sum_{i=1}^{N} \left\| \frac{p_i^{cal} - p_i^{meas}}{p_i^{cal}} \right\|^2, \tag{6.3.5}$$

where the summation is taken over N locations, here $N = 6$. The relative errors, found by using Eq. (6.3.5) in all 16 cases, are shown in Table 6.4.

6.3.3 New Model with $\beta = 0$

Here, we solve model equations (6.3.1), (6.3.2), and (6.3.4) with fully pressure dependent parameter's in our new approach but without turbulence correction $F = 1$. Our objective is twofold. First, we show that the pressure-dependent assumption for the reservoir properties, such as, gas density, gas viscosity, and rock permeability is important in reducing the errors. Secondly, we show that our new approach works very well in describing the experimental data of Pong et al. [134] and Civan et al. [42]. Moreover, we also show that it is important to consider all the reservoir parameters pressure-dependent in the transport model, and making one or more of them pressure-independent generally leads to serious erroneous.

Below, we discuss the 16 cases, with $F = 1$, to determine the effects of reservoir parameters. In Figures 6.1 - 6.16, the simulated results are compared with the data of Pong et al. [134] (symbols) and are plotted as the pressure against the distance. The inlet pressures, p_{in}, along the different solid lines are, respectively from bottom to top, 135, 170, 205, 240, and 275 kPa.

Case 1: $\zeta_\rho(p) = 0, \zeta_K(p) = 0, \zeta_f(p) = 0, \zeta_\mu(p) = 0$. (Darcy's law)

This corresponds to taking all the parameters, ρ, f, K and μ to be constants. Equation (6.3.1) becomes

$$\frac{\partial^2 p}{\partial x^2} = 0, \tag{6.3.6}$$

which is a simple linear diffusion equation with Dirichlet boundary conditions. It yields the following exact solution

$$p(x) = (p_R - p_L)x/L + p_L. \tag{6.3.7}$$

Figure 6.1 shows the plots of the pressure inside the rock sample for different inflow pressure conditions, p_{in}. These are straight lines and do not match the experimental data well, except for low p_{in}.

Case 2: $\zeta_K(p) = 0, \zeta_f(p) = 0, \zeta_\mu(p) = 0$.

Here, the parameters K_a and μ are assumed constants and the gas density ρ is considered as a function of pressure p. Equation (6.3.1) remains the same but the coefficient L_a becomes,

$$L_a = -\zeta_\rho(p)\frac{\partial p}{\partial x}. \tag{6.3.8}$$

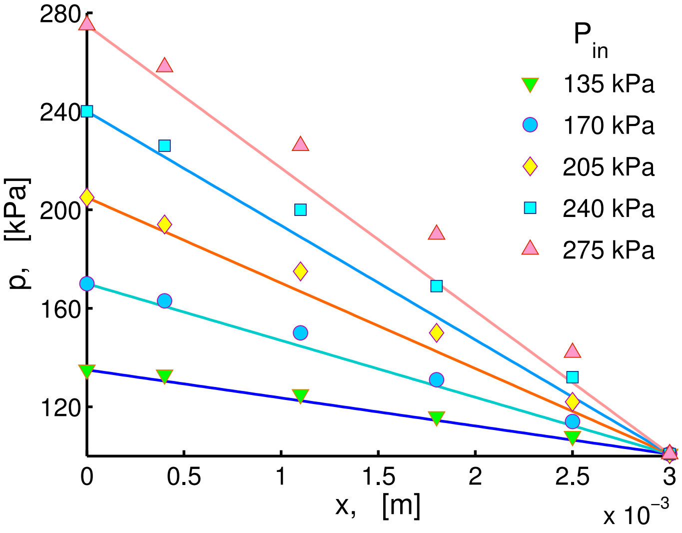

Figure 6.1: Case 1 represents steady state model with constant coefficients. Pressure profiles p are plotted against the distance x at different inlet pressures, and it is clear that numerical results do not match experimental data.

Numerical solutions of the pressure equation are plotted against the distance in the Figure 6.2, for different inlet pressures p_{in}. We note that the solution is close to the data for small inflow pressure p_{in}, but deviates wildly from the data with increasing p_{in}.

Case 3: $\zeta_\rho(p) = 0, \zeta_f(p) = 0, \zeta_\mu(p) = 0.$

Here, the parameters ρ, f and μ are assumed constants, and the intrinsic permeability K is considered as a function of pressure p. Equation (6.3.1) remains same but the coefficient L_a becomes,

$$L_a = -\zeta_K(p)\frac{\partial p}{\partial x}. \tag{6.3.9}$$

Numerical solutions of the pressure equation are plotted against distance for various inlet pressures, see Figure 6.3. In this case, the pressure distributions are

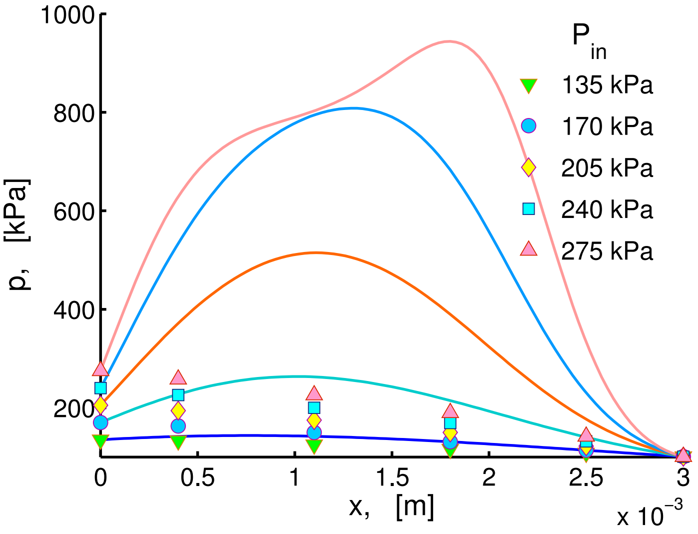

Figure 6.2: Case 2 represents steady state model with K_a and μ assumed constant. Pressure profiles p are plotted against the distance x at different inlet pressures, and it is clear that numerical results do not match experimental data. The deviations become large when the difference between the inlet and outlet boundary conditions is large.

close to the experimental data.

Case 4: $\zeta_\rho(p) = 0, \zeta_K(p) = 0, \zeta_\mu(p) = 0.$

Here, the parameters ρ, K and μ are assumed constants and the permeability correction factor K is considered as a function of pressure p. Now equation (6.3.1) remains the same but the coefficient L_a becomes,

$$L_a = -\zeta_f(p)\frac{\partial p}{\partial x}. \qquad (6.3.10)$$

Numerical solutions, pressure against distance, are plotted in the Figure 6.4. The numerical solutions are far from the data for all inflow boundary conditions.

Case 5: $\zeta_\rho(p) = 0, \zeta_K(p) = 0, \zeta_f(p) = 0.$

Here, the parameters ρ, K and f are assumed constants and the gas viscosity

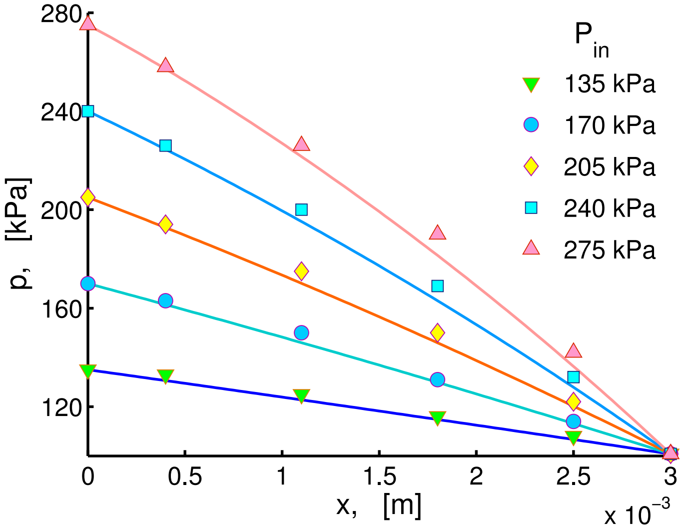

Figure 6.3: Case 3 represents steady state model with ρ, f and μ are assumed constant, whereas intrinsic permeability is considered as pressure dependent. Pressure profiles p are plotted against the distance x at different inlet pressures, and we observe a small deviation from the experimental data.

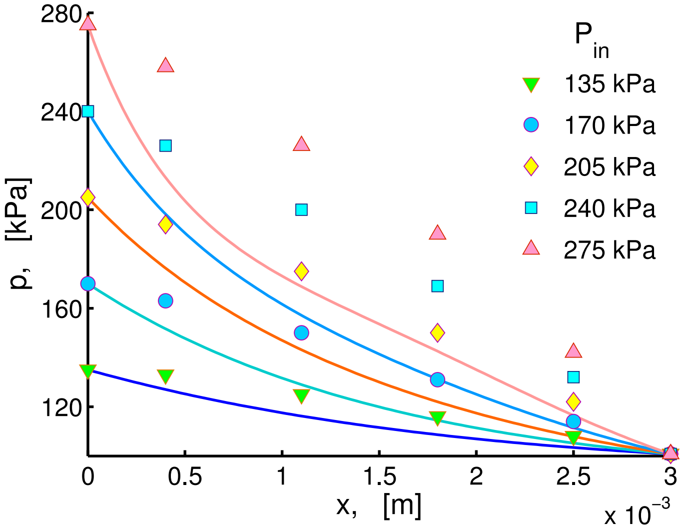

Figure 6.4: Case 4 represents steady state model with ρ, K and μ are assumed constant, and permeability correction factor f is assumed pressure dependent. Pressure profiles p are plotted against the distance x at different inlet pressures, and it is clear that numerical results do not match experimental data. There are large deviations when the difference between the inlet and the outlet boundary conditions is large.

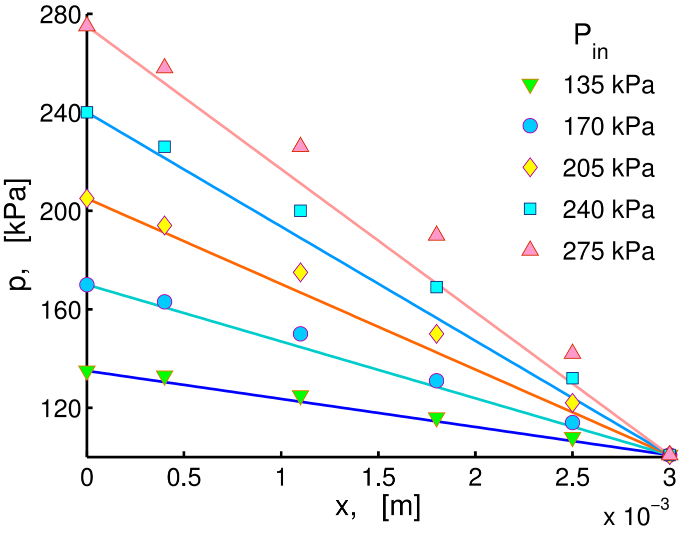

Figure 6.5: Case 5 represents steady state model with ρ, K and f are assumed constant, and gas viscosity μ is assumed pressure dependent. Pressure profiles p are plotted against the distance x at different inlet pressures, and it is clear that numerical results do not match experimental data.

μ is considered as a function of pressure p. Equation (6.3.1) remains the same but the coefficient L_a becomes,

$$L_a = \zeta_\mu(p)\frac{\partial p}{\partial x}. \tag{6.3.11}$$

Numerical solutions, pressure against distance, are plotted in the Figure 6.5. The numerical solutions for large inlet pressure p_{in} are far from the data, except for low p_{in}.

Case 6: $\zeta_f(p) = 0, \zeta_\mu(p) = 0.$

It means that the parameters f and μ are assumed constants whereas the gas density ρ and intrinsic permeability K are considered as a function of pressure p. Equation (6.3.1) remains same but the coefficient L_a becomes,

$$L_a = -[\zeta_\rho(p) + \zeta_K(p)]\frac{\partial p}{\partial x}. \tag{6.3.12}$$

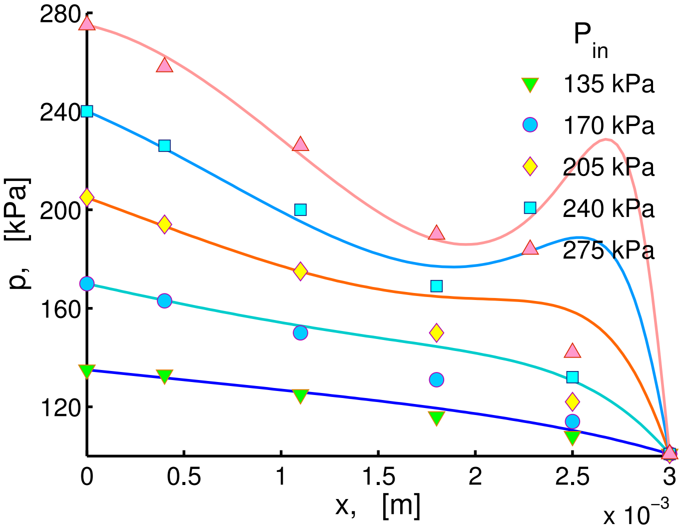

Figure 6.6: Case-6, Darcy's type equation with pressure dependent gas density ρ and intrinsic permeability K, whereas permeability correction factor f and gas viscosity μ are assumed constants. Pressure profiles p are plotted against the distance x at different inlet pressures, and it is clear that numerical results do not match experimental data.

Numerical solutions for the pressure $p(x)$ are plotted in the Figure 6.6. It is clear that the solutions do not match the data, except for small inlet pressure p_{in}.

Case 7: $\zeta_K(p) = 0, \zeta_\mu(p) = 0$.

It means that the parameters K and μ are assumed constants whereas the gas density ρ and permeability correction factor f are considered as a function of pressure p. Equation (6.3.1) remains the same but the coefficient L_a becomes,

$$L_a = -[\zeta_\rho(p) + \zeta_f(p)]\frac{\partial p}{\partial x}. \tag{6.3.13}$$

Numerical solutions are plotted in the Figure 6.7. Again in this case, simulated pressure does not match experimental data except for small inlet pressure p_{in}.

Case 8: $\zeta_K(p) = 0, \zeta_f(p) = 0$.

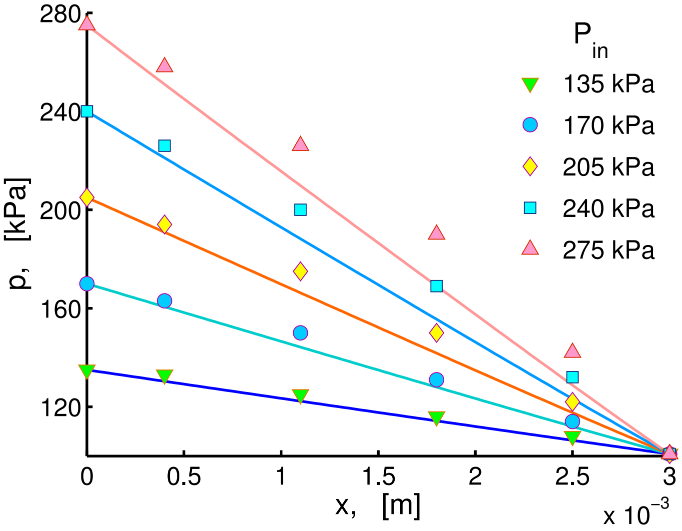

Figure 6.7: Case-7, Darcy's type equation with pressure dependent gas density ρ and permeability correction factor K, whereas intrinsic permeability K and gas viscosity μ are assumed constants. Pressure profiles p are plotted against the distance x at different inlet pressures, and it is noticed that numerical results do not match experimental data.

It means that the parameters K and f are assumed constants whereas the gas density ρ and the gas viscosity μ are considered as a function of pressure p. Equation (6.3.1) remains the same but the coefficient L_a becomes,

$$L_a = -[\zeta_\rho(p) - \zeta_\mu(p)]\frac{\partial p}{\partial x}. \tag{6.3.14}$$

Numerical solutions are plotted in the Figure 6.8 shows the pressure distribution. Also it is clear that the solutions do not match the data.

Case 9: $\zeta_\rho(p) = 0, \zeta_\mu(p) = 0.$

It means that the parameters ρ and μ are assumed constants whereas the intrinnsic permeability K and the permeability correction factor f are considered as a function of pressure p. Equation (6.3.1) remains the same but the coefficient

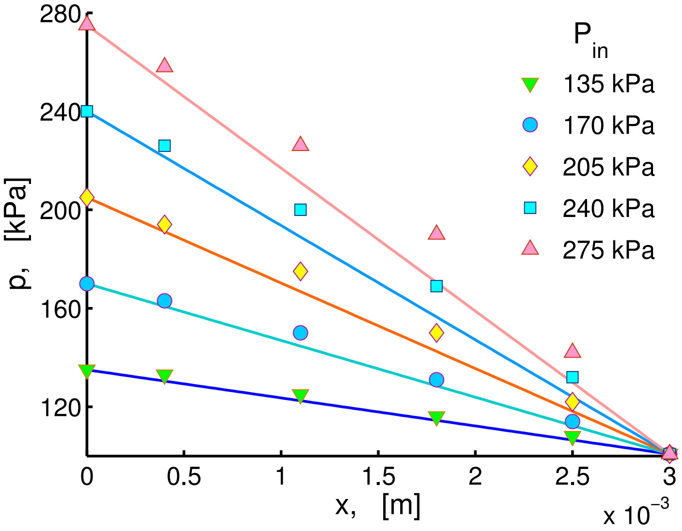

Figure 6.8: Case-8, Darcy's type equation with pressure dependent gas density ρ and gas viscosity μ, whereas intrinsic permeability K and permeability correction factor f are independent of the changes in the pressure.

L_a becomes,

$$L_a = -[\zeta_K(p) + \zeta_f(p)]\frac{\partial p}{\partial x}. \tag{6.3.15}$$

Numerical solutions are plotted in the Figure 6.9 which depict the pattern of pressure distribution. It is clear that the solutions do not match the data, except for small inlet pressure p_{in}.

Case 10: $\zeta_\rho(p) = 0, \zeta_f(p) = 0$.

It means that the parameters ρ and f are assumed constants whereas the intrinsic permeability K and the gas viscosity μ are considered as a function of pressure p. Equation (6.3.1) remains the same but the coefficient L_a becomes,

$$L_a = -[\zeta_K(p) - \zeta_\mu(p)]\frac{\partial p}{\partial x}. \tag{6.3.16}$$

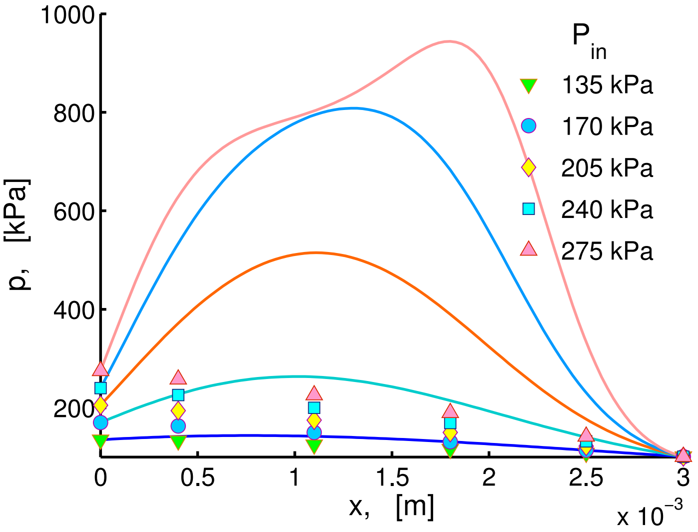

Figure 6.9: Case-9, Darcy's type equation with pressure dependent intrinsic permeability K and permeability correction factor f, whereas gas density ρ and gas viscosity μ are assumed constants. Pressure profiles p are plotted against the distance x at different inlet pressures, and it is clear that numerical results do not match experimental data. The deviations become very huge and wide when the difference between the inlet and outlet boundary conditions is large.

Numerical solutions are plotted in the Figure 6.10 which depict the pattern of pressure distribution. It is clear that the solutions do not match the data except for small inlet pressure p_{in}.

Case 11: $\zeta_\rho(p) = 0, \zeta_K(p) = 0$.

It means that the parameters ρ and K are assumed constants whereas the permeability correction f and the gas viscosity μ are considered as a function of pressure p. Equation (6.3.1) remains the same but the coefficient L_a becomes,

$$L_a = -[\zeta_f(p) - \zeta_\mu(p)]\frac{\partial p}{\partial x}. \tag{6.3.17}$$

Numerical solutions are plotted in the Figure 6.11 which shows the pattern of

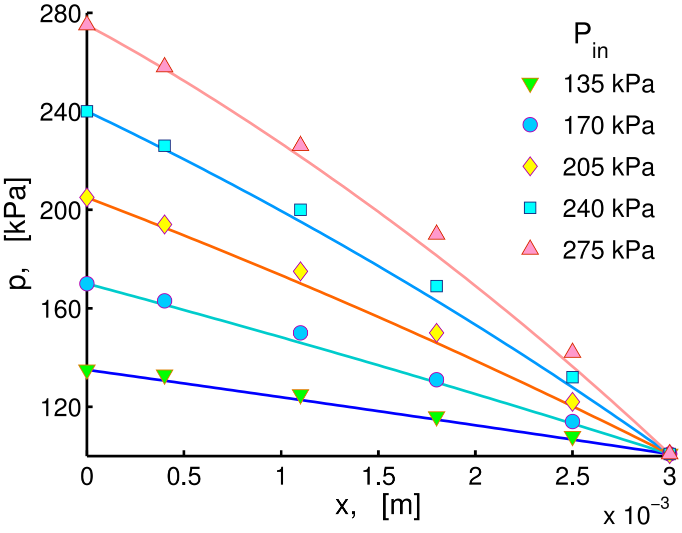

Figure 6.10: Case-10, Darcy's type equation with pressure dependent intrinsic permeability K and gas viscosity μ, whereas gas density ρ and permeability correction factor f are assumed constants. Pressure profiles p are plotted against the distance x at different inlet pressures, and we observe a very slight deviation from the experimental data.

pressure distribution. It is clear that the solutions do not match the data except for small inlet pressure p_{in}.

Case 12: $\zeta_\mu(p) = 0$.

It means that the parameters μ is assumed constant whereas the gas density ρ, the intrinsic permeability K and the permeability correction factor f are consideredf as a function of pressure p. Equation (6.3.1) remains the same but the coefficient L_a becomes,

$$L_a = -[\zeta_\rho(p) + \zeta_K(p) + \zeta_f(p)]\frac{\partial p}{\partial x}. \tag{6.3.18}$$

Numerical solutions are plotted in the Figure 6.12 which shows the pattern of pressure distribution. The solutions match the data quite well.

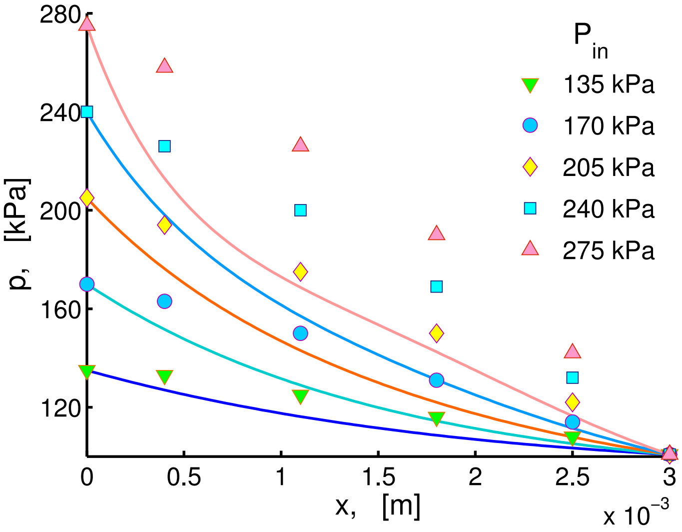

Figure 6.11: Case 11 represents the case where permeability correction factor f and gas viscosity μ are assumed pressure dependent whereas gas density ρ and intrinsic permeability K are assumed constants. Pressure profiles p are plotted against the distance x at different inlet pressures, and it is clear that numerical results do not match experimental data. There is large deviations when the difference between the inlet and the outlet boundary conditions is large.

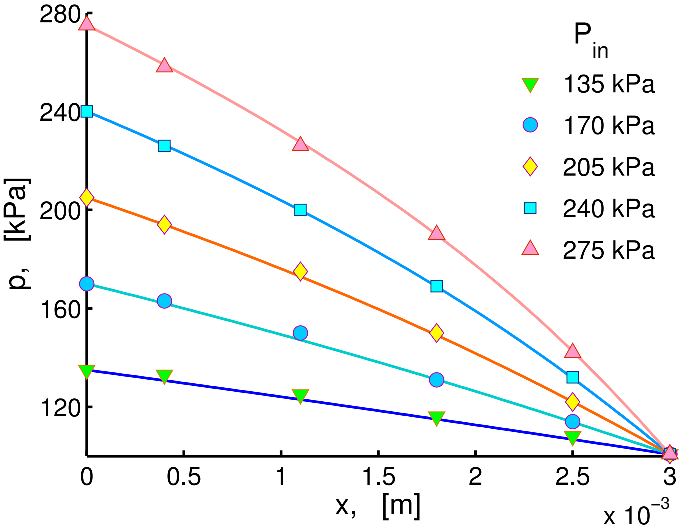

Figure 6.12: Case-12 represents the case where the gas density ρ, intrinsic permeability K and permeability correction factor f are taken as pressure dependent parameters, whereas gas viscosity μ is assumed constant. Pressure profiles p are plotted against distance x for different inlet pressures. We observe a good match between the numerical solutions and the experimental data.

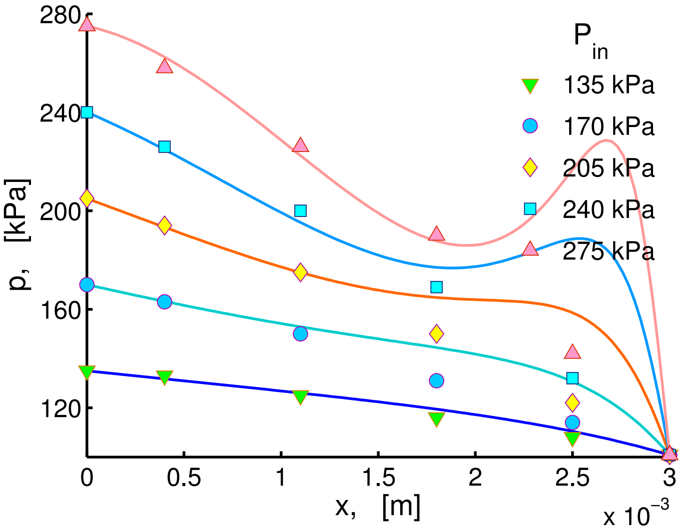

Figure 6.13: Case-13 represents the case where the gas density ρ, intrinsic permeability K and gas viscosity μ are taken as pressure dependent parameters, whereas permeability correction factor f is assumed constant. Pressure profiles p are plotted against the distance x at different inlet pressures, and it is clear that numerical results do not match experimental data. Moreover, results of the Case 13 are similar to the Case 6.

Case 13: $\zeta_f(p) = 0$.

It means that the parameters f is assumed constant whereas the gas density ρ, the intrinsic permeability K and the gas viscosity μ are considered as a function of pressure p. Equation (6.3.1) remains the same but the coefficient L_a becomes,

$$L_a = -[\zeta_\rho(p) + \zeta_K(p) - \zeta_\mu(p)]\frac{\partial p}{\partial x}. \tag{6.3.19}$$

Numerical solutions are plotted in the Figure 6.13 which shows the pattern of pressure distribution. It is clear that the solutions do not match the data except for small inlet pressure p_{in}.

Case 14: $\zeta_K(p) = 0$.

It means that the parameters K is assumed constant whereas the gas density

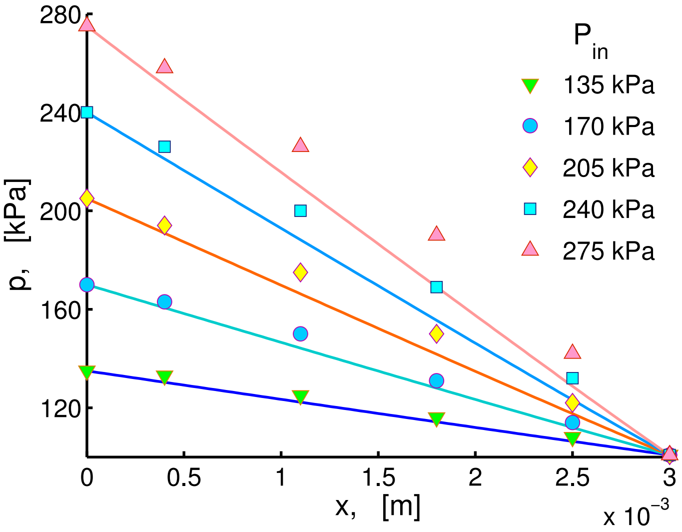

Figure 6.14: Case-14 represents the case where the gas density ρ, permeability correction factor f and gas viscosity μ are taken as pressure dependent parameters, whereas intrinsic permeability $K$is assumed constant. Pressure profiles p are plotted against the distance x at different inlet pressures, and it is clear that numerical results do not match experimental data. Moreover, results of the Case 14 are similar to the Cases 1, 5, 7, 8.

ρ, permeability correction factor f and the gas viscosity μ are considered as a function of pressure p. Equation (6.3.1) remains the same but the coefficient L_a becomes,

$$L_a = -[\zeta_\rho(p) + \zeta_f(p) - \zeta_\mu(p)]\frac{\partial p}{\partial x}. \tag{6.3.20}$$

Numerical solutions are plotted in the Figure 6.14 which shows the pattern of pressure distribution. It is clear that the solutions do not match the data except for small inlet pressure p_{in}.

Case 15: $\zeta_\rho(p) = 0$.

It means that the parameters ρ is assumed constant whereas the intrinsic permeability K, permeability correction factor f and the gas viscosity μ are considered as a function of pressure p. Equation (6.3.1) remains the same but the

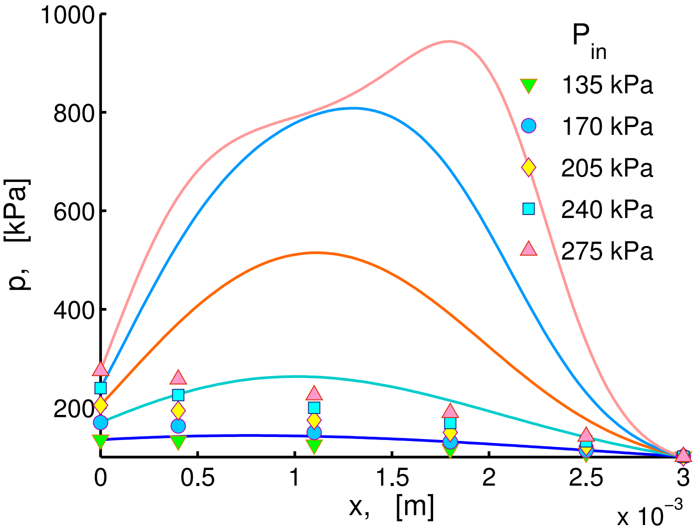

Figure 6.15: Case-15 represents the case where intrinsic permeability K, permeability correction factor f and gas viscosity μ are taken as pressure dependent parameters, whereas the gas density ρ is assumed constant. Pressure profiles p are plotted against the distance x at different inlet pressures, and it is clear that numerical results do not match experimental data. The deviations become very large and wide when the difference between the inlet and outlet boundary conditions is large.

coefficient L_a becomes,

$$L_a = -[\zeta_K(p) + \zeta_f(p) - \zeta_\mu(p)]\frac{\partial p}{\partial x}. \qquad (6.3.21)$$

Numerical solutions are plotted in the Figure 6.15 which shows the pattern of pressure distribution. It is clear that the solutions do not match the data except for small inlet pressure p_{in}.

Case 16: All the parameters, gas density ρ, intrinsic permeability K, permeability correction factor f and gas viscosity μ, are considered as a function of pressure p. Equation (6.3.1) remains the same but the coefficient L_a becomes,

$$L_a = -[\zeta_\rho(p) + \zeta_K(p) + \zeta_f(p) - \zeta_\mu(p)]\frac{\partial p}{\partial x}. \qquad (6.3.22)$$

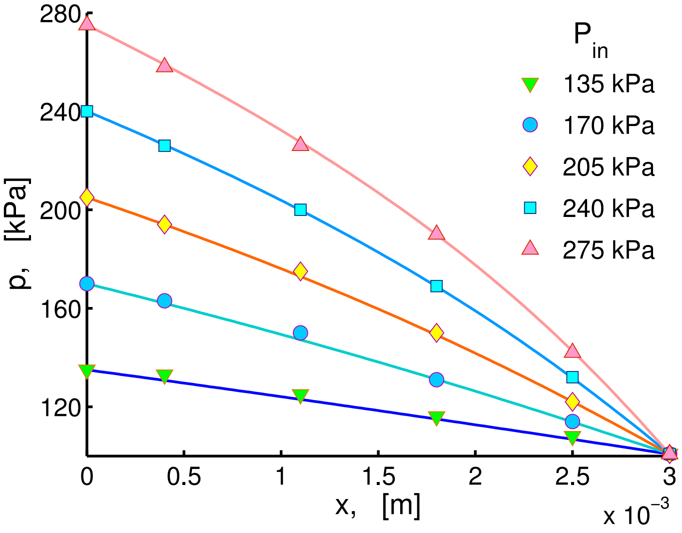

Figure 6.16: Case-16 represents the case where all the parameters, the gas density ρ, intrinsic permeability K, permeability correction factor f, gas viscosity μ are taken as pressure dependent. Pressure profiles p are plotted against distance x for different inlet pressures. We observe an excellent match between the numerical solutions and the experimental data. Moreover, Case 16 will be treated as the base case during further investigation.

Numerical solutions are plotted in the Figure 6.16 which shows the pressure distribution. We see a very good match between the numerical solution and the data. Case 16 will be treated as the "base case" henceforth.

6.3.4 Observations

It is observed from the plots of all the sixteen cases that only the Case-12 and Case-16 show good match between the numerical solutions and the experimental data, while the other cases showing significant errors. Figure 6.1, (Case-1), corresponds to Darcy's law where all reservoir parameters are taken constant through out the reservoir sample and shows that the use of Darcy's law without modification is inaccurate. Figure 6.16, (Case-16), corresponds to our new model approach

Cases	ζ_ρ	ζ_K	ζ_f	ζ_μ	Error
1	0	0	0	0	2.69e-02
2	p	0	0	0	2.68e-02
3	0	p	0	0	1.64e-01
4	0	0	p	0	1.00e+05
5	0	0	0	p	2.69e-02
6	p	p	0	0	2.23e+00
7	p	0	p	0	8.52e-01
8	p	0	0	p	2.69e-02
9	0	p	p	0	1.19e+00
10	0	p	0	p	1.64e-01
11	0	0	p	p	1.00e+05
12	p	p	p	0	1.059e-04
13	p	p	0	p	2.23e+00
14	p	0	p	p	8.52e-01
15	0	p	p	p	1.19e+00
16	p	p	p	p	1.055e-04

Table 6.4: List of simulations carried out. In columns 2-5, an entry of 0 means that the compressibility factor is zero; an entry of p means that it is nonzero and the associated physical parameter is function of pressure p. The last column shows the error obtained using equation (6.3.5).

where all the reservoir parameters, such as, gas density, gas viscosity and apparent permeability, are considered in the numerical calculations to be pressure dependent. The error calculated in Case-16 is the smallest among all the sixteen cases and gives the best fit showing excellent agreement with the data. Figure 6.17 shows the relative error on log-scale for the sixteen models considered.

It is important to note that although the results of Civan et al. [41] and the current case Figure 6.16 appear to yield similar results, but our approach is different in the sense that we have used the pressure dependent correlations in the simulations whereas Civan assumed them to be constant, except for the intrinsic permeability and its companion compressibility coefficient, in actual applications.

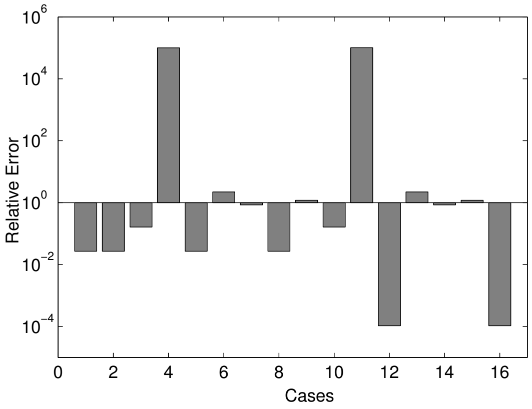

Figure 6.17: Error between the simulated and the calculated values is shown for all cases, obtained using equation (6.3.5).

In Civan's case, assuming $\phi = 0.2$ independent of pressure, the predicted value of rock permeability is $K = 10^{-15}$ m^2.

In the present calculations the porosity is in the range $0.1901 \leq \phi \leq 0.2003$; the permeability is in the range $10^{-14} \leq K \leq 10^{-15}$ m^2.

6.3.5 Sensitivity analysis of model parameters

It is important to determine how much the results and the predicted rock properties change due to small changes in model parameters. A sensitivity analysis was carried out by adjusting most of the model parameters one at a time by factors of 2 and then 1/2, starting with Case-16 as the base case. An exception is a model parameter which appears as a power; then this parameter is adjusted by a much smaller amount. This is called One-at-a-Time (OAT) methodology. Sensitivity is measured by monitoring the errors.

We determine how sensitive are the results to the changes in the following parameters, a_τ (constant in the tortuosity model), a_ϕ, b_ϕ, c_ϕ (constants in the porosity model), $\alpha_{KC},\ \beta_{KC},\ \Gamma_{KC}$ (constants in the Kozney-Carman model), $\sigma_0,\ A_\sigma,\ B_\sigma$ (constants in the rarefaction coefficient model).

In OAT sensitivity analysis, generally each of the M model parameters, say, $\xi_i^0,\ i=1,\cdots,M$, is varied for by a factor of 2 and then by a factor of 1/2; that is, given a base case ξ_i^0, we take $\xi_i^1 = 2\xi_i^0$, and then $\xi_i^2 = \xi_i^0/2$. The simulation results for the $p(x)$ are then compared. In the new steady state model, there are $M = 9$ model parameters, and we carry out a sensitivity analysis for each parameter as described above. We take the base case ξ^0, as the ones for Case-16 in Table 6.1.

First, we determine the sensitivity to the tortuosity τ by taking half and twice of the base value of a_τ. The results are shown in Figure 6.18, and it is noted that the pressure inside the core sample is little affected by the change in value of a_τ.

Next, we determine the sensitivity to porosity. There are three different constants, namely a_ϕ, b_ϕ, c_ϕ appear in the porosity correlation. First, we change the base value of a_ϕ, and the results are shown in Figure 6.19 and it is noted that the pressure is significantly affected by the changes in a_ϕ, except at low p_{in}.

Figure 6.20 shows the results for the sensitivity to b_ϕ. It is noted that the results are sensitive except at low p_{in}.

Figure 6.21 shows the results for the sensitivity to c_ϕ. The results are highly sensitive for the selected values of c_ϕ for large p_{in}. There is a large variation in the pressure close to the upstream reservoir. Moreover, effects are more significant when the difference between inlet and outlet pressures is large.

Rock permeability is the most important parameter in the reservoir simula-

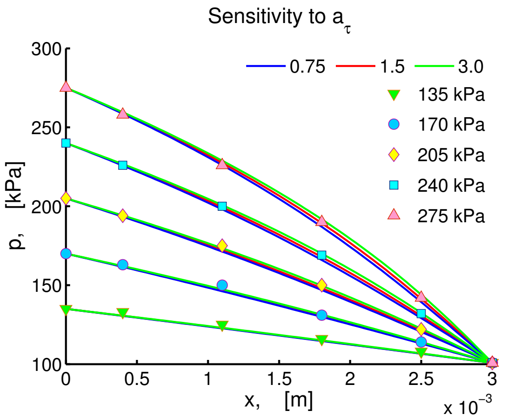

Figure 6.18: Sensitivity to a_τ, a constant appearing in tortuosity correlation, is depicted. The model outputs are insensitive for the selected values of a_τ. But a small variation in the pressure values are observed at two-third of the sample length.

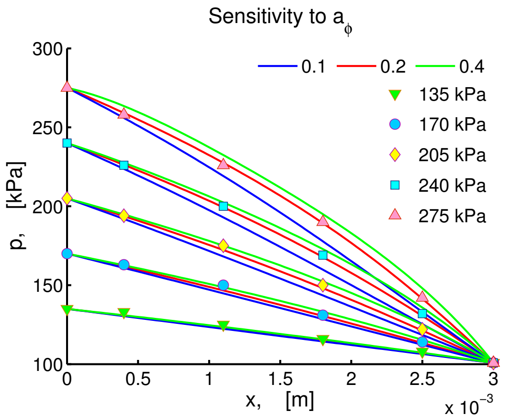

Figure 6.19: Sensitivity to a_ϕ, a constant appearing in porosity correlation, is depicted. The model outputs are highly sensitive for the selected values of a_ϕ and huge variation in the pressure values are observed at two-third of the sample length.

tions. It appears in the transport model through the power-law form of Kozeny-Carman equation. There are three different constants, namely α_{KC}, β_{KC}, and Γ_{KC} that appear in the Kozeny-Carman equation. We determine the effects of these parameters on the model outcomes.

First, we determine the sensitivity to α_{KC} by taking half and twice of the base value of α_{KC}. The results are shown in Figure 6.22 and it is noted that the reservoir pressure is significantly affected by the changes in α_{KC} at high p_{in}.

Figure 6.23 shows the results for the sensitivity to β_{KC}. The results are slightly sensitive to the changes in β_{KC}, for large p_{in}.

Figure **??** shows the results for the sensitivity to Γ_{KC}. The results are quite sensitive to the values of Γ_{KC} for large p_{in}, but not for small p_{in}.

Figures 6.25, 6.26, and 6.27, shows the sensitivity to σ_0, A_σ, and B_σ appearing in the rarefaction coefficient correlation. It is noted that the pressure inside the

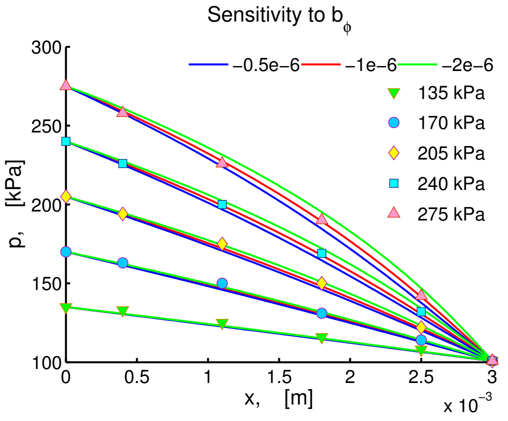

Figure 6.20: Sensitivity to b_ϕ, a constant appearing in porosity correlation, is depicted. The model outputs are less sensitive for the selected values of b_ϕ, but a small variation in the pressure values are observed at two-third of the sample length.

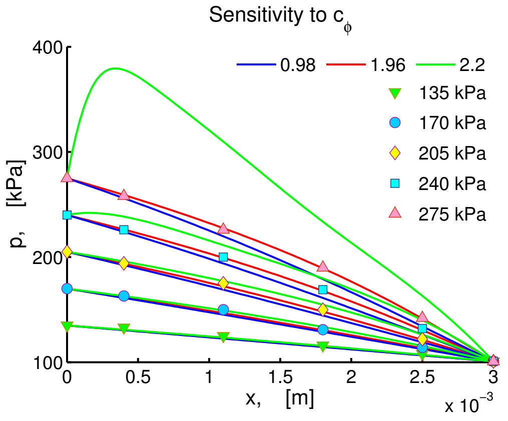

Figure 6.21: Sensitivity to c_ϕ, a constant appearing in porosity correlation, is depicted. The model outputs are highly sensitive for the selected values of c_ϕ and huge variation in the pressure values are observed close to the upstream reservoir. Moreover, effects are more significant when the difference between inlet and outlet pressures is large.

reservoir sample is unaffected by the changes in these constants, within the given ranges.

6.3.6 Summary

A general framework has been given for estimating rock properties in shale gas rock samples such as, rock permeability, porosity, and tortuosity, through solving an inverse problem corresponding to the new non-linear transport model. The model parameters are adjusted to best fit the available data, minimizing the mean square error. Here, many of model parameters and physical relationships are genuine functions of pressure, leading to nonzero compressibility coefficients

Darcy's law is clearly an inadequate model for shale gas transport in unconventional reservoirs. We have found that using the new steady state model with

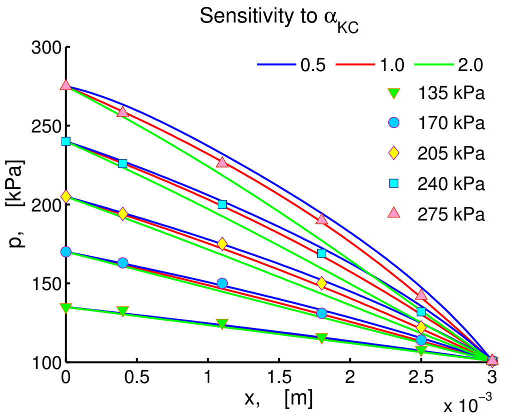

Figure 6.22: Sensitivity to α_{KC}, a constant appearing in Kozeny-Carman equation, is depicted. The model outputs are sensitive for the selected values of α_{KC}. It shows that variation in the permeability effects the pressure inside the reservoir and hence the fluid flow is also affected.

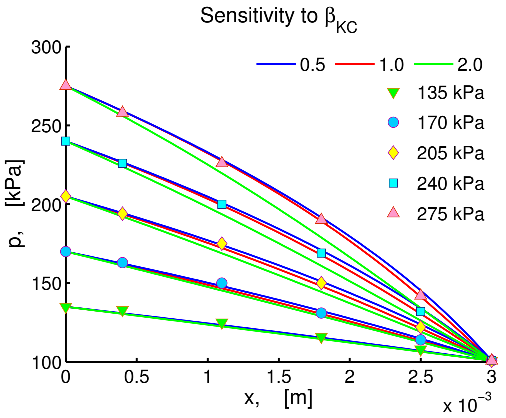

Figure 6.23: Sensitivity to β_{KC}, a constant appearing in Kozeny-Carman equation, is depicted. The model outputs are sensitive for the selected values of β_{KC}. It shows that variation in the permeability effects the pressure inside the reservoir and hence the fluid flow is also affected.

fully pressure dependent parameters in actual application, Case-16, Figure 6.16, gives the best fit to the data.

From the sensitivity analysis, we note that the results are are insensitive to some model parameters, but critically sensitive to other parameters . The model parameters that are insensitive are a_τ, σ_0, a_σ, and b_σ. Model parameters related to porosity and permeability, such as, a_ϕ, b_ϕ, c_ϕ, α_{KC}, β_{KC}, and Γ_{KC} are critically sensitive, see Figure 6.28. This is true especially of the parameters that appear as a power in a correlation. The sensitivity of such parameters is tested on a given range of pressure, in our case, typical range of pressure lies in the interval 100 kPa to 275 kPa. On the basis of the sensitivity analysis, it may be possible to reduce the pressure dependent parameters in the model.

We also remark that typically, porosity increases with the increase in pressure, and generally, $\phi > a_\phi$. The compressibility coefficient of porosity ζ_ϕ also increases

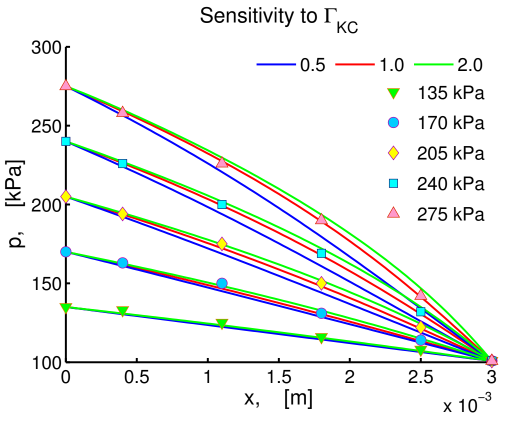

Figure 6.24: Sensitivity to Γ_{KC}, a constant appearing in Kozeny-Carman equation, is depicted. The model outputs are sensitive for the selected values of Γ_{KC}. It shows that variation in the permeability effects the pressure inside the reservoir and hence the fluid flow is also affected.

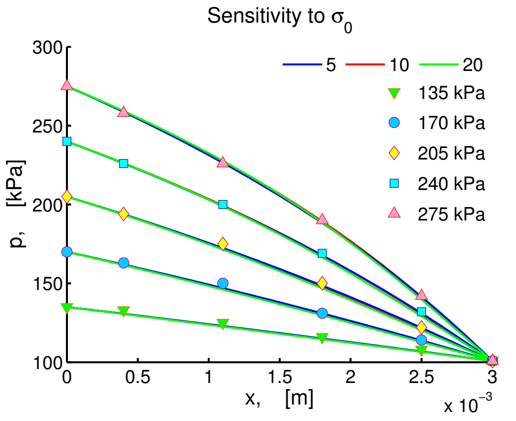

Figure 6.25: Sensitivity to σ_0, a constant appearing in the rarefaction coefficient correlation, is depicted. The model outputs are unresponsive for the selected values of σ_0.

with the increase in pressure and it's magnitude is in order of $\zeta_\phi \approx 10^{-3}$ in the range of pressure considered. The pressure varies from 100 kPa to 275 kPa, and the temperature is 314 K.

Tortuosity is much greater than 1 and it's compressibility coefficient decreases with the increase in pressure and of the order of $\tau \approx 10^{-4}$.

Intrinsic permeability lies in the range of $K \approx 10^{-16}$ m^2 to $K \approx 10^{-14}$ m^2, and it's compressibility coefficient increases with the increase in pressure and remains positive in the range of pressure considered.

Figure 6.28 summarizes all the relative errors from sensitivity analysis. c_ϕ is the most critical parameter, and insensitive to σ_0, a_σ, b_σ, and all others are moderately sensitive.

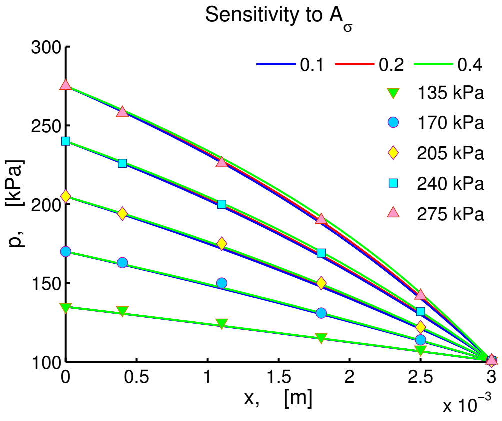

n

Figure 6.26: Sensitivity to A_σ, a constant appearing in the rarefaction coefficient correlation, is depicted. The model outputs are unresponsive for the selected values of A_σ.

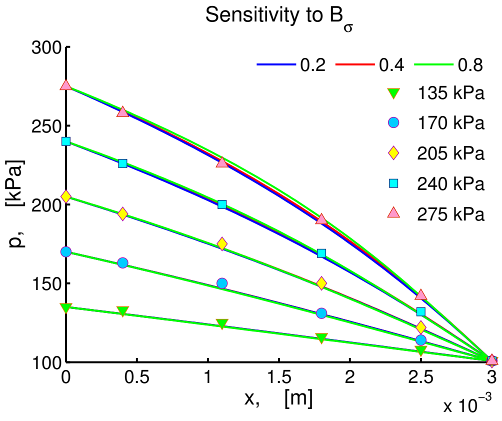

Figure 6.27: Sensitivity to B_σ, a constant appearing in the rarefaction coefficient correlation, is depicted. The model outputs are unresponsive for the selected values of B_σ.

6.4 New Steady State Model with Turbulence Correction

In this section, we consider the steady state limit of the new transport model (6.4.1) but now also including a non-zero turbulence correction $F \neq 1$, which is an advection-diffusion equation with nonlinear advection coefficient (6.4.2). The diffusion term is the same as in the Civan's model but the advection term now involves the Forchheimer's correction for turbulence, (6.4.3). Moreover, the new steady state model is a system of coupled nonlinear partial differential equations which involves two dependent variables, pressure and velocity.

The validation of the model is performed by matching the numerical results against the experimental data of Pong et al. [134]. Pong has given two experimental data sets that describe the gas flow in microchannels. The first data set already described is obtained for Nitrogen gas as the working fluid. The second

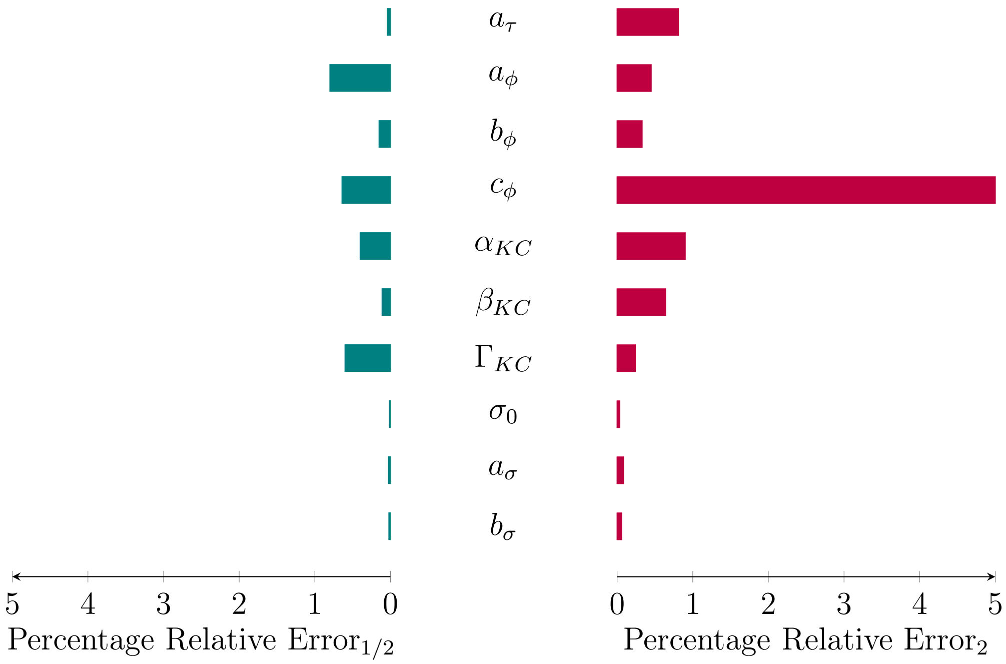

Figure 6.28: Percentage relative errors for each of the model parameters, listed in Table 6.2, are calculated from the sensitivity analysis for Pong's Data set 1. It shows that parameters related to porosity and permeability are most sensitive.

data set is obtained using Helium gas as the working fluid.

6.4.1 Simulations using the New Steady State Model

In this section, the new model is validated by finding the numerical solutions of the model (6.4.1), (6.4.2) and (6.4.3). As mentioned earlier, there are two different experimental data sets given by Pong et al. [134], first of them is obtained by first generation microflow system and second of them is obtained by second generation microflow system, for more details see Pong et al. [134].

First, we validate the new transport model against the Pong's first experimental data. We find the numerical solutions from our new steady state model for different cases by adjusting values of different parameters. There are a few param-

New Steady State Model with turbulence correction		
Reservoir Parameters	Pong's Data 1	Pong's Data2
L (m)	0.003	0.0046
N_x	100	100
R_g ($\mathrm{J\,kmol^{-1}\,K^{-1}}$)	8314.4	8314.4
M_g ($\mathrm{kg\,kmol^{-1}\,K^{-1}}$)	28.013	4.0026
T (K)	314	314
p_c (kPa)	3396	227.5
t_c (K)	126.19	5.199 982
b_{SF}	-1	-1
σ_0	1.3580	1.3580
A_σ	0.1780	0.1780
B_σ	0.4348	0.4348
a_τ	1.5	1.5
a_ϕ	0.10	0.10
b_ϕ	-0.939×10^{-1}	-0.939×10^{-1}
c_ϕ	0.39	0.57
α_{KC}	1.0	1.0
β_{KC}	0.9	0.9
Γ_{KC}	0.72×10^{-8}	0.72×10^{-8}
a_β	3.1×10^{1}	2.98×10^{1}
b_β	0.5	0.1
c_β	1.35	0.6
d_β	0.4	0.9
Error	5.972×10^{-5}	2.93×10^{-3}

Table 6.5: Model parameters used in the New Steady State Model. This data set of base values will be used for further data analysis and parameter estimation.

eters whose values are already known, but there are some other parameters whose values can be adjusted so that the error between the simulated and experimental values is minimum. In contrast to the model validation done in the Section 6.3, we have four more parameters, a_β, b_β, c_β, and d_β, that arise from the consideration of the Forchheimer's correction term. For more details, see SubSection 6.3.1.

The ***Steady State Modal*** is given by,

$$L_a\left(p, p_x\right)\frac{\partial p}{\partial x} = \frac{\partial^2 p}{\partial x^2}, \qquad 0 \le x \le L, \tag{6.4.1}$$

where

$$L_a(p, p_x) = -\zeta_3(p)\frac{\partial p}{\partial x}, \tag{6.4.2}$$

and

$$\zeta_3(p) = F\left[\zeta_\rho(p) + \zeta_K(p) + \zeta_f(p) - \zeta_\mu(p)\right] + (F-1)\left[\zeta_\beta(p) + \zeta_{|u|}(p)\right] \tag{6.4.3}$$

Boundary conditions are set as $p(0) = p_L$ and $p(L) = p_R$.

Validation against Pong's experimental data set 1 (Nitrogen) New steady state model (6.4.1) is solved numerically by the method described in Chapter 5, with the parameter's values given in Table 6.5. In numerical simulations, all reservoir parameters, for instance, the gas density ρ, intrinsic permeability K, permeability correction factor f, gas viscosity μ, and turbulence factor β are pressure dependent. Since the model (6.4.1) is a coupled nonlinear advection-diffusion equation, which depends on pressure and velocity implicitly, therefore,

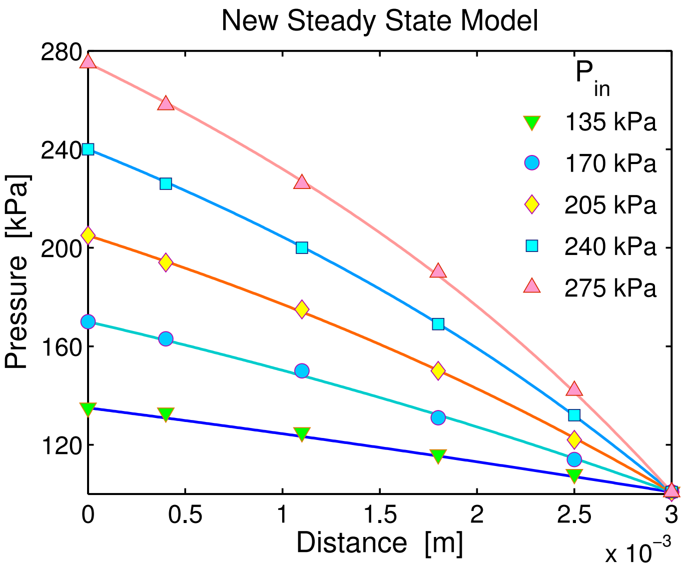

Figure 6.29: Pressure is plotted against distance for different inlet pressures. We observe an excellent match between the numerical solutions and the experimental data. Pressure profiles are obtained by numerically solving the new steady state model (6.4.1) with Forchheimer's correction $F \neq 1$ and by using the parameter values given in Table 6.5. In numerical simulations, all reservoir parameters.

we iterate both on the pressure and also on the velocity.

Pressure is plotted against distance for different inlet pressures in the Figure 6.29. We observe an excellent match between the numerical solutions and the experimental data, and the relative error between the simulated and the measured pressure values is 5.72×10^{-5}, which is smaller than for the Case-16 in Section 6.3.4. The porosity lies in the interval $(0.10, 0.1038)$ and the intrinsic permeability lies in the interval (106, 111) nD. These are more realistic of tight shale gas rocks than has been obtained from previous models.

Figure 6.30 shows the plots of the volumetric flux (velocity) u against distance x. We note that the volumetric flux depends upon the pressure gradient, that is, it is small for small pressure gradients and it is large for large pressure gradients. It means that to achieve a large volume flow rate, it would require a large pressure

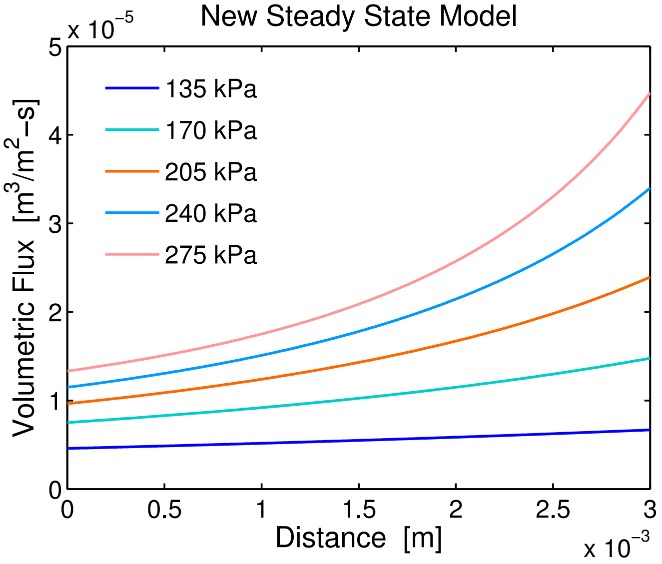

Figure 6.30: Volumetric flux u obtained from the new steady state model (6.4.1) is plotted against distance x. The volumetric flux depends on the pressure gradient, it is small for small pressure gradients and it is large for large pressure gradients.

difference between the inlet and outlet pressures.

Validation against Pong's experimental data set 2 (Helium)

Pong et al. [134] has given a second set of data describing the pressure distribution through porous media with microflow channels. The data is obtained by second generation microflow system in which pressure sensors are mounted at much shorter distance compared to the first generation data set. Here, we solve the new steady state model (6.4.1) with second set of parameter values given in Table 6.5. Pong used Helium gas as the working fluid in the second generation test, so we have taken values of parameters, such as, M_g, p_c, t_c, etc., corresponding to Helium gas. On the other hand, the gas density ρ, intrinsic permeability K, permeability correction factor f, gas viscosity μ, and turbulence factor β are pressure dependent and their values together with their compressibility coefficients are determined internally in the solver by correlations given in Chapter 4 with

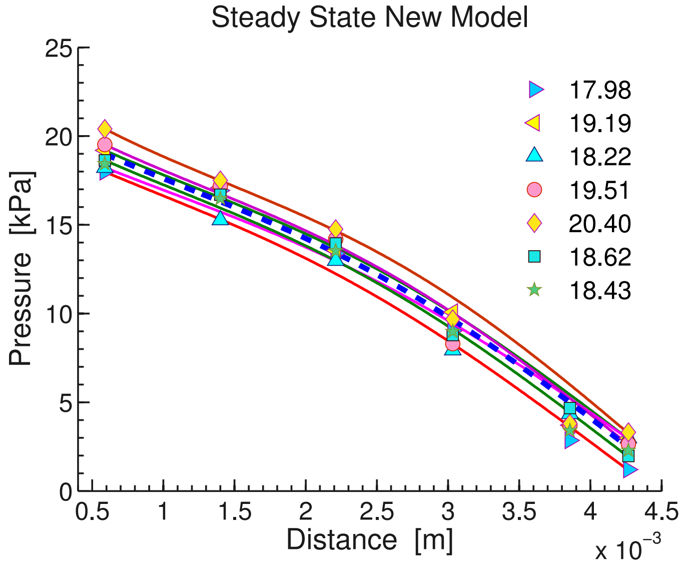

Figure 6.31: Pressure profiles obtained from the numerical solution of new steady state model (6.4.1). Symbols denote Pong's data (1994).

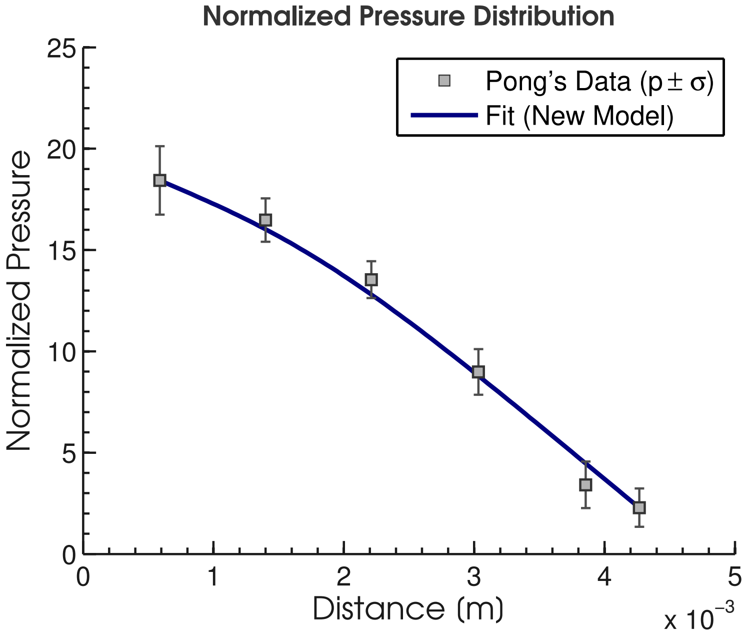

Figure 6.32: Averaged pressures at each pressure sensor location are determined for Pong's data set 2 and then again new mathematical model is solved and resulting pressure values are fitted into the experimental data. Results are plotted and it provides a fairly decent match to the data.

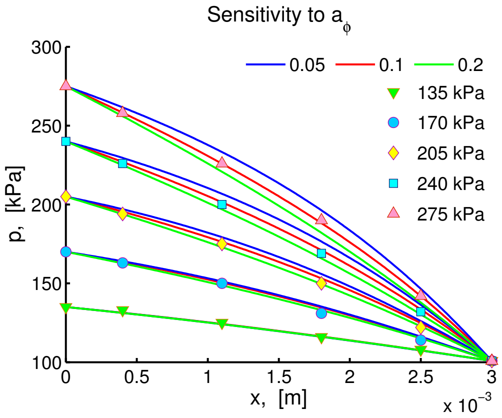

Figure 6.33: Sensitivity to a_ϕ, a constant appearing in porosity correlation, is depicted.

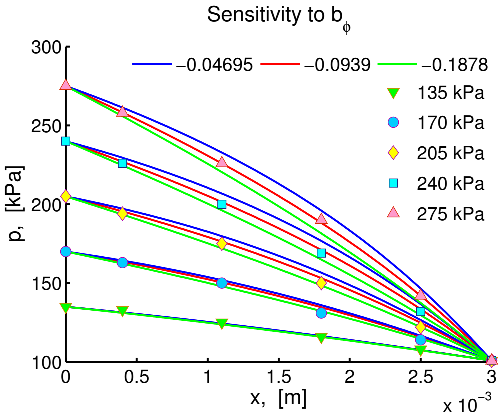

Figure 6.34: Sensitivity to b_ϕ, a constant appearing in porosity correlation, is depicted.

parameter values given in Table 6.5.

Pressure profiles are plotted against distance for different inlet pressures in figures 6.31, and 6.32. We observe an excellent match between the numerical solutions and the experimental data, and the relative error between the simulated and the measured pressure values is 2.93×10^{-3}. The values of porosity lie in the interval $(0.105, 0.145)$ and values of intrinsic permeability lie between (140, 280) nD. However, it should be noted that the data is the averaged values of pressure over several trials, and the error levels in the data are significantly higher than in data set 1.

6.5 Sensitivity Analysis for the Pong's Data Set 1

An OAT sensitivity analysis is carried out against Pong's experimental data set 1, Table 6.5.

In the numerical simulations, the values of p_c (the critical pressure), t_c (the

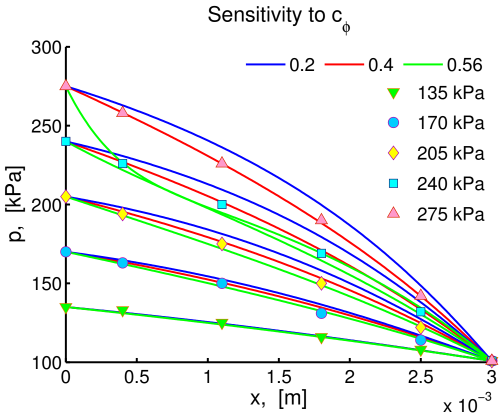

Figure 6.35: Sensitivity to c_ϕ, a constant appearing in porosity correlation, is depicted.

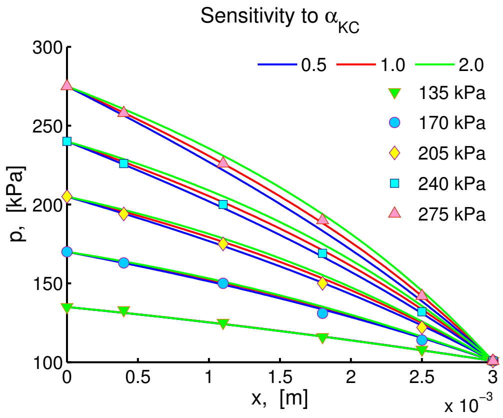

Figure 6.36: Sensitivity to α_{KC}, a constant appearing in the Kozeny-Carman equation, is depicted.

critical temperature), T (temperature), M_g molecular weight of the gas, universal gas constant R_g, slip factor b_{sf}, σ_0, A_σ, B_σ (constants in the rarefaction coefficient model), a_τ (constant in the tortuosity model), are fixed from physical consideration.

The sensitivity analysis is therefore carried out for the remaining model parameters; a_ϕ, b_ϕ, c_ϕ (constants in the porosity model), α_{KC}, β_{KC}, Γ_{KC} (constants in the Kozney-Carman model), a_β, b_β, c_β, d_β (constants in the rarefaction coefficient model). We vary the parameter values by factors of 2 and $1/2$ for their base case in Table **??**, unless otherwise stated.

Figures 6.33, 6.34, and 6.35 shows sensitivity to, respectively, a_ϕ, b_ϕ, c_ϕ. The model outputs are less sensitive for $p_{inlet} < 170$ kPa, but we observe some variations in the pressure for $p_{inlet} > 200$ kPa in the case of a_ϕ and b_ϕ. In the case of c_ϕ, we observe large variation in pressure especially when $p_{inlet} > 250$ kPa. This happens because c_ϕ appears in the porosity model as a power of p, that is, the reason c_ϕ is varied only a small amount.

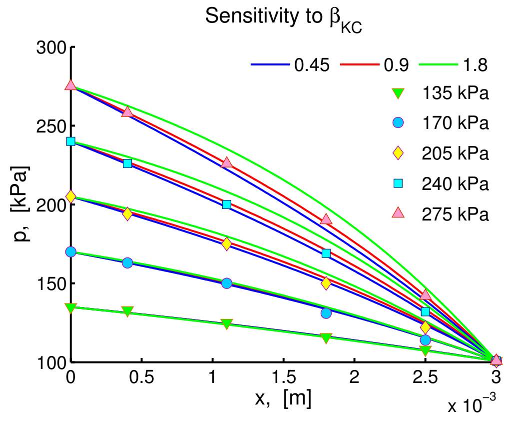

Figure 6.37: Sensitivity to β_{KC}, a constant appearing in Kozeny-Carman equation, is depicted.

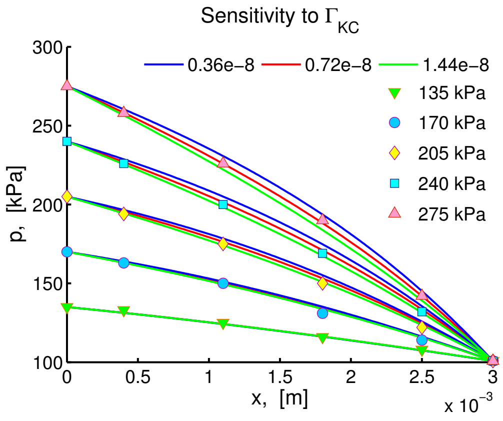

Figure 6.38: Sensitivity to Γ_{KC}, a constant appearing in Kozeny-Carman equation, is depicted.

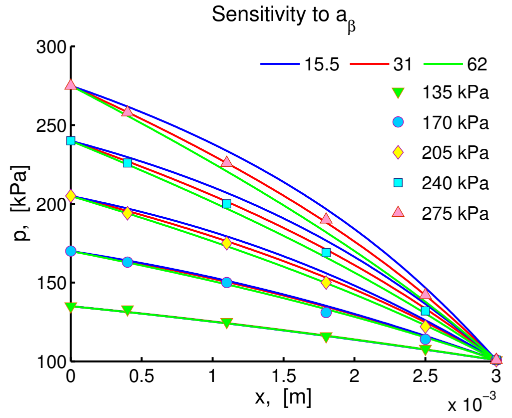

Figure 6.39: Sensitivity to a_β, a constant appearing in the turbulence factor correlation, is depicted.

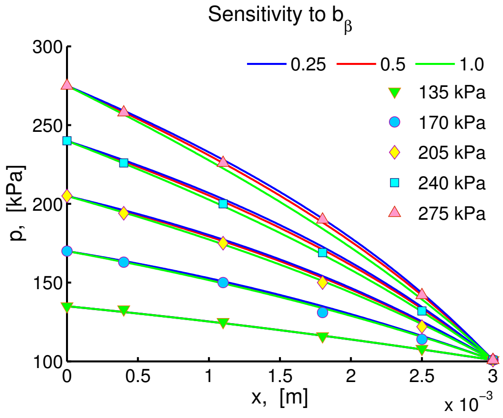

Figure 6.40: Sensitivity to b_β, a constant appearing in the turbulence factor correlation in the power of tortuosity, is depicted.

Figures 6.36, 6.37, and 6.38 show the sensitivity analysis to the model parameters, α_{KC}, β_{KC}, Γ_{KC}. These parameters appear in the power-law form of Kozeny-Carman equation. It is noted that the results are insensitive for $p_{inlet} < 200$ kPa, but some variations in the pressure are observed for $p_{inlet} > 200$ kPa.

The turbulence factor β is the reservoir parameter that accounts for the inertial effects and also for the high velocity flow fields through the fractures or near the well bore. It depends on the other reservoir parameters, such as, tortuosity,

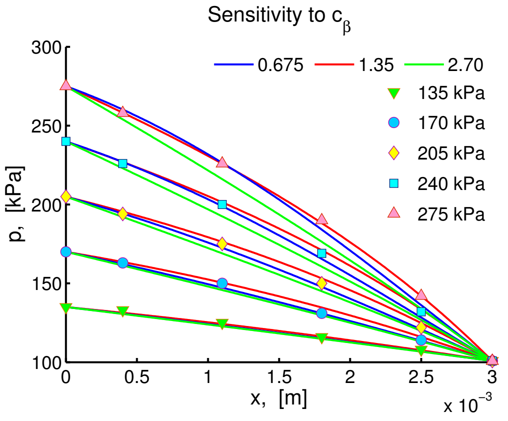

Figure 6.41: Sensitivity to c_β, a constant appearing in the turbulence factor correlation in the power of intrinsic permeability, is depicted.

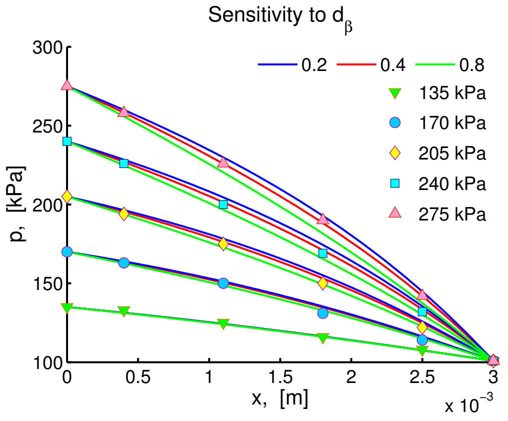

Figure 6.42: Sensitivity to d_β, a constant appearing in the turbulence factor correlation in the power of porosity, is depicted.

porosity, and permeability. The correlation for β involves four model parameters which are a_β, b_β, c_β, and d_β, and in order to determine their affects on the model output, we carry out sensitivity analysis for each of them.

Figures 6.39, 6.40, 6.41, and 6.42 show the sensitivity analysis of the parameters a_β, b_β, c_β, and d_β. It is observed that the model outputs are insensitive for $p_{inlet} < 200$ kPa and sensitive for $p_{inlet} \geq 200$ kPa.

6.5.1 Summary

Numerical solutions of the new steady state model (6.4.1) were obtained by using the values of model parameters from Table 6.5. The values of the parameters L, R_g, M_g, T, p_c, t_c, b_{SF}, σ_0, A_σ, B_σ, and a_τ are fixed, while the values of the parameters a_ϕ, b_ϕ, c_ϕ, α_{KC}, β_{KC}, Γ_{KC}, a_β, b_β, c_β, and d_β are adjusted to match the experimental data.

The values of porosity lie in the interval $(0.10, 0.1038)$ and values of intrinsic

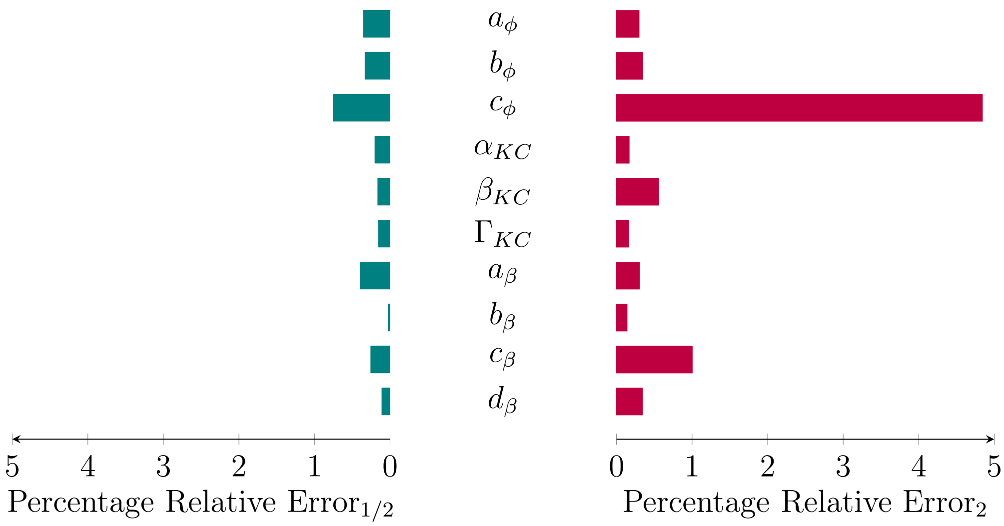

Figure 6.43: Percentage relative errors are shown, which is obtained from the sensitivity analysis of new transport model with $\beta \neq 0$, equation (6.4.1), for Pong's data set 1.

permeability lie between (106, 111) nD. The error between the simulated and the measured pressure values is 5.72×10^{-5}.

Figure 6.43 summarizes all the relative errors from sensitivity analysis. Note that the relative errors are calculated with respect to largest p_{in}. The model is critically sensitive to c_ϕ, and insensitive to α_{KC}, and Γ_{KC}, and b_β. The model is are moderately sensitive to all other parameters.

6.6 Sensitivity Analysis for the Pong's Data Set 2

We have carried out a similar sensitivity analysis of the model parameters, but now using Pong's data set 2 as a reference. The working fluid in the second experiment is Helium gas, so it's properties are taken from the standard manuals. In the numerical simulations, the values of the following parameters, p_c (the critical pressure), t_c (the critical temperature), T (temperature), M_g molecular weight of

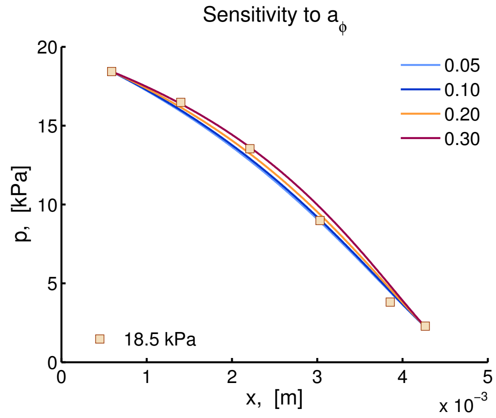

Figure 6.44: Sensitivity to a_ϕ, a constant appearing in porosity correlation, is depicted. The model outputs are less sensitive for the selected values of a_ϕ, but small variations in the pressure values are observed when the value of a_ϕ is changed.

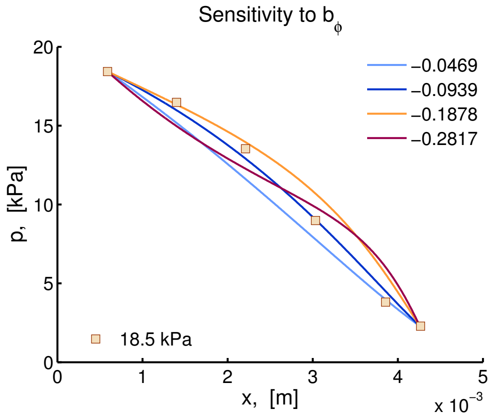

Figure 6.45: Sensitivity to b_ϕ, a constant appearing in porosity correlation, is depicted. The model outputs are highly sensitive with respect to changes in b_ϕ, and huge variation in the pressure values is observed when the value of b_ϕ is three times of the base value.

the gas, universal gas constant R_g, slip factor b_{sf}, σ_0, A_σ, B_σ (constants in the rarefaction coefficient model), a_τ (constant in the tortuosity model), are fixed.

The sensitivity analysis is carried out on the following model parameters a_ϕ, b_ϕ, c_ϕ (constants in the porosity model), α_{KC}, β_{KC}, Γ_{KC} (constants in the Kozney-Carman model), a_β, b_β, c_β, d_β (constants in the rarefaction coefficient model).

Figures 6.44, 6.45 and 6.46 show the sensitivity analysis with respect to model parameters a_ϕ, b_ϕ and c_ϕ, respectively. We observe that the results are significantly affected by changes in these parameters, especially, b_ϕ and c_ϕ; but only slightly to a_ϕ.

The sensitivity analysis to the three permeability parameters, namely α_{KC}, β_{KC}, and Γ_{KC} that appear in the Kozeny-Carman equation, are shown in the Figures 6.47, 6.48 and 6.49. In the case of α_{KC}, the results are insensitive for

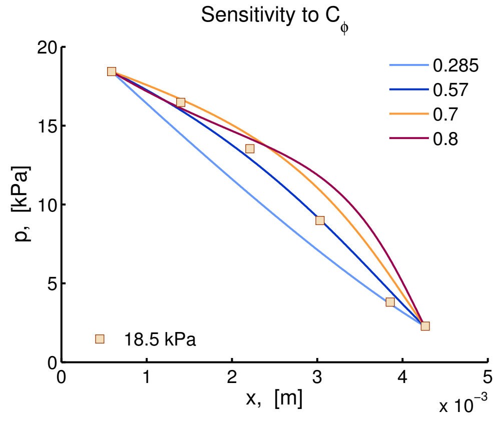

Figure 6.46: Sensitivity to c_ϕ, a constant appearing in porosity correlation, is depicted.

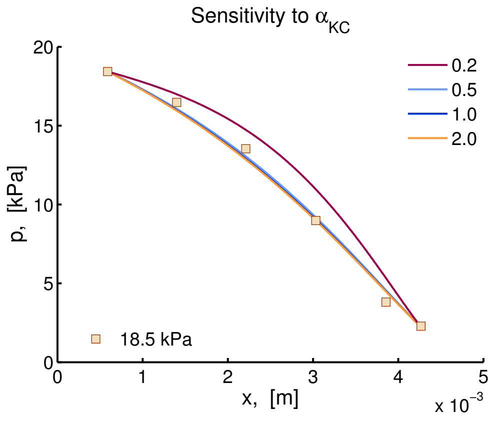

Figure 6.47: Sensitivity to α_{KC}, a constant appearing in the Kozeny-Carman equation, is depicted.

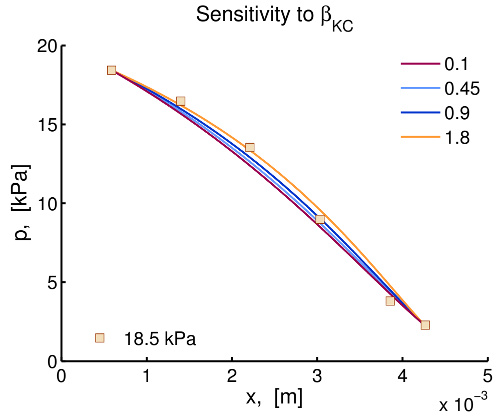

Figure 6.48: Sensitivity to β_{KC}, a constant appearing in porosity correlation, is depicted.

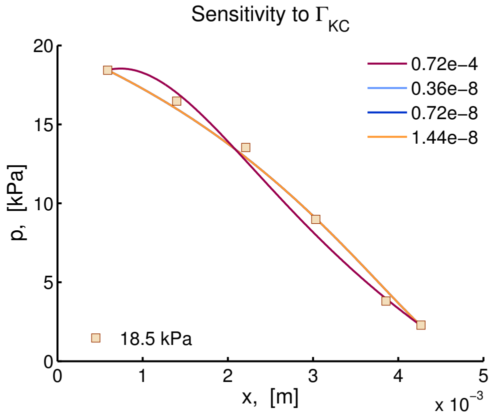

Figure 6.49: Sensitivity to Γ_{KC}, a constant appearing in porosity correlation, is depicted.

$\alpha_{KC} \geq 0.5$, but very sensitive for $\alpha_{KC} < 0.5$. In the case of β_{KC}, only small changes in the pressure are observed. Similarly, In the case of Γ_{KC}, the model outputs are insensitive for $\Gamma_{KC} \geq 0.363\times10^{-8}$, but we see large changes in pressure for $\Gamma_{KC} \leq 0.72 \times 10^{-4}$.

Figures 6.50, 6.51, 6.52 and 6.53 show the sensitivity analysis for the turbulence model parameters a_β, b_β, c_β, and d_β, respectively. The results are very sensitive to changes in a_β. Different cases are shown to illustrate the effects of the changes

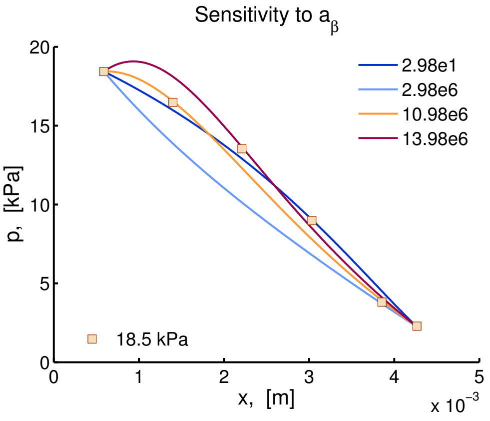

Figure 6.50: Sensitivity to a_β, a constant appearing in the turbulence factor correlation, is depicted.

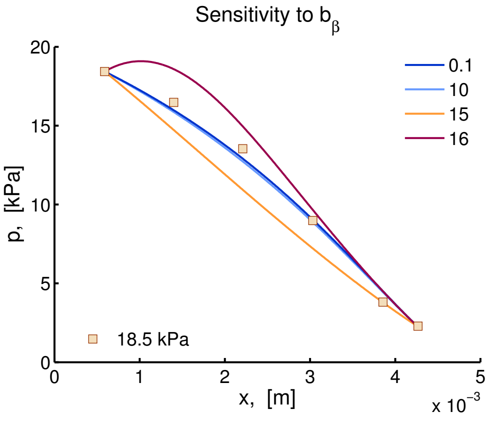

Figure 6.51: Sensitivity to b_β, a constant appearing in the turbulence factor correlation, is depicted.

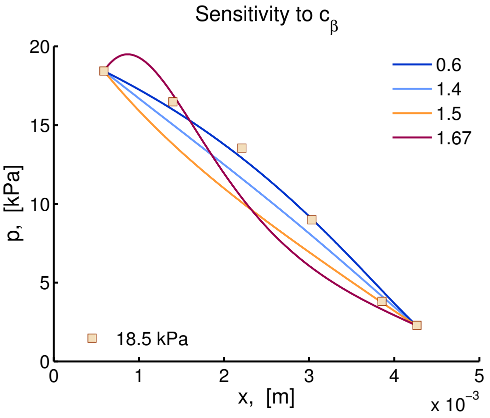

Figure 6.52: Sensitivity to c_β, a constant appearing in the turbulence factor correlation in the power of intrinsic permeability, is depicted.

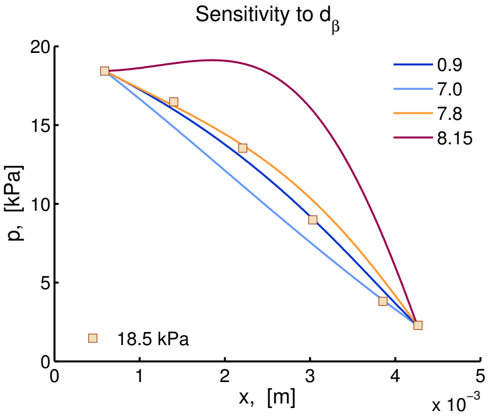

Figure 6.53: Sensitivity to d_β, a constant appearing in the turbulence factor correlation in the power of porosity, is depicted.

in a_β to the corresponding values of pressure. In the case of b_β, the results are insensitive for $b_\beta < 10$, but we see great departure from the base case for $b_\beta \geq 10$. In the case of $c_\beta = 0.6$, the results are very sensitive to the variations in the values of c_β. The base case is $c_\beta = 0.6$ and different cases are plotted to illustrate the variations in the results corresponding to changes in c_β. In the case of $d_\beta = 0.9$, the results are very sensitive to the variations in the permeability values. Different cases of d_β are shown which also includes the base case of $d_\beta = 0.9$.

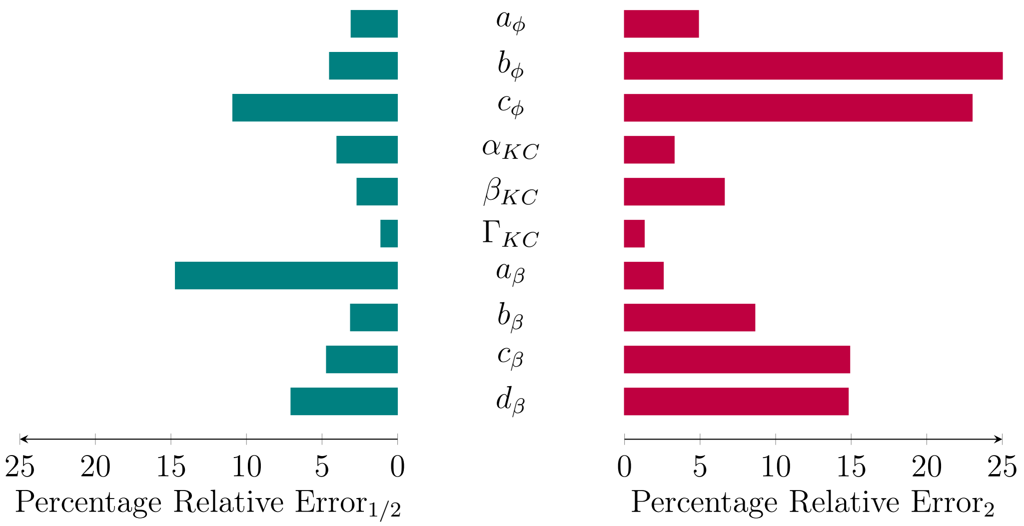

Figure 6.54: Percentage relative error is shown, which is obtained from the sensitivity analysis of new transport model with $\beta \neq 0$, equation (6.4.1), for Pong's data set 2.

The values of porosity lie in the interval $(0.105, 0.145)$ and values of intrinsic permeability lie between (140, 280) nD. The error between the simulated and the measured pressure values is 2.93×10^{-3}.

6.6.1 Summary

In this section, we have used the new transport model to analyze the Pong's dataset 2 on Helium. A set of model parameters, Table 6.5, is obtained that yields a best fit to the experimental data. A sensitivity analysis is carried out with respect to these base values given in Table 6.5. It is noted that the results are critically sensitive to b_ϕ, and c_ϕ but not to α_{KC} and Γ_{KC}. This is different to the critical and the non-critical parameters seen in the sensitivity analysis in Section 6.3, which was for the case without turbulence correction. It is also observed that Figures 6.43 and 6.54 both show moderate sensitivity to the turbulence parameters. This illustrates the importance of retaining the turbulence correction term (Forchheimer's term) in such types of transport models.

In general, the three sensitivity analyses show no consistent trend, except that c_ϕ is always critical because it appears as power. Thus, for general application, the model should retain all model parameters and pressure dependent quantities.

However the exception is for small p_{in}, where the variations in the results is very small. Thus for small p_{in} it is possible to assume pressure independent parameters.

CHAPTER 7

SIMULATIONS USING THE NEW NONLINEAR GAS TRANSPORT MODEL

7.1 Introduction

Reservoir simulation is a tool which is used in Petroleum industry to predict the future performance of a reservoir. In general, the transport of fluids through a reservoir is represented by a theoretical model which is derived from various principles, such as, continuity equation and Darcy's law. The use of reservoir simulators is not new in petroleum industry, but with the advent of new technologies, both in the technological side, such as horizontal drilling and horizontal fracturing, and in the computational side, such as super computers and high performance computing, today reservoir simulations are carried out at large scales and for complex geometries.

Reservoir simulations are used very extensively in the industry because it offers many advantages. It takes less time and costs less than field experiments, and simulations can be repeated many times with different model parameters values, and thus the general reservoir behavior can be analyzed under many conditions and assumptions. This is more convenient than drilling a well which is a time consuming and very expensive process, but also depends upon how realistic the transport model and the simulations methods are. The more realistic, then it is more reliable and can be a valuable tool for estimating future oil and gas outflow. An extensive literature is available on the subject of reservoir simulations, some of the well-known works are Aziz and Settari [14], Peaceman [131], Chen [34], Ewing [57], Economides et al. [52], Chavent and Jaffré [31], Fanchi [59], Abou-Kassem et al. [1], Shi et al. [150], Yu et al. [174], Marcondes et al. [115], Al-Shalabi et al. [4].

Hydrocarbon reservoirs are of diverse types in terms of their physical properties. They are characterized by the basis of rock types (sandstone, tight rocks, shale formations), rock structure (permeability, porosity, tortuosity), and also size, depth, temperature, and fracturing networks. Moreover, they contain different hydrocarbons, for example, oil, gas, or coalbed methane, or a mixture. The mixtures can be in multi-phase (gas, liquid, solid particles), and contains multi-species components. Different reservoir simulators are needed for different types of reservoirs. In particular, shale gas reservoirs have very complex geometries and their physical properties, such as, permeability and porosity, are quite different from the conventional reservoirs. Moreover, transport models describing the flow of fluids through shale reservoirs are much more complex than the Darcy's law diffusion models, they are highly nonlinear and they involve a great number of physical parameters. New reservoir simulators and new model solvers have to be developed in order to obtain solutions for these models which describe the fluid flow through shale formations and tight rocks. For more details, see Darishchev et al. [47], Odeh et al. [127], Fedorov and Fedorchenko [61], Li et al. [102], Fernandes et al. [63], Eshkalak et al. [55], Fernandes et al. [62], Christou and Kokou Dadzie [36], Chen et al. [32], Xu et al. [172], Guo et al. [73], Aybar et al. [13], Islam et al. [92].

Our objective in this chapter is to move from the 'inverse' problem studied in Chapter 6, to 'forward' simulation problems. The purpose is to demonstrate the predictive capability of the new model solver by applying it to predict pressure, $p(x,t)$, distribution in rock core samples over a long period of time in a simple test case. Here, we choose a simple configuration and to simulate pressure field $p(x,t)$.

7.2 Investigation of Previous Models

In this section, we solve the transient nonlinear pressure equation (3.4.3), using model solver.

7.2.1 Hsieh's Model

Hsieh et al. [84] and Neuzil et al. [125] derived a model to describe fluid flow in a transient pulse test by considering the compressive storage of the rock sample. They measured the hydraulic properties of rock samples with low permeabilities. They also employed transient pulse tests in the laboratory to estimate the sample properties. The transport model is a simple diffusion equation with constant parameter values,

$$\frac{\partial h}{\partial t} = D\frac{\partial^2 h}{\partial x^2} \qquad \text{for } 0 \leq x \leq 1 \text{ and } t > 0, \tag{7.2.1}$$

where $D = K/S_s =$ Constant. The initial condition is given by

$$h(x,0) = \begin{cases} 0 & \text{if } 0 \leq x < 1 \\ H & \text{if } x = 1 \end{cases}$$

The boundary conditions are expressed as,

$$\begin{aligned} h(0,t) &= h_d(t) && \text{for } t \geq 0 \\ h_d(0) &= 0 \\ h(L,t) &= h_u(t) && \text{for } t \geq 0 \\ h_u(0) &= H. \end{aligned}$$

Simulation Data of Hsieh et al. [84]		
Parameters	Description	Values
L [m]	Length of reservoir	1×10^{-2}
N_x	Number of intervals	101
K [m^2]	Hydraulic conductivity of the sample	6.3×10^{-15}
S_s [m^{-1}]	Specific storage	3.0
S_u [m^2]	Compressive storage of upstream reservoir	4.2×10^{-10}
S_d [m^2]	Compressive storage of downstream reservoir	4.2×10^{-10}
A [m^2]	Cross-sectional area of sample	2.8×10^{-3}

Table 7.1: Reservoir parameter values used to find the numerical solutions of the model used by Hsieh et al. [84] and Neuzil et al. [125] .

The flux conditions at the left and the right boundaries are,

$$\begin{aligned} \left(\frac{\partial h}{\partial x}\right)_{x=0} - \frac{S_d}{KA}\frac{dh_d}{dt} &= 0 \qquad\qquad \text{for } t \geq 0 \\ \left(\frac{\partial h}{\partial x}\right)_{x=L} + \frac{S_u}{KA}\frac{dh_u}{dt} &= 0 \qquad\qquad \text{for } t \geq 0. \end{aligned}$$

h is the hydraulic head in the sample, h_d is the hydraulic head in the downstream reservoir, h_u is the hydraulic head in the upstream reservoir, x denotes the distance along the sample, $x = 0$ is the down stream face, and $x = L$ is the upstream face of the sample, t is the time from the start of the experiment, H is the instantaneous increase in hydraulic head, A is the cross-sectional area of the sample, L is the length of the sample, S_u is the compressive storage of the upstream reservoir, S_d is the compressive storage of the downstream reservoir, K is the hydraulic conductivity of the sample.

Hsieh's Model (7.2.1) is solved by using the numerical solver in the limiting case when we put $U_a = 0$ and $D_a = D = K/S_s = 3.1 \times 10^{-15}$ (m^2/s) from the

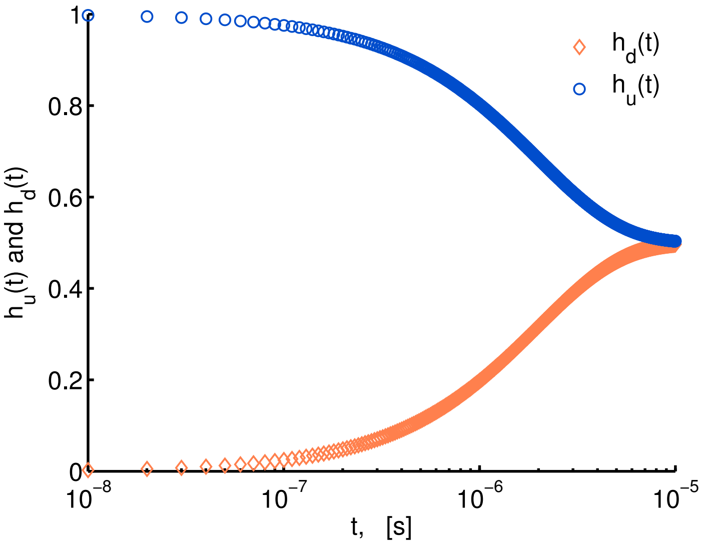

Figure 7.1: The hydraulic heads in the upstream and the down stream reservoirs, $h_d(t)$ and $h_u(t)$ respectively, are computed from Hsieh's model using the model solver. The results are plotted against the time t. The obtained results match with the results of Hsieh, see Figure 2 of Hsieh et al. [84].

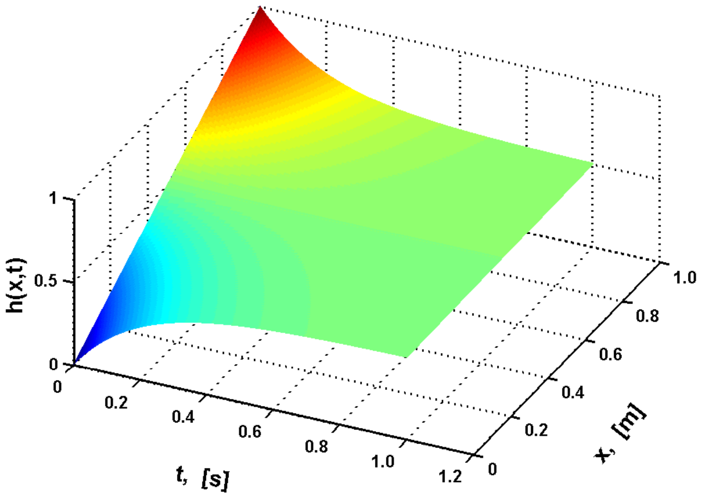

Figure 7.2: Numerical solutions from Hsieh's Model using the model solver, plotted against time t and distance x. The pressure inside the reservoir attains equilibrium state with the passage of time.

Simulation Data of Liang et al. [104]		
Parameters	Description	Values
L [m]	Length of the sample	0.0033
N_x	Number of intervals	101
ϕ	Porosity	0.03
μ [Pas]	Viscosity of gas	1.789×10^{-5}
A [m^2]	Cross-sectional area of the sample	8.55×10^{-6}
K [m^2]	Permeability	1.71×10^{-21}
ζ_K [Pa^{-1}]	Compressibility coefficient of K	6×10^{-6}
V_u [m^3]	Volume of upstream reservoir	8.3×10^{-5}
V_d [m^3]	Volume of downstream reservoir	8300
$P10$ [kPa]	Pressure pulse at $x = 0$	570
$P20$ [kPa]	Initial pressure in the sample	100
b	Slip factor	100

Table 7.2: Reservoir parameter values used to find the numerical solutions of the model used by Liang et al. [104]

data given in Table 7.1. Figure 7.1 shows the hydraulic head in the upstream and the down stream reservoirs, $h_u(t)$ and $h_d(t)$, respectively, plotted against the time t. The hydraulic head is normalized by H. It is observed that pressure in the upstream reservoir decreases while the pressure in the downstream reservoir increases with the passage of time. The obtained results match with the results of Hsieh, see Figure 2 of Hsieh et al. [84]. Figure 7.2 shows the 3D plot of hydraulic head $h(x,t)$ inside the reservoir against the time t and the distance x. It is noted that the pressure attains to an equilibrium state after time $t = 0.8$ seconds.

7.2.2 Liang's Model

Liang et al. [104] estimated the permeability of tight rocks by using a nonlinear pressure advection-diffusion equation to model the transient pressure pulse decay test. Their model is,

$$\frac{\partial p}{\partial t} + U\frac{\partial p}{\partial x} = D\frac{\partial^2 p}{\partial x^2} \qquad \text{for } 0 < x < L, \quad t > 0. \tag{7.2.2}$$

The flux conditions at the boundaries are given by,

$$\left(\frac{\partial p}{\partial x}\right)_{x=0,t>0} - \frac{V_u}{DA\phi}\frac{dp_u}{dt} = 0 \tag{7.2.3}$$

$$\left(\frac{\partial p}{\partial x}\right)_{x=L,t>0} + \frac{V_d}{DA\phi}\frac{dp_d}{dt} = 0 \tag{7.2.4}$$

The initial condition is given by

$$p(x,0) = \begin{cases} p_1(0) = P10 & \text{if } x = 0 \\ p_2(0) = P20 & \text{if } 0 < x \leq L \end{cases} \tag{7.2.5}$$

and,

$$D = \frac{K}{\phi\mu(\zeta_f + \zeta_v)} \tag{7.2.6}$$

$$U = -D(\zeta_K + \zeta_f)\frac{\partial p}{\partial x} \tag{7.2.7}$$

where x is the distance along the sample, t is the time from the start of the experiment, A is the cross-sectional area of the sample, L is the length of the sample, ϕ is porosity, p_u is the pressure in the upstream reservoir, p_d is the pressure in the downstream reservoir, V_u is the volume of the upstream reservoir, V_d is the volume of the downstream reservoir, μ is the viscosity, ζ_f is isothermal compress-

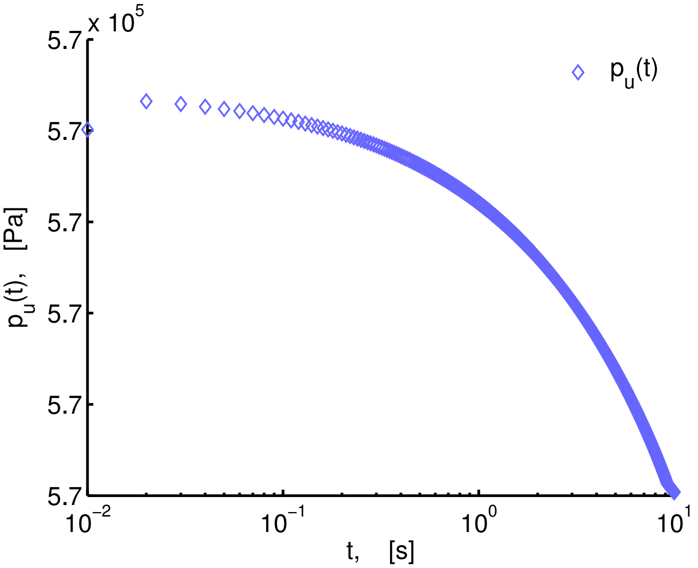

Figure 7.3: The pressure in the upstream reservoirs from Liang's model, using the new model solver. $p_u(t)$ is plotted against the time t. It shows that pressure in the upstream reservoir decays exponentially with respect to time, see Liang et al. [104].

ibility of fluid, ζ_v is the pore volume compressibility, D is function of pressure called diffusivity coefficient.

Liang's model Eq. (7.2.2) is a nonlinear advection-diffusion equation together with initial condition and flux conditions which are prescribed at the inlet and the outlet boundaries. Liang found the approximate solutions of Eq. (7.2.2) by perturbation methods. He then matched the approximate solutions with the laboratory measured pulse decay data to estimate the permeability of the test sample. Liang's calculations are valid when the volume and pressure of the interconnected pore fluid is much smaller than the volume and pressure of the upstream reservoir.

We have solved Liang's Model (7.2.2) using the new model solver by setting $D_a = D$ and $U_a = U$, from Eqs. (7.2.6). We use the data given in Table 7.2. Figure 7.3 shows the pressure in the upstream reservoir, $p_u(t)$, plotted against the time t. It is observed that the pressure in the upstream reservoir decreases with

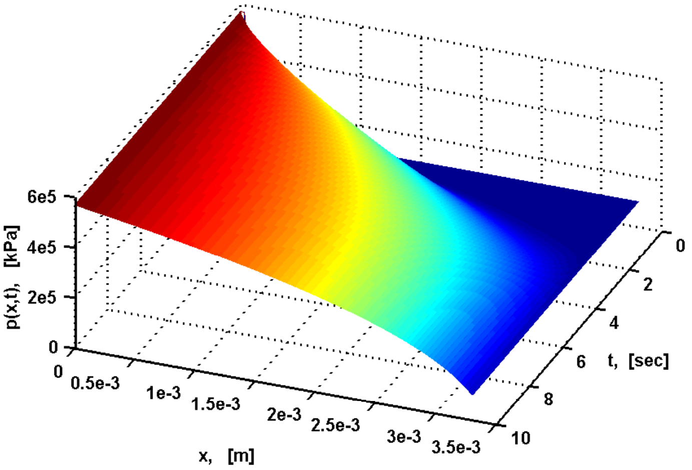

Figure 7.4: Numerical solutions from the Liang's Model using the new model solver, are plotted against time t and distance x. The pressure inside the reservoir rock sample increases with the passage of time.

the passage of time. Figure 7.4 shows the 3D plot of the pressure $p(x, t)$ inside the reservoir against the time t and the distance x. It is noted that the pressure decreases along the length of the sample with the passage of time.

7.2.3 Malkovsky's Model

Malkovsky et al. [112] modified the pressure pulse transient method to measure the permeability of rock samples. Their transport model for the pressure pulse transient method is,

$$\frac{\partial p}{\partial t} = D\frac{\partial^2 p}{\partial x^2} \qquad \text{for } 0 < x < L, \quad t > 0. \tag{7.2.8}$$

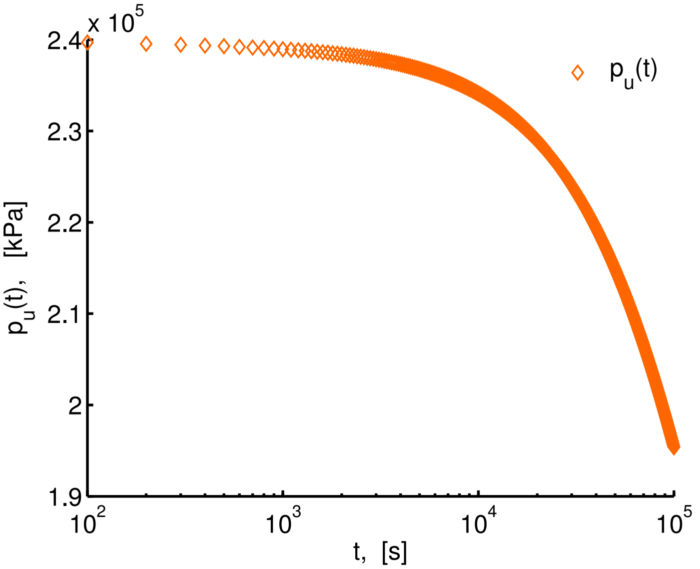

Figure 7.5: The pressure, $p_u(t)$, in the upstream reservoirs from Malkovsky's model using the new model solver, plotted against the time t. It shows that pressure in the upstream reservoir decays exponentially with time, matches Figure 6 of Malkovsky et al. [112].

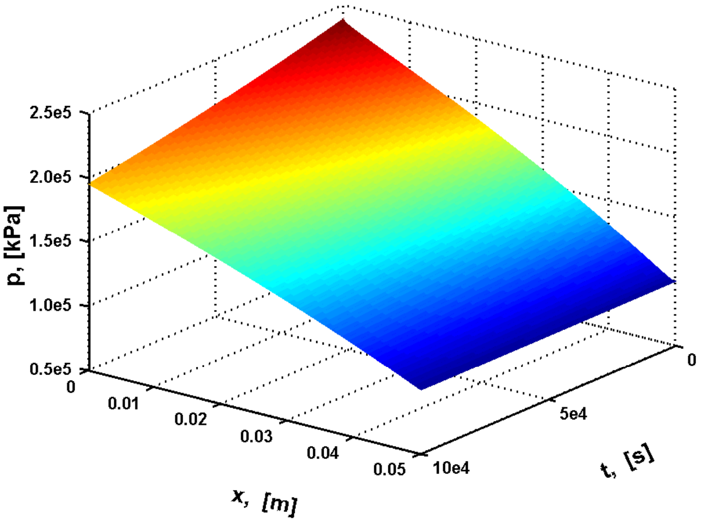

Figure 7.6: Numerical solutions from Malkovsky's Model using the new model solver, of $p(x,t)$ plotted against time t and distance x. Pressure inside the reservoir rock sample increases with the passage of time.

Simulation Data of Malkovsky et al. [112]		
Parameters	Description	Values
L [m]	Length of the sample	0.05
N_x	Number of intervals	101
ϕ	Porosity	0.13
μ [Pas]	Viscosity	1.789×10^{-5}
A [m^2]	Cross-sectional area of the sample	8.55×10^{-6}
K [m^2]	Permeability	1.71×10^{-18}
ζ_K [Pa^{-1}]	Compressibility coefficient of permeability	6×10^{-6}
V_u [m^3]	Volume of upstream reservoir	8.3×10^{-2}
V_d [m^3]	Volume of downstream reservoir	83
Pu [kPa]	Pressure in the upstream reservoir	240
Pd [kPa]	Pressure in the downstream reservoir	100
b	Slip factor	100

Table 7.3: Reservoir parameter values used to find the numerical solutions of the model used by Malkovsky et al. [112].

The flux conditions at the boundaries are given by,

$$\left(\frac{\partial p}{\partial x}\right)_{x=0,t>0} - \frac{\mu V_u \zeta_f}{AK}\frac{dp_u}{dt} = 0 \tag{7.2.9}$$

$$\left(\frac{\partial p}{\partial x}\right)_{x=L,t>0} + \frac{\mu V_d \zeta_f}{AK}\frac{dp_d}{dt} = 0 \tag{7.2.10}$$

The initial condition is given by,

$$p(x,0) = \begin{cases} p_0 & \text{if } 0 < x \leq L \\ p_0 + \Delta p & \text{if } x = 0 \end{cases} \tag{7.2.11}$$

and,

$$D = \frac{K}{\mu[\phi(\zeta_f - \zeta_s) + (\zeta_r - \zeta_s)}, \tag{7.2.12}$$

where, p is pressure, x is distance from entry end of sample, t is time from the start of the experiment, A is cross-sectional area of the sample, L is the length of the sample, ζ_f is compressibility of fluid, ζ_r is the integral rock compressibility, ζ_s is the compressibility of rock sample, μ is viscosity, V_u is volume of upstream reservoir, V_d is volume of downstream reservoir.

Malkovsky's model Eq.(7.2.8) is a nonlinear diffusion equation together with initial condition, and flux conditions which are prescribed at the inlet and the outlet boundaries. The model was derived for a single phase fluid in porous media under normal conditions and also under high pressure and temperature conditions. Malkovsky used the numerical solutions of the above model to determine the permeability of the layered rock sample to be in the range of 10^{-22} m^2 to 10^{-15} m^2.

We have solved Malkovsky's Model (7.2.8) using the new model solver and using the data given in Table 7.3 with $U_a = 0$, and $D_a = D$ from Eq. (7.2.12). Figure 7.5 shows the pressure in the upstream reservoir, $p_u(t)$, plotted against the time t. It is observed that the pressure in the upstream reservoir decreases with the passage of time. Figure 7.6 shows the 3D plot of the pressure $p(x,t)$ inside the reservoir against the time t and the distance x. It is noted that the pressure increases along the length of the sample with the passage of time.

7.2.4 Cui's Model

Cui et al. [44] considered the effects of gas adsorption and developed a relation Eq. (4.2.27) to use in the model for calculating the permeability and diffusivity

Simulation Data for Cui's Model			
Parameters	Description	Data-1	Data-2
L [m]	Length of the sample	0.0262	0.0262
D [m^2]	Diameter of the sample	0.0338	0.0338
N_x	Number of intervals	101	101
M_g	Molecular weight of gas	4	4
R_g	Universal gas constant	8314.4	8314.4
ρ_s	density of the sample	2650	2650
ϕ	Porosity	0.038	0.017
μ [Pas]	Viscosity	1.984×10^{-5}	1.984×10^{-5}
ζ_μ [Pa^{-1}]	Compressibility coefficient of viscosity	1.68×10^{-9}	1.68×10^{-9}
t_c [K]	Critical temperature	5.2	5.2
p_c [Pa]	Critical pressure	228 009.62	228 009.62
V_{std}	Volume of gas at standard conditions	22.414	22.414
T [K]	Temperature	294.15	294.15
V_u [m^3]	Volume of upstream reservoir	6.57×10^{-6}	6.57×10^{-6}
V_d [m^3]	Volume of downstream reservoir	1.83×10^{-6}	1.83×10^{-6}
V_p [m^3]	Volume of pores	2.1484×10^{-7}	2.1484×10^{-7}
$p_u(0)$ [Pa]	Pressure pulse	1 051 753.8	1 020 879.0
$p_d(0)$ [Pa]	Initial pressure	124 078	101 325
p_L [Pa]	Langmuir pressure	2×10^6	7.5×10^6
q_L [m^3/kg]	Langmuir volume	0.01	0.01
b	Slip factor	100 000	100 000
K [m^2]	Permeability	2×10^{-17}	1.71×10^{-20}
ζ_K [Pa^{-1}]	Compressibility coefficient of permeability	6×10^{-6}	6×10^{-6}

Table 7.4: Reservoir parameter values used to find the numerical solutions of the model used by Cui et al. [44]. The two sets of data are taken from Lorinczi et al. [107].

values of tight gas reservoirs. Cui's model is,

$$\frac{\partial p}{\partial t} = D\frac{\partial^2 p}{\partial x^2} \qquad \text{for } 0 < x < L, \quad t > 0. \tag{7.2.13}$$

The initial and boundary conditions are given by,

$$p(x,0) = \begin{cases} p_d(0) & \text{if } 0 < x \leq L \\ p_u(0) & \text{if } x = 0 \end{cases} \tag{7.2.14}$$

and,

$$p(0,t) = p_u(t), \qquad p(L,t) = p_d(t), \qquad \text{for } t \geq 0,$$

where,

$$D = \frac{K}{\mu[\phi\zeta_\rho + (1-\phi)\frac{q}{\rho}\zeta_q]}. \tag{7.2.15}$$

The flux conditions at the boundaries are given by,

$$\frac{\partial p}{\partial x} - \frac{\mu\zeta_\rho\phi L V_u}{\rho K V_p}\frac{dp_u}{dt} = 0, \qquad x = 0, t > 0 \tag{7.2.16}$$

$$\frac{\partial p}{\partial x} + \frac{\mu\zeta_\rho\phi L V_d}{\rho K V_p}\frac{dp_d}{dt} = 0, \qquad x = L, t > 0 \tag{7.2.17}$$

where t is time, ρ is gas density, q is adsorbate density, ϕ is porosity, p is pressure, k is permeability, μ is gas viscosity, x is distance.

Cui's model Eq. (7.2.13) incorporates the effects of gas adsorption in the tight porous rock, it describes the gas transport in the regions where the Darcy's law prevails. Cui used the late time experimental data for the measurement of rock properties of tight rocks instead of early time experimental data. Cui also mentioned in his work that the permeability determined from small sample size may not represent the true permeability of the entire rock matrix in fractured reservoir, and hence the permeability values need to be scaled as required. Moreover, he suggested that the experimental data and the numerical results for the estimation of the permeability and the diffusivity must be combined with field tests for a

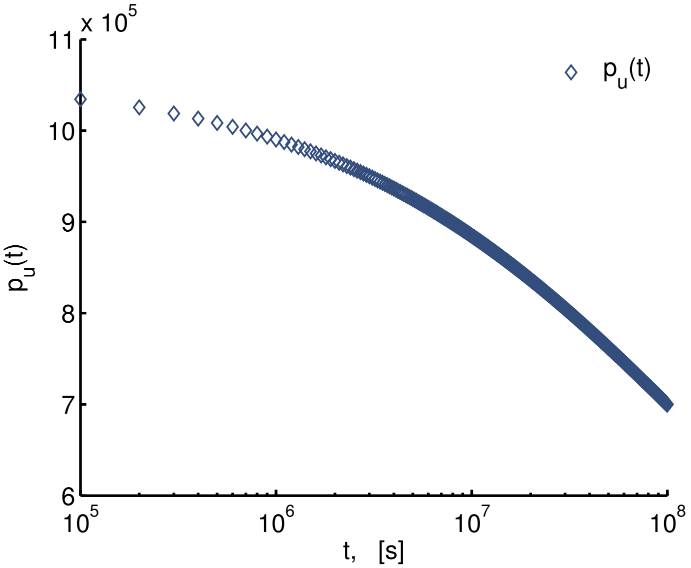

Figure 7.7: The pressure $p_u(t)$ in the upstream reservoirs from Cui's model using the new model solver, plotted against the time t. It shows that pressure in the upstream reservoir decays exponentially with respect to time.

complete description of the reservoir.

We have used the new model solver to solve Cui's Model (7.2.13) with the data given in Table 7.4 with $U_a = 0$ and $D_a = D$ from Eq. 7.2.15. Figure 7.7 shows the pressure in the upstream reservoir, $p_u(t)$, plotted against the time t. It is observed that the pressure in the upstream reservoir decreases with the passage of time. Figure 7.8 shows the 3D plot of the pressure $p(x, t)$ inside the reservoir against the time t and the distance x. It is noted that the pressure increases along the length of the sample with the passage of time.

7.2.5 Civan's Model

Civan et al. [41] derived an improved model for the determination of shale gas permeability and diffusivity. Their transport model was based on the idea of relevant gas retention (amount of gas adsorbed in the porous material) and the

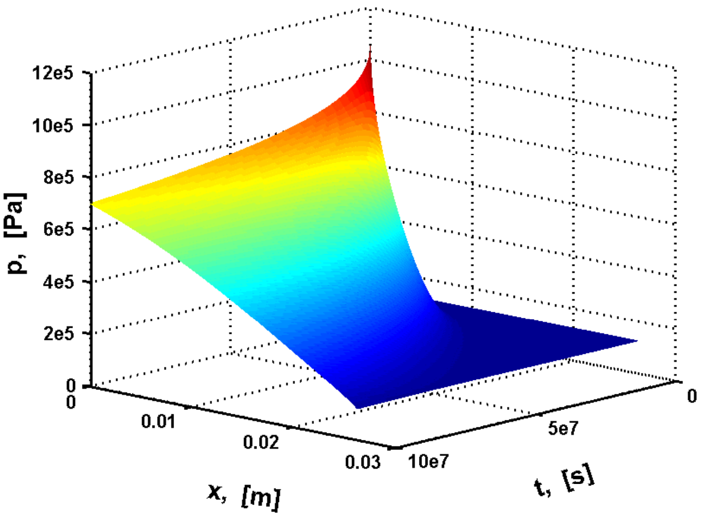

Figure 7.8: Numerical solutions of the Cui's Model using the new model solver plotted against time t and distance x. Pressure inside the reservoir rock sample increases with the passage of time.

amount of gas present in the void spaces. Civan's model is

$$\frac{\partial p}{\partial t} + U\frac{\partial p}{\partial x} = D\frac{\partial^2 p}{\partial x^2} \qquad \text{for } 0 < x < L, \quad t > 0. \tag{7.2.18}$$

where x, t, and p denote distance, time and pressure, respectively. The initial condition is given by,

$$p(x,0) = \begin{cases} p_u(0) & \text{if } x = 0 \\ p_0(x) & \text{if } 0 < x < L \\ p_d(0) & \text{if } x = L \end{cases} \tag{7.2.19}$$

and boundary conditions are given by,

$$p(0,t) = p_u(t), \qquad p(L,t) = p_d(t), \qquad \text{for } t \geq 0,$$

such that, $p(0,0) = p_u(0)$ and $p(L,0) = p_d(0)$. The diffusivity coefficient D and convective flux coefficient U have the following expressions,

$$D = \frac{K_a}{\mu\left[\phi(\zeta_\rho(p) + \zeta_\phi(p)) + \frac{q}{\rho}\left(\frac{1-\phi}{p_L+p} - \phi\zeta_\phi(p)\right)\right]} \tag{7.2.20}$$

$$U = -D[\zeta_\rho(p) + \zeta_K(p) + \zeta_f(p) - \zeta_\mu(p)]\frac{\partial p}{\partial x}. \tag{7.2.21}$$

The flux conditions at the boundaries are given by,

$$\frac{\partial p}{\partial x} - \frac{\mu\phi L\zeta_\rho V_u}{\rho K_a V_p}\frac{dp_u}{dt} = 0, \qquad x = 0, t > 0 \tag{7.2.22}$$

$$\frac{\partial p}{\partial x} + \frac{\mu\phi L\zeta_\rho V_d}{\rho K_a V_p}\frac{dp_d}{dt} = 0, \qquad x = L, t > 0 \tag{7.2.23}$$

where L is the length of the sample, ϕ is porosity, p_u is pressure in upstream reservoir, p_d is pressure in downstream reservoir, V_u is volume of upstream reservoir, V_d is volume of downstream reservoir, V_p is pore volume, μ is viscosity, ζ_ρ is isothermal compressibility of gas density, K_a is apparent permeability, D is function of pressure and it is called diffusivity coefficient, and U is function of p and p_x and it is called convective flux.

Civan's model is the limiting case of the new transport model (3.4.3), with

1. $U_a = U$, from Eq. (7.2.20)

2. $D_a = D$, from Eq. (7.2.20)

3. Forchheimer term is ignored, that is the turbulence factor is zero, $\beta = 0$.

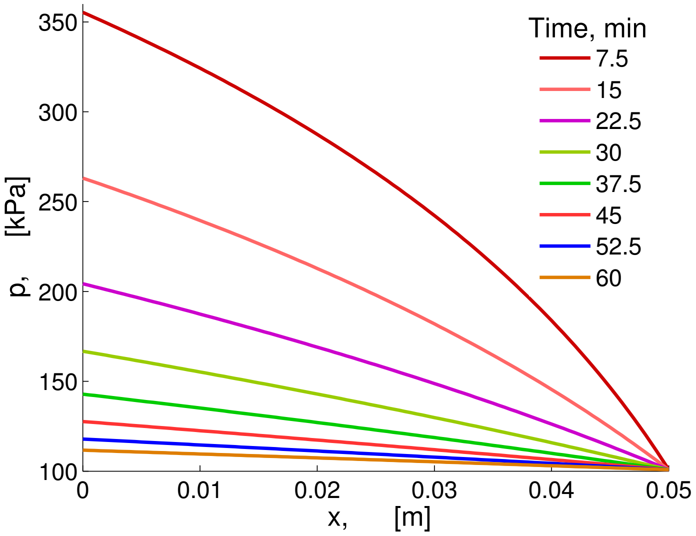

Figure 7.9: The pressure, $p(x,t)$, in the reservoirs sample obtained from Civan's model using the new model solver, plotted against x at various t. The results reproduces Figure 3 of Civan et al. [41] and matches exactly.

4. In application, parameters were made constants.

Civan's model Eq. (7.2.18) encompasses all the flow regimes by the use of Knudsen number. Civan obtained the numerical solutions of the model and matched the results with the experimental data to obtain estimates for the permeability, see Chapter 6. In Civan's model, various gas and reservoir properties are taken as pressure dependent, but in actual calculations he took them to be constant for many of these parameters, see Chapter 4 where this is discussed.

We have used the new model solver to obtain the solution from Civan's Model (7.2.18), where the data is given in Table 7.5. Figure 7.9 exactly matches with the Figure 3 of Civan et al. [41]. Figure 7.10 shows the pressure in the upstream reservoir, $p_u(t)$, plotted against the time t. It is observed that the pressure in the upstream reservoir decreases with the passage of time. Figure 7.11 shows the 3D

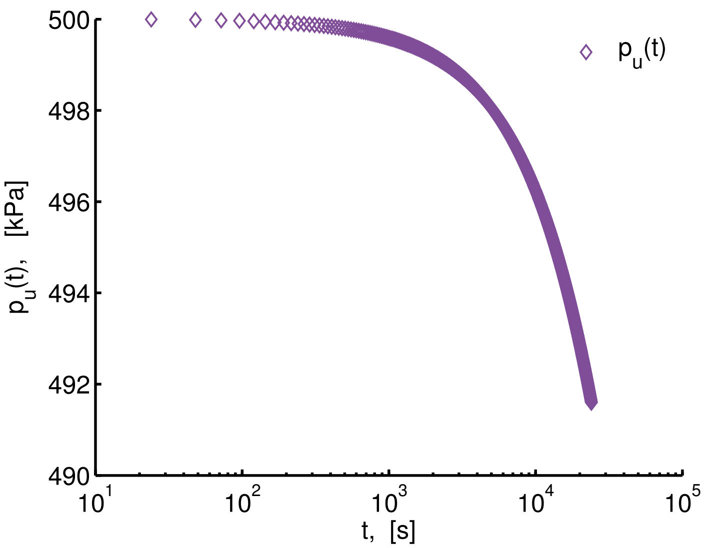

Figure 7.10: The pressure, $p_u(t)$, in the upstream reservoirs obtained from Civan's model using new model solver, plotted against the time t. It shows that pressure in the upstream reservoir decays exponentially with respect to time.

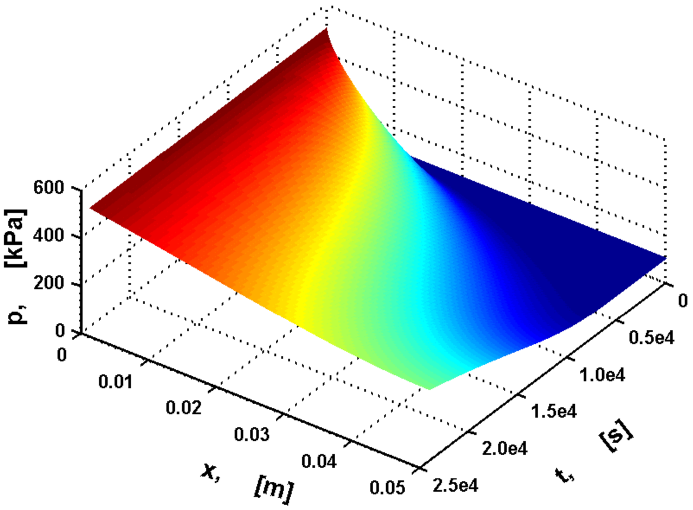

Figure 7.11: Numerical solutions from Civan's Model using new model solver, are plotted against time t and distance x. Pressure inside the reservoir rock sample increases with the increase in time t.

plot of the pressure $p(x,t)$ inside the reservoir against the time t and the distance x. It is noted that the pressure increases along the length of the sample with the passage of time.

7.2.6 Summary

The results in this section show that new transient transport model reproduces the results of the previous gas transport models, under different limiting cases .

7.3 Simulations using the New Gas Transport Model

In this section, we use the new nonlinear transient-state transport model (7.3.1) for simulating the transient pressure pulse test system.

For the sake of reference, we rewrite the transient-state transport model here,

$$\frac{\partial p}{\partial t} + U_a(p,p_x)\frac{\partial p}{\partial x} = D_a(p)\frac{\partial^2 p}{\partial x^2} \qquad \text{for } 0 \le x \le L, \quad t > 0. \tag{7.3.1}$$

where x, t, and p denote distance, time and pressure, respectively, and U_a and D_a are coefficients of advection and diffusion terms and are given by,

$$D_a(p) = \frac{FK_a}{\mu}\left(\phi\zeta_1(p) + (1-\phi)\frac{q}{\rho}\zeta_2(p)\right) \tag{7.3.2}$$

$$U_a(p,p_x) = -\zeta_3(p)D_a(p)\frac{\partial p}{\partial x}, \tag{7.3.3}$$

where, ζ_1, ζ_2, and ζ_3 are defined in Chapter 3 and Chapter 4.

The initial condition is given by,

$$p(x,0) = p_0(x), \tag{7.3.4}$$

and boundary conditions are given by

$$p(0,t) = p_u(t), \qquad p(L,t) = p_d(t), \qquad \text{for } t \geq 0. \tag{7.3.5}$$

The flux conditions at the boundaries are given by,

$$\text{Inlet} \quad \frac{\partial p}{\partial x} - \frac{\mu\phi L\zeta_\rho(p)V_u}{FK_aV_p}\frac{dp_u}{dt} = 0, \qquad x = 0, t > 0 \tag{7.3.6}$$

$$\text{Outlet} \quad \frac{\partial p}{\partial x} + \frac{\mu\phi L\zeta_\rho(p)V_d}{FK_aV_p}\frac{dp_d}{dt} = 0, \qquad x = L, t > 0 \tag{7.3.7}$$

where L is the length of the sample, ϕ is porosity, μ is viscosity, V_u is volume of upstream reservoir, V_d is volume of downstream reservoir, V_p is pore volume, p_u is pressure in upstream reservoir, p_d is pressure in downstream reservoir, ζ_ρ is isothermal compressibility of gas density, K_a is apparent permeability, F is the control factor. D_a is function of pressure and it is called diffusivity coefficient, and U_a is function of p and p_x and it is called convective flux.

Here, we solve the new transient-state transport model (7.3.1) to describe pressure distribution in rock core sample of length $L = 0.003$ m to simulate pressure-pulse decay test. We obtain pressure distribution from equation (7.3.1)

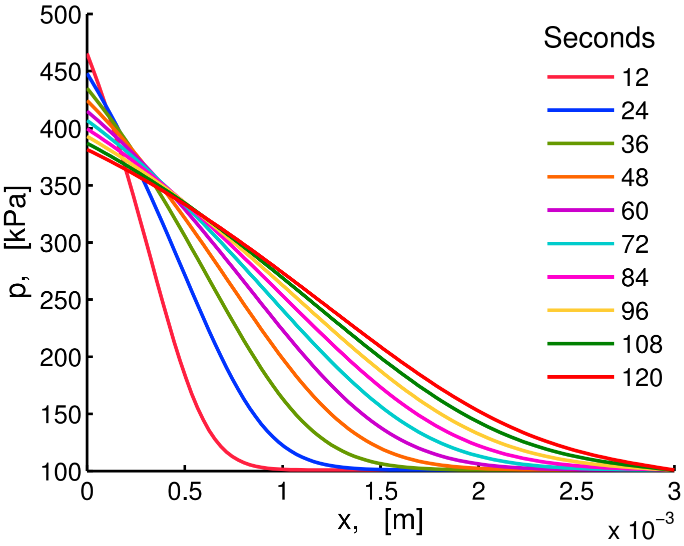

Figure 7.12: Numerical solutions from the new nonlinear transport model (7.3.1) are obtained using the new model solver and plotted against distance x at short times (in seconds). We observe that the pressure inside the rock sample increases above initial pressure with the passage of time. Although the pressure at the upstream boundary decreases but it increases inside the reservoir.

under full pressure-dependent parameters and with full nonlinear compressibility coefficients, and all the flow regimes discussed in Chapters 2-4.

We have carried out the numerical simulations with the data given in Table **??**. A pressure pulse is induced in the upstream reservoir, say, at $t = 0$, which is attached to a core plug containing a rock sample. Figures 7.12 - 7.17 show the results obtained from the numerical simulations.

Figure 7.12 shows the numerical solutions of the new nonlinear transport model (7.3.1) where the pressure is plotted against distance at various times (in seconds). The pressure inside the rock sample smoothens out and become uniform with the passage of time.

Figure 7.13 shows the numerical solutions of the new nonlinear transport model (7.3.1) where the pressure is plotted against distance at various times (in minutes).

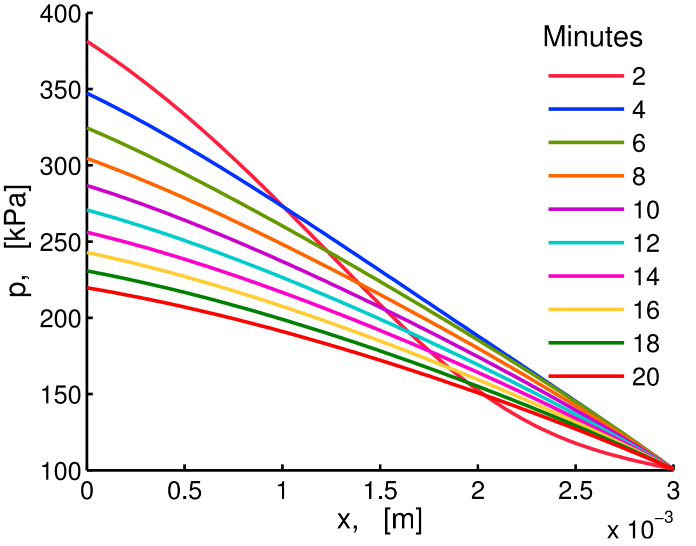

Figure 7.13: Numerical solutions from the new nonlinear transport model (7.3.1) are obtained using the new model solver, and plotted against distance x at long times (in minutes). At longer times, say after 4 minutes, the pressure inside the rock sample decreases at amounts which is proportional to time interval. Whereas, the pressure at the right boundary is fixed.

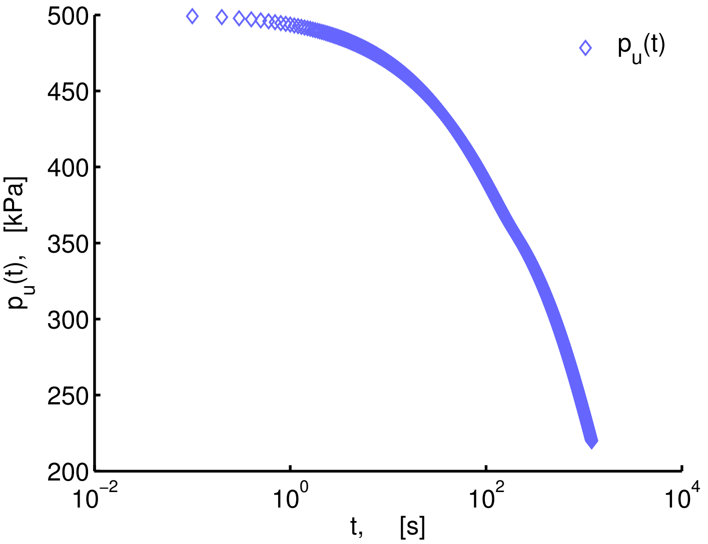

Figure 7.14: Pressure, $p_u(t)$, in the upstream reservoir is obtained from the new transport model using the new model solver and is plotted against time t. It shows an exponential decay of pressure with time.

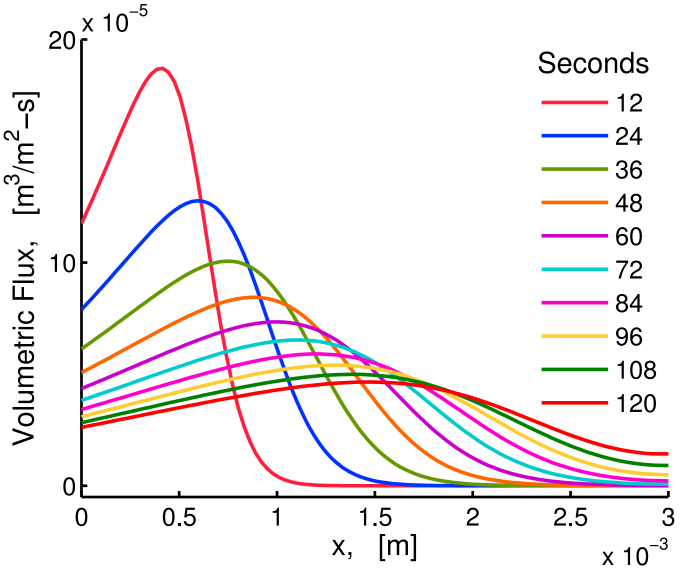

Figure 7.15: Volumetric flux u obtained from the new nonlinear model (7.3.1) is plotted against distance x at short times (in seconds). We note that the volumetric flux greatly depends on the pressure gradient, it is very large for shorter times, say for $t < 2$ minutes, but then it decreases as the pressure gradient decreases.

At longer times, say after 4 minutes, the pressure inside the rock sample decreases at amounts which are proportional to length of time interval. Whereas, the pressure at the right boundary is fixed.

Figure 7.14 shows the pressure in upstream reservoir, that is, $p_u(t)$ is plotted against time t. It shows an exponential decay of pressure with respect to time.

Figure 7.15 shows the volumetric flux u obtained from the new nonlinear model (7.3.1) where u is plotted against distance x at different times (in seconds). We note that the volumetric flux greatly depends on the pressure gradient, it is very large for shorter times, say for $t < 2$ minutes, but then it decreases as the pressure gradient decreases.

Figure 7.16 shows the plots of volumetric flux u against distance x. Here, we have shown the long time behaviour of u. We note that the magnitude of flux

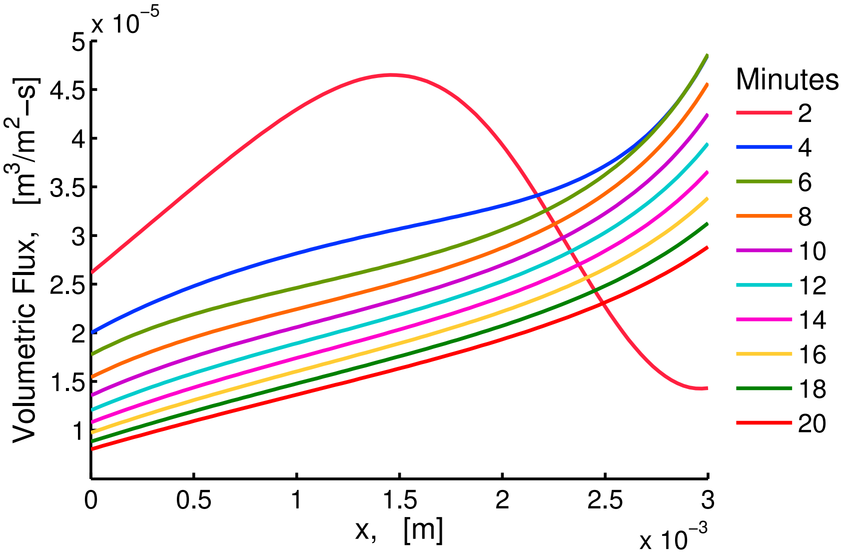

Figure 7.16: Plots of volumetric flux u against distance x. Here, we have shown the long time behaviour of u. We note that the magnitude of flux decreases with time but it decrease with the similar pattern. Moreover, flux at the right boundary is greater than the flux at the inlet boundary.

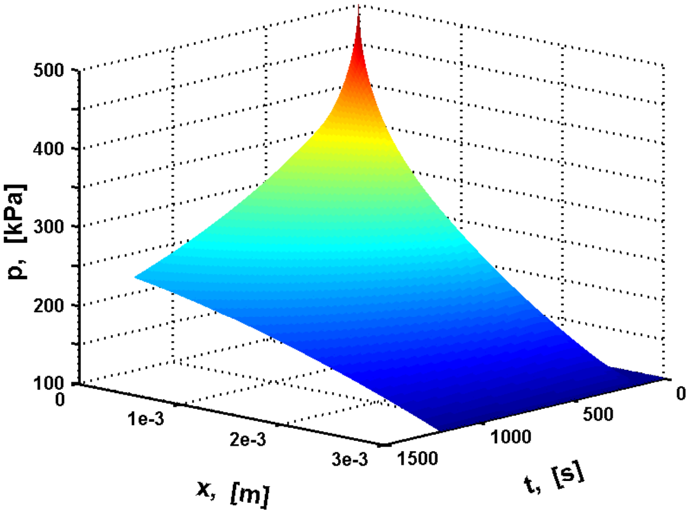

Figure 7.17: 3D plot of new transport model is shown. Pressure is plotted against distance and time.

decreases with the passage of time with the similar trend.

Figure 7.17 shows the 3D plot of new transport model. Pressure is plotted against distance and time.

7.4 Summary

In this chapter, we have demonstrated the effectiveness of new transient-state model for analyzing transient pressure-pulse test system. We have reproduced the results of previous models in Section 7.2. In section 7.3, a case for describing the pressure distribution inside a rock core sample at pore scale is studied. The pressure profiles are calculated for a long period of time.

Simulation Data for Civan et al. [41]			
Parameters	Description	Civan et al. [41]	Civan et al. [41]
L [m]	Length of the sample	0.05	0.040 57
R [m^2]	Radius of the sample	0.025	0.012 334
N_x	Number of intervals	101	101
M_g	Molecular weight of gas	16	28.01
R_g	Universal gas constant	8314.4	8314.4
ρ_s	Density of the sample	2506	2650
ϕ	Porosity	0.05	0.0575
ζ_ϕ [Pa^{-1}]	Compressibility coefficient of porosity	4×10^{-6}	9.8692×10^{-12}
ρ_g	Density of gas	0.656	0.6768
ζ_ρ [Pa^{-1}]	Compressibility coefficient of gas density	1×10^{-6}	1×10^{-6}
f	Permeability correction factor	2	2
ζ_f [Pa^{-1}]	Compressibility coefficient of f	5×10^{-3}	5×10^{-3}
μ [Pas]	Viscosity of gas	1.8×10^{-5}	1.8×10^{-5}
ζ_μ [Pa^{-1}]	Compressibility coefficient of μ	3×10^{-11}	8.388×10^{-9}
t_c [K]	Critical temperature	5.2	126.2
p_c [kPa]	Critical pressure	228.09	3 394 387.5
V_{std}	Volume at standard conditions	22.414	22.414
T [K]	Temperature	298.15	303.85
V_u [m^3]	Volume of upstream reservoir	2.1×10^{-5}	8.835×10^{-6}
V_d [m^3]	Volume of downstream reservoir	1.83×10^{-6}	1.1148×10^{-5}
V_p [m^3]	Volume of pore	4.91×10^{-6}	2.1484×10^{-7}
$P_u(0)$ [kPa]	Pressure pulse	500	3546
$P_d(0)$ [kPa]	Initial pressure	100.8	101.325
p_L [Pa]	Langmuir pressure	7.5×10^6	0
q_L [m^3/kg]	Langmuir volume	0.01	0
b	Slip factor	-1	-1
σ_0	Rarefaction coefficient	1.358	1.358
A_σ	Rarefaction coefficient	0.1780	0.178
B_σ	Rarefaction coefficient	0.4348	0.4348
K [m^2]	Permeability	5.3×10^{-18}	1.97×10^{-19}
ζ_K [Pa^{-1}]	Compressibility coefficient of K	1×10^{-6}	3.947×10^{-11}

Table 7.5: Reservoir parameter values used to find the numerical solutions of the model used by Civan et al. [41]

New Nonlinear Transport Model - Pore Scale		
Parameters	Description	Values
L (m)	Length of the sample	0.003
N_x	Number of intervals	101
R_g ($\mathrm{J\,kmol^{-1}\,K^{-1}}$)	Universal gas constant	8314.4
M_g ($\mathrm{kg\,kmol^{-1}\,K^{-1}}$)	Molecular weight of gas	28.013
T (K)	Temperature	314
p_c (kPa)	Critical pressure	3396
t_c (K)	Critical temperature	126.19
b_{SF}	Slip factor	-1
σ_0	Parameter in rarefaction correlation	1.3580
A_σ	Parameter in rarefaction correlation	0.1780
B_σ	Parameter in rarefaction correlation	0.4348
a_τ	Parameter in tortuosity correlation	1.5
a_ϕ	Parameter in porosity correlation	0.10
b_ϕ	Parameter in porosity correlation	-0.939×10^{-1}
c_ϕ	Parameter in porosity correlation	0.39
α_{KC}	Parameter in permeability correlation	1
β_{KC}	Parameter in permeability correlation	0.9
Γ_{KC}	Parameter in permeability correlation	0.19×10^{-9}
a_β	Parameter in turbulence factor correlation	3.1×10^{1}
b_β	Parameter in turbulence factor correlation	0.5
c_β	Parameter in turbulence factor correlation	1.35
d_β	Parameter in turbulence factor correlation	0.4
p_u	Pressure in upstream reservoir	500
p_d	Pressure in downstream reservoir	100.8
V_u	Volume of upstream reservoir	2.1×10^{-5}
V_d	Volume of downstream reservoir	1.83×10^{7}
V_p	Volume of pore	4.91×10^{-7}
p_L	Langmuir pressure	7.5×10^{6}
q_L	Langmuir volume	0.01
ρ_s	Density of sample	2506
V_{std}	Volume at standard conditions	22.414
tol	Tolerance	1×10^{-6}

Table 7.6: Reservoir parameters used in new nonlinear transport model. A data set is obtained which will be used for finding solutions.

CHAPTER 8

FRACTIONAL TRANSPORT MODELS

8.1 Introduction

Many transport and fluid flow phenomenon can be modeled by partial differential equations (PDE), such as systems of the time evolution of chemical or biological species in a fluid. These PDE's are of the advection-diffusion-reaction type. They are obtained from consideration of mass balance, momentum balance, and energy balance equations, and in the case of multi-component species, also individual species mass balance equations, Hundsdorfer and Verwer [89] and Bird et al. [21].

However, many complex natural processes, such as, diffusion through porous media, Chen et al. [33], crowded systems, and protein diffusion within cells, Weiss et al. [168], cannot be satisfactorily described by conventional PDE's. Fractional calculus methods have been proposed for describing such complex phenomena, see

Oldham and Spanier [128], Miller and Ross [119], Ali et al. [9], Podlubny [133], Ali and Malik [6], Ali et al. [8], and Diethelm [49]. For instance, in order to obtain a better understanding of anomalous diffusion Caputo [28] used the modified form of the Darcy's law to propose a fractional diffusion equation, which incorporates a memory formalism,

$$q = -\eta\rho_0 \frac{\partial^\alpha}{\partial t^\alpha}\left[\frac{\partial p}{\partial x}\right], \tag{8.1.1}$$

where q is the flux, and $\partial^\alpha/\partial t^\alpha$ represents the Caputo derivative define in equation (8.2.5). He obtained the following equation for fluid flow in a porous medium

$$\frac{\partial c}{\partial t} = A\frac{\partial^\alpha}{\partial t^\alpha}\left[\frac{\partial^2 p}{\partial x^2}\right], \tag{8.1.2}$$

where A is the pseudo-diffusivity defined in Caputo [28].

A question of importance here is how do we interpret fractional conservation laws such as mass balance. The conventional balance are obtained assuming Taylor expansion to represent flux change in a control volume V; the volume is then shrunk to zero and assuming that the changes in property being conserved are small, this yields the classical balance equations.

A fractional approach is not as straight forward because the control volume is not allowed to vanish, although it is small. In other words, there is some heterogeneity of the property being considered inside the control volume and a simple linear Taylor-expansion to first order is not sufficient. However, it has been shown that a fractional Taylor series can represent the nonlinear flux with only two terms, see Wheatcraft and Meerschaert [170]. As long as the flux can be represented by a power-law functions, then the fractional order conservation of mass will be exact when the fractional order α matches the power-law a, that is, when $\alpha = a$. Thus there is an optimal fractional power α at a given scale that conserves mass. Similar considerations apply to momentum and energy balance. Thus an important task is to determine the optimal fractional order α in a given system. This is outside the scope of the present work, but will be considered in the future.

Different approaches have been adopted to explain the anomalous diffusion, the most important is as a continuous time random walk process (CTRW), Havlin and Ben-Avraham [78]. Conventional (Brownian) CTRW is characterised by waiting times and jumps in particle location whose probability density function (pdf) is Gaussian and the pdf obeys the classical advection-diffusion equation. Anomalous diffusion possesses pdf's of waiting times and jumps which are non-Gaussian inverse power laws. Such a process are described by fractional advection-diffusion equations.

In a conventional diffusion process the mean square displacement, (MSD), $< x(t)^2 >$ of a particle scales linearly with the time $< x(t)^2 >\sim t$; but in anomalous diffusion the MSD scales nonlinearly with the time t, that is, $< x(t)^2 >\sim t^{\alpha}$. For $0 < \alpha < 1$, diffusion is called subdiffusion, and for $1 < \alpha < 2$, the diffusion is called superdiffusion. For $\alpha = 1$, we have the standard diffusion. Geometrically, the mean square displacement can be understood as the amount of space the particle has explored in the system, see Metzler and Klafter [117].

Metzler and Klafter [117] have obtained the following fractional advection-diffusion equation,

$$\frac{\partial}{\partial t}p(x,t) = {}_0\mathcal{D}_t^{1-\alpha}\left[K_\alpha \frac{\partial^2 p(x,t)}{\partial x^2} - A_\alpha \frac{\partial}{\partial x}\left\{u(x)p(x,t)\right\}\right]. \tag{8.1.3}$$

where $p(x,t)$ is called the propagator which is the probability density function of locating a particle at the position x at the time t, ${}_0\mathcal{D}_t^{1-\alpha}$ is the Riemann-Liouville fractional derivative of order $0 < \alpha < 1$ defined in Eq. (8.2.3), K_α and A_α are called the generalized diffusion constants. Das [48] and Saha Ray and Bera [146] have considered a special case of equation (8.1.3) under the assumsptions when $K_\alpha = 1$, $A_\alpha = 1$, and $\alpha = 1/2$.

There are alternatives to the Riemann-Liouville fractional derivative in equation (8.1.3). For instance, equation (8.1.3) can be transformed to a time-fractional diffusion equation where the fractional derivative is in the Caputo's form (8.2.5). The relationship between the Riemann-Liouville and Caputo derivative is given in equation (8.2.6).

In this study we replace the Riemann-Liouville fractional derivative in equation (8.1.3) with an other variant called the Hilfer fractional derivative; ${}_0\mathcal{D}_t^{1-\alpha}$ is replaced by the Hilfer fractional derivative $\mathcal{D}_t^{\alpha,\beta}$, (defined later in Eq. (8.2.7)). Hilfer fractional derivative $\mathcal{D}_t^{\alpha,\beta}$ is essentially an interpolation between the Riemann-Liouville fractional derivative and Caputo fractional derivative, Hilfer [82, 83].

A simplification is made in the current study, that is $K_\alpha = A_\alpha = \kappa =$ constant, which yields the linear Hilfer fractional advection-diffusion equation,

$$\frac{\partial c(x,t)}{\partial t} = \kappa \mathcal{D}_t^{\alpha,\beta} \left[\frac{\partial^2 c(x,t)}{\partial x^2} - \frac{\partial}{\partial x} \left\{ u(x) c(x,t) \right\} \right], \quad x > 0, t > 0, \tag{8.1.4}$$

where $c(x,t)$ is a scalar function that can stand for pressure, or concentration, or any other scalar physical quantity.

Equation (8.1.4) is the Hilfer advection-diffusion equation of order α and type β, $p(x,t)$ is called the propagator and it represents the probability density function of locating a particle at the position x at the time t; $\kappa > 0$ represents diffusivity; $u(x)$ represents the velocity field. Sandev et al. [148] considers a diffusion-reaction equation that involves Hilfer fractional derivative but without the advection term.

The aim is to find solutions of equation (8.1.4) for specific cases of the convection velocity $u(x)$, and to carry out numerical analysis of the solution. Exact solutions are found in power series form by using the Variation Iteration Method (VIM) which is described in Section (8.3).

Power series solution are obtained, for $u(x) = -x$ and initial condition $p(x,0) = f(x)$. The convergence of the truncated series solution is also discussed. Finally, we analyze the behavior of the fractional solution with respect to the parameters α, κ.

8.2 Preliminaries

In this section, we state some definitions and results from fractional calculus, see Kilbas et al. [96], Furati [69], and Garra et al. [72].

Riemann-Liouville Fractional Integral. Let $f \in L^1_{loc}[a,b]$, where $-\infty \leq a < t < b \leq \infty$, be a locally integrable real-valued function. The Riemann-Liouville integral is defined by,

$$\left({}_0I_t^{\alpha} f\right)(t) = \frac{1}{\Gamma(\alpha)} \int_0^t \frac{f(\tau)}{(t-\tau)^{1-\alpha}} d\tau, \quad t > 0, \alpha > 0. \tag{8.2.1}$$

Note that $\left({}_0I_t^{\alpha} f\right)(t) = (f * K_\alpha)(t)$, where $K_\alpha(t) = t^{\alpha-1}/\Gamma(\alpha)$.

Riemann-Liouville Fractional Derivative.

Let $f \in L^1[a,b]$, where $-\infty \leq a < t < b \leq \infty$, and $f * K_{1-\alpha} \in W^{1,1}[a,b]$, $\alpha > 0$ where $W^{1,1}[a,b]$ is the Sobolev space defined as

$$W^{1,1}[a,b] = \left\{ f \in L^1[a,b] : \frac{d}{dt} f \in L^1[a,b] \right\}. \tag{8.2.2}$$

The Riemann-Liouville derivative of order $\alpha > 0$ is defined as

$$\left({}_0D_t^{\alpha} f\right)(t) = \frac{1}{\Gamma(1-\alpha)} \frac{d}{dt} \int_0^t \frac{f(\tau)}{(t-\tau)^{\alpha}} d\tau, \qquad t > 0, \quad 0 < \alpha < 1 \tag{8.2.3}$$

For $n \in \mathbb{N}$, we denote by $AC^n[a,b]$ the space of real-valued functions $f(t)$ which have continuous derivatives up to order $n-1$ on $[a,b]$ such that $f^{n-1}(t)$ belongs to the space of absolutely continuous functions $AC[a,b]$:

$$AC^n[a,b] = \left\{ f : [a,b] \to \mathbb{R} : \frac{d^{n-1}}{dt^{n-1}} f(x) \in AC[a,b] \right\}. \tag{8.2.4}$$

Caputo Fractional Derivative.

Let $\alpha > 0$, $m = 1$, and $f \in AC^1[a,b]$. The Caputo derivative of order $\alpha > 0$ is defined by

$$\left({}_0^*D_t^\alpha f\right)(t) = \frac{1}{\Gamma(1-\alpha)} \int_0^t \frac{f^{'}(\tau)}{(t-\tau)^\alpha} d\tau, \qquad t > 0, \quad 0 < \alpha < 1 \tag{8.2.5}$$

Relationship between Riemann-Liouville and Caputo Fractional Derivative

In the space of the functions belonging to $AC^1[a,b]$ the following relation between Riemann-Liouville and Caputo derivatives holds. For $f \in AC^1[a,b]$, and $0\alpha < 1$, the Riemann-Liouville derivative of order α of f exists almost everywhere and it can be written as

$$\begin{aligned} \left({}_0^*D_t^\alpha f\right)(t) &= {}_0D_t^\alpha f(t) - f(0^+)\frac{t^{-\alpha}}{\Gamma(1-\alpha)} \\ &= {}_0D_t^\alpha \left[f(t) - f(0^+) \right]. \end{aligned} \tag{8.2.6}$$

Hilfer Fractional Derivative Let $f \in L^1[a,b]$, where $-\infty \le a < t < b \le \infty$, and $f * K_{(1-\alpha)(1-\beta)} \in AC^1[a,b]$. The Hilfer derivative is defined as

$$\left({}_0D_t^{\alpha,\beta} f\right)(t) = \left({}_0I_t^{\beta(1-\alpha)} \frac{d}{dt}\, {}_0I_t^{(1-\beta)(1-\alpha)} f\right)(t), \qquad t > 0, \quad 0 < \alpha < 1, 0 \le \beta \le 1. \tag{8.2.7}$$

Lemma 8.1 *Srivastava and Tomovski [153] The following fractional derivative formula holds true:*

$${}_0D_t^{\alpha,\beta}\left(t^{\gamma}\right) = \frac{\Gamma(1+\gamma)}{\Gamma(1+\gamma-\alpha)}\left(t^{\gamma-\alpha}\right), \qquad t > 0, \quad \gamma > -1, \tag{8.2.8}$$

where $0 < \alpha < 1$ *and* $0 \le \beta \le 1$.

From lemma 8.1, we obtain the following lemma,

Lemma 8.2 *On integrating equation* (8.2.8), *we obtain*

$$\int_0^t {}_0D_t^{\alpha,\beta}\left(t^{\gamma}\right) dt = \frac{\Gamma(1+\gamma)}{\Gamma(1-\alpha+\gamma+1)}\left(t^{1-\alpha+\gamma}\right), \qquad t > 0, \quad \gamma > \alpha - 1, \tag{8.2.9}$$

where $0 < \alpha < 1$ *and* $0 \le \beta \le 1$.

Remarks:

1. The Hilfer fractional derivative interpolates between Riemann-Liouville fractional derivative and Caputo fractional derivative. $\beta = 0$ corresponds to Riemann-Liouville fractional derivative; $\beta = 1$ corresponds to Caputo fractional derivative.

2. The Caputo derivative represents a regularization in the time domain (origin) for Riemann-Liouville derivative.

3. $f(0^+)$ must be finite in equation (8.2.6), see Furati et al. [70].

4. The three derivatives are equal if f is continuous on $[0,T]$ and $f(0^+) = 0$, see Lemma 3.1 of Furati et al. [71].

Mittag-Leffler Function

The Mittag-Leffler functions are the generalization of the exponential function $e^z = \sum_{k=0}^{\infty} \frac{z^k}{k!}$.

1-parameter Mittag-Leffler Function

$$E_\alpha(z) = \sum_{k=0}^{\infty} \frac{z^k}{\Gamma(\alpha k + 1)}, \quad \alpha > 0. \tag{8.2.10}$$

2-parameter Mittag-Leffler Function

$$E_{\alpha,\beta}(z) = \sum_{k=0}^{\infty} \frac{z^k}{\Gamma(\alpha k + \beta)}, \quad \alpha > 0, \beta > 0. \tag{8.2.11}$$

8.3 Variational Iteration Method

In this section, we describe the variational iteration method (VIM) and provide an outline for its implementation. Ji-Huan He, He [79, 80], proposed VIM to obtain the solutions of nonlinear differential equations. The method provides the solution in the form of a successive approximations that may converge to the exact solution if such a solution exist. In case where a closed form of the exact solution is not achievable, we use the truncated series, for instance, the nth partial sum of the series. In recent years, the VIM has been used extensively by several authors to obtain the series solutions of problems arising in different areas of applied mathematics and engineering Hetmaniok et al. [81], Zhou and Yao [180], Elsaid [54], Ali et al. [7], Malik et al. [111].

The basic concepts and main steps for the implementation of VIM are explained here. Consider the following equation:

$$\frac{\partial c(x,t)}{\partial t} = \kappa \, {}_0\mathcal{D}_t^{\alpha,\beta} \left[\frac{\partial^2 c(x,t)}{\partial x^2} - \frac{\partial}{\partial x} \left\{ u(x) c(x,t) \right\} \right], \quad x > 0, t > 0, \tag{8.3.1}$$

with initial condition $c(x,0) = f(x)$.

The variational iteration method presents acorrectional functional in t-direction for Eq. (8.3.1) in the form,

$$c_{n+1}(x,t) = c_n(x,t) + \int_0^t \lambda(\xi) \left(\frac{\partial c_n(x,\xi)}{\partial \xi} - \kappa \, {}_0\mathcal{D}_\xi^{\alpha,\beta} \left[\frac{\partial^2 \widetilde{c}_n(x,\xi)}{\partial x^2} - \frac{\partial}{\partial x} \left\{ u(x) \widetilde{c}_n(x,\xi) \right\} \right] \right) d\xi, \tag{8.3.2}$$

with c_n assumed known, and $\lambda(\xi)$ is a general Lagrange multiplier which can be identified optimally by variational theory and $\tilde{c}_n$ is a restricted value that means it behaves like a constant, hence $\delta \widetilde{c}_n = 0$, where δ is the variational derivative.

VIM is implemented in two basic steps, see Wazwaz [167];

1. the determination of the Lagrange multiplier $\lambda(\xi)$ that will be identified

optimally through variational theory,

2. with $\lambda(\xi)$ determined, we substitute the result into Eq. (8.3.2) where the restriction should be omitted.

Taking the $\delta-$variation of equation (8.3.2) with respect to c_n, we obtain

$$\delta c_{n+1}(x,t) = \delta c_n(x,t)+\delta \int_0^t \lambda(\xi) \left(\frac{\partial c_n(x,\xi)}{\partial \xi} - \kappa \ {}_0\mathcal{D}_{\xi}^{\alpha,\beta} \left[\frac{\partial^2 \widetilde{c}_n(x,\xi)}{\partial x^2} - \frac{\partial}{\partial x} \left\{ u(x)\widetilde{c}_n(x,\xi) \right\} \right] \right) d\xi. \tag{8.3.3}$$

Since $\delta\widetilde{c_n} = 0$, we have

$$\delta c_{n+1}(x,t) = \delta c_n(x,t) + \delta \int_0^t \lambda(\xi) \left(\frac{\partial c_n(x,\xi)}{\partial \xi} \right) d\xi. \tag{8.3.4}$$

To determine the Lagrange multiplier $\lambda(\xi)$, we integrate by parts the integral in equation (8.3.4), and noting that variational derivative of a constant is zero, that is, $\delta k = 0$. Hence Eq. (8.3.4) yields

$$\begin{aligned} \delta c_{n+1}(x,t) &= \delta c_n(x,t) + \delta c_n(x,\xi)\lambda(\xi)|_{\xi=t} - \int_0^t \frac{\partial}{\partial \xi}\lambda(\xi)\delta c_n(x,\xi)d\xi \\ &= \delta c_n(x,t)(1+\lambda(\xi)|_{\xi=t}) - \int_0^t \frac{\partial}{\partial \xi}\lambda(\xi)\delta c_n(x,\xi)d\xi \end{aligned} \tag{8.3.5}$$

The extreme values of c_{n+1} requires that $\delta c_{n+1} = 0$. This means that left hand side of equation (8.3.5) is zero, and as a result the right hand side should be zero as well, that is,

$$\delta c_n(x,t)(1+\lambda(\xi)|_{\xi=t}) - \int_0^t \frac{\partial}{\partial \xi}\lambda(\xi)\delta c_n(x,\xi)d\xi = 0 \tag{8.3.6}$$

This yields the stationary conditions

$$1+\lambda(\xi)|_{\xi=t}=0 \tag{8.3.7}$$

$$\text{and } \lambda'(\xi)=0 \tag{8.3.8}$$

$$\text{which implies } \lambda=-1. \tag{8.3.9}$$

Hence equation (8.3.2) becomes

$$c_{n+1}(x,t)=c_n(x,t)-\int_0^t\left(\frac{\partial c_n(x,\xi)}{\partial \xi}-\kappa\ {}_0\mathcal{D}_\xi^{\alpha,\beta}\left[\frac{\partial^2 c_n(x,\xi)}{\partial x^2}-\frac{\partial}{\partial x}\left\{u(x)c_n(x,\xi)\right\}\right]\right)d\xi, \tag{8.3.10}$$

where the restriction is removed on c_n. Equation (8.3.10) further simplifies to

$$c_{n+1}(x,t)=c_n(x,0)+\kappa\int_0^t {}_0\mathcal{D}_\xi^{\alpha,\beta}\left[\frac{\partial^2 c_n(x,\xi)}{\partial x^2}-\frac{\partial}{\partial x}\left\{u(x)c_n(x,\xi)\right\}\right]d\xi. \tag{8.3.11}$$

Starting with an initial approximation $c_0(x,t)=c(x,0)=f(x)$, we obtain a sequence of successive approximations, and the exact solution is obtained by taking the limit of the nth approximation, that is,

$$c(x,t)=\lim_{n\to\infty} c_n(x,t). \tag{8.3.12}$$

8.4 A Linear Transport Model with Hilfer Derivative

8.4.1 Polynomial Uploading

We take $u(x) = -x$ in equation (8.3.1), so it becomes

$$\frac{\partial c(x,t)}{\partial t} = \kappa \ {}_0\mathcal{D}_t^{\alpha,\beta} \left[\frac{\partial^2 c(x,t)}{\partial x^2} + \frac{\partial}{\partial x} \left\{ x c(x,t) \right\} \right], \quad x > 0, t > 0 \tag{8.4.1}$$

with the initial condition $c(x, 0) = x^p$, for $p \geq 0$. We obtain the following iteration formula by using equation (8.3.11)

$$c_{n+1}(x,t) = c_n(x,0) + \kappa \int_0^t \mathcal{D}_\xi^{\alpha,\beta} \left[\frac{\partial^2 c_n(x,\xi)}{\partial x^2} + \frac{\partial}{\partial x} \left\{ x c_n(x,\xi) \right\} \right] d\xi, \tag{8.4.2}$$

with the zeroth approximation

$$c_0(x,t) = x^p. \tag{8.4.3}$$

By taking $n = 0$ in equation (8.4.2) and using equation (8.4.3), we obtain

$$c_1(x,t) = x^p + \kappa \int_0^t \mathcal{D}_\xi^{\alpha,\beta} \left[\frac{\partial^2}{\partial x^2} x^p + \frac{\partial}{\partial x} \left\{ x^{p+1} \right\} \right] d\xi, \tag{8.4.4}$$

which can be written as

$$c_1(x,t) = x^p + \kappa a_1(x) \int_0^t \mathcal{D}_\xi^{\alpha,\beta}(1) d\xi, \tag{8.4.5}$$

where

$$a_1(x) = \frac{\partial^2}{\partial x^2} x^p + \frac{\partial}{\partial x} \left\{ x^{p+1} \right\}. \tag{8.4.6}$$

By using lemma 8.2, we obtain

$$c_1(x,t) = x^p + \kappa a_1(x) \frac{t^{1-\alpha}}{\Gamma(1-\alpha+1)}. \tag{8.4.7}$$

By taking $n = 1$ in Eq. (8.4.2) and using Eq. (8.4.7), we obtain

$$c_2(x,t) = x^p + \kappa a_1(x) \frac{t^{1-\alpha}}{\Gamma(1-\alpha+1)} + \kappa^2 a_2(x) \frac{t^{2(1-\alpha)}}{\Gamma(2(1-\alpha)+1)}, \tag{8.4.8}$$

where

$$a_2(x) = \frac{\partial^2}{\partial x^2} a_1(x) + \frac{\partial}{\partial x} \left\{ x a_1(x) \right\}. \tag{8.4.9}$$

Proceeding in this way, we obtain

$$c_n(x,t) = \Sigma_{k=0}^n a_k(x) \frac{[\kappa t^{1-\alpha}]^k}{\Gamma(k(1-\alpha)+1)}, \tag{8.4.10}$$

where

$$a_k(x) = \frac{\partial^2}{\partial x^2} a_{k-1}(x) + \frac{\partial}{\partial x} \left\{ x a_{k-1}(x) \right\}, \qquad \text{for } k \geq 1, \tag{8.4.11}$$

and $a_0(x) = x^p$.

By taking the limit $n \to \infty$ of Eq. (8.4.10) we obtain

$$c(x,t) = \lim_{n\to\infty} c_n(x,t) = \Sigma_{k=0}^{\infty} a_k(x) \frac{[\kappa t^{1-\alpha}]^k}{\Gamma(k(1-\alpha)+1)}. \tag{8.4.12}$$

8.4.2 On the Convergence of $c(x,t)$

Theorem 8.1 *The series solution* (8.4.12) *of the problem* (8.4.1) *with the initial condition* $c(x,0) = x^p$, $p \geq 0$, *converges absolutely for all* x *and* t.

Proof. We denote the nth term of Eq. (8.4.12) by

$$s_n(x,t) = a_n(x) \frac{\kappa^n t^{n(1-\alpha)}}{\Gamma[n(1-\alpha)+1]}.$$

Applying the ratio test on the series (8.4.12), we obtain

$$\begin{aligned} \left|\frac{s_{n+1}(x,t)}{s_n(x,t)}\right| &= \left|\frac{a_{n+1}(x)}{a_n(x)} \kappa t^{(1-\alpha)} \frac{\Gamma[n(1-\alpha)+1]}{\Gamma[(n+1)(1-\alpha)+1]}\right| \\ &\text{since } (1-\alpha) > 0 \text{ therefore } n(1-\alpha)+1 > 1 \\ &= \left|\frac{a_{n+1}(x)}{a_n(x)} \kappa t^{(1-\alpha)}\right| \frac{\Gamma[n(1-\alpha)+1]}{\Gamma[(n+1)(1-\alpha)+1]}. \end{aligned} \tag{8.4.13}$$

Note that $\left|\frac{a_{n+1}(x)}{a_n(x)}\right|$ is bounded above by $p+1$, where $p \geq 0$ is the integer power of x in the initial condition $c(x,0) = x^p$. Indeed, $a_n(x)$, defined in Eq. (8.4.11), is a polynomial in x whose leading term, that is, the term with the highest power of x is $(p+1)^n x^p$, and further note that degree$(a_n(x)) = p$ for all $n \geq 0$. Thus we can approximate $a_n(x)$ by its leading term $(p+1)^n x^p$ (since all the coefficients are positive) and therefore we obtain

$$\left|\frac{a_{n+1}(x)}{a_n(x)}\right| \approx \left|\frac{(p+1)^{n+1}x^p}{(p+1)^n x^p}\right| = p+1.$$

By using Wendel's double inequality [136],

$$x^{1-s} \leq \frac{\Gamma(x+1)}{\Gamma(x+s)} \leq (x+s)^{1-s},$$

for $x > 0$ and $0 < s < 1$, we deduce that

$$\lim_{n\to\infty} \frac{\Gamma[n(1-\alpha)+1]}{\Gamma[(n+1)(1-\alpha)+1]} = 0.$$

Hence, Eq. (8.4.13) gives

$$\lim_{n\to\infty} \left|\frac{s_{n+1}(x,t)}{s_n(x,t)}\right| = 0. \tag{8.4.14}$$

Thus the series solution obtained in Eq. (8.4.12) converges (absolutely) for all x and t. ▮

8.4.3 To show that $c(x,t)$ obtained in Eq. (8.4.12) satisfies Eq. (8.4.1)

Theorem 8.2 *The series solution* (8.4.12) *satisfies the equation* (8.4.1) *with the initial condition* $c(x,0) = x^p$, *where* $p \geq 0$.

Proof. First, on differentiating Eq. (8.4.12) with respect to t, we obtain

$$\begin{aligned}
\frac{\partial}{\partial t}c(x,t) &= \frac{\partial}{\partial t}\left[a_0(x) + \Sigma_{k=1}^{\infty} a_k(x)\frac{\kappa^k t^{k(1-\alpha)}}{\Gamma[k(1-\alpha)+1]}\right] \\
&= \Sigma_{k=1}^{\infty} a_k(x)\frac{\kappa^k}{\Gamma[k(1-\alpha)+1]}\frac{\partial}{\partial t}t^{k(1-\alpha)} \\
&= \Sigma_{k=1}^{\infty} a_k(x)\frac{\kappa^k}{k(1-\alpha)\Gamma[k(1-\alpha)]}k(1-\alpha)t^{k(1-\alpha)-1} \\
&= \Sigma_{k=1}^{\infty} a_k(x)\frac{\kappa^k t^{k(1-\alpha)-1}}{\Gamma[k(1-\alpha)]}. \qquad (8.4.15)
\end{aligned}$$

On the other hand substituting Eq. (8.4.12) in the right hand side of Eq. (8.4.1) yields

$$\begin{aligned}
&\kappa \mathcal{D}_t^{\alpha,\beta}\left[\frac{\partial^2 c(x,t)}{\partial x^2} + \frac{\partial}{\partial x}\left\{x c(x,t)\right\}\right] \\
&= \kappa \mathcal{D}_t^{\alpha,\beta}\left[\Sigma_{k=0}^{\infty}\left\{\frac{\partial^2}{\partial x^2}a_k(x) + \frac{\partial}{\partial x}\left(x a_k(x)\right)\right\}\frac{\kappa^k t^{k(1-\alpha)}}{\Gamma[k(1-\alpha)+1]}\right] \\
&= \kappa \Sigma_{k=0}^{\infty}\left\{\frac{\partial^2}{\partial x^2}a_k(x) + \frac{\partial}{\partial x}\left(x a_k(x)\right)\right\}\mathcal{D}_t^{\alpha,\beta}\frac{\kappa^k t^{k(1-\alpha)}}{\Gamma[k(1-\alpha)+1]} \\
&= \Sigma_{k=0}^{\infty} a_{k+1}(x)\frac{\kappa^{k+1} t^{(k+1)(1-\alpha)-1}}{\Gamma[(k+1)(1-\alpha)]} \\
&= \Sigma_{k=1}^{\infty} a_k(x)\frac{\kappa^k t^{k(1-\alpha)-1}}{\Gamma[k(1-\alpha)]}. \qquad (8.4.16)
\end{aligned}$$

The equality of equations (8.4.15) and (8.4.16) proves that $u(x,t)$ given by equation (8.4.12) is the solution of problem (8.4.1). Initial condition is easily recovered by substituting $t = 0$ in the equation (8.4.12). ▌

8.4.4 Examples

We examine the solutions for the cases $p = 1$ and $p = 2$.

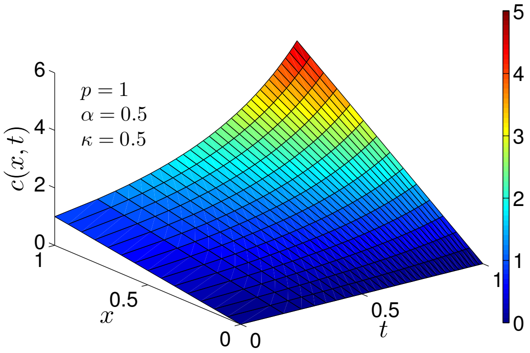

Figure 8.1: Plot of the solution $c(x,t)$, Eq. (8.4.17), for $0 \le x \le 1$ and time $0 \le t \le 1$, where $p = 1$, $\alpha = 0.5$ and $\kappa = 0.5$.

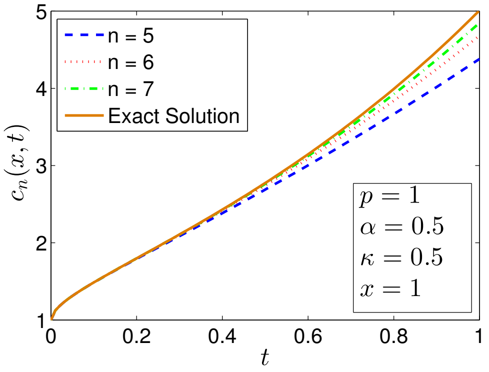

Figure 8.2: Plots of the truncated series solution $c_n(x,t)$, Eq. (8.4.18), for $0 \le t \le 1$ at $x = 1$, where $p = 1$, $\alpha = 0.5$ and $\kappa = 0.5$, for different n as indicated.

For $p = 1$, the initial condition becomes $c(x,0) = x$. Then, from Eq. (8.4.11), $a_k(x) = 2^k x$ for $k \ge 0$ and hence from Eq. (8.4.12), the solution $c(x,t)$ is expressed as follows

$$c(x,t) = x\Sigma_{k=0}^{\infty}\frac{[2\kappa t^{1-\alpha}]^k}{\Gamma[k(1-\alpha)+1]} = xE_{1-\alpha}[2\kappa t^{1-\alpha}], \tag{8.4.17}$$

where $E_\alpha(t)$, defined in Eq. (8.2.10), is the Mittag-Leffler function in one parameter. The plot of the solution (8.4.17) is shown in the Fig. 8.1 for the values $\alpha = 0.5$ and $\kappa = 0.5$. Note that the solution $c(x,t)$, for fixed t, increases linearly with respect to variable x and it increases exponentially with respect to variable t, for fixed x.

In order to see how rapidly the sequence of successive approximations provided by VIM converges to the exact solution, we use the nth partial sum as an approximation,

$$c_n(x,t) = x\Sigma_{k=0}^{n}\frac{[2\kappa t^{1-\alpha}]^k}{\Gamma[k(1-\alpha)+1]}. \tag{8.4.18}$$

In Fig. 8.2, we plot $c_n(x,t)$ against t at $x = 1$ for $\alpha = 0.5$ and $\kappa = 0.5$, for different values of n. One can see from Fig. 8.2 that the solution converges by $n = 7$. Later in Section 8.4.5, we will provide details about how many terms have to be summed up in order to obtain a given accuracy.

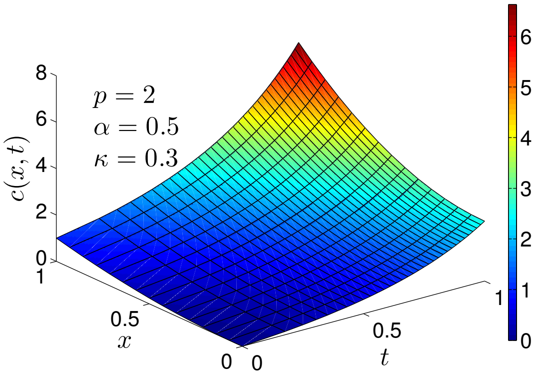

Figure 8.3: Plot of the solution $c(x,t)$, Eq. (8.4.19), for $0 \leq x \leq 1$ and time $0 \leq t \leq 1$, where $p = 2$, $\alpha = 0.5$ and $\kappa = 0.3$.

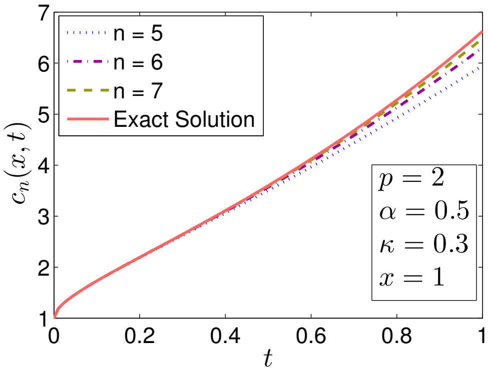

Figure 8.4: Plots of the truncated series solution $c_n(x,t)$, Eq. (8.4.20), for $0 \leq t \leq 1$ at $x = 1$, where $p = 2$, $\alpha = 0.5$ and $\kappa = 0.3$, for different n as indicated.

For $p = 2$, the initial condition becomes $c(x,0) = x^2$. Then, from equation (8.4.11), $a_k(x) = 3^k x^2 + 3^k - 1$ for $k \geq 0$ and hence from equation (8.4.12) the solution $c(x,t)$ is expressed as follows:

$$c(x,t) = x^2 E_{1-\alpha}[3\kappa t^{1-\alpha}] + E_{1-\alpha}[3\kappa t^{1-\alpha}] - E_{1-\alpha}[\kappa t^{1-\alpha}]. \tag{8.4.19}$$

The plot of the solution (8.4.19) is shown in the Fig. 8.3 for $\alpha = 0.5$ and $\kappa = 0.3$. This time, the solution $c(x,t)$, for fixed t, increases quadratically with respect to variable x and it increases exponentially with respect to variable t, for fixed x.

Again, we use the nth approximation in order to see how rapidly the sequence of successive approximations provided by VIM converges to the exact solution:

$$
\begin{aligned}
c_n(x,t) = x^2 \Sigma_{k=0}^{n} \frac{[3\kappa t^{1-\alpha}]^k}{\Gamma[k(1-\alpha)+1]} + \Sigma_{k=0}^{n} \frac{[3\kappa t^{1-\alpha}]^k}{\Gamma[k(1-\alpha)+1]} \\
- \Sigma_{k=0}^{n} \frac{[\kappa t^{1-\alpha}]^k}{\Gamma[k(1-\alpha)+1]}, \qquad (8.4.20)
\end{aligned}
$$

and plot it for different values of n. Figure 8.4 shows the plots of $c_n(x,t)$ against t for $x = 1$, $\alpha = 0.5$, $\kappa = 0.3$, and for different n as indicated. This time the approximate solutions converge at $n = 7$.

When $p \geq 3$, closed form solutions for $c(x,t)$ becomes increasingly harder to obtain. Nevertheless, for the purpose of analyzing the general behavior of the solution $c(x,t)$, we require only the dominant term in the solution. As mentioned in Section 8.4.2 that we can approximate $a_n(x)$ by its leading term, that is by $(p+1)^n x^p$. If we replace $a_n(x)$ by $(p+1)^n x^p$ in equation (8.4.12), we obtain the leading term to be,

$$
\begin{aligned}
c(x,t) &\approx \Sigma_{k=0}^{\infty} (p+1)^n x^p \frac{\kappa^k t^{k(1-\alpha)}}{\Gamma[k(1-\alpha)+1]} \\
&\approx x^p \Sigma_{k=0}^{\infty} \frac{[(p+1)\kappa t^{1-\alpha}]^k}{\Gamma[k(1-\alpha)+1]} \\
&\approx x^p E_{1-\alpha}[(p+1)\kappa t^{1-\alpha}]. \qquad (8.4.21)
\end{aligned}
$$

The solution $c(x,t)$ is thus proportional to x^p at fixed t; and it increases approximately exponentially with respect to variable t at fixed x.

In order to further investigate the trends in the fractional solution, we compare the fractional solution to the non-fractional solution at $x = 1$ and $t = 1$.

At $x = 1$ and $t = 1$, we obtain $c(1, 1) \approx E_{1-\alpha}[(p+1)\kappa]$, and by using equation (8.2.10) we obtain

$$c(1, 1) \approx \sum_{k=0}^{\infty} \frac{[(p+1)\kappa]^k}{\Gamma[k(1-\alpha)+1]}.$$

In the asymptotic limit $\alpha \to 1$, we obtain $c(1, 1) \approx \sum_{k=0}^{\infty} [(p+1)\kappa]^k$, which is a geometric series and it converges to $\frac{1}{1-(p+1)\kappa}$, when $(p+1)\kappa < 1$ or $\kappa < \frac{1}{p+1}$.

For $\alpha = 0$, we obtain

$$c(1, 1) \approx \sum_{k=0}^{\infty} \frac{[(p+1)\kappa]^k}{k!} = \exp(\kappa(p+1))$$

which converges for all κ and $p \geq 0$.

Furthermore, in Eq. (8.4.21) in the asymptotic limit $\alpha \to 1$, $t^{1-\alpha} = 1$ for all t, and thus the power series (8.4.21) converges for all t so long as $(p+1)\kappa < 1$.

8.4.5 Numerical Analysis and behavior of the solution

In this section we discuss the general behavior of the solution of the problem (8.4.1) with respect to different parameters and also we do numerical analysis of the solution.

Reciprocal Gamma Function First we analyze the reciprocal gamma function which appears in the series solution (8.4.12), that is,

$$\frac{1}{\Gamma[n(1-\alpha)+1]}.$$

The limit of this function, for a fixed $\alpha(\neq 1)$, as $n \to \infty$ is zero, that is,

$$\lim_{n\to\infty} \frac{1}{\Gamma[n(1-\alpha)+1]} = 0, \qquad \text{for fixed } \alpha \in (0,1).$$

We want an expression for the number of terms n needed in order to satisfy a given accuracy given by,

$$\frac{1}{\Gamma[n(1-\alpha)+1]} \le 10^{-\tau},$$

for a given α and tolerance level τ. For this purpose, we use the following formula, see [11],

$$\begin{aligned} &\sqrt{2\pi x}(x/e)^x(x\sinh 1/x)^{x/2}(1+a/x^5) < \Gamma(x+1) \\ &< \sqrt{2\pi x}(x/e)^x(x\sinh 1/x)^{x/2}(1+b/x^5), \end{aligned}$$

for all $x > 0$ and with the optimal constants $a = 0$ and $b = \frac{1}{1620}$, to obtain the required n. Table 8.1 summarizes this information.

Figure 8.5 shows the plots of n against τ for different values of α. For any given α the number of terms n appears to scale almost linearly with τ. Best linear fits were therefore obtained, for example for $\alpha = 0.9$, we obtain the best fit $n = 40.79 + 8.964\tau$. The value of R^2, the coefficient of determination, is 99.8% and the value of R^2_{adj} is 99.7%.

Figure 8.6 shows the plots of n against α for some tolerance levels, taken from

τ	α									
	0	0.1	0.2	0.3	0.4	0.5	0.6	0.7	0.8	0.9
4	8	9	10	11	13	15	19	25	37	74
6	10	11	12	14	16	19	24	32	48	95
8	12	13	15	17	19	23	29	38	57	114
10	14	15	17	19	22	27	33	44	66	132
12	15	17	19	22	25	30	38	50	75	150
14	17	19	21	24	28	34	42	56	83	166
16	19	21	23	26	31	37	46	61	91	182

Table 8.1: The number of terms, n, needed to achieve a given tolerance level $10^{-\tau}$ for different α.

the data in Table 8.1. The relationship between n and α is clearly non-linear.

But for $\alpha > 0.7$ we see a rapid increase in the number of terms n needed to achieve a given accuracy. It may be possible to find best-fit curves to the data plotted in Fig. 8.6. For this purpose, we assume cubic polynomial fits of the form $n(\alpha) = A + B\alpha + C\alpha^2 + D\alpha^3$, where A, B, C and D are constants to be determined from the data using the least square method, for a tolerance level of 10^{-16}, we obtain the following cubic polynomial $n(\alpha) = 13.69 + 181.3\alpha - 665.6\alpha^2 + 730.4\alpha^3$. The value of R^2, is 97.5%, and R^2_{adj} is 96.2%.

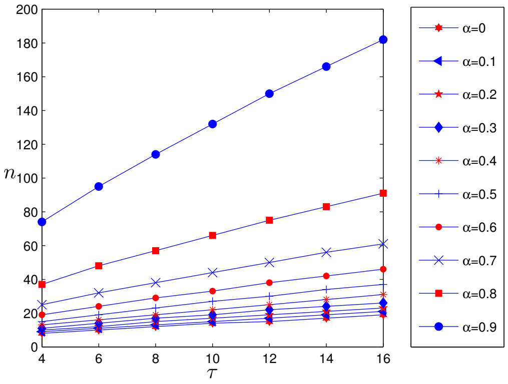

Figure 8.5: Plots of n against τ, for specific values of α.

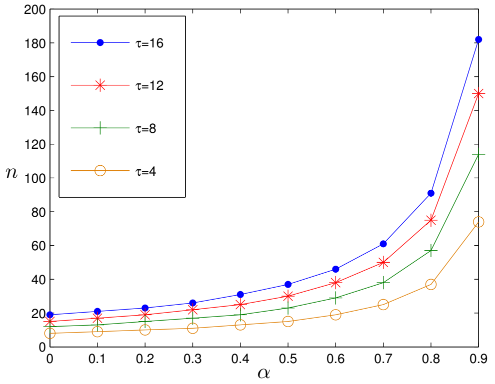

Figure 8.6: Plots of n against α, for specific tolerance levels $10^{-\tau}$.

8.4.6 Behavior of the Solution

The solution of the problem (8.4.1) is given by

$$c(x,t) = \Sigma_{n=0}^{\infty} a_n(x) \frac{[\kappa t^{1-\alpha}]^n}{\Gamma[n(1-\alpha)+1]},$$

where

$$a_n(x) = \frac{\partial^2}{\partial x^2} a_{n-1}(x) + \frac{\partial}{\partial x}\left\{ x a_{n-1}(x) \right\},$$

and $a_0(x) = x^p$.

We examine the sensitivity of the solution $c(x,t)$ to parameters p, κ and especially to α, where p is $c(x,0) = x^p$, κ is diffusivity coefficient, and α is the order of the Hilfer derivative.

We choose the following values: $p \in \{1,2,3,4\}$, $\alpha \in \{0, 0.1, ..., 0.9\}$ and we select κ according to $\kappa < \frac{1}{p+1}$. We compare the values of $c(x,t)$ at the point $(1,1)$ for different combinations of the above parameters. We choose three values of κ that are less than $\frac{1}{p+1}$ and one value that is equal (approximately) to $\frac{1}{p+1}$ and one value that is greater than $\frac{1}{p+1}$; see Table 2 Ali and Malik [6].

We see that different combinations of parameter's values affect the values of $c(x,t)$ differently. In general, we note that an increase in the values of parameters p, κ and α results into an increase in the values of $c(x,t)$. The effect of κ can be divided into two parts, first when $\kappa < \frac{1}{p+1}$ and second when $\kappa \geq \frac{1}{p+1}$.

For the first case, $\kappa < \frac{1}{p+1}$, the increase in the values of $c(x,t)$ is not significant as compare to the second case, $\kappa \geq \frac{1}{p+1}$, where $c(x,t)$ increases very rapidly with

α and κ.

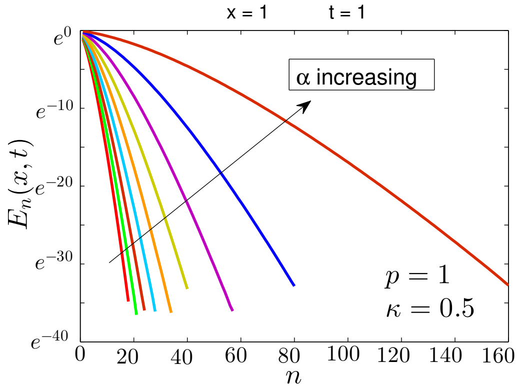

Figure 8.7: Plot of the relative error $e_n(1, 1)$ against the number of terms n, from example 1. Left: Linear-Linear, Right: Linear-Natural Log (y-axis is scaled as e^m, where $m \in \{-40, -35, \ldots, 0\}$). A line of slope $-2/5$ is shown for comparison.

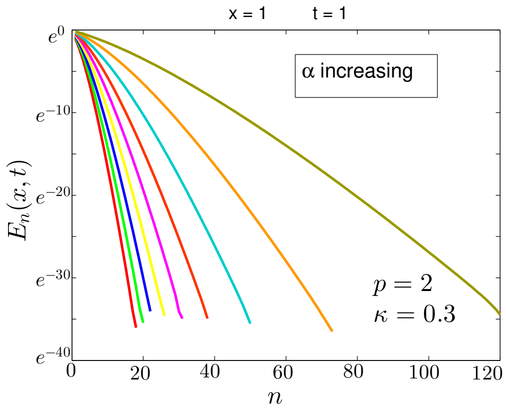

Figure 8.8: Plot of the relative error $e_n(1, 1)$ against the number of terms n, from example 2. Left: Linear-Linear, Right: Linear-Natural Log (y-axis is scaled as e^m, where $m \in \{-35, -30, \ldots, 0\}$). A line of slope $-2/5$ is shown for comparison.

8.4.7 Relative Error

Finally, we examine the truncation error when using the partial sum of first n terms of the series solution given in Eq. (8.4.12). We define the relative error as,

$$E_n(x,t) = \frac{|c(x,t) - c_n(x,t)|}{|c(x,t)|},$$

where $c_n(x,t)$ is the partial sum of the first n terms. Figures 8.7 and 8.8 show the plots of $E_n(x,t)$ versus n at the point $(1, 1)$ for, respectively, $p = 1$ and $p = 2$. The errors fall off exponentially fast with n. These results show that the VIM solutions for this problem convergence rapidly, and improves as n increases.

Note that it is not always possible to express the series solution in compact form like in the cases of $p = 1$ and $p = 2$. For values of p larger than 2, we approximate the 'exact' solution by taking a very large value of n, and then we compare this with the smaller values of n. For example, when the initial condition is $c(x,0) = x^3$, $(p = 3)$, we take $n = 200$, and $c_{200}(x,t)$ is the approximation to the exact solution. Then the formula for the relative error becomes

$$e_n(x,t) = \frac{|c_{200}(x,t) - c_n(x,t)|}{|c_{200(x,t)}|}, \text{for} 1 \leq n \leq 100$$

.

8.4.8 Fractional versus Conventional Solutions

In this section, we compare the solutions of the fractional differential equation (8.4.1) with the corresponding conventional differential equation.

Conventional version of equation (8.4.1) can be obtained by taking $\alpha = 0$, see [96], that is,

$$\frac{\partial c(x,t)}{\partial t} = \kappa \left[\frac{\partial^2 c(x,t)}{\partial x^2} + \frac{\partial}{\partial x} \{xc(x,t)\} \right], \quad x > 0, t > 0. \tag{8.4.22}$$

The exact solution of equation (8.4.22) with initial condition $c(x,0) = x$ is

$$c(x,t) = xe^{2\kappa t}, \tag{8.4.23}$$

and the general solution for $\alpha > 0$ is given by,

$$c(x,t) = xE_{1-\alpha}[2\kappa t^{1-\alpha}]. \tag{8.4.24}$$

Thus, the relative magnitude of the solutions compared to the conventional case can be estimated from,

$$\frac{c^{\alpha}(x,t)}{c^{0}(x,t)} \approx \frac{E_{1-\alpha}[2\kappa t^{1-\alpha}]}{e^{2\kappa t}}. \tag{8.4.25}$$

The asymptotic behavior of this can be analyzed through the long time behavior of Mittag-Leffler function. By using Theorem 1.3 of [133], we can write

$$\frac{c^{\alpha}(x,t)}{c^{0}(x,t)} \approx \exp\{((2\kappa)^{1/(1-\alpha)} - 2\kappa)t\}. \tag{8.4.26}$$

The long time behavior depends on the value of κ. In particular, if $\kappa < 1/2$, then the this tends to zero as t goes to infinity.

The exact solution of equation (8.4.22) with initial condition $c(x,0) = x^2$ is

$$c(x,t) = x^2 e^{3\kappa t} + e^{3\kappa t} - e^{\kappa t}, \tag{8.4.27}$$

and, the fractional solution for $p = 2$ is

$$c(x,t) = x^2 E_{1-\alpha}[3\kappa t^{1-\alpha}] + E_{1-\alpha}[3\kappa t^{1-\alpha}] - E_{1-\alpha}[\kappa t^{1-\alpha}]. \tag{8.4.28}$$

The relative magnitude of the solutions compared to the conventional case can be estimated from,

$$\frac{c^{\alpha}(x,t)}{c^{0}(x,t)} \approx \frac{x^2 E_{1-\alpha}[3\kappa t^{1-\alpha}] + E_{1-\alpha}[3\kappa t^{1-\alpha}] - E_{1-\alpha}[\kappa t^{1-\alpha}]}{x^2 e^{3\kappa t} + e^{3\kappa t} - e^{\kappa t}}. \tag{8.4.29}$$

To leading order, Eq. (8.4.29) is,

$$\frac{c^{\alpha}(x,t)}{c^{0}(x,t)} \approx \frac{E_{1-\alpha}[3\kappa t^{1-\alpha}]}{e^{3\kappa t}}. \tag{8.4.30}$$

and for the general case $p > 1$, this is

$$\frac{c^{\alpha}(x,t)}{c^{0}(x,t)} \approx \frac{E_{1-\alpha}[(p+1)\kappa t^{1-\alpha}]}{e^{(p+1)\kappa t}}. \tag{8.4.31}$$

8.5 Time-fractional linear diffusion equation with Caputo derivative, Case 1

We consider a time fractional linear diffusion equation with Caputo derivative of order α, $0 < \alpha < 1$,

$$\frac{\partial c(x,t)}{\partial t} = {}_0\mathcal{D}_t^{\alpha}[(Ac)(x,t)] + q(x,t), \quad x > 0, t > 0, \quad c(x,0) = f(x). \tag{8.5.1}$$

where ${}_0\mathcal{D}_t^{\alpha}$ represent Caputo derivative which operates on A - a linear differential operator, $q(x,t)$ is a source term, and $f(x)$ is the inital condition. Approximate

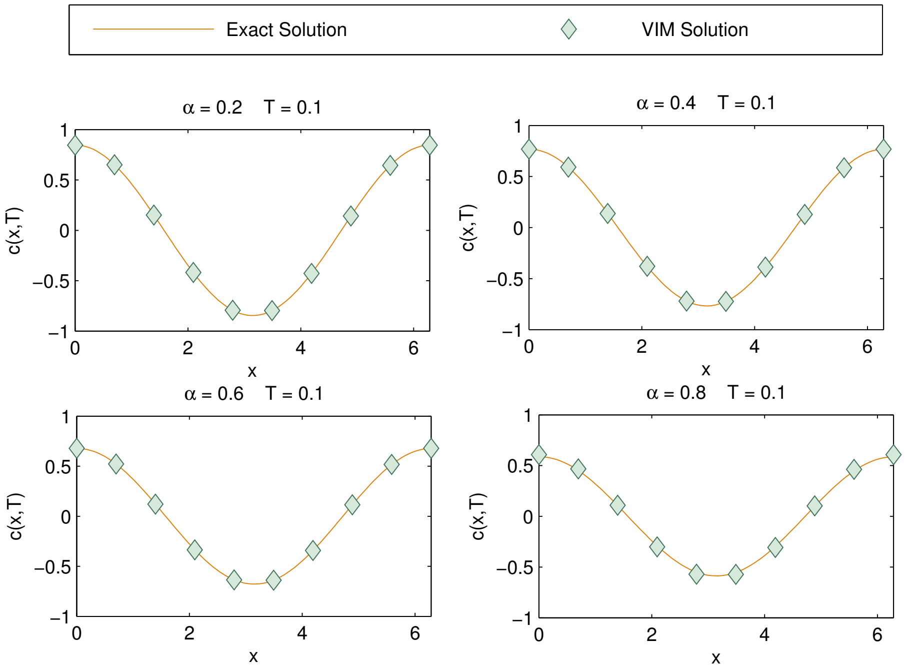

Figure 8.9: Plots of the exact solution $c(x,t)$, of equation (8.5.1), and the truncated VIM solution $c_7(x,t)$, at $t = 0.1$ and $0 \leq x \leq 2\pi$. The plots corresponds $\gamma = 0.2; 0.4; 0.6 and 0.8$, as indicated.

(truncated) series solutions are obtained by means of the Variational Iteration Method (VIM). We find the series solutions for the cases when $A = \partial^2/\partial x^2$, $q(x,t) = t\sin(x)$, and $f(x) = \cos(x)$. The results are shown in Figure 8.9. The error in truncated solution c_n diminishes exponentially fast for a given α as the number of terms in the series increases. The truncated VIM solutions often converge rapidly requiring only a few terms for fast and accurate approximations, see Figure 8.10. For more details see Ali et al. [7].

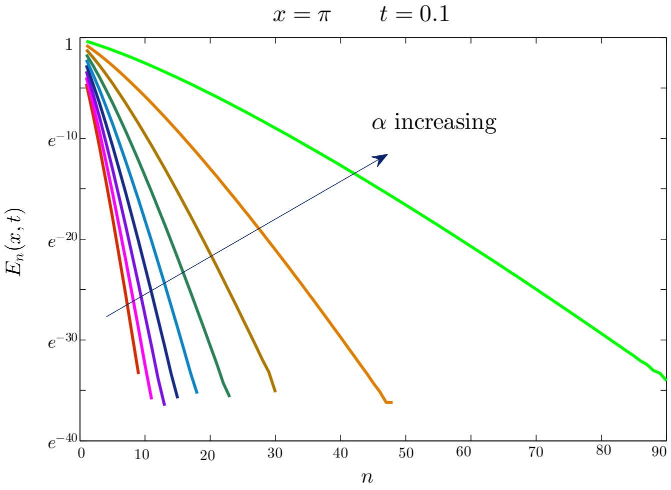

Figure 8.10: Plot of the relative error $E_n(x,t)$ at $x = \pi$, at $t = 0.1$ against the number of terms n. Vertical axis is scaled as Natural Logarithm, that is, $\ln e^m$, where $m \in \{-40, -35, \cdots, 0\}$.

8.6 Time-fractional linear diffusion equation with Caputo derivative, Case 2

In this study, We model the transport of fluid through porous media in terms of fractional diffusion equation (FDE) for the pressure $p(x,t)$, with a view of applying to shale gas recovery in tight porous media. Specifically, we pose the time FDE in a finite domain of length L,

$$_0D_t^\alpha p = Ap + f(x,t), \qquad 0 \le x \le L, \quad t > 0, \tag{8.6.1}$$

where $_0D_t^\alpha$ represents Caputo fractional derivative of order α, $0 < \alpha < 1$; which operates on the left hand side of the equation. A is a linear differential operator given by

$$A \equiv \frac{\partial}{\partial x}\left(a\frac{\partial}{\partial x}\right), \qquad a = \frac{K}{\mu}, \tag{8.6.2}$$

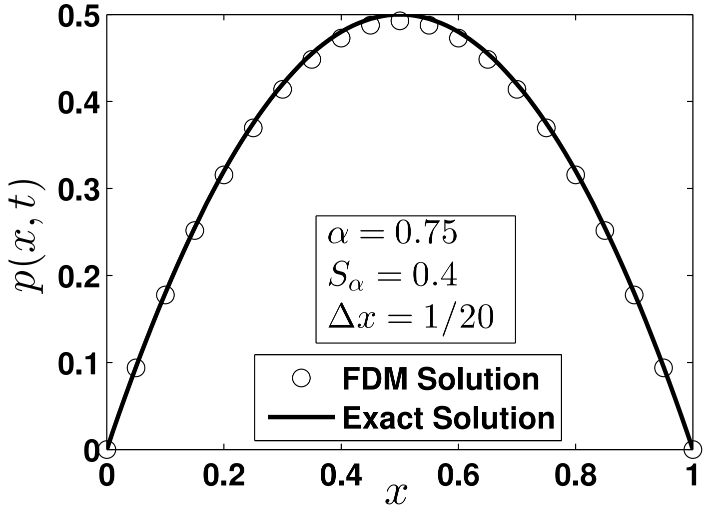

Figure 8.11: The solutions are plotted against distance x.

and K is the permeability and μ is the viscosity, $f(x,t)$, is a source term. The initial and boundary conditions are, $p(x,0) = g(x)$, and $p(0,t) = c$, and $p(L,t) = 0$. The pressure distribution $p(x,t)$ in one-dimensional porous reservoirs for different $\alpha = 0.75$, and for $f(x,t) = 2x(1-x)t^{2-\alpha}$ and $g(x) = x(1-x)$, is shown in Figure 8.11. For more details, see Ali et al. [8].

8.7 Time-Fractional Nonlinear Gas Transport Equation in Tight Porous Media, Case 1, Riemann-Liouville Fractional Derivative

In this work, we consider a time fractional nonlinear gas transport model which is proposed using Riemann-Liouville derivative. This is similar to the new transport

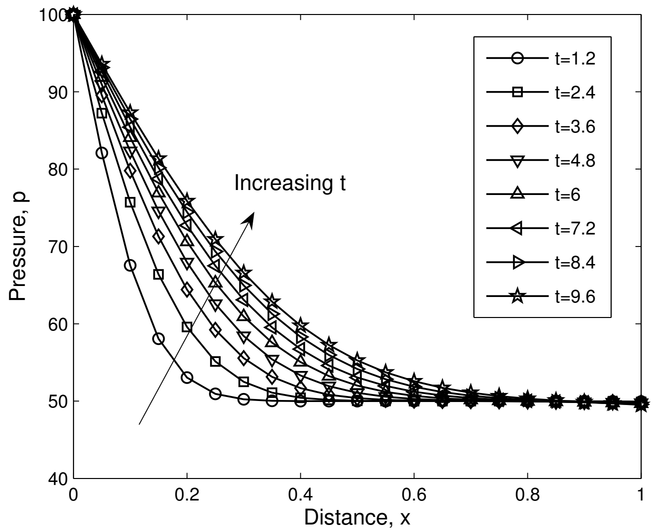

Figure 8.12: The values of the pressure are plotted against certain values of time t, and for $0 \leq x \leq 1$. It is clear from the curves that as we proceed in time the pressure values stabilize in the reservoir.

model (3.4.3), and it is given by

$$\frac{\partial p}{\partial t} + U_a(p, p_x)\frac{\partial p^{\alpha}}{\partial x} = D_a(p)\frac{\partial^2 p^{\alpha}}{\partial x^2}, \tag{8.7.1}$$

where p^{α} represents the Riemann-Liouville fractional derivative with respect to time t which operates on the spatial derivative. The main feature of this model is that it incorporates memory formalism which helps to understand the anomalous diffusion in tight porous media. Moreover, all the reservoir parameters, such as gas density, gas viscosity, permeability, porosity, etc. are considered as functions of pressure. Figures 8.12 and 8.13 present the solutions for the case when $p(x, 0) = 50$, $p(0, t) = 50\exp(-0.01t)$. For more results see Ali et al. [9]

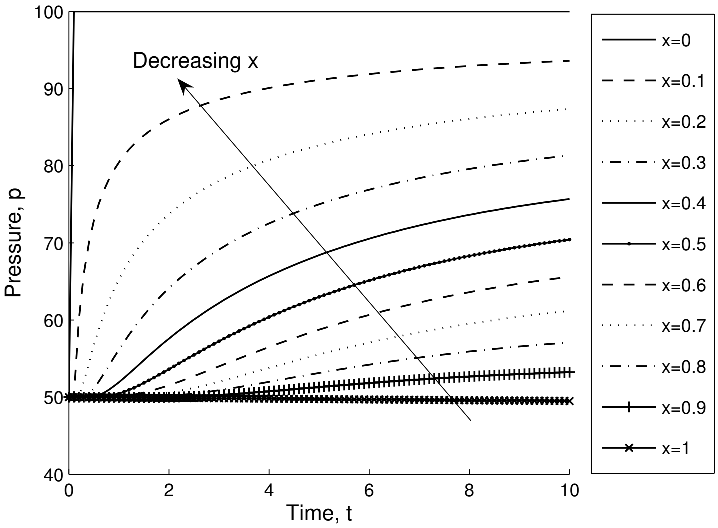

Figure 8.13: The values of the pressure are plotted at certain positions x in the reservoir at all times t. It is clear from the curves that at a given time level t, the values of pressure are higher for the locations closer to the inlet boundary but lower for the positions closer to the outlet boundary.

8.8 Time-Fractional Nonlinear Gas Transport Equation in Tight Porous Media, Case 2, Caputo Fractional Derivative

In this study, we model the transport of gas by the time-fractional advection-diffusion equation using Caputo derivative. It is given by

$$\frac{\partial^\alpha p}{\partial t^\alpha} = \frac{\partial}{\partial x}\left(K\frac{\partial p}{\partial x}\right) - U\left(\frac{\partial p}{\partial x}\right), \qquad 0 \le x \le 1, \quad t > 0, \tag{8.8.1}$$

(with suitable initial and boundary conditions) in order to study the pressure distribution $p(x,t)$ in unconventional reservoirs. In the model, $\partial^\alpha p/\partial t^\alpha$ represents Caputo fractional derivative, $K = K(p)$ is the diffusivity (which is related to

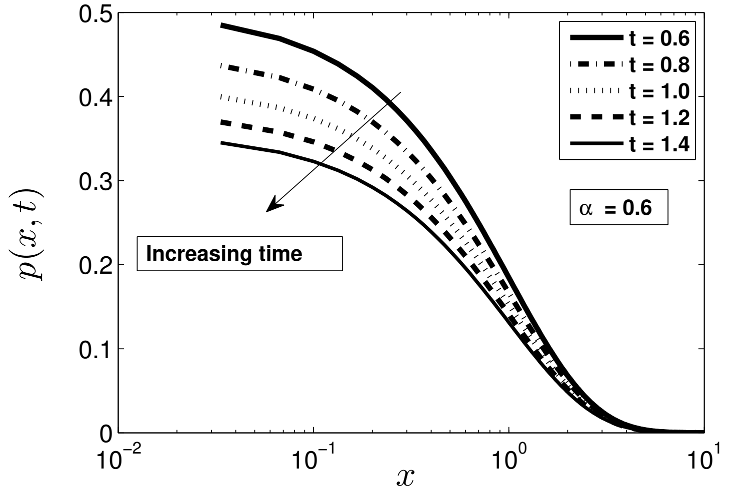

Figure 8.14: The behavior of the solution is shown as the time passes off. The magnitude of the solution increases as the time increases.

the rock permeability) and $U = U(p, p_x)$ is a convection velocity; and both K and U are non-linear. An approximate series solution, for the case $K(p) = 1/p$ and $U = K\partial p/\partial x$, and $p(x, 0) = \exp(-x)$, is found by using variational iteration method (VIM) and shown in the Figure 8.14. Truncation errors are found between the exact solution and the approximate solutions, and are plotted in Figure 8.15 for different values of α. For more details, see Malik et al. [111].

8.9 Summary

Some complex physical phenomenon such as crowded systems, and transport through porous media are not fully understood at the present time, and in order to shed new light into such phenomena a new modeling strategy has emerged in recent years which involves casting the system of interest in terms of fractional calculus.

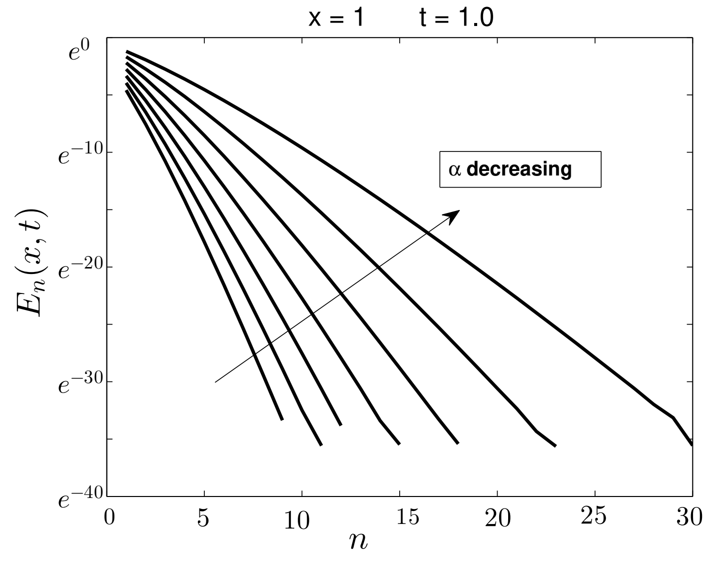

Figure 8.15: Plots of relative errors are shown for the subcase (ii) against the number of terms n.

We have carried out several studies in such systems. The most important was with the Hilfer fractional advection-diffusion equation of order $0 < \alpha < 1$ and type $0 \leq \beta \leq 1$,

$$\frac{\partial c(x,t)}{\partial t} = \kappa \mathcal{D}_t^{\alpha,\beta} \left[\frac{\partial^2 c(x,t)}{\partial x^2} - \frac{\partial}{\partial x} \left\{ u(x) c(x,t) \right\} \right], \quad x > 0, t > 0,$$

with advection term $u(x) = -x$, and power law initial conditions of the type $c(x,t=0) = x^p$ for $p > 0$, was investigated numerically using the Variational Iteration Method (VIM) method, with a view of comparing its solution to the conventional non-fractional advection-diffusion system, and also to analyze the system numerically in order to investigate the efficiency of solving such systems numerically. Power series solutions were obtained, equation (8.4.12). These yield closed form solutions for specific $p > 0$ in terms of the Mittag-Leffler functions, although it becomes increasingly difficult to actually calculate it for $p > 2$. Nevertheless, the leading order term can readily be obtained even for $p > 2$, which allows us to investigate the asymptotic behavior of the solutions and to carry out some numerical analysis of the method used. The power series is (absolutely) convergent (for all x, and all t, and for $p \geq 0$) and it satisfies the problem (8.4.1) along with the initial condition $c(x, 0) = x^p$, for $p > 0$.

The behavior of the solution was examined by comparing the value of the solution at a fixed point, namely $|c(1, 1)|$. Asymptotically, the relative magnitude of the solutions is, $|\frac{c^{\alpha}(x,t)}{c^{0}(x,t)}| \approx \frac{E_{1-\alpha}((p+1)\kappa t)}{e^{(p+1)\kappa t}}$ which shows that the fractional solution increases approximately exponential faster than the conventional solution.

Variational iteration method (VIM) has proven to be an efficient method for obtaining the series solution of the Hilfer fractional advection-diffusion equation with the given power law initial data. Truncation errors $E_n(x, t)$, arising when using the partial sum as approximate solutions, decay exponentially fast with the number of terms n used. The number of terms n required for a given level of accuracy for $\alpha < 0.7$ are relatively insensitive to both the α and to the accuracy level required; but for $\alpha > 0.7$ the number of terms increases rapidly with α and with the accuracy level required. This threshold $\alpha \approx 0.7$ is consistent with the analysis of the solutions $|c(1, 1)|$ above.

Additional studies including different types of fractional derivatives, (Caputo, Riemann-Liouville, Hilfer), were also carried and briefly summarized in Sections 8.4 - 8.7.

CHAPTER 9

DISCUSSION AND CONCLUSIONS

The transport systems investigated and reported here feature many elements from which we can draw important conclusions, and from which future research directions can be planned. The chief goal in these studies was to explore different types of transport models for gas flow in tight porous media. Little is known about these systems at the current time, so it is prudent to explore such systems from a wide perspective. As such we have explores both conventional systems, as well as fractional transport systems.

Conventional PDEs for transport through tight porous media systems have been previously proposed, but the physical realism has been lacking leading to unrealistic rock property estimates. A principle aim here was to incorporate as much physical realism into the model as possible.

Fractional calculus is a newly developing area of mathematics and it is desirable at this exploratory stage to also explore fractional transport models. In this case, even less is known about fractional systems. The aim is to produce some fractional models to lay a foundation for future development.

The most important component of this work has been the development of a new non-linear transport model for flow in tight porous media, and the construction and validation of an associated numerical solver. The new non-linear transport model builds upon previous works, Brace et al. [26], Hsieh et al. [84], Neuzil et al. [125], Liang et al. [104], Malkovsky et al. [112], Cui et al. [44], Civan et al. [41]. The new model is thus based upon the principles of mass balance and momentum balance, gas adsorption in the porous medium, and also turbulence effects through the use of the Forchcheimer's quadratic correction term. Included also are the different flow regimes through a Hagen-Poiseiulle-type equation (4.2.42) defined through the Knudsen number. In this way, continuous free flow, slip flow, transition flow, and Knudsen diffusion (or free molecular flow) are all included as functions of the local Knudsen number, K_n.

The new model is cast in terms of a non-linear advection-diffusion partial differential equation (PDE) for the pressure field $p(x,t)$, with associated boundary and initial conditions. Here, the apparent advection velocity $U_a(p,p_x)$ and the apparent diffusivity $D_a(p)$ are highly non-linear functions of the local pressure $p(x,t)$ and the pressure gradient $p_x(x,t)$. Importantly, compressibility coefficients $\zeta(p)$ associated with each model parameter in the system appear in the expressions for U_a and D_a; formulae for the compressibility coefficients were derived from up to date correlations obtained from the literature. These are used in the solver at every location and time where they needed; only then can the numerical system be made fully pressure dependent which is a crucial feature of the new model.

The resulting model thus incorporates a much greater degree of realism than previous models. It can also be said to be a universal model in the sense that it incorporates the previous transport models as limiting cases. For example in the limit of large porosity and large permeability the new model asymptotes to Darcy's diffusion model.

An implicit finite volume method (FVM) was developed and validated against the results from previous models and also against known exact results in simple cases for the purposes of numerical analysis. The FVM was found to be stable and $O(\Delta x^{1.6})$ accurate in Δx, and $O(\Delta t)$ accurate in Δt, thus validating the model and the numerical code.

The most important application of the new model was the determination of rock properties. The simulations were matched against experimental pressure pulse test data which was available in the open literature, Pong et al. [134]. The rock properties were estimated by running the new model solver for sixteen different cases with different combinations of pressure-dependent and pressure-independent parameters, fitting the results to the experimental data as closely as possible. The case that yielded the minimum error was taken as the best fit set of parameter values. Our results show that the case retaining all parameters to be pressure dependent yielded the best results. However, the estimates of porosity ϕ and the permeability K were unrealistic for shale rocks. It was only when the Forchheimer's correction term was included, in a second set of simulations, that much more realistic values for ϕ and K were obtained. This illustrates the importance of retaining this term in a realistic model.

In this way it was found that the fully pressure dependent model, like Civan et al. [42], yields a more realistic range of values for the rock porosity ϕ, and the rock permeability K. There are in fact two sets of data from Pong et al. [134], one using Nitrogen as the working fluid, and the other using Helium. Both sets of data yielded consistently more realistic rock properties than previous models. (However, it should be noted that Pong's data for Helium is subject to a much greater degree of experimental error than the Nitrogen data, so the simulations were only matched to the averaged data from several experiments.) These results provide validation of the new non-linear model.

A second investigation was carried out to determine the most critical model parameters in the new non-linear model. This was done through a One-At-a-Time (OAT) sensitivity analysis of the model parameters. Three sensitivity analyses were carried out. First, in the limit of steady-state and without the turbulence correction term, see Section 6.3, the results were matched against Pong's Nitrogen data set (this was the case also considered by Civan et al. [41]). It was found that the most critical parameter was c_ϕ. Some parameters had very little effect on the results, these were, σ_0, a_σ, b_σ and b_ϕ.

A second OAT sensitivity analysis was carried out with the full pressure dependent model including the turbulence correction $F \neq 1$, see Section 6.4, matched against Pong's Nitrogen data set. A third OAT sensitivity analysis was carried and matched against Pong's Helium data set. The three sensitivity analyses indicate that different model parameters are critical, or moderate, or non-critical under different conditions (except for c_ϕ which is always critical because it is a power), especially for high input pressures p_{in}. This implies that in order to retain the generality of the model, all model parameters must be kept fully pressure-dependent in the model. Furthermore, the turbulence parameters were found to be moderately sensitive in the two cases above. The inclusion of the turbulence term produced much better estimates for rock properties such as the porosity and the permeability, which implies that the turbulence term is important and must be included in such types of transport models.

An exception is for low flow rates p_{in}, where the results are insensitive to variations in model parameters.

The most important conclusion that we can draw from this is that to obtain the best model parameter values and the best rock property estimates, experiments should be carried out at high p_{in}, low p_{in} will give too wide a margin of error to be useful.

In order to demonstrate the capability of the new model, a simple 'forward' simulation was carried for the pressure field distributions $p(x, t)$ over a period of time. Shale rocks contain ultra-low porosities and permeabilities, and the mean pore radius is also very small. A full reservoir simulation over hundreds of metres and over months in time is therefore not possible without simplifying the model which would negate the realism of the model upon which it is constructed. We have therefore restricted these simulations to a simple context, a rock core sample. The results show that the model can be used for long time simulations of the pressure field, which could be used to estimate the total production of gas over a period of time.

Additional work was carried out using fractional transport models, in the form of fractional partial diffusion equations (FPDE) with boundary and initial conditions. This is a promising modeling approach which is being widely investigated. Several models with different versions of the fractional derivatives - Hilfer derivative, Caputo derivative, Riemann-Liouville derivative - were considered in separate studies. These models were solved using different numerical methods such as the variational iteration method (VIM), and also finite difference methods (FDM). Solutions of different FPDE's were obtained and numerical analyses were carried out. The main idea of such fractional transport models is that the particle and flow transport processes are non-Gaussian in reality, and that they display a type of memory retention. Fractional calculus allows you to incorporate both these effects and thus it is believed that fractional transport models could provide a more realistic description of transport in porous media in some circumstances. This field is a new and developing field and much work still needs to be done. With these investigations we have demonstrated that linear and non-linear fractional transport models can be solved numerically using different techniques and that they could also provide predictions of the future pressure field $p(x, t)$ over a period of time. The results are highly sensitive to the fractional order of the system, an important consideration when applying to real physical cases.

CHAPTER 10

FUTURE DIRECTIONS

Our investigations provide a platform for further research in these important and exciting areas. The new nonlinear model has been developed in the first instance for a fully 3-dimensional flow system, although we have only applied the 1-dimensional version of the model in this work. A clear step forward would be to address the same problems in this investigation for 2D and then 3D contexts. Of course, the numerical costs would increase dramatically, probably necessitating the use of supercomputers and parallel algorithms.

A step towards realistic applications is to combine the new model with fracturing models, such as Yu et al. [175], because that is what is actually done in the petroleum industry.

A further step forward would be to include transport in multi-phase flow, such as, liquid-gas, and even liquid-gas-solid phases. Then multi-component species with chemistry.

Finally, we are interested in the development of the equivalent fractional transport models that are based on the fractional calculus methods. The approach is to derive nonlinear, multi-phase, multi-spices, models in fractured porous media, and then compare the fractional versus the non-fractional models, a preliminary study of which is reported in Ali et al. [9], Ali et al. [8]. The interest here is that it may be possible to pose a simpler fractional transport model, for some fractional order $0 < \alpha < 1$, which better fit the data.

APPENDIX

A-Glossary

1. **Pressure** is force per unit area applied in a direction perpendicular to the surface of an object. The SI unit of pressure is (the newton per square metre), which is called the pascal (Pa).

2. **Absolute pressure** is zero-referenced against a perfect vacuum, so it is equal to gauge pressure plus atmospheric pressure.

3. **Porous Medium** [Wikipedia] A porous medium (or a porous material) is a material containing pores (voids).

4. **Porosity** of porous media is defined as the fraction of volume of void spaces to the bulk volume.

5. **Permeability** of porous media is defined as the rate of flow of a liquid or gas through a porous material. The ability of a medium to permit such flow.

6. **Shale** A fine-grained sedimentary rock consisting of compacted and hardened clay, silt, or mud.

7. **Tight Porous Medium** has very low permeabilities due to very hard shale formations.

8. **Heterogenous Porous Media** has nonuniform composition, character, and other physical properties.

9. **Representative Elementary Volume (REV)** is a part of porous medium that can be used to determine different physical properties of the porous medium.

10. **Hydraulic Tube** The flow channels in the porous media are approximated by tortuous hydraulic flow tubes.

11. **Tortuosity** of porous medium is defined as the ratio of apparent length of the effective mean hydraulic tube to the physical length of the bulk porous medium.

12. **Pore Volume** is the total volume of hydraulic tubes in porous medium and is given by $V_p = nA_hL_h = V_b\phi$.

13. **Adsorption** [Wikipedia] Adsorption is the adhesion of atoms, ions, or molecules from a gas, liquid, or dissolved solid to a surface. This process creates a film of the adsorbate on the surface of the adsorbent. This process differs from absorption, in which a fluid (the absorbate) permeates or is dissolved by a liquid or solid (the absorbent). Note that adsorption is a surface-based process while absorption involves the whole volume of the

material. The term sorption encompasses both processes, while desorption is the reverse of adsorption. It is a surface phenomenon.

14. **Advection** The rate of change of a physical property (e.g. density) caused by the horizontal movement of gas. The advection equation for a conserved quantity described by a scalar field ρ is expressed mathematically by a continuity equation.

$$\frac{\partial \rho}{\partial t} + \nabla \cdot (\rho \mathbf{u}) = 0, \tag{10.0.1}$$

where $\mathbf{u}$ is the velocity field. In case of incompressible flow ($\nabla \cdot \mathbf{u} = 0$), the above equation becomes

$$\frac{\partial \rho}{\partial t} + \mathbf{u} \cdot \nabla \rho = 0. \tag{10.0.2}$$

15. **Compressibility** is a measure of the relative volume change of a fluid or solid as a response to a pressure (or mean stress) change.

$$\beta_F(p) = \frac{1}{F}\frac{\partial F}{\partial p}, \tag{10.0.3}$$

where F represents some physical quantity and p denotes pressure.

16. **The compressibility factor (Z)**, also known as the compression factor, is the ratio of the molar volume of a gas to the molar volume of an ideal gas at the same temperature and pressure.

17. **Knudsen diffusion** is a means of diffusion that occurs when the scale length of a system is comparable to or smaller than the mean free path of

the particles involved. For example in a long pore with a narrow diameter (2 to 50 nm) because molecules frequently collide with the pore wall. Consider the diffusion of gas molecules through very small capillary pores. If the pore diameter is smaller than the mean free path of the diffusing gas molecules and the density of the gas is low, the gas molecules collide with the pore walls more frequently than with each other. This process is known as Knudsen flow or Knudsen diffusion. The Knudsen number is a good measure of the relative importance of Knudsen diffusion. A Knudsen number much greater than one indicates Knudsen diffusion is important. In practice, Knudsen diffusion applies only to gases because the mean free path for molecules in the liquid state is very small, typically near the diameter of the molecule itself.

18. **Mass flow rate** is the mass of a substance which passes through a given surface per unit of time. Its unit is kilogram per second in SI units.

$$\dot{m} = \frac{dm}{dt}. \tag{10.0.4}$$

Mass flow rate is also called mass current, denoted by $I_m = dm/dt$. For the above problem, $\dot{m}_h = \rho q_h$.

19. **Mass flux** is the rate of mass flow per unit area. It is denoted by j_m. Its SI units are kg s^{-1} m^{-2}.

$$j_m = \lim_{A \to 0} \frac{I_m}{A}. \tag{10.0.5}$$

It is also defined as $j_m = \rho\mathbf{u}$, where $\mathbf{u}$ is the velocity field of mass elements flowing.

20. **Volumetric flow rate** is the volume of fluid which passes through a given surface per unit time. The SI unit is m^3 s^{-1} (cubic meters per second). It is usually represented by the symbol Q. Volumetric flow rate should not be confused with volumetric flux, as defined by Darcy's law and represented by the symbol q, with units of m^3/(m^{2}Â·s). The integration of a flux over an area gives the volumetric flow rate.

    $$Q = \frac{dV}{dt}. \tag{10.0.6}$$

    Volumetric flow rate can also be defined by: $Q = v \cdot A$. For the problem in consideration, we have, $q_h = \frac{\pi}{4} D_h^2 v_h$, where, $A_h = \frac{\pi}{4} D_h^2$ is the cross-sectional area of flow tube.

21. **Volumetric flux** is the rate of volume flow across a unit area (m^{3}Â·s^{-1}Â·m^{-2}). Volumetric flux = liters/(second*area). The density of a particular property in a fluid's volume, multiplied with the volumetric flux of the fluid, thus defines the **advective flux** of that property.

22. **Hydraulic properties** are characteristics of a rock such as permeability and porosity that reflect its ability to hold and transmit fluids such as water, oil or natural gas. Shale has a very small particle size so the interstitial spaces are very small.

23. **Critical Temperature** Gases can be converted to liquids by compressing the gas at a suitable temperature. As the temperature increases, the kinetic energies of the particles that make up the gas also increase, and the gases become more difficult to liquefy. The critical temperature of a substance is the temperature at and above which vapor of the substance cannot be liquefied, no matter how much pressure is applied. For example, the critical temperature of water is 374Â°C and carbon dioxide is 31.2Â°C.

    Critical temperature represents the temperature above which distinct liquid and gas phases do not exist. As the critical temperature is approached, the properties of the gas and liquid phases become the same, resulting in one phase known as supercritical fluid. The critical temperature value is used in the definition of reduced temperature ($t_r = t/t_c$) which in turn is used directly in correlations or equations of state to determine various PVT properties of natural gases (e.g. viscosity, compressibility, gas compressibility factor, etc.).

24. **Critical Pressure** The critical pressure of a substance is the pressure required to liquefy a gas at its critical temperature. For example, the critical pressure of water is 217.7 atm and carbon dioxide is 73.0 atm.

    Critical pressure represents the pressure above which distinct liquid and gas phases do not exist. As the critical pressure is approached, the properties of the gas and liquid phases become the same, resulting in one phase known as supercritical fluid. The critical pressure value is used in the definition of reduced pressure ($p_r = p/p_c$) which in turn is used directly in correlations or equations of state to determine various PVT properties of natural gases (e.g. viscosity, compressibility, gas compressibility factor etc.).

25. **Types of Rocks** Rocks are divided into three classes, sedimentary, metamorphic and igneous. Composition of sedimentary rocks are explained below.

26. **Sedimentary** are formed when sand and mineral particles, such as shells, pebbles are fused together. Sediments are accumulated in layers, they are soft and easily breakable. Examples are limestone, conglomerate. Hydrocarbons are usually found in sedimentary rocks because these rocks are full of void spaces in which energy-rich carbon compounds can settle.

27. **Shales** are sedimentary rocks and are found abundantly (40%). These are source of natural fuels which are produced through extraction process.

28. **Sandstones** are porous rocks which are formed above shale beds and trap low density carbon compounds. These are created from grains of minerals like quartz bound by other compounds, such as silica. Within sandstones beds, carbon compounds exist in liquid form.

29. **Carbonates** are found in conjunction with shale and are formed usually from the remains of marine life, such as shells, bones combined with other minerals. Since these rocks are full calcium therefore they are further classified into limestone and dolomites.

30. **Extraction** is the process of releasing hydrocarbons from rocks. It is a complex process which sometimes involves heating the kerogen within the shale and then producing liquid oil and gas. Oftentimes, hydraulic fracturing is used to enhance the oil recovery process.

31. **One-at-a-Time (OAT) methodology:** An input parameter is changed while keeping other parameters fixed at the base values. It's effects on the model output are determined and then the input variable is returned to the base value and repeating the process for the other input parameters. Sensitivity is measured by monitoring the changes in the model output and by plotting the results.

Tensor Notation

Bird [20] has given the definition of tensor in the following way. Let $\mathbf{e}_1$, $\mathbf{e}_2$, and $\mathbf{e}_3$ be the unit vectors in the x, y, and z directions respectively. Then a vector $\mathbf{v}$ can be written as $\mathbf{v} = \sum_{i=1}^{3} \mathbf{e}_i v_i$, and a matrix (tensor of rank two) can be written as $\mathbf{A} = \sum_{i=1}^{3} \sum_{j=1}^{3} \mathbf{e}_i \mathbf{e}_j a_{ij}$. Let $\mathbf{u}$ be another vector $\mathbf{u} = \sum_{j=1}^{3} \mathbf{e}_j u_j$, then $(\mathbf{A} : \mathbf{uv})$ is defined as $(\mathbf{A} : \mathbf{uv}) = \sum_{i=1}^{3} \sum_{j=1}^{3} a_{ij} u_j v_i$.

Unit Conversion

Notes

1. The prefixes k (kilo) and M (Mega) stand for 1000 and 1 000 000, respec-

tively.

2. km^3 means cubic kilometer (not thousands of cubic meter).

3. 1000 cubic meters = 10^3 m^3.

4. 1 million cubic meters = 10^6 m^3 (not km^3).

Pressure

- 1 atm = 101,325 Pa = 101.325 kPa
- 1 bar = 100 kPa $\approx$ 1 atm
- 1 atm = 14.503 Psi = 1.01325 bar
- 1 psi = 0.6897 $\times 10^4$ Pa
- 1 kpsi = 6.894 MPa
- 1 Mpsi = 6.894 GPa
- 1 Pa = 1 N/m^2 = 10^{-5} bar

Permeability

- 1 Darcy = 9.869233 $\times 10^{-13}$ m^2
- 1 Darcy = 0.831 m/day
- 1 Darcy = 9.86923 $\times 10^{-9}$ cm^2
- 1 md = 0.9901 $\times 10^{-15}$ m^2

Compressibility

- 1 Pa^{-1} = 6879 psi^{-1}

Viscosity

- 1 cp = 1.0×10^{-3} Pa.s

- 1 Pa.s = 1000 cp

Gas Flow Rate

- 1 bbl/day = 0.1589873 m^3/day = 1.840130×10^{-6} m^3/sec

- 1 m^3/sec = 543439.6505653 bbl/day

- 1 m^3/s = 3049 Mscf/d

REFERENCES

[1] J. H. Abou-Kassem, S. M. Farouq-Ali, and M. R. Islam. *Petroleum Reservoir Simulations*. Elsevier, 2013.

[2] R. Aguilera. Flow units: from conventional to tight gas to shale gas reservoirs. In *Trinidad and Tobago Energy Resources Conference*, 2010.

[3] R. Aguilera. Flow units: From conventional to tight-gas to shale-gas to tight-oil to shale-oil reservoirs. *SPE Reservoir Evaluation & Engineering*, 17(02):190–208, 2014.

[4] E. W. Al-Shalabi, K. Sepehrnoori, and M. Delshad. Numerical simulation of the lswi effect on hydrocarbon recovery from carbonate rocks. *Petroleum Science and Technology*, 33(5):595–603, 2015.

[5] F. Alcrudo and P. Garcia-Navarro. A high-resolution godunov-type scheme in finite volumes for the 2d shallow-water equations. *International Journal for Numerical Methods in Fluids*, 16(6):489–505, 1993.

[6] I. Ali and N. A. Malik. Hilfer fractional advection–diffusion equations with power-law initial condition; a numerical study using variational iteration

method. *Computers & Mathematics with Applications*, 68(10):1161–1179, 2014.

[7] I. Ali, B. Chanane, and N. A. Malik. Approximate solutions of a time-fractional diffusion equation with a source term using the variational iteration method. *arXiv preprint arXiv:1408.2783*, 2014.

[8] I. Ali, N. A. Malik, and B. Chanane. Fractional diffusion model for transport through porous media. In *5th International Conference on Porous Media and Their Applications in Science, Engineering and Industry.* ECI Symposium Series, ECI Symposium Series, 2014.

[9] I. Ali, N. A. Malik, and B. Chanane. Time-fractional nonlinear gas transport equation in tight porous media: An application in unconventional gas reservoirs. In *Fractional Differentiation and Its Applications (ICFDA), 2014 International Conference on*, pages 1–6. IEEE, 2014.

[10] I. Ali, B. Chanane, and N. A. Malik. Compressibility coeffcients of nonlinear transport models in unconventional gas reservoirs. In *The 2015 AMMCS-CAIMS Congress*, pages 1–10. Springer, 2015.

[11] H. Alzer. Sharp upper and lower bounds for the gamma function. *Proceedings of the Royal Society of Edinburgh: Section A Mathematics*, 139(04): 709–718, 2009.

[12] J. D. Arthur, B. Langhus, and D. Alleman. An overview of modern shale gas development in the united states. *All Consulting*, 3:14–17, 2008.

[13] U. Aybar, M. O. Eshkalak, K. Sepehrnoori, and T. W. Patzek. The effect of natural fracture's closure on long-term gas production from unconventional resources. *Journal of Natural Gas Science and Engineering*, 21:1205–1213, 2014.

[14] K. Aziz and A. Settari. *Petroleum reservoir simulation*, volume 476. Applied Science Publishers London, 1979.

[15] T. Barth and M. Ohlberger. Finite volume methods: foundation and analysis. *Encyclopedia of computational mechanics*, 2004.

[16] J. Bear. *Dynamics of fluids in porous media.* Courier Corporation, 2013.

[17] M. Behnia, K. Goshtasbi, G. Zhang, and S. H. Mirzeinaly Yazdi. Numerical modeling of hydraulic fracture propagation and reorientation. *European Journal of Environmental and Civil Engineering*, 19(2):152–167, 2015.

[18] A. A. Benzerga. Micromechanical models of ductile damage and fracture. In *Handbook of Damage Mechanics*, pages 939–962. Springer, 2015.

[19] A. Beskok and G. E. Karniadakis. Report: a model for flows in channels, pipes, and ducts at micro and nano scales. *Microscale Thermophysical Engineering*, 3(1):43–77, 1999.

[20] G. A. Bird. Definition of mean free path for real gases. *Physics of Fluids (1958-1988)*, 26(11):3222–3223, 1983.

[21] R. B. Bird, W. E. Stewart, and E. N. Lightfoot. *Transport phenomena*. John Wiley & Sons, 2007.

[22] G. Bockstiegel. The porosity-pressure curve and its relation to the pore-size distribution in iron powder compacts. In *Modern Developments in Powder Metallurgy*, pages 155–187. Springer, 1966.

[23] S. Boggs. *Petrology of sedimentary rocks*. Cambridge University Press, 2009.

[24] F. Bouchut. *Nonlinear stability of finite Volume Methods for hyperbolic conservation laws: And Well-Balanced schemes for sources*. Springer Science & Business Media, 2004.

[25] C. Boyer, B. Clark, V. Jochen, R. Lewis, and C. K. Miller. Shale gas: A global resource. *Oilfield review*, 23(3), 2011.

[26] W. Brace, J. B. Walsh, and W. T. Frangos. Permeability of granite under high pressure. *Journal of Geophysical research*, 73(6):2225–2236, 1968.

[27] A. Bressan, G. G. Chen, M. Lewicka, and D. Wang. *Nonlinear Conservation Laws and Applications*, volume 153. Springer, 2011.

[28] M. Caputo. Diffusion of fluids in porous media with memory. *Geothermics*, 28(1):113–130, 1999.

[29] P. C. Carman and P. C. Carman. *Flow of gases through porous media*. Butterworths Scientific Publications London, 1956.

[30] Y. Chang, G. A. Pope, and K. Sepehrnoori. A higher-order finite-difference compositional simulator. *Journal of Petroleum Science and Engineering*, 5 (1):35–50, 1990.

[31] G. Chavent and Jérôme Jaffré. *Mathematical models and finite elements for reservoir simulation: single phase, multiphase and multicomponent flows through porous media*. Elsevier, 1986.

[32] L. Chen, L. Zhang, Q. Kang, H. S. Viswanathan, J. Yao, and W. Tao. Nanoscale simulation of shale transport properties using the lattice boltzmann method: permeability and diffusivity. *Scientific reports*, 5, 2015.

[33] W. Chen, H. Sun, X. Zhang, and D. Korošak. Anomalous diffusion modeling by fractal and fractional derivatives. *Computers & Mathematics with Applications*, 59(5):1754–1758, 2010.

[34] Z. Chen. *Reservoir Simulation: Mathematical Techniques in Oil Recovery*, volume 77. SIAM, 2007.

[35] J. Cheng, K. Wang, and T. Liu. A general high-order multi-domain hybrid dg/weno-fd method for hyperbolic conservation laws. *Journal of Computational Mathematics*, 34(1):30–48, 2016.

[36] C. Christou and S. Kokou Dadzie. Direct simulation monte carlo method in porous media with varying knudsen number. *Society of Petroleum Engineers. doi:10.2118/MS*, 2015.

[37] F. Civan. Scale effect on porosity and permeability: Kinetics, model, and correlation. *AIChE journal*, 47(2):271–287, 2001.

[38] F. Civan. Effective correlation of apparent gas permeability in tight porous media. *Transport in porous media*, 82(2):375–384, 2010.

[39] F. Civan. *Porous media transport phenomena.* John Wiley & Sons, 2011.

[40] F. Civan. Improved permeability prediction for heterogeneous porous media by bundle-of-leaky-tubes with cross-flow model. In *5th International Conference on Porous Media and Their Applications in Science, Engineering and Industry.* ECI Symposium Series, ECI Symposium Series, 2014.

[41] F. Civan, C. S. Rai, and C. H. Sondergeld. Shale-gas permeability and diffusivity inferred by improved formulation of relevant retention and transport mechanisms. *Transport in Porous Media*, 86(3):925–944, 2011.

[42] F. Civan, C. S. Rai, C. H. Sondergeld, et al. Shale permeability determined by simultaneous analysis of multiple pressure-pulse measurements obtained under different conditions. In *North American Unconventional Gas Conference and Exhibition.* Society of Petroleum Engineers, 2011.

[43] F. Civan et al. Improved permeability equation from the bundle-of-leaky-capillary-tubes model. In *SPE Production Operations Symposium.* Society of Petroleum Engineers, 2005.

[44] X. Cui, A. M. M. Bustin, and R. M. Bustin. Measurements of gas perme-

ability and diffusivity of tight reservoir rocks: different approaches and their applications. *Geofluids*, 9(3):208–223, 2009.

[45] E. L. Cussler. *Diffusion: mass transfer in fluid systems.* Cambridge university press, 2009.

[46] H. Darcy. *Les Fontaines publiques de la Ville de Dijon.* Dalmount, Paris, 1856.

[47] A. Darishchev, P. Rouvroy, and P. Lemouzy. On simulation of flow in tight and shale gas reservoirs. In *2013 SPE Middle East Unconventional Gas Conference & Exhibition*, 2013.

[48] S. Das. Analytical solution of a fractional diffusion equation by variational iteration method. *Computers & Mathematics with Applications*, 57(3):483–487, 2009.

[49] K. Diethelm. *The analysis of fractional differential equations: an application-oriented exposition using differential operators of Caputo type*, volume 2004. Springer, 2010.

[50] L. S. dos Santos, F. Marcondes, and K. Sepehrnoori. A 3d compositional miscible gas flooding simulator with dispersion using element-based finite-volume method. *Journal of Petroleum Science and Engineering*, 112:61–68, 2013.

[51] M. Dumbser and V. Casulli. A conservative, weakly nonlinear semi-implicit

finite volume scheme for the compressible navier- stokes equations with general equation of state. *Applied Mathematics and Computation*, 272:479–497, 2016.

[52] M. J. Economides, K. G. Nolte, U. Ahmed, and D. Schlumberger. *Reservoir stimulation*, volume 18. Wiley Chichester, 2000.

[53] EIA. Country analysis brief: Saudi arabia, September 2014. URL `http://www.eia.gov`.

[54] A. Elsaid. The variational iteration method for solving riesz fractional partial differential equations. *Computers & Mathematics with Applications*, 60 (7):1940–1947, 2010.

[55] M. O. Eshkalak, U. Aybar, and K. Sepehrnoori. Physics of unconventional shale gas reservoirs for a long-term production perspective. *International Journal of Oil, Gas and Coal Technology*, 10(1):1–22, 2015.

[56] R. D. Evans and F. Civan. Characterization of non-darcy multiphase flow in petroleum bearing formations. report, us doe contract no. Technical report, DE-AC22-90BC14659, School of Petroleum and Geological Engineering, University of Oklahoma, 1994.

[57] R. E. Ewing. *The mathematics of reservoir simulation*. Siam, 1983.

[58] R. Eymard, T. Gallouët, D. Hilhorst, and Y. Naït Slimane. Finite volumes and nonlinear diffusion equations. *RAIRO-Modélisation mathématique et analyse numérique*, 32(6):747–761, 1998.

[59] J. R Fanchi. *Principles of applied reservoir simulation.* Gulf Professional Publishing, 2005.

[60] B. Faybishenko, S. M. Benson, J. E. Gale, and F. Molz. A complex systems approach to describing flow and transport in fractured-porous media. *Fluid Dynamics in Complex Fractured-Porous Systems*, 7(623):5, 2015.

[61] A. V. Fedorov and I. A. Fedorchenko. Mathematical modeling of methane flow in coal beds. *Journal of mining science*, 45(1):9–21, 2009.

[62] B. R. B. Fernandes, A. Varavei, F. Marcondes, and K. Sepehrnoori. Comparison of an impec and a semi-implicit formulation for compositional reservoir simulation. *Brazilian Journal of Chemical Engineering*, 31(4):977–991, 2014.

[63] B. R. B. Fernandes, A. D. R. Gonçalves, E. P. D. Filho, I. da Costa Menezes Lima, F. Marcondes, and K. Sepehrnoori. A 3d total variation diminishing scheme for compositional reservoir simulation using the element-based finite-volume method. *Numerical Heat Transfer, Part A: Applications*, 67(8):839–856, 2015.

[64] C. Fletcher. Computational techniques for fluid dynamics. volume 1-fundamental and general techniques. volume 2-specific techniques for different flow categories. In *Berlin and New York, Springer-Verlag, 1988, p. Vol. 1, 418 p.; vol. 2, 493 p.*, volume 1, 1988.

[65] C. Fletcher. *Computational techniques for fluid dynamics 2: Specific tech-*

niques for different flow categories. Springer Science & Business Media, 2012.

[66] K. Y. Foo and B. H. Hameed. Insights into the modeling of adsorption isotherm systems. *Chemical Engineering Journal*, 156(1):2–10, 2010.

[67] P. Forchheimer. Wasserbewegung durch boden. *Z. Ver. Deut. Ing.*, 45: 1782–1788, 1901.

[68] C. M. Freeman, G. J. Moridis, and T. A. Blasingame. A numerical study of microscale flow behavior in tight gas and shale gas reservoir systems. *Transport in porous media*, 90(1):253–268, 2011.

[69] K. M. Furati. A cauchy-type problem with a sequential fractional derivative in the space of continuous functions. *Boundary Value Problems*, 2012(1): 1–14, 2012.

[70] K. M. Furati, M. D. Kassim, et al. Existence and uniqueness for a problem involving hilfer fractional derivative. *Computers & Mathematics with Applications*, 64(6):1616–1626, 2012.

[71] K. M. Furati, M. D. Kassim, and N. Tatar. Non-existence of global solutions for a differential equation involving hilfer fractional derivative. *Electronic Journal of Differential Equations*, 2013(235):1–10, 2013.

[72] R. Garra, R. Gorenflo, F. Polito, and Z. Tomovski. Hilfer–prabhakar derivatives and some applications. *Applied Mathematics and Computation*, 242: 576–589, 2014.

[73] C. Guo, J. Xu, M. Wei, and R. Jiang. Experimental study and numerical simulation of hydraulic fracturing tight sandstone reservoirs. *Fuel*, 159:334–344, 2015.

[74] C. Guo, J. Xu, K. Wu, M. Wei, and S. Liu. Study on gas flow through nano pores of shale gas reservoirs. *Fuel*, 143:107–117, 2015.

[75] A. D. Gupta, L. W. Lake, G. A. Pope, K. Sepehrnoori, and M. J. King. High-resolution monotonic schemes for reservoir fluid flow simulation. *In Situ;(United States)*, 15(3), 1991.

[76] H. Hajibeygi and P. Jenny. Multiscale finite-volume method for parabolic problems arising from compressible multiphase flow in porous media. *Journal of Computational Physics*, 228(14):5129–5147, 2009.

[77] R. Hanea, G. Evensen, L. Hustoft, T. Ek, A. Chitu, F. Wilschut, et al. Reservoir management under geological uncertainty using fast model update. In *SPE Reservoir Simulation Symposium*. Society of Petroleum Engineers, 2015.

[78] S. Havlin and D. Ben-Avraham. Diffusion in disordered media. *Advances in Physics*, 36(6):695–798, 1987.

[79] J. He. Approximate analytical solution for seepage flow with fractional derivatives in porous media. *Computer Methods in Applied Mechanics and Engineering, Volume 167, Issues 1-2, 1 December 1998, Pages 57-68*, 1998.

[80] J. He. Variational iteration method–a kind of non-linear analytical technique: some examples. *International journal of non-linear mechanics*, 34 (4):699–708, 1999.

[81] E. Hetmaniok, D. Słota, R. Wituła, and A. Zielonka. Comparison of the adomian decomposition method and the variational iteration method in solving the moving boundary problem. *Computers & Mathematics with Applications*, 61(8):1931–1934, 2011.

[82] R. Hilfer. Applications of fractional calculus in physics. 2000. *Word Scientific, Singapore.*

[83] R. Hilfer. Experimental evidence for fractional time evolution in glass forming materials. *Chemical physics*, 284(1):399–408, 2002.

[84] P. A. Hsieh, J. V. Tracy, C. E. Neuzil, J. D. Bredehoeft, and S. E. Silliman. A transient laboratory method for determining the hydraulic properties of tight rocks i. theory. In *International Journal of Rock Mechanics and Mining Sciences & Geomechanics Abstracts*, volume 18, pages 245–252. Elsevier, 1981.

[85] C. Huang, Y. Matsuda, J. W. Gregory, H. Nagai, and K. Asai. The applications of pressure-sensitive paint in microfluidic systems. *Microfluidics and Nanofluidics*, 18(5-6):739–753, 2015.

[86] H. Huang, J. A. Ayoub, et al. Applicability of the forchheimer equation for non-darcy flow in porous media. *SPE Journal*, 13(01):112–122, 2008.

[87] Z. Huang, P. H. Winterfeld, Y. Xiong, Y. Wu, and J. Yao. Parallel simulation of fully-coupled thermal-hydro-mechanical processes in co 2 leakage through fluid-driven fracture zones. *International Journal of Greenhouse Gas Control*, 34:39–51, 2015.

[88] M. K. Hubbert and D. G. Willis. Mechanics of hydraulic fracturing. 1972.

[89] W. Hundsdorfer and J. G. Verwer. *Numerical solution of time-dependent advection-diffusion-reaction equations*, volume 33. Springer, 2003.

[90] IER. Institute for energy research, September 2015. URL `http://www.instituteforenergyresearch.org`.

[91] M. R. Islam. *Unconventional Gas Reservoirs: Evaluation, Appraisal, and Development*.

[92] M. R. Islam, S. H. Moussavizadegan, S. Mustafiz, and J. H. Abou-Kassem. *Advanced petroleum reservoir simulation*, volume 40. John Wiley & Sons, 2010.

[93] H. Jasak. *Error analysis and estimation for the finite volume method with applications to fluid flows*. PhD thesis, Imperial College London (University of London), 1996.

[94] F. Javadpour et al. Nanopores and apparent permeability of gas flow in mudrocks (shales and siltstone). *Journal of Canadian Petroleum Technology*, 48(08):16–21, 2009.

[95] F. O Jones, W. W. Owens, et al. A laboratory study of low-permeability gas sands. *Journal of Petroleum Technology*, 32(09):1–631, 1980.

[96] A. A. Kilbas, H. M. Srivastava, and J. J. Trujillo. *Theory and Applications of Fractional differential equations*. North-Holland Mathematics Studies, Elsevier, 2006.

[97] L. J. Klinkenberg et al. The permeability of porous media to liquids and gases. In *Drilling and production practice*. American Petroleum Institute, 1941.

[98] KPMG. Shale gas–a global perspective. 2011.

[99] N. Kumar. *Compressibility factors for natural and sour reservoir gases by correlations and cubic equations of state*. M.sc. thesis, Texas Tech University, USA, 2004.

[100] A. Kurganov and E. Tadmor. New high-resolution central schemes for nonlinear conservation laws and convection–diffusion equations. *Journal of Computational Physics*, 160(1):241–282, 2000.

[101] R. J. LeVeque. Nonlinear conservation laws and finite volume methods. In *Computational methods for astrophysical fluid flow*, pages 1–159. Springer, 1998.

[102] C. Li, W. Jia, X. Wu, and E. Liu. Transient modeling and simulation of coal bed methane transmission pipeline. *Journal of Computers*, 6(2):329–336, 2011.

[103] D. Li, T. W. Engler, et al. Literature review on correlations of the non-darcy coefficient. In *SPE Permian Basin Oil and Gas Recovery Conference*. Society of Petroleum Engineers, 2001.

[104] Y. Liang, J. D. Price, D. A. Wark, and E. B. Watson. Nonlinear pressure diffusion in a porous medium: Approximate solutions with applications to permeability measurements using transient pulse decay method. *Journal of Geophysical Research: Solid Earth (1978–2012)*, 106(B1):529–535, 2001.

[105] J. Liu, M. Delshad, G. A. Pope, and K. Sepehrnoori. Application of higher-order flux-limited methods in compositional simulation. *Transport in Porous media*, 16(1):1–29, 1994.

[106] L. B. Loeb. *The kinetic theory of gases.* Courier Dover Publications, 2004.

[107] P. Lorinczi, A. D. Burns, D. Lesnic, Q. J. Fisher, A. J. Crook, C. Grattoni, and K. Rybalcenko. Direct and inverse methods for determining gas flow properties of shale. In *SPE/EAGE European Unconventional Resources Conference and Exhibition*, 2014.

[108] P. Macini, E. Mesini, and R. Viola. Laboratory measurements of non-darcy flow coefficients in natural and artificial unconsolidated porous media. *Journal of Petroleum Science and Engineering*, 77(3):365–374, 2011.

[109] R. A. Mahdi, H. A. Mohammed, K. M. Munisamy, and N. H. Saeid. Review of convection heat transfer and fluid flow in porous media with nanofluid. *Renewable and Sustainable Energy Reviews*, 41:715–734, 2015.

[110] M. Mahmoud. Development of a new correlation of gas compressibility factor (z-factor) for high pressure gas reservoirs. *Journal of Energy Resources Technology*, 136(1):012903, 2014.

[111] N. A. Malik, I. Ali, and B. Chanane. Numerical solutions of non-linear fractional transport models in unconventional hydrocarbon reservoirs using variational iteration method. In *5th International Conference on Porous Media and Their Applications in Science, Engineering and Industry*. ECI Symposium Series, ECI Symposium Series, 2014.

[112] V. I. Malkovsky, A. V. Zharikov, and V. M. Shmonov. New methods for measuring the permeability of rock samples for a single-phase fluid. *Izvestiya, Physics of the Solid Earth*, 45(2):89–100, 2009.

[113] F. Marcondes and K. Sepehrnoori. An element-based finite-volume method approach for heterogeneous and anisotropic compositional reservoir simulation. *Journal of Petroleum Science and Engineering*, 73(1):99–106, 2010.

[114] F. Marcondes, L. S. Santos, A. Varavei, and K. Sepehrnoori. A 3d hybrid element-based finite-volume method for heterogeneous and anisotropic compositional reservoir simulation. *Journal of Petroleum Science and Engineering*, 108:342–351, 2013.

[115] F. Marcondes, A. Varavei, and K. Sepehrnoori. An eos-based numerical simulation of thermal recovery process using unstructured meshes. *Brazilian Journal of Chemical Engineering*, 32(1):247–258, 2015.

[116] M. Matyka, A. Khalili, and Z. Koza. Tortuosity-porosity relation in porous media flow. *Physical Review E*, 78(2):026306, 2008.

[117] R. Metzler and J. Klafter. The random walk's guide to anomalous diffusion: a fractional dynamics approach. *Physics reports*, 339(1):1–77, 2000.

[118] R. S. Middleton, J. W. Carey, R. P. Currier, J. D. Hyman, Q. Kang, S. Karra, J. Jiménez-Martínez, M. L. Porter, and H. S. Viswanathan. Shale gas and non-aqueous fracturing fluids: Opportunities and challenges for supercritical co 2. *Applied Energy*, 147:500–509, 2015.

[119] K. S. Miller and B. Ross. An introduction to the fractional calculus and fractional differential equations. 1993.

[120] V. Mohan, S. K. Mishra, S. Sengupta, et al. Fractional derivative approach in pressure transient analysis of multi-porosity fractal reservoir model for shale gas with phase redistribution. In *SPE Offshore Europe Conference and Exhibition*. Society of Petroleum Engineers, 2015.

[121] F. Moukalled, L. Mangani, and M. Darwish. *The Finite Volume Method in Computational Fluid Dynamics*. Springer, 2016.

[122] O. Møyner, S. Krogstad, K. A. Lie, et al. The application of flow diagnostics for reservoir management. *SPE Journal*, 20(02):306–323, 2015.

[123] B. P. Muljadi, M. J. Blunt, A. Q. Raeini, and B. Bijeljic. The impact of porous media heterogeneity on non-darcy flow behaviour from pore-scale simulation. *Advances in Water Resources*, 2015.

[124] E. Müller-Huber, J. Schön, and F. Börner. The effect of a variable pore radius on formation resistivity factor. *Journal of Applied Geophysics*, 116: 173–179, 2015.

[125] C. E. Neuzil, C. Cooley, S. E. Silliman, J. D. Bredehoeft, and P. A. Hsieh. A transient laboratory method for determining the hydraulic properties of tight rocks ii. application. In *International Journal of Rock Mechanics and Mining Sciences & Geomechanics Abstracts*, volume 18, pages 253–258. Elsevier, 1981.

[126] S. Nia, D. Dasani, T. Tsotsis, and K. Jessen. Pore-scale characterization of oil-rich monterey shale: A preliminary study. In *Unconventional Resources Technology Conference*, 2013.

[127] A. S. Odeh et al. Reservoir simulation... what is it. *Journal of Petroleum technology*, 21(11):1–383, 1969.

[128] K. B. Oldham and J. Spanier. *The fractional calculus: theory and applications of differentiation and integration to arbitrary order*, volume 111. Academic press New York, 1974.

[129] James M Ortega and Werner C Rheinboldt. *Iterative solution of nonlinear equations in several variables*, volume 30. Siam, 1970.

[130] Ozlem Ozcan. Fractional diffusion in naturally fractured unconventional reservoirs. 2007.

[131] D. W. Peaceman. *Fundamentals of numerical reservoir simulation.* Elsevier, New York, 2000.

[132] Y. Pinchover and J. Rubinstein. *An introduction to partial differential equations.* Cambridge university press, 2005.

[133] I. Podlubny. *Fractional differential equations: an introduction to fractional derivatives, fractional differential equations, to methods of their solution and some of their applications*, volume 198. Academic press, 1998.

[134] K. Pong, C. Ho, J. Liu, and Y. Tai. Non-linear pressure distribution in uniform microchannels. *ASME-PUBLICATIONS-FED*, 197:51–51, 1994.

[135] A. Prada and F. Civan. Modification of darcy's law for the threshold pressure gradient. *Journal of Petroleum Science and Engineering*, 22(4):237–240, 1999.

[136] F. Qi and L. Losonczi. Bounds for the ratio of two gamma functions. *Journal of Inequalities and Applications*, 2010:204, 2010.

[137] F. A. Radu, J. M. Nordbotten, I. S. Pop, and K. Kumar. A robust linearization scheme for finite volume based discretizations for simulation of two-phase flow in porous media. *Journal of Computational and Applied Mathematics*, 289:134–141, 2015.

[138] R. Raghavan. Fractional diffusion: Performance of fractured wells. *Journal of Petroleum Science and Engineering*, 92:167–173, 2012.

[139] R. Raghavan, C. Chen, et al. Fractured-well performance under anomalous diffusion. *SPE Reservoir Evaluation & Engineering*, 16(03):237–245, 2013.

[140] T. S. Ramakrishnan and P. A. Goode. Measurement of off-diagonal transport coefficients in two-phase flow in porous media. *Journal of colloid and interface science*, 449:392–398, 2015.

[141] E. Rathakrishnan. *Gas Dynamics*. PHI Learning Pvt. Ltd., New Delhi, 2013.

[142] L. A. Raymond. *Petrology: the study of igneous, sedimentary, and metamorphic rocks*. McGraw-Hill Science Engineering, 2002.

[143] J. B. Regnet, C. David, J. Fortin, P. Robion, Y. Makhloufi, and P. Y. Collin. Influence of microporosity distribution on the mechanical behavior of oolithic carbonate rocks. *Geomechanics for Energy and the Environment*, 3:11–23, 2015.

[144] S. Roy, R. Raju, H. F. Chuang, B. A. Cruden, and M. Meyyappan. Modeling gas flow through microchannels and nanopores. *Journal of applied physics*, 93(8):4870–4879, 2003.

[145] N. Saad, G. A. Pope, K. Sepehroori, et al. Application of higher-order methods in compositional simulation. *SPE Reservoir Engineering*, 5(04): 623–630, 1990.

[146] S. Saha Ray and R. K. Bera. Analytical solution of a fractional diffu-

sion equation by adomian decomposition method. *Applied Mathematics and Computation*, 174(1):329–336, 2006.

[147] T. Samardzioska and V. Popov. Numerical comparison of the equivalent continuum, non-homogeneous and dual porosity models for flow and transport in fractured porous media. *Advances in water resources*, 28(3):235–255, 2005.

[148] T. Sandev, R. Metzler, and Z. Tomovski. Fractional diffusion equation with a generalized riemann–liouville time fractional derivative. *Journal of Physics A: Mathematical and Theoretical*, 44(25):255203, 2011.

[149] A. Satter, J. E. Varnon, M. T. Hoang, et al. Integrated reservoir management. *Journal of Petroleum Technology*, 46(12):1–057, 1994.

[150] J. Shi, L. Huang, X. Li, and K. Sepehrnoori. Production forecasting of gas condensate well considering fluid phase behavior in the reservoir and wellbore. *Journal of Natural Gas Science and Engineering*, 24:279–290, 2015.

[151] D. J. Soeder. *Shale gas development in the United States*. INTECH Open Access Publisher, 2012.

[152] C. W. Spencer. Geologic aspects of tight gas reservoirs in the rocky mountain region. *Journal of petroleum technology*, 37(07):1–308, 1985.

[153] H. M. Srivastava and Z. Tomovski. Fractional calculus with an integral op-

erator containing a generalized mittag–leffler function in the kernel. *Applied Mathematics and Computation*, 211(1):198–210, 2009.

[154] Y. Su and J. H. Davidson. A uniform theoretical model for fluid flow and heat transfer in porous media. In *Modeling Approaches to Natural Convection in Porous Media*, pages 9–15. Springer, 2015.

[155] H. Sun, J. Yao, D. Fan, C. Wang, and Z. Sun. Gas transport mode criteria in ultra-tight porous media. *International Journal of Heat and Mass Transfer*, 83:192–199, 2015.

[156] F. Thauvin and K. K. Mohanty. Network modeling of non-darcy flow through porous media. *Transport in Porous Media*, 31(1):19–37, 1998.

[157] K. Vafai. *Handbook of porous media.* Crc Press, 2005.

[158] B. Van Leer. Towards the ultimate conservative difference scheme. ii. monotonicity and conservation combined in a second-order scheme. *Journal of computational physics*, 14(4):361–370, 1974.

[159] B. Van Leer. Towards the ultimate conservative difference scheme. iv. a new approach to numerical convection. *Journal of computational physics*, 23(3): 276–299, 1977.

[160] B. Van Leer. Towards the ultimate conservative difference scheme. v. a second-order sequel to godunov's method. *Journal of computational Physics*, 32(1):101–136, 1979.

[161] B. Van Leer. Towards the ultimate conservative difference scheme. *Journal of Computational Physics*, 135(2):229–248, 1997.

[162] H. Versteeg and W. Malalasekera. *An introduction to computational fluid dynamics: the finite volume method*. Pearson Education, 2007.

[163] J. B. Vesters, P. L. J. Zitha, and E. H. Blandamour. An improved method for the monitoring of the productivity of. 2013.

[164] J. B. Walsh and W. F. Brace. The effect of pressure on porosity and the transport properties of rock. *Journal of Geophysical Research: Solid Earth (1978–2012)*, 89(B11):9425–9431, 1984.

[165] J. Wang, H. Luo, H. Liu, Y. Ji, F. Cao, Z. Li, K. Sepehrnoori, et al. Variations of gas flow regimes and petro-physical properties during gas production considering volume consumed by adsorbed gas and stress dependence effect in shale gas reservoirs. In *SPE Annual Technical Conference and Exhibition*. Society of Petroleum Engineers, 2015.

[166] Y. Wang, B. Yan, and J. Killough. Compositional modeling of tight oil using dynamic nanopore properties. In *SPE Annual Technical Conference and Exhibition*, 2013.

[167] A. Wazwaz. *Partial differential equations and solitary waves theory*. Springer, 2009.

[168] M. Weiss, M. Elsner, F. Kartberg, and T. Nilsson. Anomalous subdiffusion

is a measure for cytoplasmic crowding in living cells. *Biophysical journal*, 87(5):3518–3524, 2004.

[169] J. Wendt. *Computational fluid dynamics: an introduction*. Springer Science & Business Media, 2008.

[170] S. W. Wheatcraft and M. M. Meerschaert. Fractional conservation of mass. *Advances in Water Resources*, 31(10):1377–1381, 2008.

[171] H. Xie, J. Xie, M. Gao, R. Zhang, H. Zhou, F. Gao, and Z. Zhang. Theoretical and experimental validation of mining-enhanced permeability for simultaneous exploitation of coal and gas. *Environmental Earth Sciences*, 73(10):5951–5962, 2015.

[172] J. Xu, R. Jiang, J. Fu, and Y. Jiang. A new numerical simulation method for horizontal well in tight sandstone reservoirs. *Journal of Petroleum Science Research*, 2015.

[173] P. Xu and B. Yu. Developing a new form of permeability and kozeny–carman constant for homogeneous porous media by means of fractal geometry. *Advances in water resources*, 31(1):74–81, 2008.

[174] W. Yu, A. Varavei, and K. Sepehrnoori. Optimization of shale gas production using design of experiment and response surface methodology. *Energy Sources, Part A: Recovery, Utilization, and Environmental Effects*, 37(8): 906–918, 2015.

[175] W. Yu, K. Wu, K. Sepehrnoori, et al. A semianalytical model for production simulation from nonplanar hydraulic-fracture geometry in tight oil reservoirs. *SPE Journal*, 2015.

[176] A. Zhang. *Numerical investigation of multiphase Darcy-Forchheimer flow and contaminant transport during SO_2 co-injection with CO_2 in deep saline aquifers*. Thesis, Georgia Institute of Technology, 2013.

[177] W. Zhang, J. Yao, Y. Gao, Q. Zhang, and H. Sun. Analysis of electrokinetic coupling of fluid flow in porous media using a 3-d pore network. *Journal of Petroleum Science and Engineering*, 134:150–157, 2015.

[178] Y. Zhang, Z. Li, Z. Yu, L. Guo, X. Jin, and T. Xu. Evaluation of developing an enhanced geothermal heating system in northeast china: Field hydraulic stimulation and heat production forecast. *Energy and Buildings*, 88:1–14, 2015.

[179] J. Zheng, L. Zheng, H. Liu, and Y. Ju. Relationships between permeability, porosity and effective stress for low-permeability sedimentary rock. *International Journal of Rock Mechanics and Mining Sciences*, 78:304–318, 2015.

[180] X. Zhou and L. Yao. The variational iteration method for cauchy problems. *Computers & Mathematics with Applications*, 60(3):756–760, 2010.

[181] A. S. Ziarani and R. Aguilera. Knudsen's permeability correction for tight porous media. *Transport in porous media*, 91(1):239–260, 2012.

Vitae

Personal Information

Name	Iftikhar Ali
Nationality	Pakistan
Email	iali@kfupm.edu.sa & iftikharali4u@gmail.com
Permanent Address	Bait-Saida Colony, Rawalpindi Cantt, Pakistan.

Employment

2010-present	Lecturer-B	Department of Mathematics and Statistics King Fahd University of Petroleum and Minerals Dhahran, Saudi Arabia.
2008-2010	Teaching Assistant	Department of Mathematics Syracuse University, Syracuse, USA.
2007-2008	Lecturer	Department of Mathematics International Islamic University Islamabad, Pakistan.
2005-2007	Lecturer	Department of Mathematics Riphah International Univeristy Islamabad, Pakistan.

Education

2016	PhD in Mathematics	King Fahd University of Petroleum and Minerals, Saudi Arabia.
2010	MS in Mathematics	Syracuse University, USA.
2005	MSc & MPhil in Mathematics	Quaid-e-Azam University, Pakistan.

Awards and Scholarships

1. Student Travel Award: For PIRE-CNA 2016 Summer School on New Frontiers in Nonlinear Analysis for Materials, Center for Nonlinear Analysis, Carnegie Mellon University, Pittsburgh, PA June 2-10, 2016.

2. Student Travel Award: For 2015 AARMS-PIMS Summer School in Differential Equations and Numerical Analysis, and Workshop on Domain Decomposition Methods for PDEs held at Dalhousie University, July 01 - August 08, 2015.

3. Student Travel Award: For The 2015 ICIAM at Beijing, China, August 10-14, 2015.

4. Student Travel Award: For The 2015 AMMCS-CAIMS Congress at Waterloo, Ontario, Canada, June 7-12, 2015.

5. SIAM Student Travel Award: For SIAM CSE 2015 conference at Salt Lake City, Utah, March 14-18, 2015.

6. Sustainable Horizons Institute Student Travel Award: For SIAM CSE 2015, Broader Engagement Pilot Mentoring Program, my mentor was Prof. Susan

Minkoff from University of Texas, Dallas.

7. Grunwald-Letnikov Award: Best student paper award won at International Conference on Fractional Differentiation and its Applications, Catania, Italy, 23-25 June 2014.
8. King Fahd University of Petroleum and Minerals, Saudi Arabia PhD Scholarship Award, Fall 2010 - present.
9. Syracuse University, Syracuse, USA MS Scholarship Award, Fall 2008 - Spring 2010

Professional Training and Courses

1. "Workshop on High Performance Computing and GPU Programming", held at Information Technology Center of King Fahd University, February 02 - 04, 2016.
2. "Domain Decomposition Methods for PDEs", held at Dalhousie University, August 03 - 08, 2015. Instructors: M. Gander, University of Geneva and V. Dolean, University of Strathclyde.
3. "Waves and patterns in nonlinear systems", AARMS Summer School held at Dalhousie University, July, 2015. Instructors: R. Carrettero, Sandiego State University and T. Kolokolnikov, Dalhousie University.

4. “Structure-preserving discretization of differential equations”, AARMS Summer School held at Dalhousie University, July, 2015. Instructors: E. Celledoni and B. Owren, Norwegian University of Science and Technology.
5. “ Introduction to Geomechanics and Hydraulic Fracturing in Unconventional Resources”, organized by Society of Petroleum Engineers-Saudi Arabian Section on April 20, 2014.
6. “Research Skill Development in the Kingdom: From Idea to Outcome”, organized by King Abdulaziz City for Science and Technology at KFUPM on Feb 12, 2014.
7. “Getting Started with Blackboard 9.1”, organized by Deanship of Academic Development, KFUPM on September 4, 2013.
8. “Introduction to MYMATHLAB PLUS-Online Teaching Tool”, organized by Department of Mathematics and Statistics, KFUPM.